Measurements and Modelling of a Novel Oil-free Refrigeration System

Zhaohua Li

A thesis submitted to the University of Sussex

For the degree of Doctor of Philosophy

October 2020

Declaration

I hereby declare that this thesis has not been and will not be, submitted in whole or in part to another University for the award of any other degree.

Signature:.....

Date:.....

Abstract

Vapour compression refrigeration (VCR) system is one of the most commonly used refrigeration methods for domestic refrigeration, heat pump, and automobile air conditioning. The ever rapid rise in the number of VCR units causes a dramatic increase in energy demand and greenhouse emissions, which results in a significant contribution to the global warming. To mitigate the greenhouse gas emission and improve energy efficiency, high efficiency and low carbon oil-free refrigeration system with capacity modulation can be considered as a potential solution for VCR units. A novel oil-free refrigeration system (ORS) is introduced in this thesis. The performance of the ORS has been experimentally and numerically investigated.

The ORS consisting of two balanced novel oil-free linear compressors, an off-the-shelf water-cooled coaxial condenser and an evaporator with an electric heater has been instrumented. A series of experiments have been carried out over a wide range of test conditions to investigate the performance of the linear compressor using R134a. At a compressor stroke of 11 mm and a pressure ratio of 2.0, the oil-free linear compressor can achieve a volumetric efficiency of 71%. The oil-free linear compressor is capable of capacity modulation in response to heat load. Part load efficiency is even higher. An analytical model of the linear compressor has been developed.

The drop-in performance of R1234yf for R134a system also has been experimentally investigated using the ORS test rig. At a condenser temperature of 40 °C, the coefficient of performance (CoP) of R1234yf is 5-20% lower than R134a.

The effect of the refrigerant charge and refrigerant distribution for the ORS using R134a has been experimentally evaluated. The experimental results show that an optimal refrigerant charge, which allows the system to achieve the highest efficiency, varies with operating conditions. A higher compressor stroke and a lower pressure ratio tend to have a higher optimal refrigerant charge.

To provide the numerical ORS model with evaporation heat transfer and pressure drop of refrigerants, two existing correlations for heat transfer and pressure drop for R1234yf, R152a and R134a have been improved based on the experimental data. Overall, the modelling results agree well with the measurements.

A comprehensive numerical system model for the ORS consisting of linear compressor model, a heat exchanger model, and a refrigerant distribution model has been proposed using MATLAB and Simulink. The model is able to predict mass flow rate, power input, pressure drop and heat transfer in heat exchangers, and CoP of the refrigeration system. Overall, the modelling results agree well with measurements. The numerical model can be used for future work on low charge ORS design using oil-free linear compressor and microchannel heat exchangers for various applications.

Acknowledgements

First and foremost, I would like to thank my supervisors, Dr. Kun Liang, for his patience, guidance, encouragement, and inspiration throughout my study. Without his supervision and extensive experience, it would be impossible for me to complete the project work and this thesis. I have learned a lot from him, not only about academic knowledge but also about how to be a researcher.

I would like to thank my colleagues in Richmond 3A1, Ce Liang, Hanying Jiang, Tom. Nasbwa Kigezi, and Zhennan Zhu for their support. They always tried their best to help me when I had a problem and helped me to conduct experiments and analyze data. I also shall take this opportunity to thank technicians Andy White, Mark Lands, and Barry Jackson for providing technical support for my experiments.

At last, my special thanks should be given to my family. I would like to thanks my parents for their company, advice, and support during my study. I also would like to thank my grandparents for their understanding and long waiting.

Contents

Nomenclature

Acronyms

3D	3-Dimensional
AC	Alternatging current
ASHRAE	American Society of Heating, Refrigerating and Air-Conditioning Engineers
CFC	Chlorofluorocarbon
CFD	Computational fluid dynamics
CoP	Coefficient of performance
DAQ	Data acquisition device
DC	Direct current
EER	Energy efficiency ratio
FFT	Fast Fourier transform
GWP	Global warming potential
HFC	Hydrofluorocarbon
LabVIEW	Laboratory Virtual Instrument Engineering Workbench
LVDT	Linear variable differential transducer
MAE	Mean absolute error
MAPE	Mean absolute percentage error
MATLAB	Matrix Laboratory
Nu	Nussel number
ODP	Ozone depletion potential
ORS	Oil-free refrigeration system
PID	Proportional-integral-derivative
PR	Pressure ratio
Pr	Prandtl number
P-V	Pressure-volume
PWM	Pulse-width-modulation
Re	Reynold number
REFPROP	Reference Fluid Thermodynamic and Transport Properties Database
RLC	Resistor, inductor, and capacitor
RMS	Root mean square
SR	Stroke ratio
VCR	Vapour compression refrigeration

Greek

α	Shaft force constant/void fraction

β	Thrust coefficient
γ	Isentropic index
δ	Liquid film thickness
ζ	Damping ratio
η	Efficiency
θ	Phase difference between velocity and motor force acquiring
κ	Thermal conductivity
μ	Viscosity
ρ	Density
σ	Surface tension
ϕ	Phase in each harmonic term
ϕ	Phase lag
ω	Frequency

Roman

A	Area
C	Constant/capacitance
c	Clearance ratio
D	Diameter
f	Frequency
F	Force
G	Mass flux
h	Enthalpy
I	Current
k	Stiffness
L	Length
m	Mass
$\dot{m}$	Mass flow rate
n	Polytropic index
P	Pressure
$\dot{Q}$	Cooling capacity
R	Specific gas constant or resistance
S	Stroke
t	Time
T	Temperature
u	Average velocity of vapour
V	Voltage/volume
$\dot{W}$	Power
X	Martinelli parameter
x	Displacement
$\dot{x}$	Velocity
$\ddot{x}$	Acceleration

Subscripts

c	Cooling
clr	Clearance
cop	Copper
comp	Compensation
dis	Discharge
full	Full
g	Gas
in	Input or inlet
m	Motor or mechanical
o	Operating
rms	Root mean square
shaft	Shaft
suc	Suction
min	Minimum
max	Maximum
l	Liquid
o	Outter
i	Inner
annular	Annular
tw	Two-phase
h	Hydraulic
f	Frictional/flow
out	Outlet
w	Wall
r	Refrigerant
dis	Discharge
1	Evaporator inlet or compression outlet
2	Evaporator outlet or compression inlet

List of Figures

List of Tables

Chapter 1 Introduction

1.1 Background

As modernization progresses, industrialization and the advancement of living standards lead to increased energy consumption, which in turn leads to rapid increase of greenhouse emissions. Air conditioning and refrigeration are two of the most substantial causes of energy demand. In the UK, the refrigeration and air conditioning industries consume approximately 16% of UK electricity and are responsible for up to 10% of UK greenhouse gas emissions **[1]**. In Europe, about 40% of the overall energy usage is consumed for cooling and heating **[2]**. In the US, electricity use for residential and commercial cooling is responsible for a share of approximately 10% of the total US electricity consumption **[3]**. In Malaysia, refrigerators and air conditioners use 22% and 14% of energy, respectively **[4]**. In China, the building sector accounts for over 40% of China's total energy use while air conditioning comprises approximately 47% of operational energy consumption in buildings across the country **[5, 6]**. Refrigeration units contribute to greenhouse emission through energy consumption and refrigerant leakage. Francis et al. **[7]** stated that fluorinated gases (F-gases), which contribute to global warming, will increase total anthropogenic CO_2 emissions from approximately 1.3% in 2004 to 7.9% by 2050. Thus, using eco-friendly refrigerants and improving efficiencies for refrigeration system have significant impacts on the energy and environment.

1.2 Vapour Compression Refrigeration System

Any process that removes heat can be defined as refrigeration. For centuries, melting ice is one of the typical methods for refrigeration. With William Cullen's first demonstration of an artificial refrigeration system in 1755 and Jacob Perkins' invention of the first prototype refrigerator in 1834 **[8]**, the refrigeration industry has been phasing in the

development over decades. Several technologies have been proposed for refrigeration such as vapour compression refrigeration (VCR) system, thermoelectric, and absorption cooling system. Bansal and Martin **[9]** conducted a comparative study on a VCR system, a thermoelectric system, and an absorption system and found that the VCR system is the most energy efficient and the least expensive unit among the three systems. Liang et al. **[10]** compared a heat pipe, a thermoelectric system, and a VCR system for electronic cooling. Results indicate that the VCR system has much higher cooling capacity and coefficient of performance (CoP) than the thermoelectric system. Benefitting from high efficiency, simple structure, wide operating temperature range, and high system reliability, VCR systems have been widely used will likely continue to be the dominant cooling technology in the foreseeable future **[11]**. A typical VCR system mainly consists of a compressor, a condenser, an expansion valve, and an evaporator as shown in Fig.1.1. The hot-pressured refrigerant vapour is released from compressor and reject heat in condenser. Then the cooled refrigerant liquid flows to evaporator via an expansion valve. The pressure ratio can be adjusted by changing the lift of the expansion valve. After absorbing heat from evaporator, hot low pressure refrigerant vapour flows back to compressor and starts a new cycle.

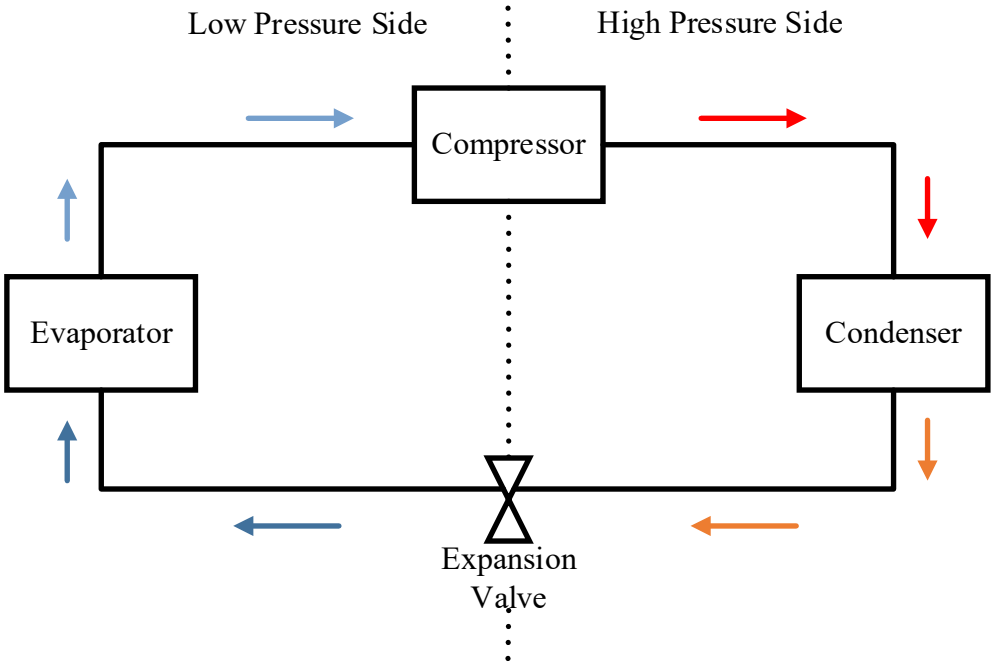

Fig. 1.1 Schematic representation of a VCR system

1.3 Research Aim and Objectives

The aims of this work are to experimentally evaluate the performance of a novel oil-free refrigeration system (ORS) using low GWP refrigerants and novel oil-free linear compressor, and to develop a comprehensive numerical model that could be of significance to future development of ORS for various applications. The aim is achieved through the following objectives:

- To construct and instrument a novel ORS.
- To experimentally and analytically evaluate the performance of linear compressor.
- To experimentally compare the performance between R1234yf and R134a in the ORS.
- To develop correlations of pressure drop and Nusselt number for R1234yf, R152a, and R134a.

- To evaluate the impact of refrigerant charge and refrigerant distribution.
- To develop a comprehensive numerical model for ORS.

1.4 Structure of the Thesis

The thesis is arranged in following sequence:

(1) Chapter 1: background and objectives of the project have been stated. A comprehensive literature review has been presented.

(2) Chapter 2: an ORS consisting of two balanced novel oil-free linear compressors, an off-the-shelf water-cooled coaxial condenser, and an evaporator with an electric heater has been instrumented.

(3) Chapter 3: using R134a, a series of compressor experiments have been undertaken over a wide range of experimental conditions to investigate the performance of the oil-free linear compressor in ORS.

(4) Chapter 4: a simplified analytical model for the linear compressor has been developed to investigate the linear compressor performance under higher pressure ratio using low GWP refrigerants.

(5) Chapter 5: the drop-in performance of R1234yf for R134a system has been experimentally investigated. The elimination of oil lubricant enables comparable test conditions for better evaluating the performance of R1234yf and R134a.

(6) Chapter 6: the effect of refrigerant charge and energy efficiency of the ORS using R134a have been experimentally evaluated. Due to the elimination of oil lubricant in the system, the impact of the refrigerant charge can be better evaluated under comparable test conditions.

(7) Chapter 7: two existing correlations have been improved based on experimental data (Chapter 3 and 5) to predict the Nusselt number and two-phase frictional pressure drop in evaporator for three refrigerants (R134a, R152a, R1234yf).

(8) Chapter 8: a comprehensive numerical model for the ORS consisting of a linear compressor model, a heat exchanger model, and a refrigerant distribution model has been developed. The model can predict mass flow rate, power input, optimal refrigerant charge, pressure drop, heat transfer, and CoP of the ORS. The model can be used to design and prototype any VCR system.

(9) Chapter 9: the conclusions of the project and a list of future work have been presented.

Chapter 2 Literature Review

2.1 VCR System

2.1.1 Recent Development

Low cost, high efficiency, compact structure, and low environmental impact are desired features for VCR systems. Numerous studies have been conducted on sustainable development for VCR systems. A refrigeration unit ordinarily operates under a wide range of conditions due to the variation of ambient temperature and heat loads. The energy can be saved by optimizing the control strategy according to various demands. Two of the most common methods for capacity modulation are on-off control and variable speed compressors **[12]**. On-off cycle is the easiest method for modulating the capacity of the refrigeration system. Li et al. **[13]** developed an optimal compressor on-off control algorithm. Yan et al. **[14]** conducted a theoretical study on a VCR system using on-off control for freezer applications. Improvements are found in volumetric efficiency, cooling capacity, and CoP when using the presented control strategy. Cho et al. **[15]** investigated the performance of a refrigeration system during on-off cycling. An inrush current, however, which is several times higher than normal fill-load current, could be applied on circuit, leading to significant losses and circuit load. On-off cycling losses are responsible for 5-37% of efficiency losses **[16-18]**. Additionally, the refrigerant redistribution process following a start-up gives a temporary condenser fill-up and evaporator superheat, resulting in a capacity loss of 4-30% and an efficiency loss of 1-9% **[19]**.

Compared with fixed-speed compressors, variable speed compressors are able to adjust the rotation speed and utilize less energy. Dechesne et al. **[20]** experimentally investigated the performance of a heat pump with a variable speed compressor. Ekren et al. **[21]** compared different control strategies for variable speed compressors. The results show that the artificial neural network controller presents more stable superheat and evaporator

temperature against to a disturbance comparing with Fuzzy control. This is because the overshoot is small and the stabilization of system parameters is faster for artificial neural network controller. Also, the artificial neural network controller can achieve 6.6% lower power consumption than the Fuzzy controller. Chretien et al. **[22]** studied the energy efficiency of a variable speed compressor and a fixed-speed compressor for a VCR system and concluded that the variable speed compressor provides a 10-25% higher sessional energy efficiency ratio than that of the fixed-speed compressor. Tassou et al. **[23-25]** investigated control methods for the variable speed compressor and concluded that the variable speed compressor achieves a 15% improvement on energy conversion efficiency comparing with conventional on-off system. Though a variable speed compressor can improve the performance through system capacity modulation, it nonetheless needs to be combined with on-off cycling because it is difficult to achieve sufficient reduction of compressor speed to perfectly match the heat load **[19]**. Linear compressor as a type of positive displacement compressor without crank mechanism is able to change the compressor stroke according to the heat load. No on-off cycling loss will be present. Heo et al. **[26]** investigated the capacity modulation of a linear compressor for domestic refrigeration. Lee et al. **[27]** conducted experiments to investigate the performance of an LG type linear compressor and concluded that the linear compressor can easily modulate capacity without causing significant loss between 50-100% of compressor capacity. Though LG type linear compressor can achieve capacity modulation with higher efficiency than that of conventional compressor, the oil lubricant within the linear compressor restricts the further improvement of the efficiency for the LG type linear compressor. In addition, low reliability, high cost, and manufacture also limited the wide application of linear compressors.

Refrigerant charge also represents a significant contribution to system efficiency improvement and energy saving. Overcharged system results in significant refrigerant leakage and reduction of system reliability while undercharged system may cause deterioration of system capacity and efficiency. Rossi et al. **[28]** tested the system

performance of a long-period food storage vertical freezer. The results indicate that a higher refrigerant charge provides a higher mass flow rate resulting in higher electrical consumption. However, due to the limitation of the test rig, the pressure ratio was not controlled at fixed value during the experiments. Kim et al. **[29]** evaluated the impacts of refrigerant charge on air conditioner and heat pump performance. The results show that a refrigerant undercharged in the range of 25% can lead to an average reduction of 20% in cooling capacity and 15% in energy efficiency. Poggi et al. **[30]** reviewed the refrigerant charge in refrigeration system and the strategies of charge reduction, and concluded that an overcharged system causes flooding the condenser resulting in a rise of condenser pressure thus a decrease of volumetric efficiency. Several works were also conducted to minimise the refrigerant charge for refrigeration systems. Shanmugam and Mital **[31]** proposed an ultra-low charge system using R717 for industrial refrigeration. However, the model based on the proposed system was not discussed in details. Palm **[32]** investigated the possibility for decreasing the refrigerant charge in VCR systems and pointed out that low charge systems can be built with capillary tube, microchannel exchanger, and low pressure receivers. Hrnjak and Litch **[33]** pointed out that using microchannel as condenser is the most efficient way to reduce refrigerant charge. Walker and Baxter **[34]** developed a model for large capacity refrigeration systems with minimal refrigerant charge. A 12.6% cost reduction can be achieved by the proposed condenser control method. However, the detailed simulation process was not given in the study. In conclusion, operating VCR systems at optimal refrigerant charge and applying refrigerant reduction technologies can provide significant advantages on the capacity, efficiency, reliability, cost, environmental impact, and stability of VCR systems.

Heat exchanger also have significant impacts on VCR system performance and great contribution to system miniaturization. In recent years, with the increase of the demand for compact systems and high heat transfer coefficient, conventional heat exchangers are unable to meet requirements. Microchannel as a high efficiency and compact heat transfer element is considered as next generation heat exchanger. Microchannel heat exchanger

normally has a small hydraulic diameter (200 μm to 3 mm) and a large contact surface area. Hrnjak and Tu **[35]** tested a rectangular microchannel with hydraulic diameters from 69.5 to 304.7μm and aspect ratios from 0.09 to 0.24. Palaskar **[36]** reviewed the performance of different microchannel condensers and concluded that the round shape microchannel achieved the highest CoP over square and triangle shape. Dollera and Villanueva **[37]** studied the heat transfer coefficient of a minichannel evaporator using R134a. Experimental results show that the minichannel with a diameter of 3.0 mm has the highest heat transfer coefficient. Qi et al. **[38]** experimentally compared the performance of a conventional laminated evaporator and a novel microchannel and pointed out that the novel microchannel evaporator has advantages on volume (17.2% smaller), weight (2.8% lighter), and heat transfer (4.7% higher), with a slightly higher pressure drop. Yan and Lin **[39]** studied the performance of a horizontal circular microchannel with a hydraulic diameter of 2 mm and pointed out that the boiling heat transfer coefficient is a function of vapour fraction and saturation temperature in microchannel. Agostini and Bontemps **[40]** studied the relationship between boiling heat transfer coefficient and hydraulic diameters for a vertical rectangular microchannel. Kwon et al. **[41]** studied the performance of a high-power density microchannel heat exchanger and claimed that thermally developing high-speed air enabled a convention coefficient greater than 2000 W/m^2K. A number of correlations are reported in literature to investigate the characteristics of heat transfer and pressure drop in microchannels. However, large proportion of the correlations are valid for the specific geometry **[42-46]**. Microchannel is also able to reduce refrigerant charge due to the compact structure which can significantly minimise the refrigerant leakage and system cost. One key drawback of microchannel is oil lubricant that exists inevitably in VCR systems using conventional compressors. Microchannel heat exchangers can be easily blocked by oil lubricant due to the extremely small diameter **[47]**, which can limit the application of microchannel for conventional VCR systems. A VCR system without oil lubricants will allow a wider

application of microchannel heat exchangers that can increase the efficiency and reduce the refrigerant charge.

2.1.2 Oil-free Refrigeration System

Nearly all commonly used refrigeration system involves oil lubricants to seal gaps, lubricate the moving parts of compressor, and remove heat produced by the compressor. Oil lubricant frequently escapes from compressor and circulates with refrigerant. Oil film can form at the surface of evaporator when liquid refrigerant fully vaporizes. Thus, oil film inevitably deteriorates the heat transfer coefficient of the evaporator. Crenaschi et al. **[48]** experimentally analyzed lubricant effects on microchannel evaporators working with low global warming potential (GWP) refrigerants. Results show that at a similar mass flow rate, oil retention volume ranges from 6 % to 13% of the microchannel evaporator's internal volume. The heat transfer factor decreases by 13% for R410A. The pressure drop for R410A decreases up to 38% and even worse for low GWP refrigerants. Lottin et al. **[49]** pointed out that CoP decrease can reach 13% with an oil concentration of 5%. Youbi-ldrissi and Bonjour **[50]** reviewed the effect of oil lubricants in refrigeration and pointed out that oil tends to accumulate in the evaporator and suction pipe leading to a reduction of the refrigerating capacity and CoP, especially when the oil circulation ratio increases. Popovic **[51]** mentioned that a lubricant circulation rate of 1% leads to a 4% cooling capacity reduction while a 5% concentration leads to a 30% cooling capacity reduction. Oil lubricated refrigeration systems also require higher refrigerant charge due to the solubility of refrigerants in oil lubricants. 5-40% of refrigerant could dissolve in oil lubricant depending on system temperature, type of refrigerant and oil lubricant **[50, 52, 53]**. Zou et al. **[54]** experimentally investigated the impact of oil lubricants on microchannel evaporator and concluded that the refrigerant distribution is worse than pure R134a flow at low amount of oil circulating in the system. Cremaschi et al. **[55]** conducted experiments to investigate the oil impact on microchannel heat exchanger and pointed out that oil involved flow can have 10-25% higher pressure losses than pure

refrigerant flow. Kuang et al. **[56]** presented an experimental study of the effect of oil lubricants on microchannel heat transfer. The experimental results show that oil addition has significant negative effects on heat transfer coefficient. However, the comparative study between oil-free system and oil lubricated system can be hardly found in literature. Further research is need in this field. Oil-free operation is one of the most desirable features of VCR systems. The advantages of ORS can be summarised as follow:

- Allow the use of microchannel heat exchangers for high efficiency, low weight and low refrigerant charge.
- Enable a wider option of refrigerants and operating conditions.
- Provide significant improvement on heat transfer and pressure drop for heat exchangers.
- Eliminate oil leakage and lubricant aging avoiding refilling, retrofitting and changing for oil lubricants.
- Significantly reduce the refrigerant charge of the system.
- Simplify the refrigeration system due to the abandon of oil separator and oil return line.
- Avoid mechanical breakdown possibility due to oil starvation.

A number of studies on ORS have been conducted by researchers. Lissandrin et al. **[57]** investigated the optimal operation efficiency of a chiller using an oil-free centrifugal compressor. Pearson **[58]** tested an oil-free variable speed centrifugal chiller using R1234ze. Yu et al. **[59]** analyzed the energy performance of an ORS using a centrifugal compressor. The results show that the ORS with variable speed control can reduce the total electricity consumption by 9.6%. Deng et al. **[60]** tested the performance of a variable speed centrifugal chiller with an oil-free magnetic bearing. The experimental

results show that the novel system provides an approximately 29-67% higher CoP than conventional chillers. Yanagisawa et al. **[61]** developed a novel oil-free scroll compressor for refrigeration system and pointed out that the overall efficiency of the compressor can reach 56%. Wang et al. **[62]** tested the reliability of a novel oil-free hermetic scroll compressor for refrigeration and pointed out that the prototype oil-free scroll compressor had been operating reliably for more than 200 hours at a condenser temperature of 55 °C and an evaporator temperature of 5 °C. Peng et al. **[63]** experimentally and numerically studied the performance of a novel oil-free scroll compressor for refrigeration system. Bin et al. **[64]** reviewed recent advances on oil-free scroll compressors and concluded that long-life tip sealing materials can be used to reduce friction coefficient for scrolls and frame. Tian et al. **[65]** numerical studied the mass and heat transfer performance of a refrigeration system using an oil-free screw compressor and R717. Dmitirev et al. **[66]** conducted a comparative study of the energy efficiency for oil-free screw and scroll compressors and concluded that conical screw compressor can be an attractive alternative in micro and small oil-free applications. Tang et al. **[67]** developed a numerical model for an oil-free reciprocating air compressor. Despite many works on ORSs, most of these studies used magnetic bearing **[57-60]**, gas bearing **[62, 67]**, or sealing tips **[57-59, 65-67]** resulting in a heavy weight, high cost and relatively large size. The systems mentioned above are not absolutely oil-free. These systems mainly separated the oil lubricant from the compressed refrigerant. The oil lubricant is confined to the bearing cavities **[65]**.

Unlike conventional reciprocating compressor, linear compressor can drive the piston without crank mechanism. Recent advances in oil-free linear compressor technology have revolutionized the refrigerator technology by achieving fully oil-free operation and superior capacity modulation methods **[68]**.

2.1.3 Alternative Refrigerants

Unavoidable refrigerant leakage in refrigerant units during operation results in a small but growing contribution to overall global warming. The Montreal Protocol restricted the

production and use of chlorofluorocarbons (CFC) as refrigerant due to very high Ozone Depletion Potential (ODP). This led to a shift toward the use of hydrofluorocarbons (HFC). However, HFCs still produce significant emissions causing global warming. In order to further reduce the impact on climate change, traditional HFCs such as R134a are being replaced by lower GWP refrigerants. According to the latest EU F-gas Regulation, all F-gases with GWP of more than 150 will be banned as the refrigerant or foam blowing agent in any hermetically sealed system from 2022 **[69]**. Several low GWP refrigerants such as R717, R600a, R152a, and R1234yf are considered as next generation refrigerants for refrigeration units.

Table 2.1 lists the physical, environmental, and safety characteristics of R134a, R1234yf, R152a, R717, and R600a **[70-73]**. R717 has zero GWP while R1234yf and R600a have a GWP of 4 and 3, respectively, which are both over than 300 times smaller than R134a. R152a has a GWP of 137, which is the highest among four low GWP refrigerants. R717 has the highest latent heat while R1234yf has the lowest. Though R600a has been widely used in domestic refrigerators in Europe, due to the high flammability (A3), the use of R600a in the USA and Japan is restricted **[74, 75]**. R134a, R1234yf, and R152a show similar boiling and critical points. R1234yf and R134a have similar liquid and vapour density, while R152a has an approximately 25% and 50% lower liquid and vapour density than that of R1234yf and R134a. R1234yf and R152a are classified as mildly flammable refrigerant and flammable refrigerant with the ASHRAE safety level of A2L and A2, respectively. Hihara **[76]** pointed out that due to low burning velocity, the flammability of R1234yf is manageable for automobile air conditioning. However, due to higher flammability than that of R1234yf, R152a is not recommended to be used in automobiles **[77]**.

Table 2.1 Physical, environmental and safety characteristics of R134a, R1234yf, R152a, R717, and R600a adapted from **[70-73, 78, 79]**

Properties	R134a	R1234yf	R152a	R717	R600a
Normal boiling temperature (°C)	-26.3	-29.4	-24.02	-33.34	-11.67
Critical temperature (°C)	102	95	113.26	132.4	134.6
Critical pressure (bar)	40.07	33.8	45.2	11.28	36.5
Molar Mass (g/mol)	102	114	66	17	58.12
Latent heat at 30 °C (kJ/kg)	173.1	148.866	273.15	1143	325.2
Liquid density at 30 °C (kg/m^3)	1187.5	1073.3	886.61	595.17	544.31
Vapour density at 30 °C (kg/m^3)	37.535	43.729	21.357	9.0533	10.480
GWP	1430	4	137	0	3
ODP	0	0	0	0	0
Toxicity	No	No	No	Yes	No
Atmospheric lifetime (years)	13	0.03	0.6	0.019	12
ASHRAE safety level	A1	A2L	A2	B2L	A3
OEL (ppmv)	1000	500	1000	1000	25
LEL (vol%)	N/A	6.2	4.8	16	1.8

A number of comparative studies of R1234yf, R152a, R600a, R717, and R134a have been conducted in literature as shown in Table 2.2. Overall, R717 has the highest CoP among five refrigerants due to its high latent heat while R600a provides the second highest CoP due to its low power requirement. R152a has slightly higher CoP than R134a while R1234yf gives a 1-30% deterioration on CoP. Despite a lot of studies on low GWP refrigerants, measurements that have been reported so far all involved oil lubricants for compressors. R1234yf and R152a can be considered as two potential drop-in replacements for the VCR system using R134a as working fluid due to similar thermodynamic properties thus similar system performances.

Oil lubricants inevitably affect the heat transfer in evaporator and condenser thus the overall performance as mentioned in the Section 2.1.2. ORS can eliminate oil impact on

heat transfer and enable comparable test conditions for better evaluating the performance of low GWP refrigerants.

Table 2.2 Performance of refrigeration systems using R134a and low GWP alternatives in literature

Authors	Refrigerants	Conditions	Conclusions
Gond et al. **[80]**	R152a, R600a, R717, R134a	T_{cond}: 45 °C T_{evap}: -25-10 °C	R717, R600a, and R152a have 13.37%, 14.19%, and 1.3% higher CoP than R134a.
Gupta et al. **[81]**	R1234yf, R152a, R717, R134a	T_{cond}: 50 °C T_{evap}: -40-10 °C	The CoP for R1234yf, R152a, R717, and R134a is 2.51, 2.75, 2.73, and 2.65.
Yang and Yeh **[82]**	R1234yf, R152a, R600a	N/A	R1234yf performs the best thermo-economic performance.
Bolaji et al. **[83]**	R152a, R600a, R134a	T_{cond}: 40 °C T_{evap}: -30-10 °C	The average CoP for R152a and R600a is 13.4% and 5.4% lower than R134a.
Paula et al. **[84]**	R1234yf, R600a, R134a	T_{cond}: 45 °C, 50 °C T_{evap}: -30-10 °C	R1234yf, R600a, and R134a provide CoP of 1.85, 2.18, and 2.05, respectively.
Hamza and Khan **[85]**	R1234yf, R152a, R134a	T_{cond}: 40-55 °C T_{evap}: 15 °C	R152a shows 6.3-11% higher CoP than R134a while R1234yf has a 7.6-12% lower CoP.
Sánchez et al. **[86]**	R1234yf, R152a, R600a, R134a	T_{cond}: 25 °C, 35 °C, 45 °C T_{evap}: 0 °C	R152a and R1234yf have relatively the same CoP to R134a, while R600a presents a

			significant reduction on cooling capacity and CoP.
Navarro et al. **[87]**	R1234yf, R134a	T_{cond}: 40~60 °C T_{evap}: -8~7 °C	The cooling capacity of R1234yf is about 9% lower than R134a in the test range. The CoP using R1234yf is 5%~30% lower than R134a in the test range.
Lee and Jung **[88]**	R1234yf, R134a	T_{cond}: 41 °C and 45 °C T_{evap}: -7 °C and 7 °C	The CoP for R1234yf is 0.8%-2.7% lower than R134a.
Cabello et al. **[89]**	R152a, R134a	T_{cond}: 40 °C T_{evap}: -10 °C	The cooling capacity for R152a is 10% lower than R134a while CoP is 13% higher.

2.1.4 Key Challenges

Despite a lot of works on efficiency improvement, miniaturization, and cost reduction of VCR system, a few key issues remain unsolved. These key challenges are listed as follow:

- The use of microchannel for refrigeration system is very challenging due to the oil blockage and oil film in the evaporator. Using refrigerant itself as lubricant or oil-free compressor is potential solution;

- Capacity modulation should be developed to replace on-off operation but variable speed compressor technology inevitably sacrifices the motor efficiency at the off-design-point frequency. It is recommended to use linear compressor instead of conventional compressor due to various strokes and frequencies leading to a wide range of operating capacity with high efficiency;

- Though utilizing microchannel offers significant advantages on system compactness, designing compact compressor without oil lubricants is one key issue for system compactness. Oil-free linear compressor can be a promising choice;

- High cost for magnetic bearing and electric motor restrict the promotion for ORSs. An oil-free compressor with small magnet and simple structure is needed;

- It is possible to further increase the efficiency of refrigeration system by using oil-free linear compressor and compact heat exchangers. However, the only one commercially available linear compressor developed by LG is not oil-free. More research and development will be needed;

- Driven by environmental regulations and sustainable development of refrigeration industry, low environmental impact refrigeration systems using low GWP refrigerants are imperative. Further investigations on the performance of low GWP refrigerants especially under oil-free conditions are necessary;

- Due to the safety concerns and high cost for low GWP refrigerants, minimising refrigerant charge is necessary which needs a comprehensive structure optimization. Microchannel and oil-free linear compressor offer a significant reduction on refrigerant charge by reducing system volume and avoiding refrigerant dissolution.

2.2 VCR System Modelling

Modelling of VCR system helps predict system performance, understand key parameters and optimize system components and structures, build control system and establish control strategies. Table 2.3 lists the VCR system modelling in literature. As can be seen from the literature, most researchers used MATLAB as software for VCR system modelling. MATLAB is capable of achieving computation, visualization, and programing

in a single environment. Researchers can develop a specific numerical model and solve governing equations simply and efficiently. ANSYS CFX also can be used for VCR system modelling. However, due to the software mechanism, massive work needs to be conducted on geometry model and boundary conditions resulting in a sophisticated modelling and calculation process. ANSYS CFX is more suitable for system component simulation rather than system modelling. Several commercial refrigeration system modelling software are also mentioned in the literature as shown in Table 2.3. TRNSYS and IMST-ART are two building performance simulation software which are more suitable for transient system performance modelling. CoolPack is a collection of simulation models for refrigeration system with a specific purpose (cycle analysis, refrigerant performance, energy analysis, etc.) **[90]**. Coildesigner is mainly used for heat transfer performance prediction **[91]**. Though these commercial software are able to predict the performance of VCR system, the highly integrated modelling software are unable to meet the research purposes for specific system design and characteristics. The cost is also considerable. The relationship between intermediate variables cannot be identified thus it will be difficult to optimize the system design. These commercial software are more suitable for investigating a conventional or existing system performance under various conditions rather than investigate and optimize a novel system design. As for theoretical equations for the modelling from literature in Table 2.3, the cooling capacity for most modelling work in the literature is calculated by the product of enthalpy change and mass flow rate according to the predicted mass flow rate and pre-set temperatures and pressures. Very few models use heat transfer correlation to calculate cooling capacity **[92, 93]**. Some models **[94-96]** utilize energy balance equations to predict compressor performance offering a relatively high accuracy. The compressor for these models was considered to be isentropic. A heat transfer model can further improve the accuracy in these studies.

Table 2.3 VCR system modelling in literature

Authors	Modelling software	Working fluid	Model inputs	Conclusion and comments
Kwak et al. **[91]**	CoilDesigner	R410A	$\dot{m}$, T_a	The heat transfer coefficient of heat exchangers with various load conditions were reported; compressor and expansion valve models were not mentioned.
Lei and Zaheeruddin **[92]**	MATLAB	R22	T_{evap}, T_{cond}, P_d, P_s	Theoretical methods were used for compressor modelling; two-phase region is calculated by two-phase length as a function of time.
Yao et al. **[93]**	MATLAB Simulink tool	R134a	h_{hx}, ω_n, P_d,P_s	Theoretical equations were used for mass flow rate calculation; compression process was assumed to be isentropic; Hughmark correlation was used for void fraction calculation in heat exchangers.
Polzot et al. **[94]**	TRNSYS 17	R744	T_{evap}, T_{cond}, P_d, P_s, ΔT_{sp},	The refrigeration model can predict system performance under different climate; two-stage compression were adopted.
Vjacheslav et al. **[95]**	N/A	R410A	T_{evap}, T_{cond}, P_d, P_s, Q,	The proposed model was capable to predict refrigerant distribution of the system.
Liu et al. **[96]**	ANSYS CFX	N/A	N/A	The effects of geometric parameters for heat exchanger were investigated; in order to minimise the calculation process of the compressor, only the representative thin section was modelled.
Tagliafico et al. **[97]**	N/A	N/A	T_a, h_{hx}, η_v, ω_n, Q, P_d,P_s	On-off regulation behaviour was simulated; evaporation and condensation processes were not modelled in detail; a simplified model was used to calculate mass flow rate.
Librado et al. **[98]**	MATLAB	R134a	T_a, $\dot{m}$, P_d, P_s	The lumped model is able to predict compression work and discharge temperature by using

				given mass flow rate; heat transfer to the system from environment was considered; a simplified heat transfer equation was used for heat exchanger.
Roy et al. **[99]**	CoolPack	R152a, R404A, R600a	T_{evap}, T_{cond}, η_{isen}, η_v, ΔT_{sb}	A comparative study of the system performance using three refrigerants were studied; heat exchanger models were omitted.
Siddharth et al. **[100]**	MATLAB	R134a	P_d, P_s, T_{evap}, T_{cond}	Enthalpy changes in the system simply depend on pressures and temperature input; phase change material was applied to improve system performance.
Nasution et al. **[101]**	CoolPack	R600a, R134a	T_{evap}, T_{cond}, P_d, P_s	Numerical simulations were carried out to investigate the system performance using R134a and R600a. Due to the limitation of the modelling software, the model was simplified.
Jackson **[102]**	MATLAB	R134a	ω_n, Q, valve dynamic, water flow rate	A linear model was used to describe a simple VCR system; a linear quadratic regulator was proposed to improve the controller performance; refrigerant phase change was not considered.
Schurt et al. **[103]**	MATLAB	R134a	ΔT_{sp}, P_d, P_s,	An expansion valve model was included, compression work was simply calculated according to the enthalpy change.
Zubair **[104]**	N/A	R134a	T_{evap}, T_{cond}, Q, h_{hx}	The total power input was simply the sum of the compressor work for both subcooling and main cycles; the compressor wasn't fully investigated.
Rasmussen and Alleyne **[105]**	MATLAB	R134a and R744	P_d, P_s, h_{in}	A comprehensive non-linear VCR system model was developed; compression process was assumed to be isentropic process;
Pisano et al. **[106]**	IMST-ART	R290	Pressure ratio,	The refrigerant distribution and impact of heat exchanger

			heat losses, η_v, ω_n	diameters can be predicted using proposed model; mass flow rate was estimated by cylinder volume and rotation speed.

Despite many studies on VCR system modelling have been carried out, most of these studied adopted simplified component models especially for the compressor model **[91-93, 95, 96, 98-100, 104, 106, 107]**, only suitable for high pressure systems **[94],** or assumed isentropic process in the compressor **[92, 93, 100, 103]**. A comprehensive system model including detailed compressor movement, phase change, refrigerant distribution, and pressure drop in heat exchangers allows a realistic simulation result for system optimization. Critical challenges for a comprehensive VCR system model are:

- Heat transfer in compressor cylinder needs to be considered;
- Modelling the system performance requires the correlations of heat transfer and pressure drop in heat exchangers;
- Phase change and fluid region distribution in heat exchangers need to be considered;
- Refrigerant distribution model needs to be integrated into system model to optimize refrigerant charge and component performance;
- An appropriate balance of simplicity and accuracy is needed to avoid a long computation time.

2.3 Linear Compressor

Due to high thermal efficiency, low cost, simple structure, and wide range of applications, reciprocating compressors have been widely used for decades. Several other types of compressors are invented in recent 50 years. However, due to the limitation of their mechanism, these newly developed compressors only work for the specific applications. Centrifugal compressors mainly work for the low pressure system and have low

efficiency for small volumes. Screw compressors are preferred when the power is in the range of 10-500 kW with the discharge pressure below 30 bar **[108]**. Thus, reciprocating compressors will still be a dominated compressor type for VCR systems in the near future.

2.3.1 Comparison with Conventional Reciprocating Compressor

Unlike conventional reciprocating compressor, linear compressor can drive the piston without a crank mechanism. A typical linear compressor as shown in Fig. 2.1 mainly consists of a linear motor, a free piston, suspension springs, and two reed valves. The free piston is directly driven by the linear motor providing significant advantages on efficiency improvement, oil-free operation, miniaturization compared with conventional reciprocating compressor. Several studies have been carried out to compare the performance of conventional crank-driven reciprocating compressors and linear compressors. Park et al. **[109]** conducted comparative studies for the motor efficiency of a linear motor and a rotary induction motor. Experimental results indicate that the linear compressor provides 20-30% higher efficiency than that of the reciprocating compressor with a rotary induction motor. The compressor stroke during the experiments for Park's study is calculated according to input voltage and current. Applying a displacement transducer in compressor to measure the actual stroke can improve the accuracy of the experiments. Ku et al. **[110]** experimentally compared the energy efficiency of a linear compressor and a crank-driven compressor for household refrigerator and concluded that the efficiency of the novel linear compressor has 20% higher than the brushless direct current reciprocating compressor while the cooling capacity is 8% higher. Liang et al. **[111]** experimentally compared the performance of a prototype moving magnet linear compressor with a crank-driven reciprocating compressor. Results show that the novel linear compressor can achieve a motor efficiency of 86% while the conventional reciprocating compressor only provides a motor efficiency of 60%. The overall efficiency of the novel linear compressor ranges from 52-60% while 28-45% overall efficiency is achieved by the conventional compressor. However, a deterioration of the volumetric

efficiency is found for the novel linear compressor comparing with the conventional compressor in Liang's study **[111]** due to the large dead volume for the linear compressor. Another drawback for linear compressor is piston offset as a consequence of clearance leakage between cylinder wall and piston. Due to the piston offset, compressor piston may hit cylinder head resulting in damage to the compressor. Lee et al. **[112]** developed a novel linear compressor for domestic refrigerator. Experimental results show that the power consumption for the proposed linear compressor is 25% and 12% lower than the conventional constant speed and brushless direct current reciprocating compressor. Bradshaw et al. **[113]** compared the energy recovery characteristics of a linear compressor with a crank-driven reciprocating compressor based on the compressor model in Bradshaw et al. **[114]**. Results show that the linear compressor has a unique ability to operate efficiently over a wide range of dead volumes. Lamantia et al. **[115]** carried out both numerical and experimental analysis on a linear compressor. Results show that the linear compressor has higher efficiency than conventional crank-driven reciprocating compressor due to lower friction losses. Bansal et al. **[68]** reviewed advances in household appliances and pointed out that linear compressor offers higher efficiency and a more promising alternative to control the refrigeration capacity. Liang **[116]** summarised the advantages of linear compressor over conventional crank-driven reciprocating compressor as follow:

- Due to the absence of crank mechanism resulting in a reduction of mechanical frictional losses, the mechanical efficiency for linear compressor is higher than conventional reciprocating compressor.

- Oil-free operation can be achieved using linear compressor to improve the heat transfer performance in the evaporator.

- Motor efficiency of linear motor is higher than rotating induction motor.

- Miniaturization can be achieved by reducing compressor stroke and increasing operating frequency for linear compressor.

- Linear compressor can avoid stop-start operation.

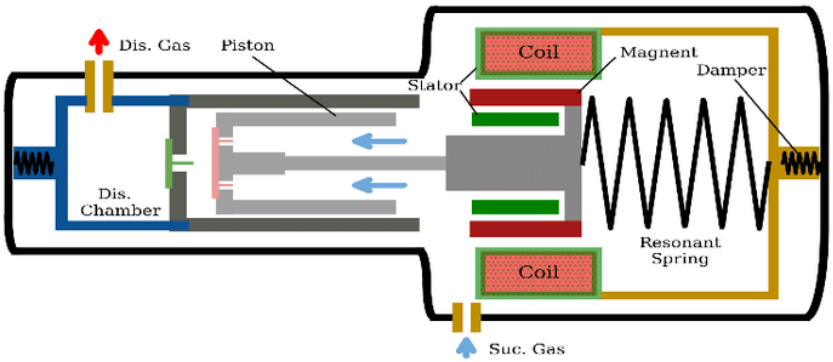

Fig. 2.1 Schematic of a linear compressor adapted from **[117]**

2.3.2 Linear Compressor for VCR System

Linear compressors were firstly used for cryogenic refrigerators such as pulse tube type cryogenic refrigerator. Due to the characteristics of oil-free, compact structure, low frictional loss, and high efficiency, researchers started to investigate the performance of linear compressor for VCR system. Currently, VCR systems using linear compressor mainly focus on domestic refrigeration and electronics cooling. LG company has been licensed Sunpower's linear technology and developed an LG linear compressor for household refrigeration. A mechanical resonant spring such as a leaf spring and coil is used for conventional linear compressor to oscillate the piston. Lee et al. **[118]** tested an LG linear compressor for household refrigerator and claimed that its potential efficiency can reach approximately 80%. Bradshaw **[114]** tested an LG type linear compressor in a refrigerator. Results show that for an evaporator temperature of -5 °C, a 150 W cooling capacity and a 65% isentropic efficiency is achieved. Lee et al. **[119]** utilized an LG type linear compressor for air conditioning as shown in Fig. 2.2. At ASHRAE-T condition,

82.5% of the isentropic maximum energy efficiency ratio can be achieved for the LG linear compressor using R410A. Unger **[120]** tested an LG linear compressor using R600a for domestic refrigeration. Results show that under a freezer condition (-18 °C), a CoP of 2.5 and a cooling capacity of 40 W are achieved while under a fresh food condition (4 °C), a CoP of 3.0 and a cooling capacity of 120 W are achieved. Alzoubi and Zhang **[121]** experimental investigated the performance of a VCR system using a 300 W linear compressor for domestic refrigerator. Experimental results indicate that a high CoP of 4.5 can be achieved for the prototype system. Though the Sunpower type linear compressor is able to achieve oil-free, the LG type linear compressors utilize oil lubricant to reduce friction and remove heat. Also, a high reliability cannot be achieved at large compressor stroke **[122]**. These systems are unable to avoid the oil impact on heat transfer and cannot prevent the blockage of the heat exchanger like conventional VCR systems using crank-driven reciprocating compressors.

Fig. 2.2 LG type linear compressor for air conditioning **[119]**

In order to take advantage of linear motor, a gas spring type linear compressor with gas bearing and a flexure spring was proposed. Zou et al. **[123]** proposed an oil-free linear compressor using R290 for commercial refrigerator as shown in Fig. 2.3 and mentioned that a cooling capacity of 672 W and a CoP of 1.97 is achieved at a condenser temperature of 54.4 °C and an evaporator of -23.3 °C. Zhang et al. **[124]** tested an oil-free linear compressor for domestic refrigeration and pointed out that the overall efficiency decreases from 68% to 55% with the pressure ratio increases from 3.0 to 10.0. Jomde et

al. **[125]** conducted an experimental investigation of the performance of a moving coil oil-free linear compressor for domestic refrigeration using R134a. Experimental results show that with the evaporator temperature changing from -20 °C to 2 °C, the CoP of the system increases from 1.4 to 2.13. Bijanzad et al. **[126]** proposed an oil-free solenoid based linear compressor for household refrigerator. Experimental results show that the linear compressor can achieve an electrical efficiency of 87% and an isentropic efficiency of 47% at the resonant frequency. Bradshaw **[114]** developed a prototype oil -free linear compressor for electronics cooling. This prototype linear compressor mainly aims to validate the compressor model. It only achieves a volumetric efficiency of 24% and an isentropic efficiency of 31%. Possamai et al. **[127]** adopted an Embraco type moving magnet linear compressor and a microchannel heat exchanger in a miniature VCR system using R600a for electronic cooling. Results show that a CoP of 2.55 is achieved at a condenser temperature of 45 °C and an evaporator temperature of 10 °C. Mongia et al. **[128]** proposed a prototype oil-free VCR system for electronics cooling using R600a and linear compressor. Experimental results show that the prototype VCR system is able to obtain a CoP of 2.25. Liang et al. **[129]** conducted experiments to investigate the performance of a novel oil-free linear compressor for electronics cooling using R134a. Experiments show that a CoP of 3.2 and a cooling capacity of 384 W are achieved at an evaporator temperature of 20 °C. Despite a lot of studies on VCR system using oil-free linear compressor, linear compressor with large capacity and using low GWP refrigerants can hardly be found.

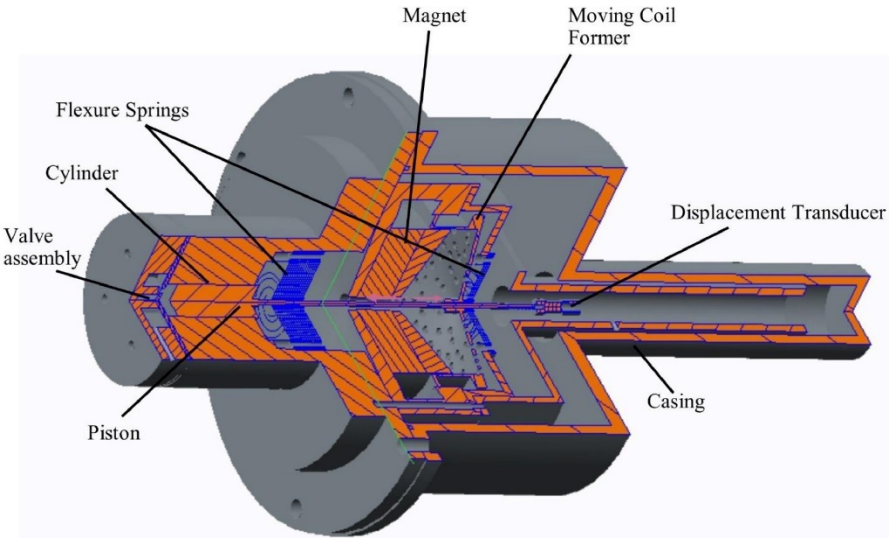

Fig. 2.3 Moving coil linear compressor adapted from Zou **[123]**

2.3.3 Recent Developments for Oil-free Linear Compressor

According to the moving part, linear compressors can be categorized as moving iron linear compressor, moving coil linear compressor, and moving magnet linear compressor. With the development of permanent magnet materials and motor design, moving iron motor (low efficiency) and moving coil motor (high cost and large size) have been gradually phased out. Zhang et al. **[130]** pointed out that the moving magnet type is a major trend of the linear compressor for household refrigerator. Improving linear compressor design and developing more efficient control strategy can improve the performance of the linear compressor for refrigeration.

Leakages through the clearance between piston and cylinder wall results in an unbalance between cylinder pressure and body pressure, and therefore a piston offset. Zou et al. **[131]** experimentally investigated the impact of piston offset and validated a formula proposed by Choe and Kim **[132]**. Liang et al. **[133]** measured the motor efficiency for a novel linear compressor with various dead volumes (piston offset). Results show that the fixed clearance operation requires higher current input thus higher power input. Bradshaw **[114]** pointed out that the piston offset increases with the stroke-diameter ratio of the piston.

Due to the free piston in linear compressors, sensing both piston stroke and piston offset is necessary to prevent damage and achieve capacity modulation. A novel sensor-less stroke detection technique was proposed by Jiang et al. **[134]** to predict the compressor stroke for a novel oil-free linear compressor. A good agreement is achieved between the calculations and measurements by the proposed method. Lee et al. **[27]** developed an lternatging current (AC) voltage controller for linear compressor to control the compressor stroke. Liang et al. **[135]** used a search coil to predict compressor stroke. The compressor stroke can be detected by calculating the peak-to-peak flux linkage in relation to the measured drive voltage and current. The force constant of a novel oil-free linear compressor was measured by Liang et al. **[136]** as shown in Fig. 2.4. The motor force constant decreases with the increase of the absolute value of armature position. The motor force constant is about 35 N/A at an armature position of ±8 mm. A 3D map of the linear compressor as shown in Fig. 2.5 was also developed which can be used to predict the compressor stroke based on the input current **[137]**. More studied on piston control can be found in **[118, 138-141].**

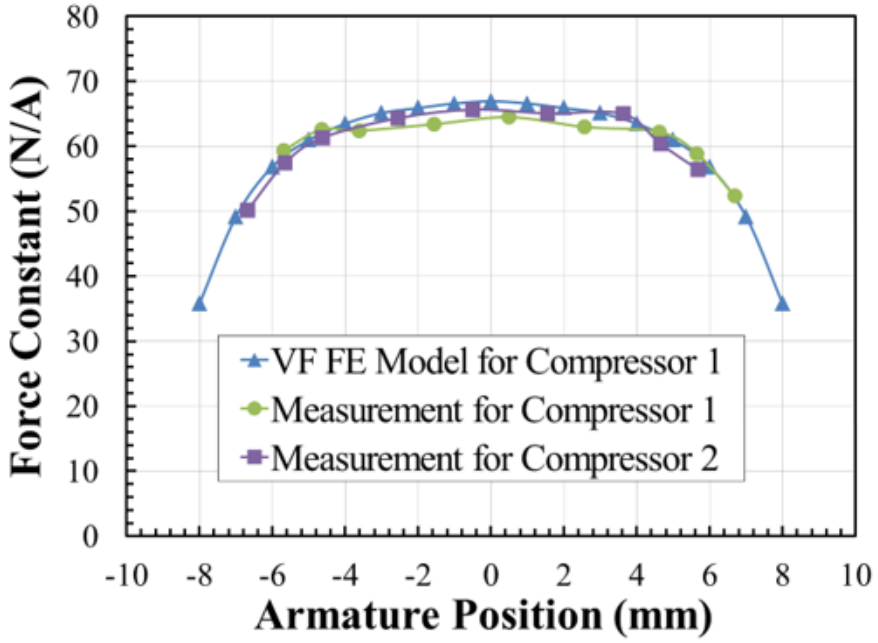

Fig. 2.4 Motor force constant variation with armature position for a novel linear compressor adapted from **[136]**

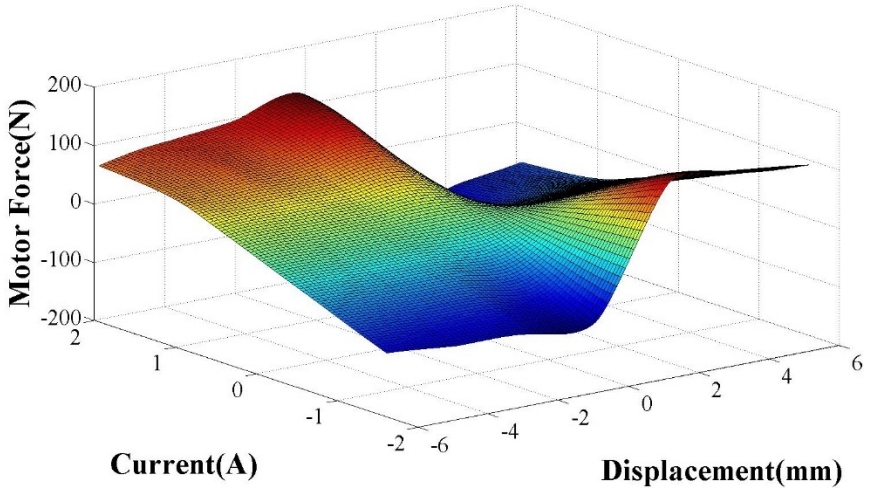

Fig. 2.5 Linear motor Force-Current-Displacement calibration map **[137]**

As mentioned in Section 2.1.1, linear compressor can achieve capacity modulation without stop-start operation by simply changing the compressor stroke. You et al. **[141]** proposed a new expression of compressor stroke with a deviation less than 10% compared with experimental data. Liang et al. **[129]** investigated the relationship of power input and stroke for an oil-free linear compressor. The power input and mass flow rate change linearly with the increase of compressor. Kim and Jeong **[142]** pointed out that the

capacity modulation can be achieved by changing the dead volume (piston offset) of linear compressors.

Operating linear compressors at the resonant frequency can reduce the required input current. Jomde et al. **[143]** conducted a resonance analysis of a valved linear compressor. Dang et al. **[144]** conducted experiments to investigate the effect of operating frequency and cooling temperature on dynamic and thermodynamic characteristics of a moving coil linear compressor for pulse tube cryocooler. Results find out a significant influence of operating frequency on current, power input, cooling capacity, and Carnot efficiency. Dainez et al. **[145]** proposed an adaptive resonant controller for linear compressors. The proposed controller can simultaneously control the amplitude and the phase of the motor current with piston speed. Xia and Chen **[146]** investigated the resonant frequency for a linear compressor using CFD and FEM. Kim et al. **[147]** experimentally and analytically studied the effects of resonant frequency on system performance. A finite element analysis was conducted by Jiang et al. **[148]** to predict the resonant frequency of a novel oil-free linear compressor. Liang et al. **[137]** measured the off-resonance performance of a linear compressor using R134a. The results show that 11% higher power input and 12% CoP reduction are caused by 5% change of operating frequency. The compressor capacity is linearly proportional to the operating frequency. High operating frequency and low compressor stroke provide significant advantages on linear compressor miniaturization without capacity reduction. Further studies on the design of miniature linear compressors for higher frequency are recommended **[116]**.

2.3.4 Linear Compressor Modelling

A comprehensive linear compressor model can evaluate the performance of linear compressors, help the optimization of the design, and provide theoretical knowledges for compressor control strategies. Table 2.4 summarised numerical linear compressor models in literature. Most of these studies utilized piston dynamics and energy balance equations to predict the compressor performance allowing a relatively high accuracy. However,

Liang **[116]** pointed out that a comprehensive model of a linear compressor should include sub-models of dynamics, mass and heat transfer, thermodynamics, coupling of electric and mechanical systems, motor force, pressure drop across valves, piston drift, gas leakage, and very non-linear gas spring. None of the models mentioned in Table 2.4 include all necessary sub-models. Moreover, compressor valve model has significant impacts on simulation accuracy due to the free piston in linear compressor. The in-cylinder pressure and piston displacement can be miscalculated without a proper compressor reed valve model due to the unrestricted compressor piston. Electric model and compressor valves model are rarely mentioned in literature.

Table 2.4 Numerical linear compressor models in literature (MAE is mean absolute error)

Author	Main outputs	Accuracy	Comments
Bradshaw et al. **[114]**	Mass flow rate and piston stroke	Mass flow rate has a 24% MAE; Piston stroke has a 1.3% MAE	Sinusoidal force for the motor was assumed.
Lamantia et al. **[115]**	Cylinder pressure and current	Only numerical	Piston dynamic, heat transfer, and seal leakage were neglected.
Jomde et al. **[125]**	Stroke and cylinder pressure	Cylinder pressure agree well to measurements, predicted stroke has an error rate within 3%	Pressure drop cross valve was neglected.
Kim et al. **[147]**	CoP and resonant frequency	The difference for CoP and resonant frequency is within 3%	Heat transfer and seal leakage in the compressor were neglected.
Davies et al. **[149]**	Mass flow rate, leakage flow rate, and piston displacement	Only numerical	Heat transfer, and valve movement were neglected.
Chen et al. **[150]**	Stroke and magnetic force	Magnetic force has a 20% discrepancy at full stroke	Valve movement, heat transfer, and

			seal leakage were neglected.
Park et al. **[151]**	Energy efficiency ratio (EER)	Simulation results for EER has less than 5% error rate	Piston dynamic, seal leakage, and valve movement were neglected.
Alzoubi et al. **[152]**	Cylinder pressure and leakage flow rate	Only numerical	Piston dynamic was assumed to be sinusoidal motion.

Apart from establishing a numerical model based on first thermodynamic law, several compressor models also were developed using CFD **[153-156]**. These models mainly focus on the heat and mass transfer within linear compressors. However, clearance between cylinder wall and piston in the linear compressor can be less than 10μm requiring extremely fine meshes in the simulation resulting in long calculation time. A comprehensive numerical model of linear compressor is still in demand.

Chapter 3 A Novel ORS and Instrumentation

3.1 System Configuration

3.1.1 Overview

A novel ORS system has been proposed and developed. The ORS mainly consists of two oil-free linear compressors, an off-the-shelf water-cooled coaxial condenser, and an evaporator with an electric heater. A test rig was built to experimentally evaluate the performance of the novel ORS as shown in Fig. 3.1. The test rig was designed for the measurements using various working fluids, e.g. nitrogen, R134a and R1234yf. Primarily, leakage detection and sensor calibration were carried out using nitrogen for the test rig. Then investigations of the system performance of the ORS were carried out using R134a, R1234yf, and R152a. Fig. 3.2 shows the schematic of the instrumentations and test rig. The refrigeration loop is shown as black line in the figure. The hot-pressured refrigerant vapour was released from the compressor to the condenser. After rejecting heat in the condenser, the cooled high-pressure refrigerant liquid flowed to the evaporator via an expansion valve. The pressure ratio was adjusted by the lift of the expansion valve. The liquid refrigerant transformed to superheated refrigerant vapour by absorbing heat from an electric heater in the evaporator. The electric heater simulates the heat load. A bleed flow loop connecting the compressor body and suction line was added to control the piston offset at zero. The bleed flow loop, which is shown as orange line, consists of a solenoid valve, a refrigerant return line, and a proportional-integral-derivative (PID) controller. The refrigerant flowed from the compressor body to the suction line to balance the cylinder and body pressure. Cooling water (blue line) was used to control the condenser temperature during experiments. The water cooling of the condenser is an open-loop. The mass flow rate of the cooling water was controlled by a tap. An oscilloscope was used to monitor the compressor control signal and the duty cycle of

solenoid valve. The bleed flow rate was controlled by changing the duty cycle of the solenoid valve using pulse-width-modulation (PWM) generated by the PID controller. A 12 V direct current (DC) power supplier was used to drive the solenoid valve. The current test rig is a prototype ORS system aiming to evaluate the performance of the ORS using various refrigerants, conventional heat exchangers and prototype linear compressors are used in the system. Microchannel heat exchanger and optimized linear compressor will be used in the future.

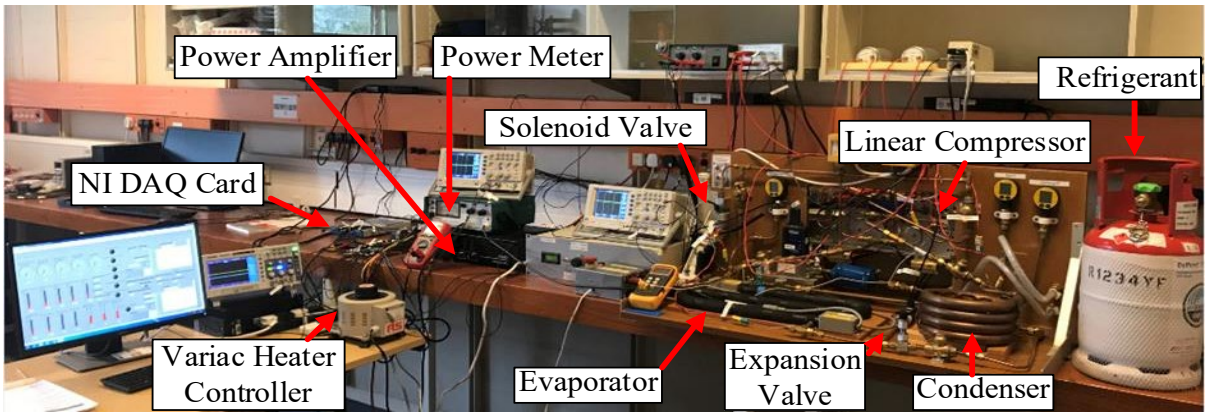

Fig. 3.1 Complete ORS and key components

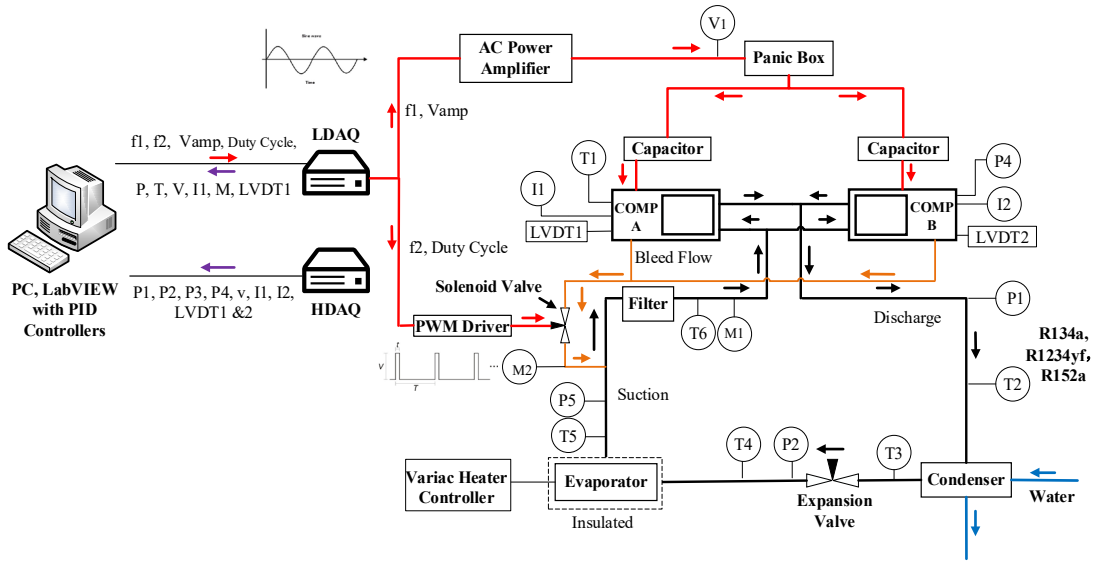

Fig. 3.2 Schematic of the instrumentation (P: pressure transducer; T: thermocouple; $\dot{m}$: mass flow meter; V: voltage sensor, I: current transducer, LVDT: displacement transducer; Black line: refrigeration loop; Orange line: bleed loop; Red line: power supply and control system; Purple line: data acquisition system)

Table 3.1 lists the specification of the key components for the ORS. Two linear compressors were adopted to the system to achieve oil-free operation for the system. The linear compressors were operated in opposite direction to reduce vibration. Conventional heat exchangers were used for the system to evaluate the refrigeration performance. The use of microchannel heat exchangers to reduce refrigerant charge and improve system efficiency is in the scope of future work. Table 3.2 lists the dimensions of pipeline and filter for the ORS.

Table 3.1 Specification of the key components for the ORS

Components	Specifications
Compressor	Two identical oil-free linear compressors working in opposite, piston diameter of 19 mm, maximum compressor stroke of 14 mm, rated power of 100 W for each
Condenser	Coaxial water-cooled, copper, off-the-shelf, coolant connection diameter of 12.7 mm, refrigerant connection diameter of 16 mm
Evaporator	Copper, electric heater (resistance of 50 Ω), length of 128 cm, inner diameter of 7.9 mm, outer diameter of 12.7 mm
Expansion valve	Needle valve, stainless steel medium flow high pressure
Refrigerant	R134a, R1234yf, R152a

Table 3.2 Dimensions of pipeline and filter for the ORS

Section	Length (mm)	Size (mm)	Total volume (mm^3)
Discharge line	1115	d6×0.75	4.76×10^4
	595	d10×1	
Refrigerant liquid line	740	d6×0.75	2.77×10^4
Refrigerant two-phase line	490	d6×0.75	2.46×10^4
Suction line	1400	d10×1	8.31×10^4
	800	d6×0.75	
Filter	120	d=64	3.86×10^5
Bleed flow line	2320	d6×0.75	3.69×10^4

3.1.2 Novel Linear Compressor

Two identical novel linear compressors were employed to achieve oil-free operation. Fig. 3.3 shows the prototype oil-free moving magnet linear compressor and cross section of the linear compressor adapted from **[137]**. The linear compressor mainly consists of a moving magnet linear motor, a flexure spring suspension system, a piston-cylinder assembly and two reed valves. Two linear compressors operate in opposite directions to minimise vibrations. Table 3.3 gives the specifications of the linear compressor.

(a) Prototype oil-free moving magnet linear compressor

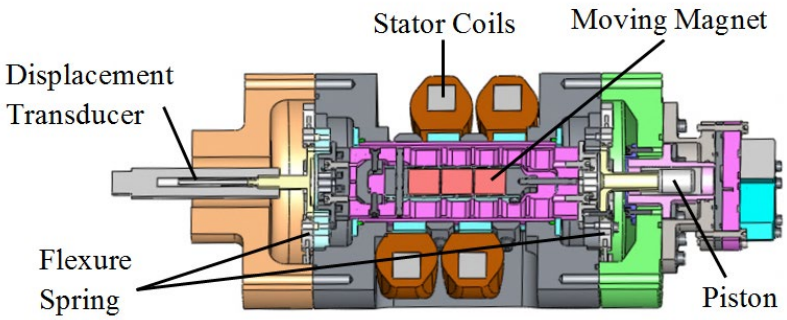

(b) Cross section of the linear compressor

Fig. 3.3 Novel linear compressor configuration adapted from **[137]** (a) Prototype oil-free moving magnet linear compressor; (b) Cross section of the linear compressor and motor

Table 3.3 Linear compressor specifications

Total mass of piston (kg)	0.66
Resistance of coil per compressor (Ω)	3.5
Mechanical spring rate (N/mm)	17
The distance between the datum position and cylinder head (mm)	7.57
Piston diameter (mm)	18.99
Piston length (mm)	31
Maximum stroke (mm)	14
Operating frequency (Hz)	30 – 50
Motor force constant (N/A)	30
Damping coefficient (N•s/m)	0.0475

As mentioned above, two reed valves were adopted in the linear compressor for suction and discharge. Fig. 3.4 shows the valve plate, discharge reed, and suction valve. Due to higher volumetric flow rate at the compressor suction than that of the compressor discharge, the suction reed valve has a larger size than the discharge reed valve. Table 3.4 lists the key parameters of two reed valves.

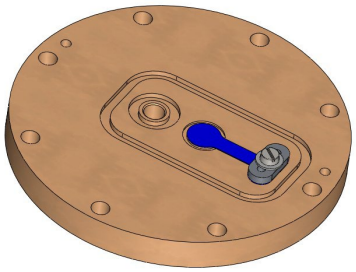

(a)

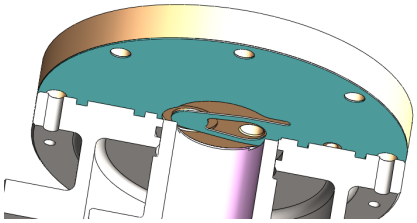

(b)

Fig. 3.4 Discharge and suction valve. (a) View of top surface of valve plate; discharge reed shown blue. (b) Suction valve location.

Table 3.4 Key parameters of compressor valves

Valve name	Discharge valve	Suction valve
Thickness (mm)	0.2	0.3
Length (mm)	14	20
Valve seat Inner diameter (mm)	5	5
Max valve lift (mm)	1.05	1.00
Resonant frequency (Hz)	405	246
Stiffness (N/mm)	0.561	0.361

3.1.3 Heat Exchangers

Fig. 3.5 shows the heat exchangers for the ORS. The condenser is an off-the-shelf water-cooled coaxial copper condenser while the evaporator is an annular evaporator with an electric heater in the middle. By adjusting the power to the electric heater, the heat load can be simulated. The cross section for the evaporator is shown in Fig. 3.6. The evaporator is covered by insulation to prevent the heat transfer from the evaporator to ambient. The detailed parameters for the heat exchangers are listed in Table 3.5.

(a)

(b)

Fig. 3.5 Heat exchangers for the ORS (a) Water-cooled coaxial condenser. (b) Evaporator with heater

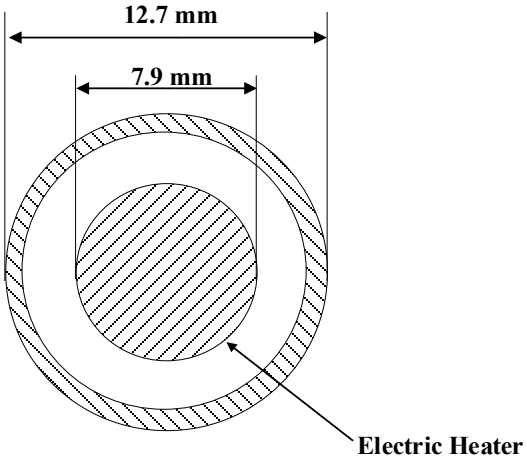

Fig. 3.6 Cross section of the horizontal annular evaporator

Table 3.5 Parameters for heat exchangers

Component	Condenser	Evaporator
Total length (mm)	2325	1280
Inner diameter (mm)	12.7	7.9
Outer diameter (mm)	16	11.9
Material	Copper	Copper

3.2 Instrumentation

3.2.1 Overview

The instrumentation of the ORS consists of a data acquisition system, a power supply system, and a control system as shown in Fig. 3.2. The power and control systems are shown as red line while the data acquisition system is shown as purple line. A filter as shown in Fig. 3.7 was added before the main mass flow rate meter (M1) to prevent damage of the mass flow meter and compressors. Seven temperature transducers, four pressure transducers, two power amplifiers, a current transducer, a voltage transducer, two mass flow meters, a power meter, two linear variable differential transducers (LVDT), three oscilloscopes, and two data acquisition devices (DAQ) were adopted for the test rig. The instruments and their accuracies are listed in Table 3.6. Seven K-type thermocouples were used to measure the temperatures at compressor suction, compressor discharge, condenser outlet, evaporator inlet, evaporator outlet, evaporator wall, and compressor body. The K-type thermocouple has an accuracy of ±1.5 °C **[157]**. The thermocouples were manually calibrated with a temperature meter to ensure the accuracy. The measured temperatures were mainly used to calculate the enthalpy of the refrigerant. As the enthalpy change remains rarely the same for temperature change in the range of 3 °C, the error range for the thermocouple is acceptable. The output voltage of the K-type thermocouple can be small as a few mV voltages. An AD595CQ amplifier was employed to enlarge the temperature signals to 50 mV per °C. Four Druck PMP1400 pressure transducers with an output voltage range of 0-5 V and a gauge pressure of 0-25 bar measured the pressures at compressor discharge, compressor suction, compressor body, and evaporator inlet. The compressor current and voltage were measured by two LA LEM 25-NP current transducers and a Fylde 261 HVA HV voltage attenuator. A power meter was used to record the real power of the electrical heater to be compared with the cooling capacity that can be calculated from pressure-enthalpy diagram (as shown in Fig. 5.5). Two thermal-type mass flow meters (Hastings HFM-201 and a Tylan FM-360) were used to

measure the main flow rate and bleed flow rate, respectively. The output voltage of these mass flow meters ranging from 0-5 V. The gas calibration factors for the two mass flow meters were calculated according to MKS Instruments **[158, 159]** and Hastings Instruments **[160]**. The detailed calculation for gas calibration factors can be found in Appendix A.

Fig. 3.7 Filter for the ORS test loop

Table 3.6 Specifications and accuracies of the instruments for the test rig

Instruments	Model	Quantity	Accuracy (refer to value)
Data acquisition card	NI USB-6341	2	N/A
Current transducer	LA LEM 25-NP	2	± 0.5 %
Voltage attenuator	Fylde 261HVA HV	1	± 0.5 %
Isolation amplifier	Fylde 4600A	1	± 0.5 %
LVDT	Lucas Schaevitz	2	± 0.025 mm
LVDT signal conditioner	ATA-101	2	N/A
Pressure transducer	DRUCK PMP1400	4	±0.15 %
Capacitor	EPCOS B32361	2	± 5 %
AC power amplifier	Vonyx VXA-2000 (class A)	1	± 1.2dB
Thermocouple	K-type	8	± 1.5 °C
Main mass flow meter	Hastings HFM-201	1	± 1 %
Bleed flow meter	Tylan FM-360	1	± 1 %
Oscilloscope	RS Pro IDS1000 Series IDS1072AU	3	N/A
Power meter (heater)	Electronic Wattmeter EW604	1	< 2.5% (50Hz, unity power factor, 25 °C)

Four resistors powered by two DC supplies were placed in series at the bottom of the compressor rack to warm up the compressor body to eliminate refrigerant liquid in the compressors. Two sight glasses as shown in Fig. 3.8 were placed at the outlet of the heat exchangers to monitor the state of leaving fluid. According to the refrigerant state in the evaporator side sight glass, the heat into the evaporator was adjusted by a variac power controller to let the refrigerant fully evaporate to achieve the maximum cooling capacity.

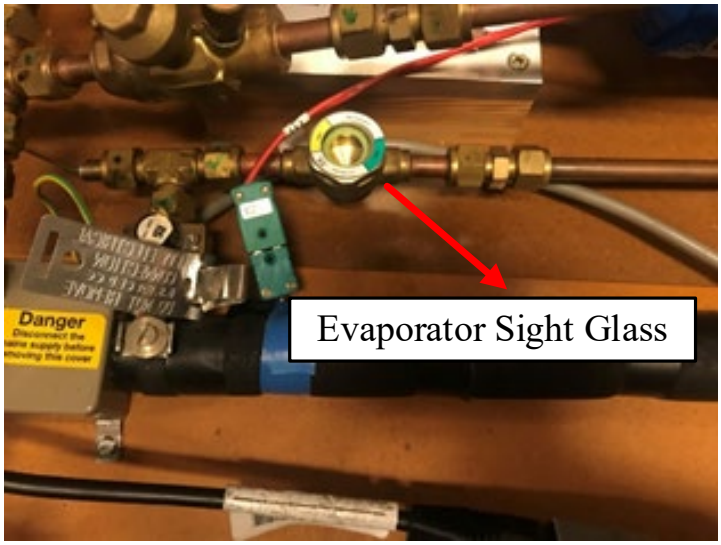

(a) Sight glass at evaporator outlet.

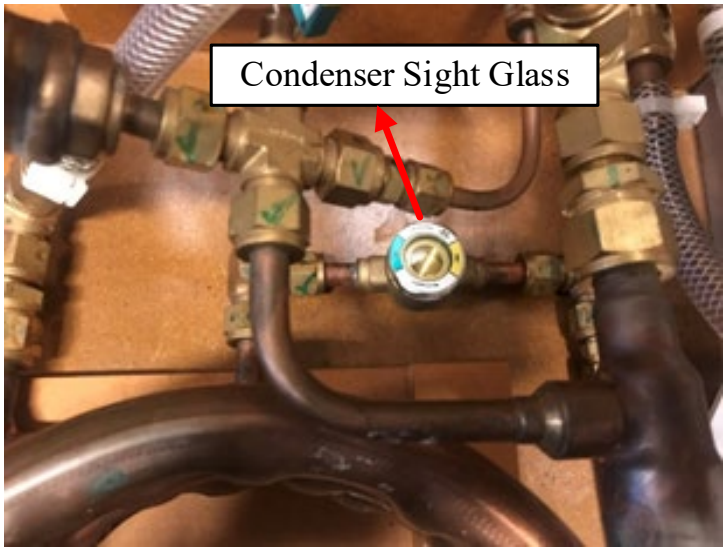

(b) Sight glass at condenser outlet.

Fig. 3.8 Sight glasses for the ORS

3.2.2 Power Supply System

The power supply and control system are shown as red line in Fig. 3.2. The power supply system consists of an alternatging current (AC) power amplifier, two capacitors and a panic box. As the maximum output voltage of DAQ card is 5 V, an AC power amplifier was used to amplify the control signal to drive the linear compressors. Fig. 3.9 shows a typical RLC circuit consisting of a resistor, and inductor, and a capacitor for linear motor adapted from Jiang et al. **[161]**. At resonance, a minimum of impedance was achieved at the resonoant frequency for linear compressors. The voltage waveform and current waveform are in phase at resonance which can minimise the voltage requirement of linear compressors. Normally, a capacitance is employed to achieve the in phase of voltage and current. The capacitance compensation can be calculated according to inductance and operating frequency as follow **[137]**

$$C_{\mathrm{comp}} = \frac{1}{4\pi^2 f^2 L} \tag{3.1}$$

where C_{comp} is the capacitance, f is the operating frequency, and L is the inductance.

Jiang et al. **[161]** also experimentally evaluated the cpacitance compensation for the lienar compressor used in this project with compressor strokes of 8-3 mm and pressure ratios of 1.5-3.0. The experimental results indicate that the cpacitance compensation is around 150 μF among the test conditions. As the experiments were mainly carried out with compressor strokes of 9-13 mm and pressure ratios of 2.0-4.0 for this project, two 150 μF capacitors were adopted to reduce the voltage of the linear compressors. Two oscilloscopes were used to monitor the current, voltage, and displacements of the linear compressors. A panic box, which can be manually pressed to cut down the circuit, was added between capacitors and power amplifier to prevent the damage of the test rig if any emergency occurs.

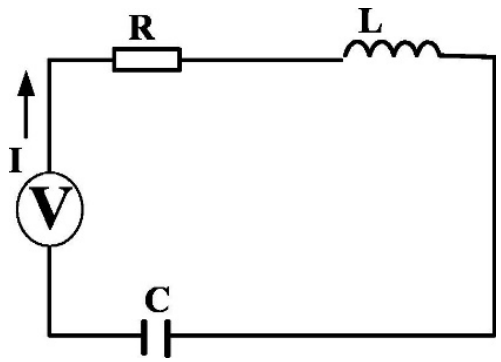

Fig. 3.9 A typical RLC circuit for linear motor **[161]**

3.2.3 Control System

The control system consists of a low-speed data acquisition (LDAQ), a LabVIEW control panel, and two PID controllers. An analogue signal generated by a PID controller in the computer was sent to the AC power amplifier via the LDAQ card to control the compressor stroke. An power amplifier amplified the analogue signal to drive the compressors. Two LVDTs fed back the actual compressor displacement to the controller to improve accuracy. Two PID controllers were developed to control the compressor stroke and piston offset. Fig. 3.10 (a) shows the flowchart of the PID controller for compressor stroke control in the linear compressor. The PID controller can adjust output voltage amplitude based on the difference between the measured compressor stroke and set compressor stroke. The measured compressor stroke can be calculated according to the peak and valley displacement collected by the LVDTs. Fig. 3.10 (b) shows the control panel in LabVIEW for operating frequency and compressor stroke. A waveform graph of the measured compressor stroke amplitude, setpoint for compressor stroke, and control signal amplitude was also added to the control panel as shown in Fig. 3.10 (c). The output signal of the LDAQ and measured compressor stroke can be monitored by this waveform graph. The setpoint for the compressor stroke was set as zero at the beginning for each test. In addition, a continuous analogue signal, which remained the same as the output signal before the program stopped, can be generated by LabVIEW when the control program was stopped. This output signal can drive the compressors continuously without

stroke control leading to damage of the linear compressors. A 'No Stroke' button was added to the LabVIEW program to set the output signal to zero. This button was pressed before stop the program to protect the compressors.

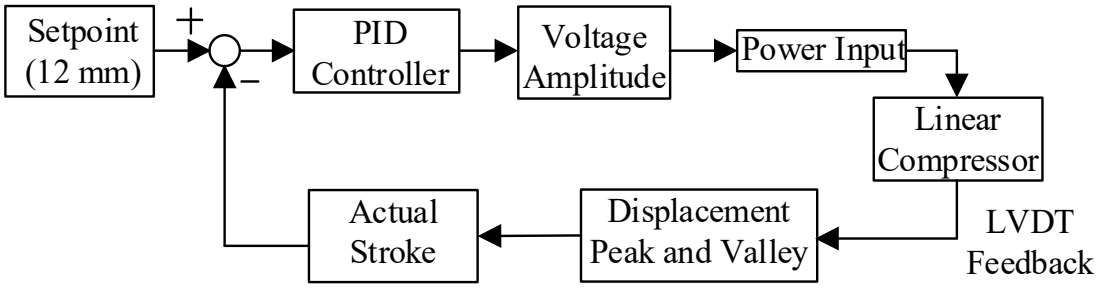

(a) Schematic of the PID controller for the compressor stroke control in the linear compressor

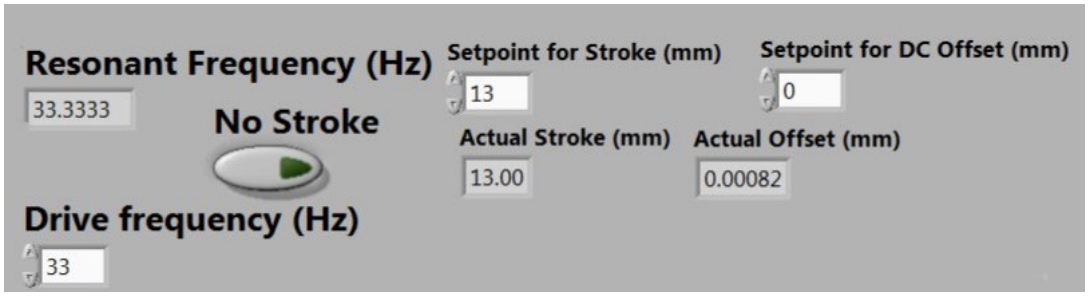

(b) Control panel of the compressor stroke and operating frequency in LabVIEW

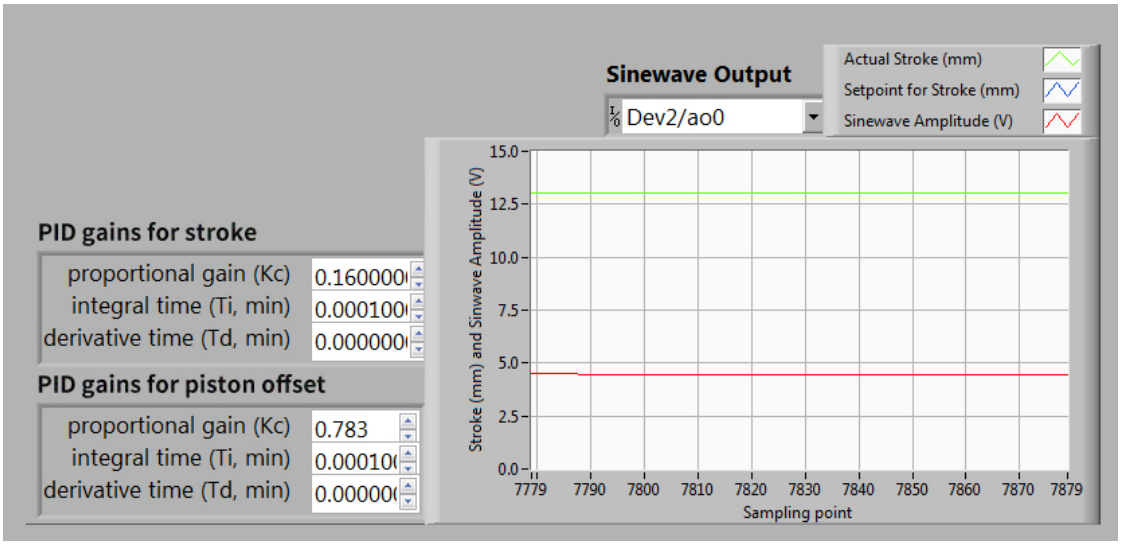

(c) Waveform graph for the compressor stroke and PID gains for piston offset and stroke

Fig. 3.10 Compressor stroke, piston offset, and operating frequency control

As mentioned in Section 3.2.2, linear compressor achieves the highest efficiency at resonance due to minimal voltage requirement. The operating frequency for the linear

compressors was manually adjusted in LabVIEW for each test condition to ensure resonance based on calculated resonant frequency. The linear spring stiffness of the gas k_{g} and resonant frequency f can be calculated as follow **[111]**

$$k_{\mathrm{g}} = \frac{(P_{\mathrm{dis}} - P_{\mathrm{suc}})\pi \mathrm{D_p^2}}{4S} \tag{3.2}$$

where P_{dis} is the discharge pressure, P_{suc} is the suction pressure, S is the compressor stroke, and $\mathrm{D_P}$is the piston diameter.

The resonant frequency f can be calculated as

$$f = \frac{1}{2\pi}\sqrt{\frac{k_{\mathrm{g}} + k_{\mathrm{m}}}{\mathrm{m}}} \tag{3.3}$$

where k_{m} is the mechanical spring stiffness and m is the total mass of the piston and moving assembly.

Due to the net seal leakage from the compressor cylinder to the compressor body, the imbalance force between the mean cylinder pressure and body pressure leads to a piston offset toward cylinder head. Thus, the effective compressor stroke is reduced. Moreover, the linear compressor could be easily damaged if the piston hits the cylinder head. A PID controller together with a solenoid valve and a bleed flow loop were used to control the piston offset at zero. Fig. 3.11 shows the flowchart of the PID controller for the piston offset control. A bleed flow loop was added between compressor body and the suction line of refrigeration loop as shown in Fig. 3.2. Based on the difference between set point and actual piston offset, the controller can adjust the duty cycle of the solenoid valve to adjust the bleed flow rate then body pressure to control the piston offset at zero.

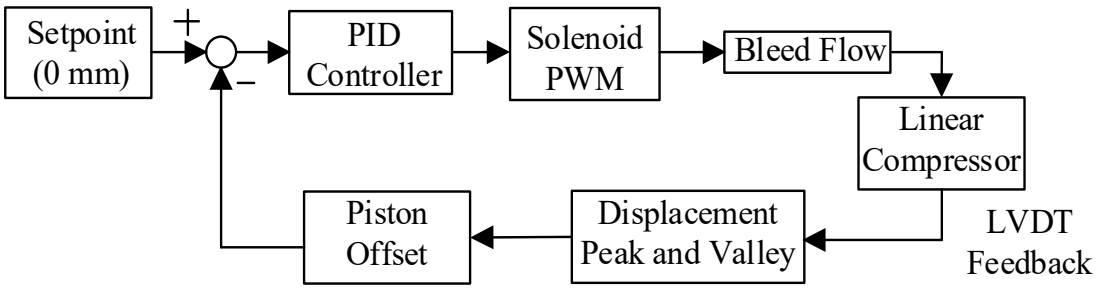

Fig. 3.11 Flowchart of the PID controller for the piston offset control

3.2.4 Data Acquisition System

The data acquisition system is shown as purple line in Fig. 3.2. Parameters including pressures (discharge, suction, body, evaporator inlet), temperatures (discharge, condenser, evaporator inlet/outlet, suction, body), mass flow rates (main flow and bleed flow), currents, and voltage were collected by the LDAQ. High-speed data acquisition (HDAQ) collected data of pressures, voltage, currents, and displacements. Two NI USB-6341 data acquisition cards were employed for the LDAQ and HDAQ. The NI USB-6341 data acquisition card has sixteen analogue inputs and two analogue output channels with a maximum sample rate of 500 kS/s. The input signal range is -5-5 V. Fig. 3.12 shows the front panel of the LDAQ in LabVIEW. The detailed channel allocation for the LDAQ and HDAQ can be found in Appendix B. The sample rate for the LDAQ was set as 2 kS/s. The raw voltage signals for pressures, temperatures, mass flow rates, currents, and voltage were converted to physical values according to the calibration factors in the LabVIEW program. The physical values from 16 LDAQ channels can be then displayed in the front panel.

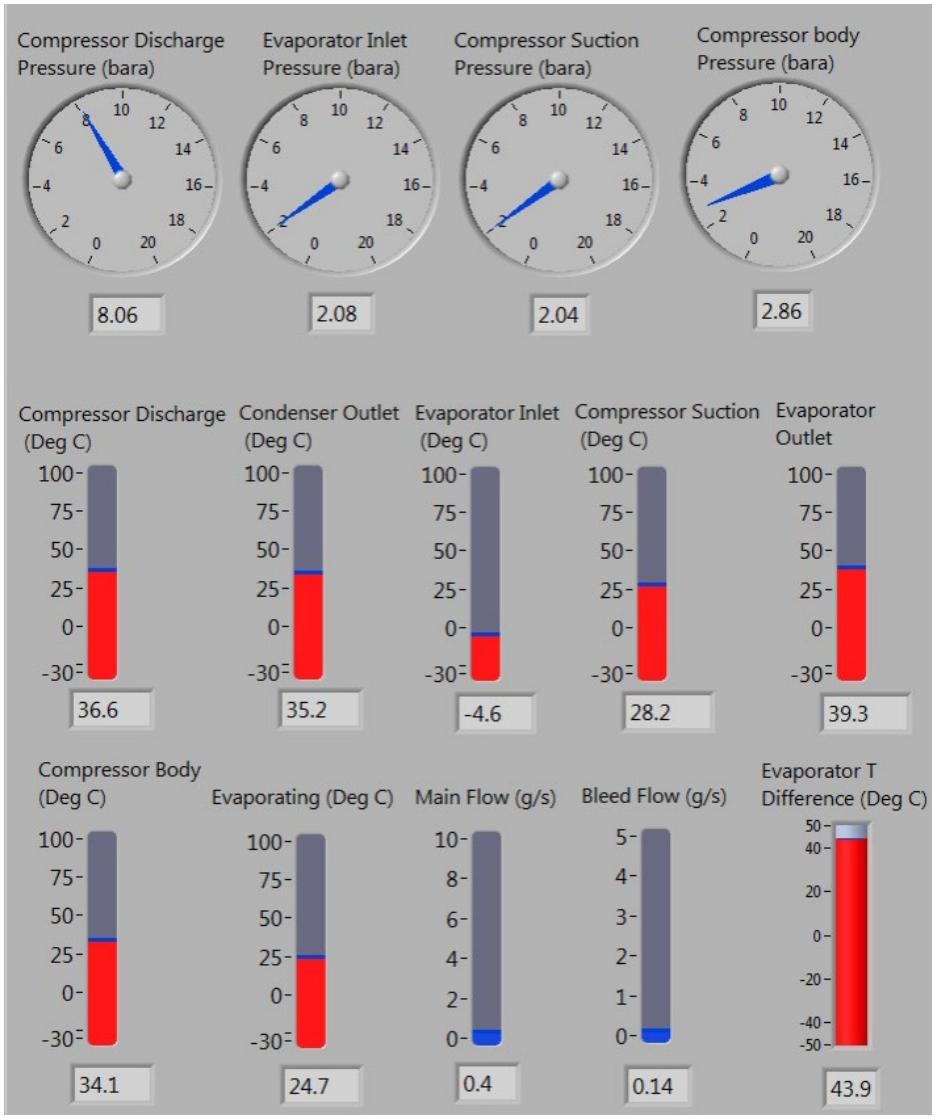

Fig. 3.12 Data displace front panel for LDAQ in LabVIEW

Fig. 3.13 shows the waveform graph for the HDAQ in the front panel of LabVIEW. The raw voltage signals such as pressures, currents, voltage, mass flow rates, and displacement were collected by the HDAQ and shown in graphs. As this panel is mainly used to place the data record button, the waveform for the data mentioned above are not shown in details. According to Nyquist–Shannon sampling theorem, the sampling rate of the HDAQ was 5 kS/s which is 100 times of the highest operating frequency for compressors (50 S/s). A data saving button was set in the HDAQ panel which can be pressed to record the data from the LDAQ and HDAQ. The file name of the recorded data can be filled in ‘file name (C:\data\)’. 400 and 5000 data points can be recorded, respectively, by the LDAQ and HDAQ in .txt files once the ‘write data?’ button was

pressed. In addition, some parameters were recorded manually such as power of the electric heater, duty cycle of solenoid valve, and operating frequency.

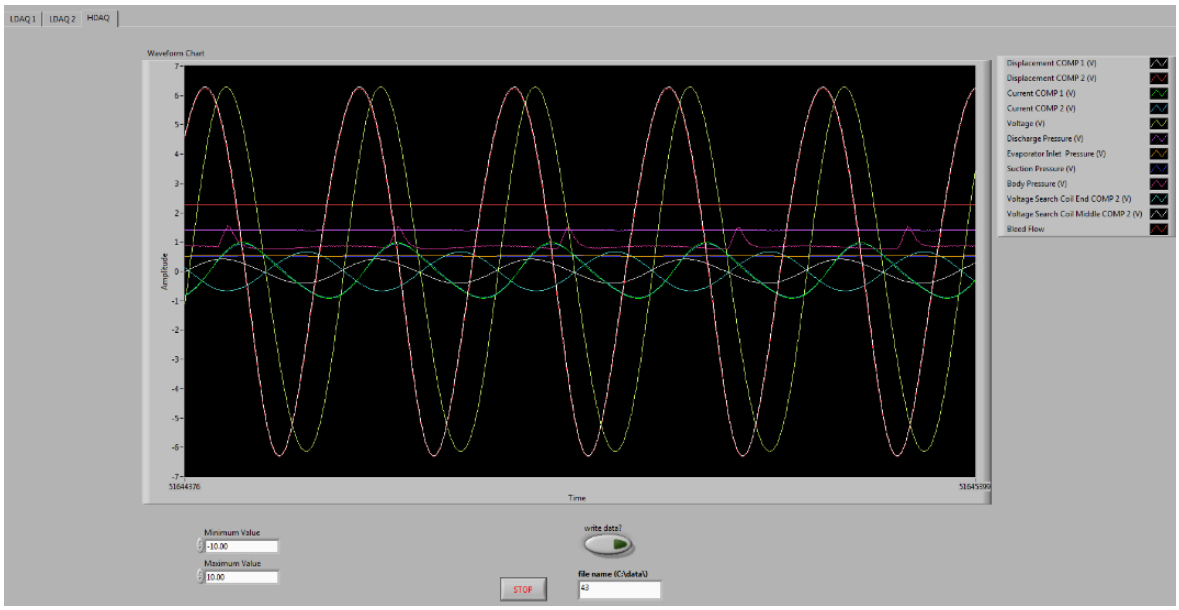

Fig. 3.13 Waveform graph for the HDAQ in the front panel of LabVIEW

3.3 Data Analysis

The manually recorded data such as operating frequency and the data recorded by the LDAQ and HDAQ were imported into a data processing system called ‘Data processing’ in MATLAB. The imported data and results can be saved in ‘LDAQ averaging’, ‘HDAQ calibration’, and ‘Result Summary’ .xls files. Fig. 3.14 shows the flowchart of the data analysis process. All the data from the LDAQ for each channel were averaged to calculate the pressures, temperatures, and mass flow rates at stable situation. Based on pressures, temperatures, and mass flow rates, the cooling capacity, heat transfer coefficient, pressure drop, and CoP can be determined.

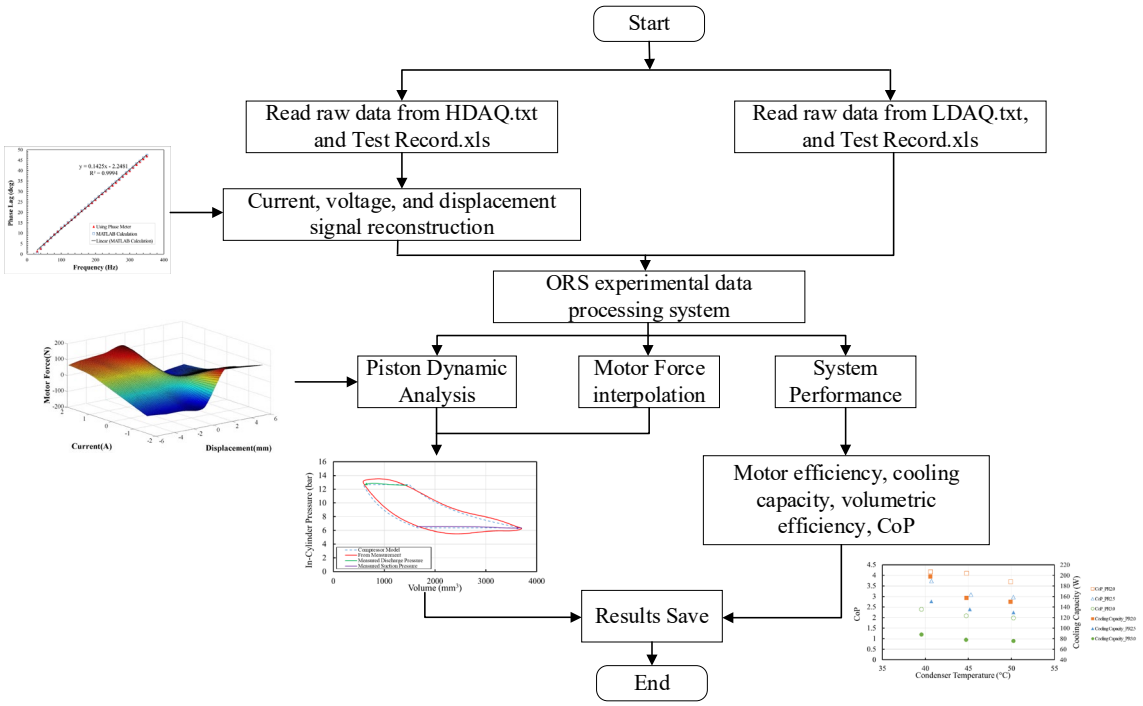

Fig. 3.14 Flowchart of the data analysis

The data from the HDAQ for each channel were first in MATLAB converted to corresponding physical values. A time delay exists between the output signal and input signal for all transducers and amplifiers. The delay depending on frequency results in signal distortion. In order to improve accuracy, the reconstruction of the signals of displacements, voltage, and current is necessary. Liang **[137]** conducted phase lag analysis for the LA LEM 25-NP current transducer, Fylde 261HVA Hz voltage attenuator, and LVDT. A correlation equation for the LVDT was proposed as shown in Fig. 3.15. The phase lag of the LVDT increases linearly with the increase of the frequency. A phase lag of 4.8 degrees is caused by the LVDT at a frequency of 50 Hz. Based on the proposed correlation equation, the displacement signal for linear compressors can be constructed. Liang **[137]** also pointed out that a 0.2 degree and a 0.4 degree phase lags were found for the current transducer and the voltage transducer at a frequency of 50 Hz. These phase lags remain nearly the same with the change of frequency. Thus, the phase lags for current transducer and voltage transducer can be considered as a constant value for experiments.

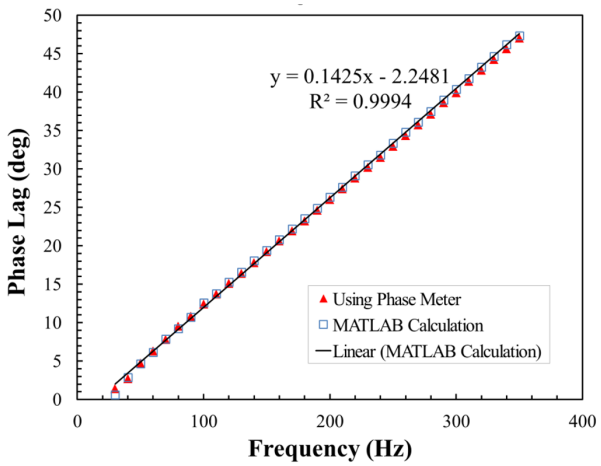

Fig. 3.15 Phase lag characteristic of the LVDT **[137]**

Fig. 3.16 shows an overview of the signal reconstruction system proposed by Liang **[162]**. Combining with a fast Fourier transform (FFT) with zero-padding, a minimisation algorithm, and the transducer phase lag, the signal reconstruction can be achieved. Based on the harmonic parameters calculated by using FFT with zero-padding, the minimization algorithm was executed to improve the accuracy of harmonic parameters **[162]**. The reconstructed displacement signal can be expressed as

$$x_{\mathrm{H}} = a_0 + \sum_{n=1}^{6}(a_{\mathrm{n}} cos\,(n\omega_0 t + \emptyset_{\mathrm{n}} - \varphi_{\mathrm{f}})) \tag{3.4}$$

where a_0 is the piston offset, n is the order of the harmonic term, a_{n} is the amplitude of term n, ω_0 is the fundamental frequency, $\emptyset_{\mathrm{n}}$ is the optimized harmonically determined phase of term n, and φ_{f} is the phase lag of transducer.

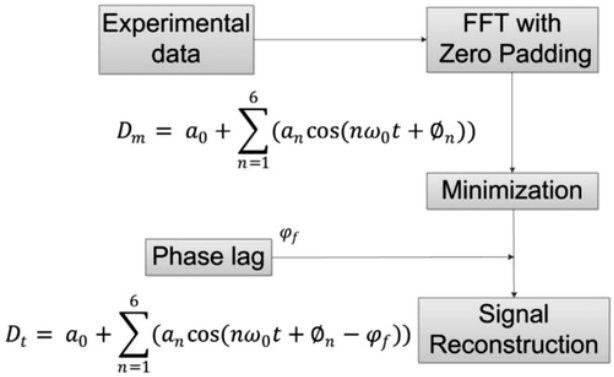

Fig. 3.16 Overview of the signal reconstruction system proposed by Liang **[162]**

According to the reconstructed current and displacement signals, the shaft force can be determined using the Force-Current-Displacement calibration map as shown in Fig. 2.5.

Then the compressor cylinder volume, in-cylinder pressure, motor losses, and thermodynamic efficiency can be evaluated.

3.4 Uncertainty Analysis

Uncertainty represents the quality of the measured variables. Uncertainty analysis is necessary for experiments to assess the confidence in the results. The combined uncertainty for two independent uncertainties can be expressed as

$$u_{\bar{x}} = \sqrt{s_{\bar{x}}^2 + w_{\bar{x}}^2} \tag{3.5}$$

where $u_{\bar{x}}$ is the combined uncertainty, $s_{\bar{x}}$ is Type A uncertainty, and $w_{\bar{x}}$ is Type B uncertainty.

In some cases, the measured values are used to compute the results R. Thus, the combined uncertainty for multiplying measurement can be expressed as

$$u_{\bar{R}}^2 = \sum_{i=1}^{n} (u_{\bar{x}_i} \frac{\partial R}{\partial x_i})^2 \tag{3.6}$$

According to Eq. 3.5 and Eq. 3.6, at a condenser temperature of 45 °C , a compressor stroke of 12 mm, and a pressure ratio of 2.5, the power input, cooling capacity, CoP, and volumetric efficiency have relative uncertainty of, 0.93%, 2%, 2.2%, and 0.23%, respectively. The detailed calculation process for uncertainty can be found in Appendix C.

3.5 Summary

A test rig has been developed for an ORS to evaluate the performance of the oil-free linear compressor, refrigerants, and system. The ORS mainly consists of two oil-free linear compressors, an off-the-shelf water-cooled coaxial condenser, and an evaporator with an electric heater. The test rig can work with nitrogen, R134a, R1234yf, and R152a. The

instrumentation for the test rig consisting of a data acquisition system, a power supply system, and a control system has been described in Section 3.2. A LabVIEW program has been developed to monitor and log the data from the corresponding instruments. Mass flow meters have been calibrated according to refrigerant properties.

A data analysis system has developed to process and analyze the logged data. Signal reconstruction for displacement, current, and voltage has been conducted by using harmonic fitting together with the phase lag of the instruments. The processed data are saved in ‘LDAQ averaging’, ‘HDAQ calibration’, and ‘Result Summary’ .xls files. An uncertainty analysis also has been conducted for experimental parameters.

Chapter 4 Measurement of the Oil-free Linear Compressor Performance using R134a

4.1 Experimental Method

4.1.1 Experimental Procedure

The novel oil-free linear compressor was tested using R134a as working fluid to give an essential knowledge of the linear compressor performance in the ORS. During the experiments, the linear compressor was operated under resonant frequency to acquire the best performance. An off-resonance experiment was also carried out to evaluate the impact of the operating frequency.

During the experiments, multiple parameters were required to be carefully monitored at the same time such as compressor stroke, piston offset, operating frequency, pressure ratio, condenser temperature, suction temperature, and refrigerant state at the evaporator outlet. Prior to experiments, the compressor body was first heated up to 45 °C to eliminate refrigerant liquid in the compressor. The instruments and LabVIEW program were turned on before increasing the setpoint of the compressor stroke. Meanwhile, the signal of compressor current, voltage, displacements, and control signals were shown on LabVIEW control panel and oscilloscopes. The values of these parameters should remain zero before increasing the setpoint of the compressor stroke. After the preparing and checking process, the green bottom on the panic box was pressed to connect the control and power circuit. The setpoint of the compressor stroke was gradually increased to reach the test condition (0.2 mm each step). The offset of the piston was automatically controlled by the PID controller. The duty cycle of the solenoid valve for the bleed flow loop can be observed from the oscilloscope as mentioned in Chapter 3. However, due to the overshoot of PID control, the piston offset should be carefully monitored. The tolerance of the piston offset

during experiments is ± 0.2 mm. The compressor stroke needs to be decreased immediately if the piston offset exceeds the tolerance.

As mentioned in Section 3.2.3, the operating frequency of the linear compressor was manually adjusted according to the calculated resonant frequency. The compressor stroke should be decreased slightly to avoid the overshoot of the compressor power input when reducing the operating frequency especially at high compressor strokes.

The pressure ratio and system temperatures were also monitored when adjusting the operating parameters of the compressor. To ensure a comparable condition for different refrigerant, the condenser temperature was controlled at fixed temperature. Also, in order to prevent the refrigerant liquid damage of the compressor, the electrical heater was adjusted to make sure the fully evaporation of the refrigerant at evaporator outlet. The evaporator temperature was mainly controlled by adjusting the pressure ratio of the system. The value of the pressure ratio for the system was manually adjusted by changing the lift of the expansion valve. As pressure ratio varies with the compressor stroke, piston offset, and system temperatures, the pressure ratio needs to be adjusted from time to time. The prototype ORS test rig was not designed for high pressures and large pressure ratios (mainly for domestic refrigeration). In order to protect the refrigeration loop, the discharge pressure was controlled lower than 17 bar while suction pressure was controlled higher than two bar. The condenser temperature for the system can be controlled by adjusting the cooling water flow rate via a tap. The evaporator outlet temperature was controlled by adjusting the power input of the electric heater via the variac heater controller. The evaporator outlet temperature was controlled below 45 °C to avoid the damage of system components and overshoot of suction pressure. A minimal 5 K superheat of refrigerant was required to ensure fully evaporation. Fig. 4.1 shows the warnings of the LabVIEW program. The green light will turn red if the system pressure or evaporator temperature exceeds the specific range to warn the operator to adjust the

operating parameters. When the system settled at the required test conditions, the ‘Write data?’ button was pressed to record the data from the LDAQ and HDAQ to .txt files.

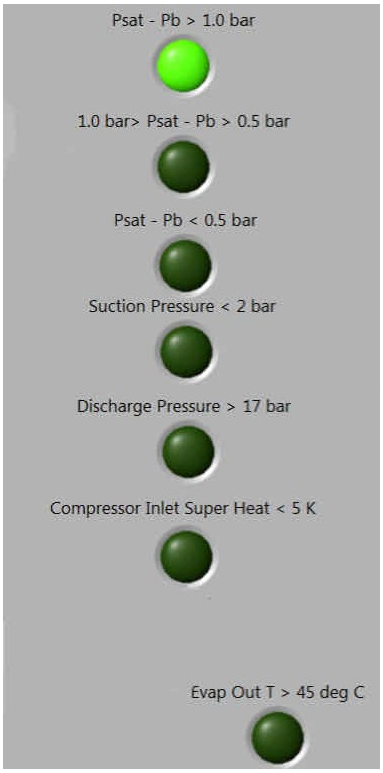

Fig. 4.1 Warnings of the LabVIEW program

When the experiments were finished, the electric heater was firstly shut down to prevent overheating the evaporator. The compressor stroke was gradually decreased to lower than 1 mm. The ‘No stroke’ button was pressed to cut down the control signal and the red button on the panic box was pressed to cut down the circuit. Finally, the power of instruments was turn off.

4.1.2 Test Conditions

Table 4.1 lists the test conditions of the oil-free linear compressor using R134a. The condenser temperature was controlled at 40 °C, 45 °C, 50 °C, and 55 °C which is the typical condensation temperature for domestic units. The maximum compressor stroke was set as 13 mm which is 1 mm lower than the designed stroke to protect the linear compressor in case the compressor stroke is out of control.

Table 4.1 Test conditions for the linear compressor

Refrigerant	R134a
Refrigerant charge (g)	300
Pressure ratio	2.0, 2.5, 3.0, 3.5, 4.0
Compressor stroke (mm)	9, 10, 11, 11, 12, 12, 13
Condenser temperature (°C)	40, 45, 50,55
Operating frequency (Hz)	32-39

4.2 Resonant Frequency

Linear compressor can achieve the highest motor efficiency at resonance. The resonant frequency of linear compressors is mainly determined by the moving mass, mechanical spring stiffness, and gas spring stiffness as shown in Eq. 3.2 and Eq. 3.3. Fig. 4.2 shows the resonant frequency against compressor stroke with various pressure ratios at a fixed condenser temperature of 40 °C. For a fixed compressor stroke, a higher pressure ratio leads to a higher resonant frequency due to higher induced gas spring stiffness. For a fixed pressure ratio, the resonant frequency does not change much. A higher compressor stroke tends to have a slightly lower resonant frequency. For a pressure ratio of 2.5 and 3.0, the resonant frequency remains the same for two adjacent strokes. This is because the small gas spring change between two compressor strokes is not large enough to cause a resonant frequency change over 1 Hz.

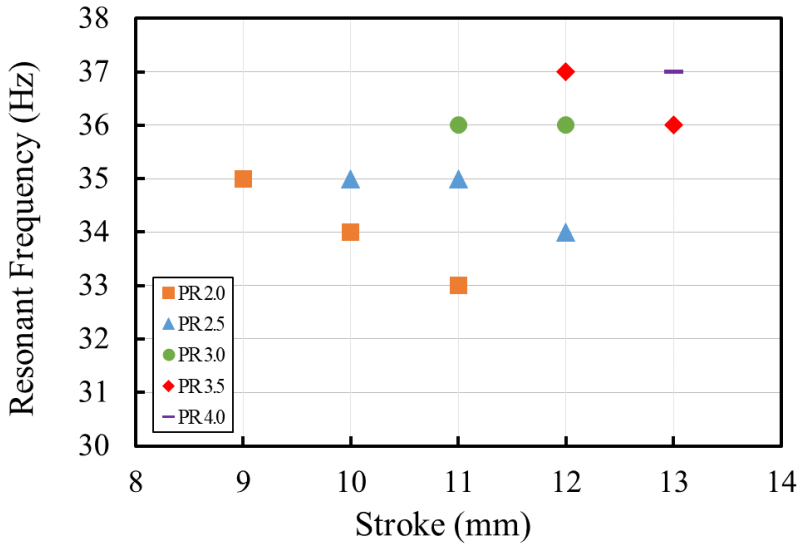

Fig. 4.2 Resonant frequency against compressor stroke of the oil-free linear compressor with various pressure ratios at a fixed condenser temperature of 40 °C

Fig. 4.3 shows the resonant frequency against the pressure ratio of the oil-free linear compressor with various pressure ratios at a fixed compressor stroke of 12 mm. As can be seen from Fig. 4.3, the resonant frequency increases with the increase of the condenser temperature due to an increase of the difference between the discharge and suction pressure leading to an increase of the gas spring stiffness.

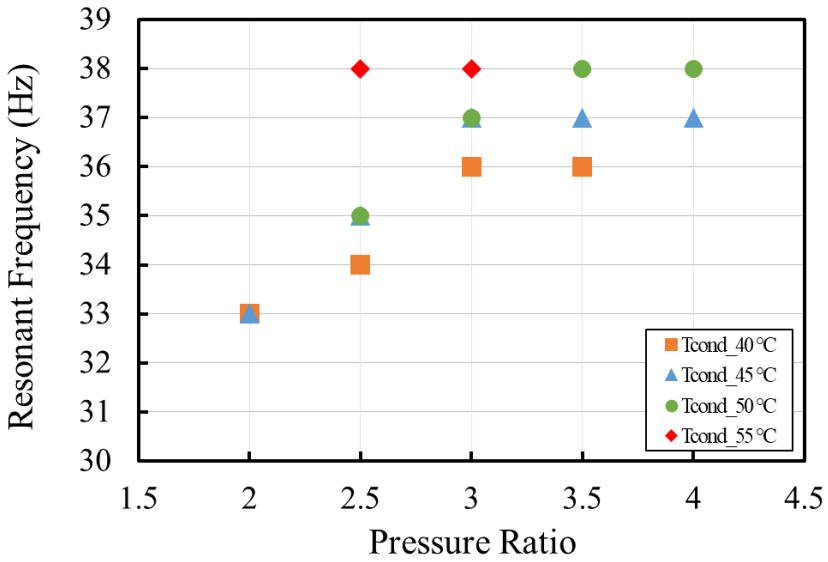

Fig. 4.3 Resonant frequency against pressure ratio of the oil-free linear compressor with various condenser temperatures at a compressor stroke of 12 mm

4.3 Cylinder Pressure Inferring

Due to the compact design of the linear compressor, an approximately 300 mm^3 dead volume was left at a compressor stroke of 13 mm. This value can be as small as 161 mm^3 at the maximum designed compressor stroke of 14 mm. A pressure transducer is impracticable to install in such a compact space. Thus, the in-cylinder pressure of the linear compressor is derived according to piston dynamics and other parameters such as body pressure and shaft force rather than directly measure. The forces acting on the compressor piston consists of mechanical spring force F_{spring}, damping force F_{damping} due to the friction between cylinder wall and piston, shaft force (or motor force) F_{shaft}, cylinder force F_{c} caused by cylinder pressure, body gas pressure force F_{b}, and piston force F_{pitson} which is the sum of the other forces. Thus, the cylinder pressure P_{c} can be expressed as

$$P_{\text{c}} = \frac{(F_{\text{shaft}} - m\ddot{x} - k_{\text{m}}x - \beta\dot{x})}{A} + P_{\text{b}} \tag{4.1}$$

where $\ddot{x}$ is piston acceleration, $\dot{x}$ is the piston velocity, x is the piston displacement, β is the damping coefficient, and P_{b} is the body pressure.

The shaft force can be calculated according to the Force-Current-Displacement calibration map as shown in Fig. 2.5. The shaft force after signal reconstruction can be expressed as

$$F_{\text{H}} = \sum_{n=1}^{6}(a_{\text{n}} cos\,(n\omega_0 t + \emptyset_{\text{n}})) \tag{4.2}$$

The cylinder volume can be expressed as

$$V_{\text{c}} = \frac{(7.57 - x)\cdot\pi \text{D}_{\text{p}}^2}{4} \tag{4.3}$$

Fig. 4.4 shows the *P-V* diagram of the oil-free linear compressor with a compressor stroke 11 mm, pressure ratio of 2.5, an operating frequency of 36 Hz, and a condenser temperature of 45 °C. The in-cylinder pressure shows overshoot during discharge process

and undershoot during suction process. This is because the compressor reed valves cannot be fully opened immediately when in-cylinder pressure meets the requirement.

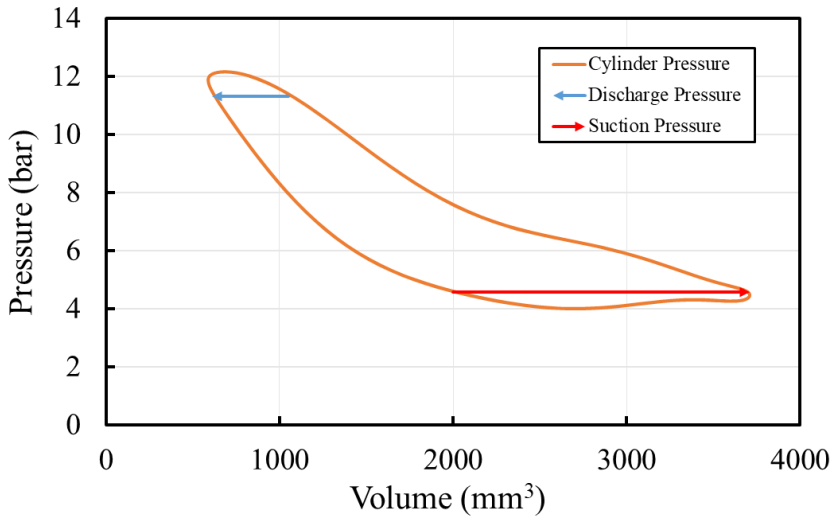

Fig. 4.4 *P-V* loop of the oil-free linear compressor

Due to unavoidable heat transfer through cylinder wall and gas leakage, the compression process and expansion process cannot be considered as isentropic. A correlated polytropic process is realistic. According to the ideal gas law, the relationship of the in-cylinder pressure, cylinder volume and polytropic index can be expressed as

$$\ln P = -n \ln V + \mathrm{C} \tag{4.4}$$

where P is the in-cylinder pressure, V is the cylinder volume, n is the polytropic index and C is a constant.

Fig. 4.5 shows a *P-V* loop in log-scale of the oil-free linear compressor with a compressor stroke of 11 mm, an operating frequency of 36 Hz, a pressure of 2.5, and a fixed condenser temperature of 45 °C. The logged in-cylinder pressure varies linearly with the logged cylinder volume during compression and expansion process. Thus, the slope can be considered as the polytropic indexes for two processes.

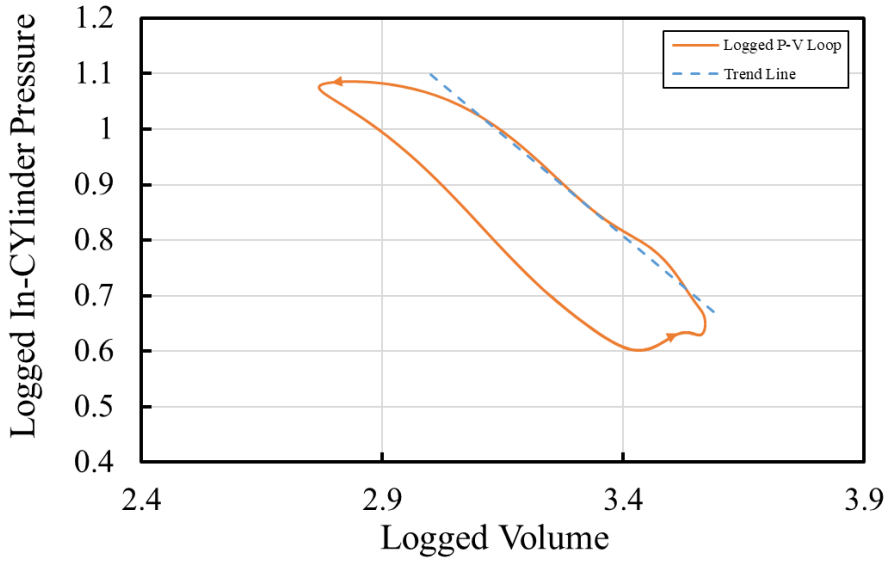

Fig. 4.5 Logged P-V loop of the oil-free linear compressor for a compressor stroke of 11 mm, a pressure of 2.5, an operating frequency of 36 Hz, and a fixed condenser temperature of 40 °C

4.4 Power Input and Mass Flow Rate

Fig. 4.6 shows the mass flow rate against compressor stroke with various pressure ratios at a fixed condenser temperature of 40 °C. For a fixed pressure ratio, the mass flow rate increases with the increase of the compressor stroke due to the increase of the actual stroke. An opposite trend can be found for a fixed compressor stroke, the mass flow rate decreases with the increase of the pressure ratio due to a larger proportion of the compressor stroke is used to deliver the refrigerant from low pressure to high pressure. A mass flow rate of 2.4 g/s is achieved at a compressor stroke of 11 mm and a pressure ratio of 2.0 while a mass flow rate of 0.73 g/s mass flow rate is achieved at a compressor stroke of 13 mm and a pressure ratio of 4.0.

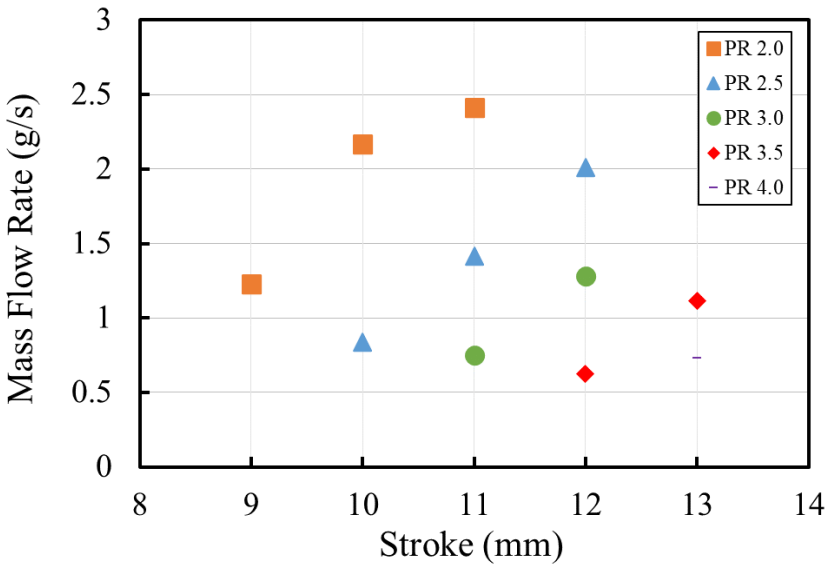

Fig. 4.6 Mass flow rate against compressor stroke with various pressure ratios at a fixed condenser temperature of 40 °C

The electrical power input $\dot{W}_{\text{in}}$ into the linear compressor can be calculated as

$$\dot{W}_{\text{in}} = \frac{1}{t}\int_0^t V \cdot I dt \tag{4.5}$$

where t is the period, V is the voltage, I is the current.

Fig. 4.7 shows the power input of the oil-free linear compressor various with pressure ratios and compressor strokes. For a fixed pressure ratio, the power input increases linearly with compressor stroke. For a fixed compressor stroke, the increase of pressure ratio leads to a decrease of the power input due to a lower mass flow rate. At a compressor stroke of 12 mm and a pressure ratio of 2.5, the oil-free linear compressor requires 85 W power input. The capacity modulation can effectively reduce the power consumption of the oil-free linear compressor for domestic refrigeration at part load conditions.

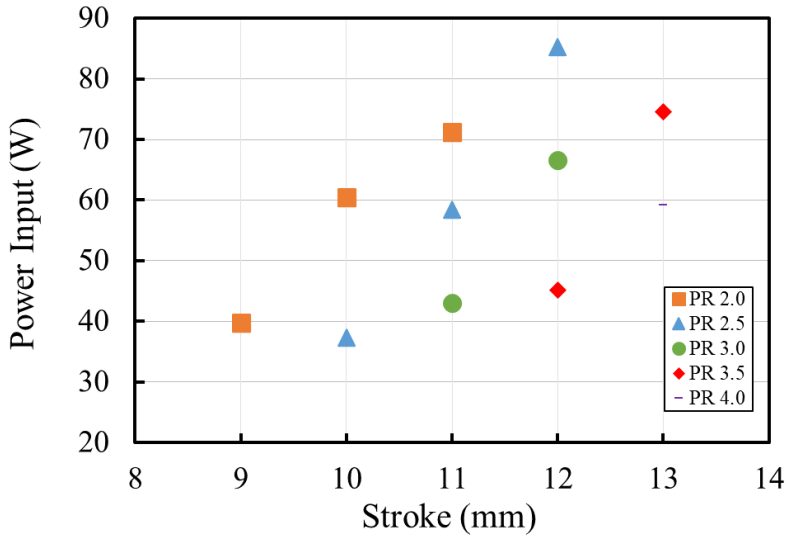

Fig. 4.7 Power input against compressor stroke with various pressure ratios at a fixed condenser temperature of 40 °C

Specific mass flow rate is used to acquire more intuitive understanding of the relationship between mass flow rate and power input under various test conditions. The specific mass flow rate is calculated as

$$\dot{m}_{\mathrm{sp}} = \frac{\dot{m}}{\dot{W}_{\mathrm{in}}} \tag{4.6}$$

where $\dot{W}_{\mathrm{in}}$ is the power input and $\dot{m}$ is the mass flow rate.

Fig. 4.8 shows the specific mass flow rate against the pressure ratio of the oil-free linear compressor for condenser temperature from 40 °C to 55 °C. For a fixed pressure ratio, the specific mass flow rate decreases with the increase of the condenser temperature due to the decrease of the vapour density and increase of the pressure difference between suction and discharge. At a fixed condenser temperature of 40 °C and a fixed pressure ratio of 2.0, the oil-free linear compressor can achieve a specific mass flow rate of 0.034 g/s/W.

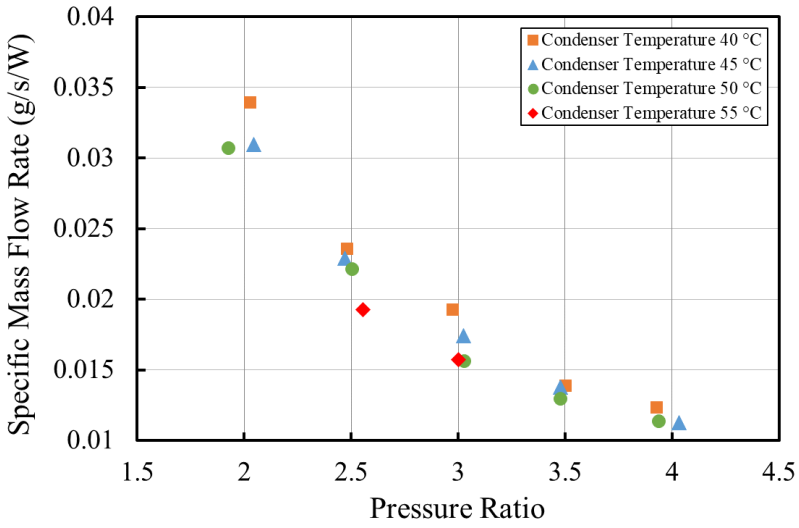

Fig. 4.8 Specific mass flow rate against pressure ratio using R134a for pressure ratios from 40 °C to 55 °C

4.5 Compressor Efficiency

4.5.1 Motor Efficiency

Due to the small radial clearance (10 μm), the mechanical friction loss can be ignored. Thus, the copper losses become the main motor loss. The copper losses $\dot{W}_{copper}$ can be calculated as

$$\dot{W}_{copper} = I_{rms}{}^2 R \tag{4.7}$$

where R is the total resistance of the coil for two compressors and I_{rms} is the root mean square (RMS) value of current which is supplied to the linear compressor.

Thus, the motor efficiency can be expressed as

$$\eta_m = \frac{\dot{W}_{in} - \dot{W}_{copper}}{\dot{W}_{in}} \tag{4.8}$$

Fig. 4.9 shows the motor efficiency changes with the compressor stroke and pressure ratio of the oil-free linear compressor. For a fixed pressure ratio, the motor efficiency decreases with the compressor stroke due to the increase of the shaft force leading to an increase of

current. At a pressure ratio of 2.5, the motor efficiency decreases from 91% to 86% while the compressor stroke increases from 10 mm to 12 mm. For a fixed compressor stroke, the motor efficiency increases with the pressure ratio. This is because a lower pressure ratio tends to require a higher power input resulting in a larger current and copper losses. The highest motor efficiency is 92.6% which is achieved at a compressor stroke of 12 mm and a pressure ratio of 3.5 while the lowest is 85.7% at a compressor stroke of 12 mm and a pressure ratio of 2.5. Part load operation can occupy 95% of refrigeration units operating time **[163-165]**. Fig. 4.9 along with Fig. 4.6 and Fig. 4.7 show that the oil-free linear compressor can achieve high part load efficiency with small power input and mass flow rate at low compressor stroke. Thus, the linear compressor with capacity modulation can effectively save the power consumption under part load conditions.

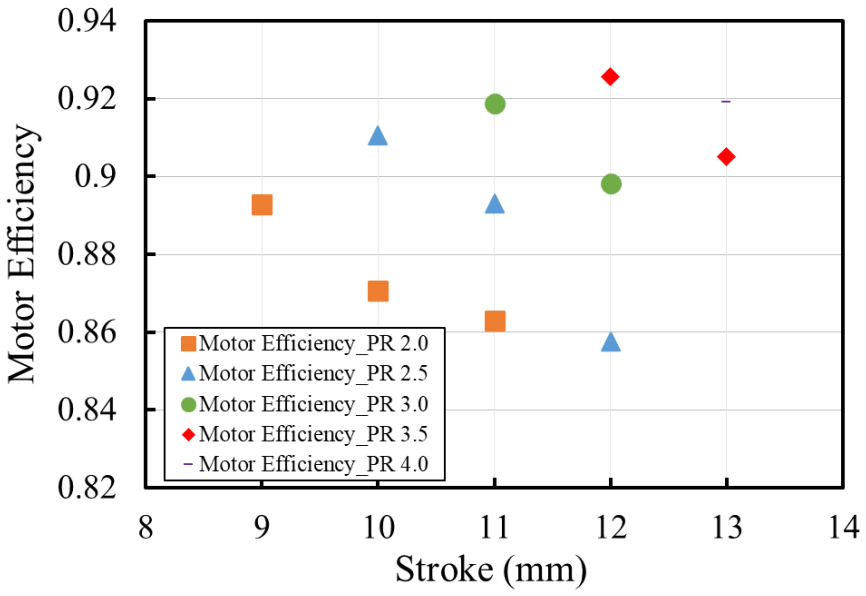

Fig. 4.9 Motor efficiency changes with compressor stroke and pressure ratio for the oil-free linear compressor

As mentioned in Section 4.2, the motor loss can be minimised by operating the oil-free linear compressor at resonance. Fig. 4.10 shows the motor efficiency and RMS value of current against the operating frequency for a pressure ratio of 3.0, a compressor stroke of 12 mm, and a condenser temperature of 50 °C. The motor efficiency varies from 82.5% to 90% while the RMS current changes from 0.96 A to 0.9 A. At the operating frequency

of 37 Hz, the linear compressor is operated at the resonant frequency achieving the minimum current and highest motor efficiency for this test condition.

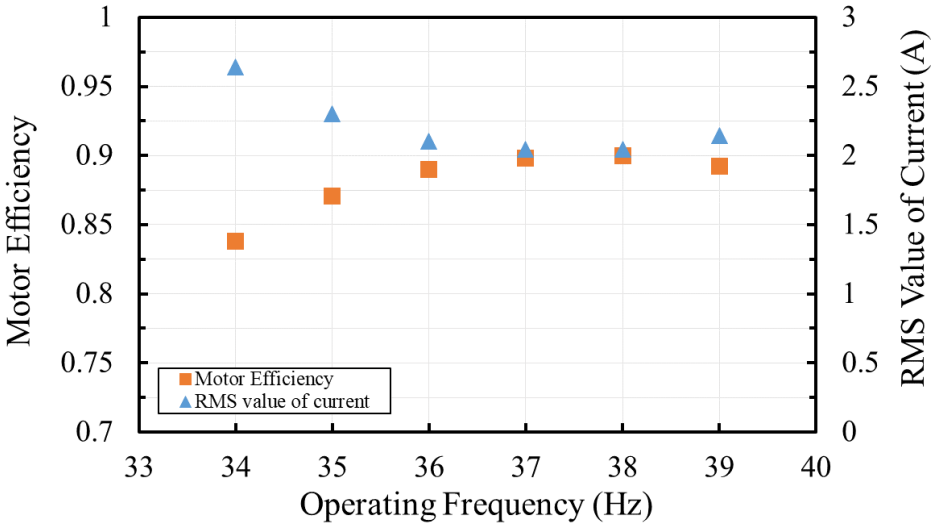

Fig. 4.10 Motor efficiency and RMS value of current against operating frequency of the oil-free linear compress for a pressure ratio of 3.0, a compressor stroke of 12 mm, and a condenser temperature of 50 °C

4.5.2 Volumetric Efficiency

The volumetric efficiency is calculated according to the following equation

$$\eta_{\mathrm{V}} = \frac{4\dot{m}R_{\mathrm{g}}T_{\mathrm{suc}}}{\pi S f P_{\mathrm{suc}} \mathrm{D_p^2}} \tag{4.9}$$

where S is the compressor stroke, T_{suc} is the temperature at the compressor inlet, P_{suc} is the pressure at the compressor inlet, and R_{g} is the specific gas constant.

Fig. 4.11 shows the volumetric efficiency against compressor stroke with various pressure ratios at a fixed condenser temperature of 40 °C. For a fixed pressure ratio, the volumetric efficiency increases with the compressor stroke due to smaller dead volume thus higher mass flow rate. For a fixed compressor stroke, the volumetric efficiency decreases with the increase of the pressure ratio. At a compresosr stroke of 11 mm and a pressure ratio of 2.0, a volumetric efficiency of 71% is achieved. However, the oil-free linear compressor only achieved a volumetric efficiency of 28% at a compressor 12 mm and a

pressure ratio of 3.5. A higher compressor stroke can further improve the performance of the oil-free linear compressor at high pressure ratios due to the decrease of the dead volume.

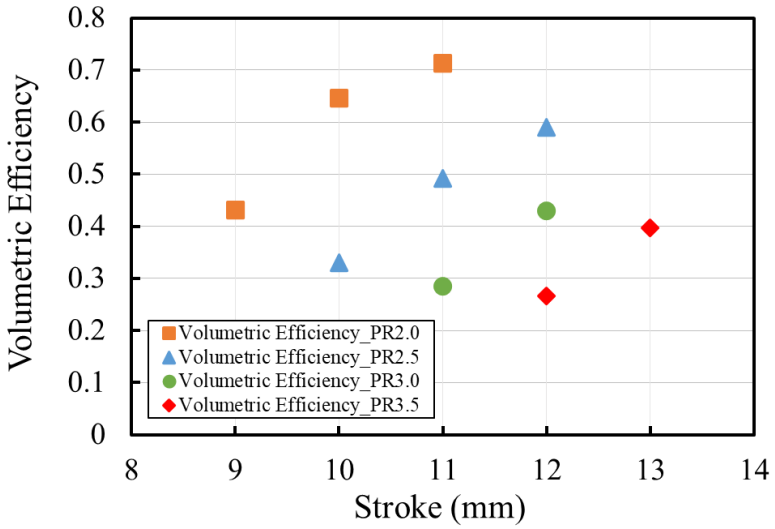

Fig. 4.11 Volumetric efficiency against compressor stroke with various pressure ratios at a fixed condenser temperature of 40 °C

Fig. 4.12 shows the volumetric efficiency against the pressure ratio with various condenser temperatures. As can be seen, the volumetric efficiency decreases with the increase of the conenser temperature among all pressure ratios due to the lower vapour density at lower condenser temperature. It is worth mentioning that the difference of the volumetric efficiency for different condenser temperatures increases with pressure ratio. This is because the difference of suction pressure becomes greater at higher pressure ratios leading to a greater difference of vapour density.

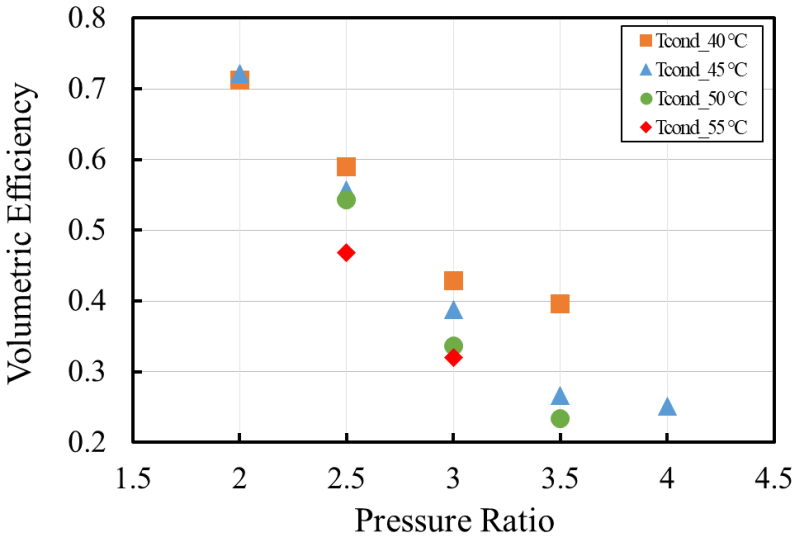

Fig. 4.12 Volumetric efficiency against pressure ratio with various condenser temperatures

4.5.3 Thermodynamic Efficiency

According to the polytropic index acquired from Eq. 4.4, the thermodynamic power $\dot{W}_{\mathrm{th}}$ can then be calculated as

$$\dot{W}_{\mathrm{th}} = \frac{n}{n-1}\dot{m}R_{\mathrm{g}}T_{\mathrm{suc}}\left[\left(\frac{P_{\mathrm{dis}}}{P_{\mathrm{suc}}}\right)^{\frac{n-1}{n}} - 1\right] \tag{4.10}$$

Thus, the thermodynamic efficiency η_{th} can be expressed as

$$\eta_{\mathrm{th}} = \frac{\dot{W}_{\mathrm{th}}}{\dot{W}_{\mathrm{in}}} \tag{4.11}$$

Fig. 4.13 shows the thermodynamic efficiency against compressor stroke for pressure ratios of 2.0, 2.5, 3.0, and 3.5 at fixed condenser temperatures of 40 °C and 50 °C. The thermodynamic efficiency increases with compressor stroke due to the increase of mass flow rate. For a fixed compressor stroke, the thermodynamic efficiency decreases with the increase of pressure ratio. It is worth mentioning that a higher condenser temperature has a higher negative influence on thermodynamic efficiency. This is due to the higher discharge pressure resulting in higher shaft force thus power input. At a fixed compressor stroke of 10 mm and a fixed pressure ratio of 2.0, the thermodynamic efficiency of the

linear compressor at 40 °C (50%) is 5% higher than 50 °C. At a fixed pressure ratio of 3.5, the difference of thermodynamic efficiency between two condenser temperatures is reduced. This is due to the low mass flow rate for both condenser temperatures.

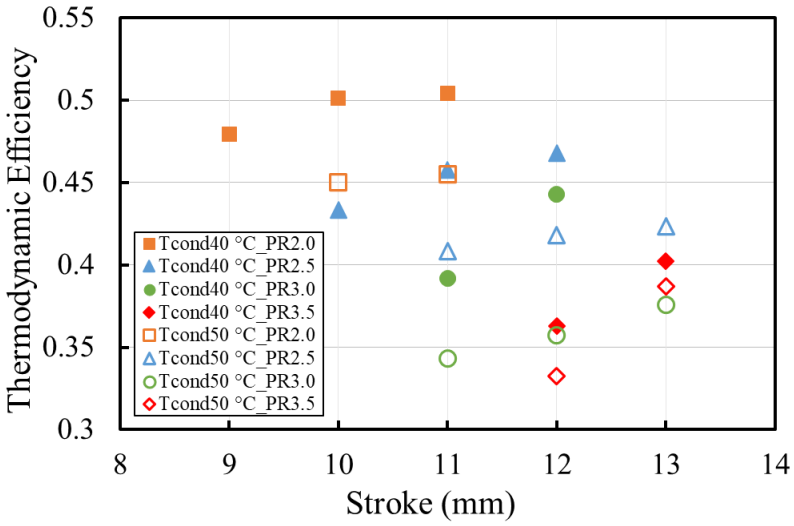

Fig. 4.13 Thermodynamic efficiency against compressor stroke for pressure ratios of 2.0, 2.5, 3.0, and 3.5 at fixed condenser temperatures of 40 °C and 50 °C.

4.6 Summary

In this chapter, measurements of the performance of the oil-free linear compressor have been reported. The experiment procedure and test conditions are first introduced. Then the oil-free linear compressor performance is evaluated by resonant frequency, power input, mass flow rate, motor efficiency, volumetric efficiency, and thermodynamic performance. Key findings are listed below:

(1) The oil-free linear compressor shows a higher resonant frequency at a higher pressure ratio while a lower resonant frequency tends to be achieved at a lower compressor stroke due to a lower gas spring stiffness.

(2) Overshoots of the in-cylinder pressure are found during discharge and suction process due to the delay of the reed valve movement.

(3) The polytropic index can be calculated from the logged *P-V* loop which can be

used for thermodynamic analysis.

(4) Both mass flow rate and power input increase with the increase of the compressor stroke. For a fixed compressor stroke, the mass flow rate and power input decrease with the increase of the pressure ratio due to the decrease of the actual stroke.

(5) For a fixed compressor stroke, the motor efficiency increases with the pressure ratio due to the decrease of the power input resulting in a decrease of the copper loss. A reverse trend is found for a fixed pressure ratio. At a compressor stroke of 12 mm and a pressure ratio of 3.5, the highest motor efficiency of 92.6% is achieved for the oil-free linear compressor.

(6) At a compresosr stroke of 11 mm and a pressure ratio of 2.0, the oil-free linear compressor can achieve a volumetric efficiency of 71%.

(7) The thermodynamic efficiency increases with the compressor stroke and decreases with the pressure ratio. At a condenser temperature of 40 °C and a pressure ratio of 2.0, the oil-free linear compressor can achieve a thermodynamic efficiency of 50%.

(8) Overall, the oil-free linear compressor shows good compressor efficiencies. The reed valve of the linear compressor can be modified to further improve the performance of the piston dynamics and reduce the pressure drop losses.

(9) The oil-free linear compressor shows good efficiencies with small power input and mass flow rate under part load conditions. The oil-free linear compressor along with capacity modulation control can be achieved to reduce the power consumption and greenhouse gas emissions.

Chapter 5 Analytical Model of the Oil-free Linear Compressor using Low GWP Refrigerants with Capacity Modulation

5.1 Introduction

Refrigerators are responsible for 14% electricity consumption of a residential sector **[1]**. Domestic refrigerator contributes to greenhouse gas emissions through refrigerant leakage and energy consumption. As mentioned in Chapter 2, linear compressor provides significant advantages such as oil-free operation, high efficiency and non-start/stop operation for refrigeration system. Linear compressor also enables a flexible control strategy of capacity modulation and wider selection range of working fluid for domestic refrigeration. Alzoubi and Zhang **[121]** adopted a linear compressor for a compact VCR system which can achieve a CoP of 4.5. Liang **[166]** predicted the power input and resonant frequency of a linear compressor for domestic refrigeration at high pressure ratios using R600a. Bradshaw et al. **[113]** carried out experiments to investigate the compressor performance for different dead volumes. The results indicated that the overall efficiency shows only minor degradation with the increase of the dry friction coefficient.

To minimise the impact of the leaking refrigerants from VCR systems on the environment, traditional HFCs such as R134a are being replaced by low GWP refrigerants. R717, R600a, and R1234yf are considered as potential environment-friendly refrigerants due to their low GWP. R717 as one of the oldest refrigerants is still being used in the modern refrigeration industry due to the low cost and high efficiency. However, because of its toxicity, flammability, and corrosivity, R717 is mainly used in industrial refrigeration system. As pointed by Liang **[137]**, with moving magnet linear compressor, the windings are placed outside of the pressure containment providing a possibility to design a compressor for domestic application to avoid the contact of copper and working fluids.

Fig. 5.1 shows the saturation pressure for R717, R600a, R1234yf and R134a adopted from **[167]**. R1234yf has similar saturation pressure to R134a and this offers an opportunity of R1234yf as a drop-in replacement for R134a domestic refrigerator with minimum modification. R717 has the highest saturation pressure while R600a has the lowest. Due to various saturation pressures of the low GWP refrigerants and the limitation of the test rig, the performance of the oil-free linear compressor can vary by using different refrigerants and experiments cannot be carried out for high pressure ratios. An analytical model of the oil-free linear compressor for domestic refrigeration with capacity modulation is introduced in this chapter. Four refrigerants (R134a, R717, R600a, and R1234yf) are used as working fluid for the system. The cooling capacity modulation of the system using oil-free linear compressor is achieved by changing the compressor stroke ratio.

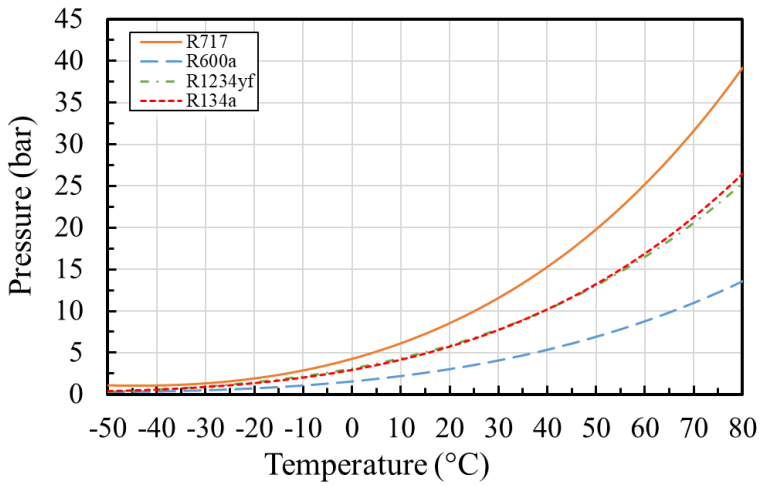

Fig. 5.1 Saturation pressure against temperature of four refrigerants (R717, R600a, R1234yf, and R134a) adapted from **[167]**

The absence of oil lubricants can extend the range of refrigerant selection. The use of microchannel heat exchangers can reduce the refrigerant charge and thus improve the safety of domestic refrigerators using flammable refrigerants. However, limited work was found in the literature related to oil-free domestic refrigerator using low GWP refrigerants, especially for R717. This chapter compares the system performance of low GWP

refrigerants (R717, R600a and R1234yf) with R134a for the oil-free linear compressor which is suitable for all four refrigerants. Cooling capacity modulation can be achieved by changing the compressor stroke ratio. An analytical model has been developed to evaluate the system performance for the refrigerants with very quick calculation.

5.2 Analytical Model of the Oil-free Linear Compressor

5.2.1 Overview and Assumptions of Model

Fig. 5.2 shows the schematic diagram of the analytical model of the oil-free linear compressor for domestic refrigeration using R717, R600a, R1234yf, and R134a. The linear compressor has a full stroke of 14 mm. Compression and expansion processes are considered as isentropic. Pressure drop across the reed valves of the linear compressor is ignored. Operating frequency is set to be 50 Hz at the beginning. Motor force constant is assumed to be 30 N/A. Motion of the free piston is assumed to be sinusoidal. Suction temperature is set to be 25 °C. Piston offset is assumed to be zero. Based on pressure-enthalpy (*p*-*h*) diagram, pressure ratio, condenser temperature, subcooling, and superheat can be determined. Combining with stroke ratio and isentropic index (γ), pressure-volume (*P*-*V*) loop can be inferred based on piston dynamics and the ideal gas law. Shaft power (enclosed area of *P*-*V* loop), mass flow rate (through discharge process) and resonant frequency (non-linear gas spring) can be calculated from the *P*-*V* loop. The operating frequency is adjusted to be the same as the resonant frequency to improve the accuracy of the model. The power input, cooling capacity and CoP can then be calculated. The detailed parameters of the oil-free linear compressor can be found in Table 3.3.

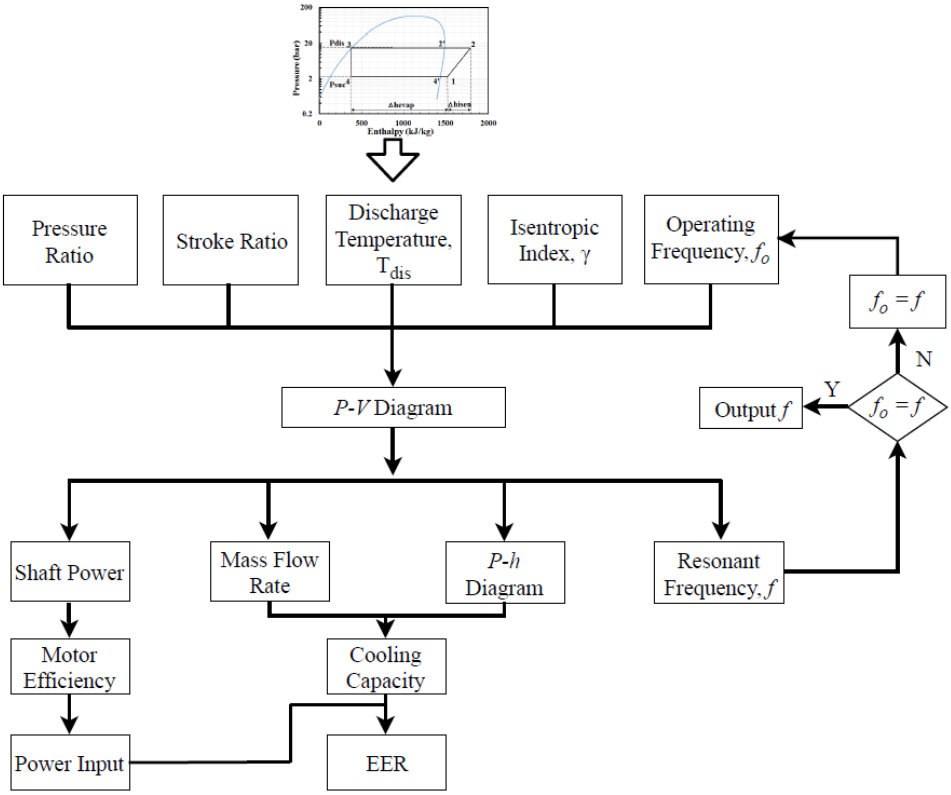

Fig. 5.2 Flowchart of the mathematical model of the system performance using R717, R600a, R1234yf, and R134a

5.2.2 Compressor Model

Fig. 5.3 shows the simplified schematic diagram of the linear compressor. The free piston is directly connected to the moving magnet and driven by the shaft force generated from the linear motor. The discharge valve and suction valve are placed at the opposite side of linear motor. V_{min} is the dead volume of the linear compressor which can be varied according to the compressor stroke.

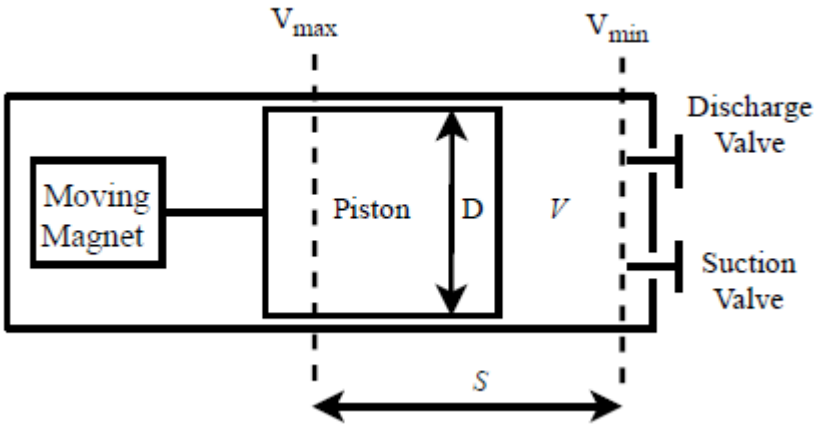

Fig. 5.3 Simplified schematic diagram of the linear compressor ($V_{\min}$: dead volume, $V_{\max}$: maximum cylinder volume)

The dead volume $V_{\min}$ can be calculated as shown below

$$V_{\min} = \frac{(7.57-\frac{S}{2})\pi D_p^2}{4} \tag{5.1}$$

The maximum cylinder volume $V_{\max}$ is defined as follow

$$V_{\max} = V_{\min} + \frac{S\pi D_p^2}{4} \tag{5.2}$$

The cylinder volume V can be expressed as a cosine function of the operating frequency, time, and compressor stroke. The in-cylinder pressure can be calculated by the cylinder volume V, maximum cylinder volume $V_{\max}$, dead volume $V_{\min}$, and isentropic index γ. The cylinder volume V and in-cylinder pressure P_C can be defined as follow

$$V = V_{\min} + \frac{S\pi D_p^2[\cos(2\pi ft)+1]}{8} \tag{5.3}$$

For compression process:

$$P_C = P_{suc}(\frac{V_{\max}}{V})^{\gamma} \tag{5.4}$$

where γ is the isentropic index.

For expansion process:

$$P_{\mathrm{C}} = P_{\mathrm{dis}}(\frac{V_{\mathrm{min}}}{V})^{\gamma} \tag{5.5}$$

In Eq. 3.2, the linear spring stiffness of the gas k_{g} is calculated directly using the difference between the discharge pressure and suction pressure. However, at high pressure ratios, the very non-linear gas spring cannot be simply considered as a linear line, the very non-linear gas spring curve should be calculated by averaging the in-cylinder pressure during the compression and expansion processes **[166]**. Thus, the effective non-linear spring stiffness of the gas k_{g} in the compressor chamber can be expressed as

$$k_{\mathrm{g}} = (\int_1^2 PdV - \frac{\oint PdV}{2})\frac{2}{S^2} \tag{5.6}$$

where 1 is the start of compression process and 2 is the end of discharge process. Then the resonant frequency f can be calculated according to Eq. 3.2.

The shaft work generated by linear motor is equal to the area of the *P-V* loop. The shaft power $\dot{W}_{\mathrm{shaft}}$ can be calculated by the shaft work and operating frequency f as follow

$$\dot{W}_{\mathrm{shaft}} = f \oint PdV \tag{5.7}$$

Owing to the small clearance between piston and cylinder wall (10 μm), mechanical friction loss can be ignored. Copper loss resulting from resistive heating becomes the main motor loss. The RMS value of the current I_{rms} can be expressed as

$$I_{\mathrm{rms}} = \frac{\dot{W}_{\mathrm{shaft}}}{v_{\mathrm{rms}}\alpha} \tag{5.8}$$

where v_{rms} is the RMS value of the piston speed which can be calculated based on Eq. 5.3 and α is the motor force constant.

The copper loss $\dot{W}_{\mathrm{copper}}$ and power input $\dot{W}_{\mathrm{in}}$ can be expressed as

$$\dot{W}_{\mathrm{copper}} = {I_{\mathrm{rms}}}^2\mathrm{R} \tag{5.9}$$

Thus, the power input can be expressed as

$$\dot{W}_{\text{in}} = \dot{W}_{\text{shaft}} + \dot{W}_{\text{copper}} \tag{5.10}$$

The motor efficiency can be calculated as

$$\eta_{\text{m}} = \frac{\dot{W}_{\text{in}} - \dot{W}_{\text{copper}}}{\dot{W}_{\text{in}}} \tag{5.11}$$

The refrigerant mass containing in the swept volume during the discharge process is the actual refrigerant mass to be circulated in the ORS. Thus, the mass flow rate $\dot{m}$ can be expressed as

$$\dot{m} = \frac{(V_2 - V_1) P_{\text{dis}} f_o}{\text{R}_\text{g} T_{\text{dis}}} \tag{5.12}$$

where V_2 is the start volume cylinder volume of discharge process, V_1 is the end cylinder volume of discharge process, and T_{dis} is the discharge temperature of linear compressors.

The stroke ratio SR is defined as follow

$$\text{SR} = \frac{S}{\text{S}_{\text{full}}} \tag{5.13}$$

where S_{full} is the full compressor stroke.

5.2.3 Cooling Capacity and CoP

Based on the suction pressure, discharge pressure, subcooling and superheat, the corresponding enthalpies can be determined. Thus, the cooling capacity $\dot{Q}_c$ can be expressed as follow

$$\dot{Q}_{\text{c}} = \dot{m}(h_2 - h_1) \tag{5.14}$$

where h_1 is the enthalpy of the refrigerant at evaporator inlet, h_2 is the enthalpy of the refrigerant at suction.

The CoP for the system is defined as

$$CoP = \frac{\dot{Q}_{\mathrm{c}}}{\dot{W}_{\mathrm{in}}} \tag{5.15}$$

5.3 Model Validation

The compressor model has been validated by experiments using R134a as refrigerant given in Chapter 4. The details of the experimental setup and refrigeration data at low pressure ratios can be found in Chapter 3 and 4. Fig. 5.4 shows the mass flow rate and cooling capacity against evaporator temperature using R134a for a compressor stroke of 12 mm at a fixed condenser temperature of 40 °C. Both mass flow rate and cooling capacity increase with evaporator temperature. The compressor model agrees very well with measurements with 9% error in mass flow rate. The mass flow rate from modelling is slightly higher than the measurement due to neglecting friction loss in the condenser and evaporator. The close agreement between the modelling and measurements verifies the model to be used for other refrigerants for assessment on system performance.

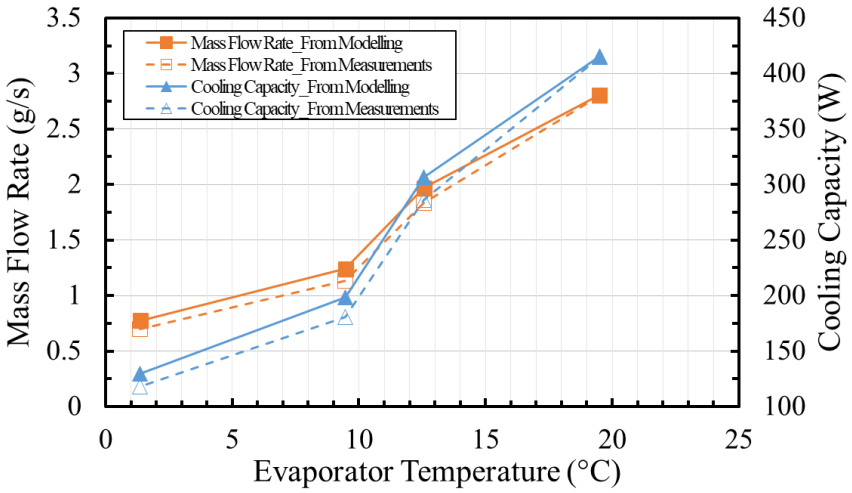

Fig. 5.4 Mass flow rate and cooling capacity against evaporator temperature using R134a for a compressor stroke of 12 mm at a fixed condenser temperature of 40 °C

5.4 Results and Discussions

5.4.1 *P-h* Diagram

Fig. 5.5 shows the *p-h* diagram of R717, R600a, R1234yf, and R134a for a full compressor stroke at a fixed evaporator temperature of -23 °C and a fixed condenser temperature of 50 °C. The condenser temperature of 50 °C and evaporator of -23 °C are typical working temperatures for domestic refrigerator. R717 gives a cooling capacity of 580 W which is much higher than R600a (86 W), R1234yf (247 W), and R134a (252 W). This is because of the very high latent heat of R717. To achieve similar cooling capacity, compressor using R717 can have much smaller stroke (low mass flow rate) which will lead to an even higher motor efficiency as the input current will be lower. However, R717 has the highest evaporating and condensing pressures among four refrigerants for given operating conditions which means R717 could have the highest gas leakage across the radial clearance during operation.

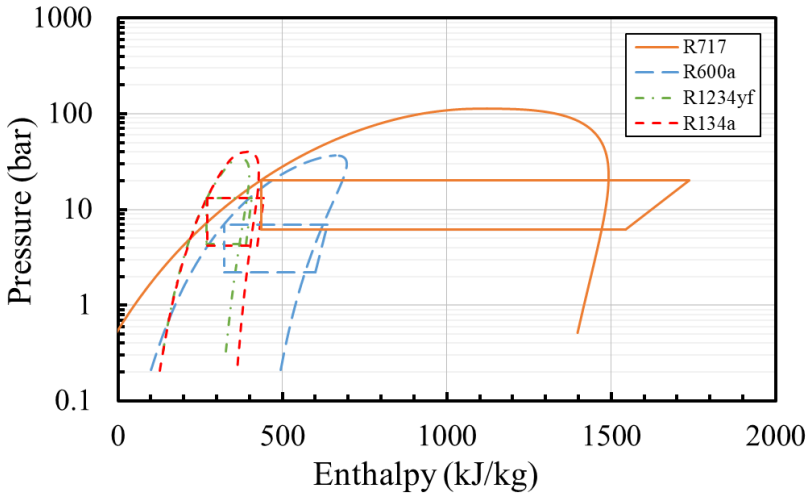

Fig. 5.5 Pressure against enthalpy of the linear compressor using four refrigerants (R717, R600a, R1234yf, and R134a) for a full stroke at a fixed evaporator temperature of -23 °C and a fixed condenser temperature of 50 °C

5.4.2 *P-V* Diagram

Fig. 5.6 shows the *P-V* loop for the oil-free linear compressor using four refrigerants with a full compressor stroke, at a fixed evaporator temperature of -23 °C and a fixed condenser temperature of 50 °C. The shaft work can be expressed as the area of the *P-V* loop. R717 requires the highest shaft work among four refrigerants, while R600a requires the lowest shaft work. The discharge pressure of R717 is 35%, 34%, and 65% higher than R1234yf, R134a and R600a, respectively. This means R717 requires higher power input as well.

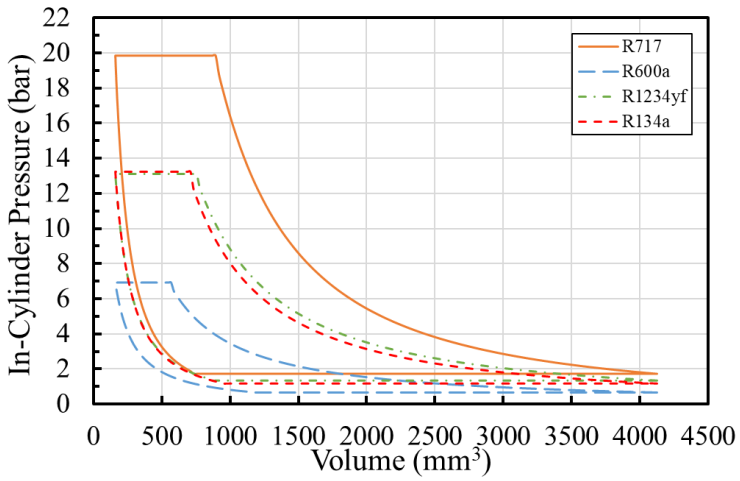

Fig. 5.6 *P-V* loop for the linear compressor using four refrigerants (R717, R600a, R1234yf, and R134a) with a full compressor stroke, at a fixed evaporator temperature of -23 °C and a fixed condenser temperature of 50 °C

Fig. 5.7 compares the pressure ratio of four refrigerants for evaporator temperatures of 10 °C to -25 °C at a fixed condenser temperature of 50 °C. R1234yf has the lowest pressure ratio curve due to the smallest saturation pressure variation for temperature range of -25-50 °C, while R717 has the highest pressure ratio. R1234yf is the easiest to achieve a low evaporator temperature at a fixed condenser temperature of 50 °C among four refrigerants. For an evaporator temperature of -20 °C, the pressure ratios for R717, R600a, R1234yf and R134a are 10.4, 9.4, 8.6, and 9.8, respectively. High pressure ratio for single stage oil-free linear compressor is not desirable due to significant gas leakage across the radial clearance (27% of power input at pressure ratio of 13.6 using R600a **[121]**). A linear compressor with a smaller radial clearance can reduce the seal leakage loss across the radial clearance. However, simply decreasing the radial clearance of the linear compressor can increase the friction between the piston and cylinder. Multiple stage compressor can be considered as a potential solution due to the reduction of the pressure ratio for each stage.

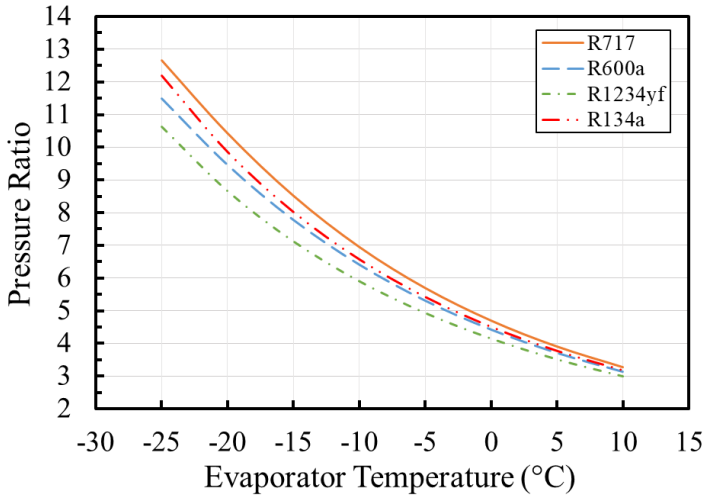

Fig. 5.7 Pressure ratio against evaporator temperature of the linear compressors using four refrigerants (R717, R600a, R1234yf, and R134a) for full stroke at a fixed condenser temperature of 50 °C

5.4.3 Resonant Frequency

Fig. 5.8 shows the resonant frequency against evaporator temperature of the linear compressors using four refrigerants for a full stroke at a fixed condenser temperature of 50 °C. Resonant frequency increases with the evaporator temperature. As can be seen, for given evaporator temperature, R717 has the highest resonant frequency due to the high gas spring stiffness resulting from the high in-cylinder pressure, while R600a has the lowest. R1234yf and R134a have the similar resonant frequency at the same operating condition due to their similar saturation pressure. It is interesting to see that for a wide range of the evaporation temperatures, the resonant frequency for R600a only has maximum difference of 5 Hz. This means that it is not necessary to tune the operating frequency constantly for high efficiency resonant operation.

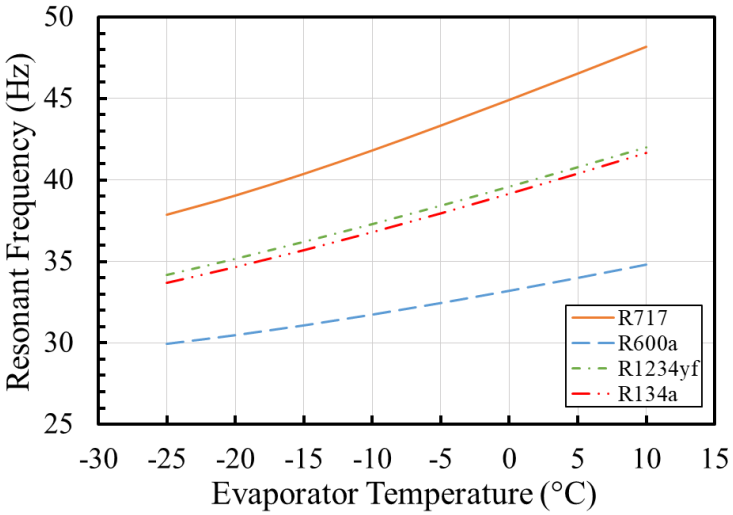

Fig. 5.8 Resonant frequency against evaporator temperature of the linear compressors using four refrigerants for a full compressor stroke at a fixed condenser temperature of 50 °C

5.4.4 Mass Flow Rate and Power Input

Fig. 5.9 shows the mass flow rate and power input varies with stroke ratio for the oil-free linear compressor at a fixed condenser temperature of 50 °C. R1234yf shows the highest mass flow rate among four refrigerants due to the highest vapour density. R717 has a lower vapour density than R600a but achieves a higher mass flow rate. This can due to the low isentropic index of R600a than R717 resulting a shorter discharge process as shown in Fig. 5.6. R717 requires the highest power input due to the highest saturation pressure while R600a requires the lowest. R1234yf and R134a shows a similar power input due to the similar saturation pressure.

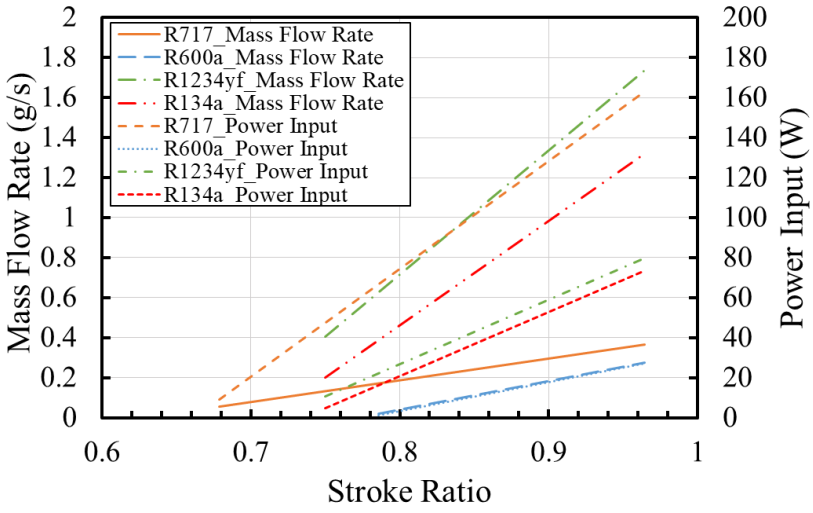

Fig. 5.9 Mass flow rate and power input varies with stroke ratios for the oil-free linear compressor

Fig. 5.10 shows the specific mass flow rate against the evaporator temperature for domestic refrigeration using the oil-free linear compressor. The specific mass flow rate for both four refrigerants increases with the increase of the evaporator temperature due to the reduction of the pressure ratio. R1234yf provides the highest specific mass flow rate due to its high vapour density while R717 has the lowest specific mass flow rate mainly due to its large power input, originating from its high in-cylinder pressure.

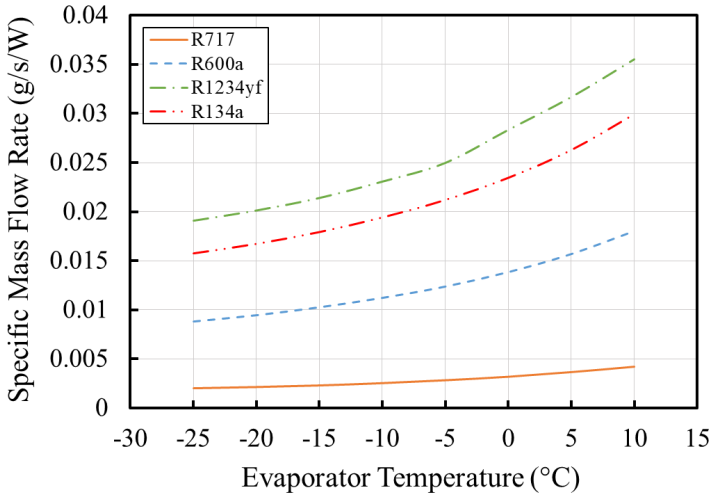

Fig. 5.10 Specific mass flow rate against evaporator temperature for domestic refrigeration using the oil-free linear compressor

Fig. 5.11 shows the motor efficiency against evaporator temperature for domestic refrigeration using the oil-free linear compressor. R600a shows the highest motor efficiency due to its low in-cylinder pressure resulting in low power input while R717 shows the lowest motor efficiency. The motor efficiency for R717 can as low as 77%. R134a and R1234yf show almost the same motor efficiency due to the similar in-cylinder pressure.

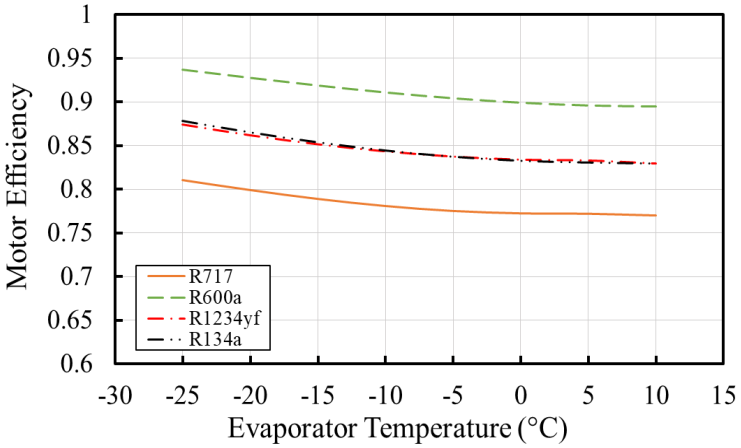

Fig. 5.11 Motor efficiency varies with evaporator temperature for domestic refrigeration using oil-free linear compressor

5.4.5 Cooling Capacity and CoP

Fig. 5.12 shows the cooling capacity and CoP against evaporator temperature for a full compressor stroke at a fixed condenser temperature of 50 °C. Both cooling capacity and CoP increase with the evaporator temperature for four refrigerants. R600a offers the lowest cooling capacity and the highest CoP due to its low mass flow rate and copper loss. Though the mass flow rate of R1234yf is 15% higher than R134a as mentioned above, R1234yf provides a similar cooling capacity to R134a due to lower latent heat. R717 offers the largest cooling capacity among four refrigerants at the same operating conditions benefited by its high latent heat. At full compressor stroke and an evaporator temperature of 5 °C, the cooling capacity for R717, R600a, R1234yf and R134a are 1635 W, 318 W, 730 W, and 775 W, respectively. Even though the high copper loss and high

pressure ratio mean more power input for R717, R717 still offers the second highest CoP among four refrigerants for evaporator temperatures over 0 °C.

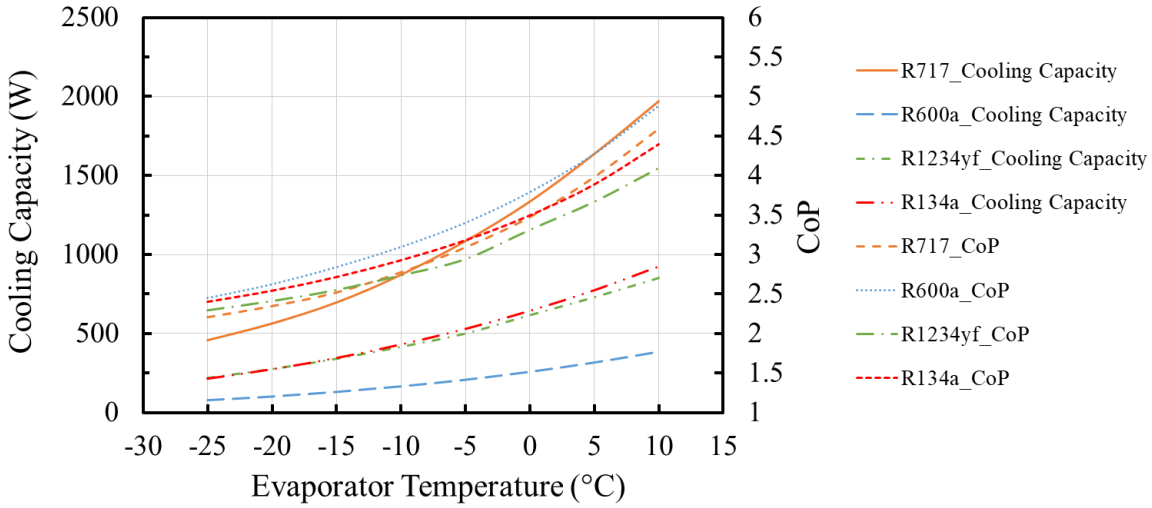

Fig. 5.12 Cooling capacity and CoP against evaporator temperature using four refrigerants (R717, R600a, R1234yf, and R134a) for a full stroke at a fixed condenser temperature of 50 °C

Fig. 5.13 shows the cooling capacity and CoP against stroke ratio of the linear compressors using four refrigerants at a fixed evaporator temperature of -23 °C and a fixed condenser temperature of 40 °C. The cooling capacity of four refrigerants increases with the stroke ratio while a reverse trend is found in CoP due to the increase of the copper loss resulting from the increased power input. To achieve a cooling capacity of 75 W, R717 needs a stroke ratio of 0.67 while R1234yf, R134a and R600a need 0.78, 0.82, and 0.96, respectively. R717 can operate at a lower stroke ratio with a higher CoP to achieve the same cooling capacity as the other three refrigerants. Therefore, the domestic refrigerator using R717 will have significant advantages including higher cooling capacity, higher energy efficiency, and lower cost. The capacity modulation is more crucial for the system using R717 due to high power consumption at full compressor stroke.

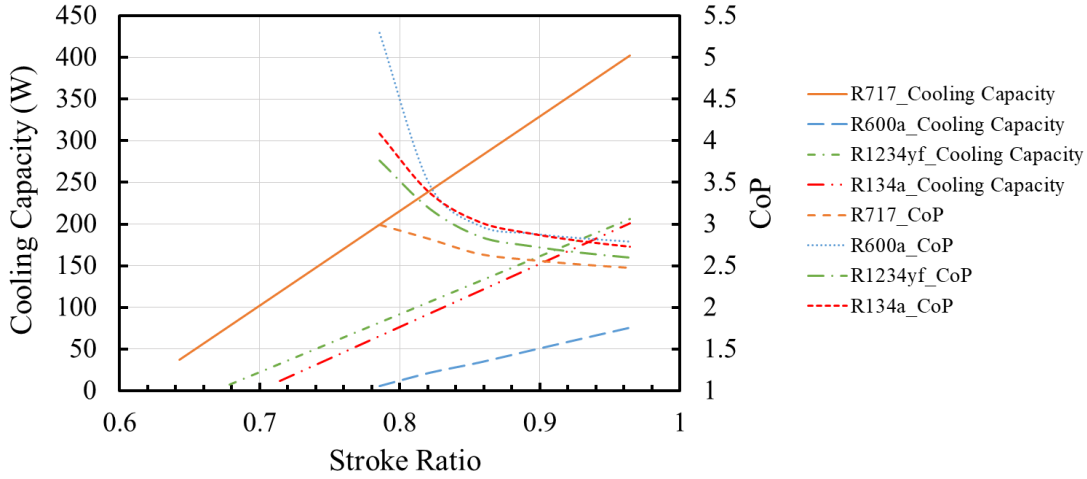

Fig. 5.13 Cooling capacity and CoP against stroke ratio of the linear compressors using four refrigerants (R717, R600a, R1234yf, and R134a) at a fixed evaporator temperature of -23 °C and a fixed condenser temperature of 40 °C

5.5 Summary

In Chapter 5, an analytical model of the oil-free linear compressor was presented allowing a comparative study on system efficiency of four refrigerants for domestic refrigeration. Key findings are listed below:

(1) R717 has the highest resonant frequency at the same operation conditions due to its high saturation pressure while R600a has the lowest.

(2) R717 requires the highest power input at the same operation conditions and offers the highest cooling capacity of four refrigerants at the same operating conditions because of extremely high latent heat.

(3) To achieve a cooling capacity of 75 W, the stroke ratios for R717, R600a, R1234yf and R134a are 0.67, 0.96, 0.78, and 0.82 respectively. The CoP for R717 is the highest.

(4) R600a has the highest CoP among four refrigerants at full stroke. However, R600a shows a much lower cooling capacity due to its low mass flow rate. A larger capacity compressor is needed for R600a to achieve the same cooling capacity as the other three refrigerants.

(5) R1234yf has similar saturation pressure, mass flow rate, resonant frequency, and power input to R134a which can be considered as an ideal drop-in alternative to R134a with minor modification and slight efficiency drop for an existing refrigerator. The experimental performance of R1234yf as alternative to R134a is given in Chapter 6.

(6) The analytical model investigate the performance of the linear compressor using low GWP refrigerants at high pressure ratios. R717 has potential to be used for domestic refrigeration.

Chapter 6 Performance of R1234yf as Alternative to R134a in the ORS

6.1 Introduction

6.1.1 Background

R134a is required to be phased out after 2020 in any hermetically sealed refrigeration system in Europe due to high GWP **[69]**. R152a and R1234yf are synthetic refrigerants with GWP of 4 and 137 and have similar thermodynamic properties to R134a. R1234yf and R152a are considered as potential alternatives to R134a. A number of studies have been conducted by researchers to investigate the drop-in performance of R1234yf and R152a in R134a VCR system. Gupta et al. **[81]** carried out experiments using R1234yf, R152a, and R134a. The experimental results show that R152a can achieve a CoP of 2.73 while R1234yf and R134a achieve CoPs of 2.51 and 2.65, respectively. Yang and Yeh **[82]** conducted a thermo-economic analysis of R152 and R1234yf and pointed out that R1234yf has higher thermo-economic performance. Sánchez et al. **[86]** investigated the energy performance of R1234yf and R152a as low GWP alternatives to R134a. Experimental results show that R152a provides a 1%-4.8% higher CoP than R134a for the same test conditions while R1234yf shows a slightly lower CoP. Meng et al. **[168]** theoretically analyzed three low GWP refrigerants as drop-in replacements of R134a in a VCR system and pointed out that R152a has a nearly equal cooling capacity to R134a. Sethi et al. **[169]** presented an experimental evaluation of R1234yf and R1234ze (E) in a R134a refrigeration system. The results show that the cooling capacity of R1234yf is 2% lower than R134a. Belman-Flores et al. **[170]** performed an experimental study of R1234yf as a drop-in replacement to R134a in a domestic refrigerator. The results indicate that the power consumption of R1234yf is 4% higher than R134a. Cabello et al. **[89]** conducted comparative studies between R134a and R152a in a VCR system with a

hermetic compressor. The results show that the cooling capacity of R152a is 1.13%-9.75% lower than R134a while CoP is 4.7% higher. Though R152a has an outstanding heat transfer performance comparing with R1234yf, the flammability can lead to safety concern when using R152a as the drop-in replacement to R134a.

As mentioned in Chapter 2, measurements that have been reported so far all involved oil lubricants for compressor. Also, due to the limitation of the conventional compressor, the refrigerant performance are compared at fixed condenser temperatures and pressure ratios but with different compressor conditions. The oil-free linear compressor can achieve compressor stroke control by changing power input. The oil-free operation also benefits the refrigeration system from preventing the blockage of the tube especially for small diameter heat exchangers and heat transfer deterioration due to oil lubricant. This chapter compares the performance of R1234yf with R134a based on the novel ORS introduced in Chapter 3 over a wide range of operating conditions. The elimination of oil lubricant enables comparable test conditions for better evaluating the performance of R1234yf and R134a and provides a potential for the ORS system using microchannel heat exchangers in the future. R152a experiments were also conducted at the same refrigerant charge. However, the ORS was overcharged using R152a due to its low vapour density. R152a is not included in the comparison of the system performance of the ORS.

6.1.2 Experimental Method

The experiments for R1234yf, R152a, and R134a were carried out using the test rig introduced in Chapter 3 and following the experimental procedure mentioned in Chapter 4. The operating frequency was manually adjusted to be resonance according to the Eq. (3.2) and (3.3). One hundred and two steady-state tests were conducted for the three refrigerants. Table 6.1 listed the test conditions for three refrigerants in the ORS. The refrigerant charge was 250 g for two refrigerants. The body temperature was above 35 °C to eliminate the refrigerant liquid within compressor.

Table 6.1 Test conditions for three refrigerants in the ORS system.

Refrigerant	R1234yf, R134a, R152a
Charge (g)	250
Pressure ratio	2.0, 2.5, 3.0, 3.5, 4.0
Compressor stroke (mm)	9, 10, 11, 12, 13
Condenser temperature (°C)	40, 45, 50
Operating frequency (Hz)	32-38
Suction temperature (°C)	20-30
Compressor body temperature (°C)	>35
Ambient temperature (°C)	22

6.2 *P-h* Diagram

Fig. 6.1 shows the *p-h* diagram of R1234yf and R134a for a pressure ratio of 3.5 and a compressor stroke of 13 mm at a condenser outlet temperature of 40 °C. R134a gives a cooling capacity of 171 W while R1234yf only gives 125 W. The cooling capacity of R1234yf is 27% lower than R134a mainly due to the smaller enthalpy difference of R1234yf though the compression work is similar (35 W). The discharge and suction pressures for R1234yf are 0.23 bar and 0.14 bar higher than R134a, respectively. Higher discharge and suction pressures of R1234yf result in a higher in-cylinder pressure thus a higher seal leakage loss and lower efficiency of the linear compressor.

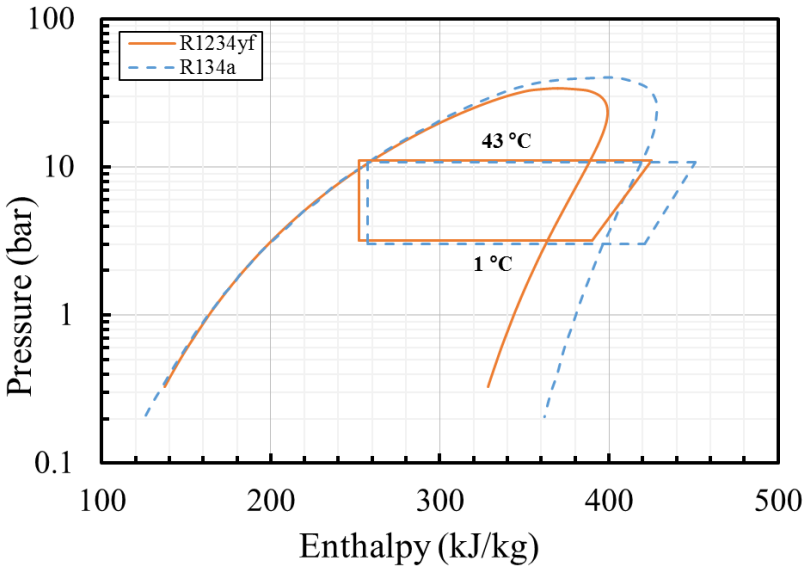

Fig. 6.1 *p-h* diagram of R1234yf and R134a for a pressure ratio of 3.5, a compressor stroke of 13 mm and a condenser temperature of 40 °C.

6.3 System Pressures and Temperatures

Fig. 6.2 shows the discharge temperature and discharge pressure of the ORS using R1234yf and R134a at a fixed condenser temperature of 40 °C and a compressor stroke of 12 mm. As can be seen, the discharge temperature for both refrigerants increases with the pressure ratio due to the increase of the compression work. R1234yf has the similar discharge temperature as R134a due to similar saturation pressure. The discharge pressure for both refrigerants rarely changes with the pressure ratio due to the fixed condenser temperature. The obviously high discharge pressure for R134a at the pressure ratio of 3.0 may due to the high condenser outlet temperature resulted by experimental error. The condenser temperature is 1.8 °C higher than the standard condenser temperature (40 °C) resulting in a higher discharge pressure. R1234yf shows a slightly higher discharge pressure than R134a due to higher vapour density.

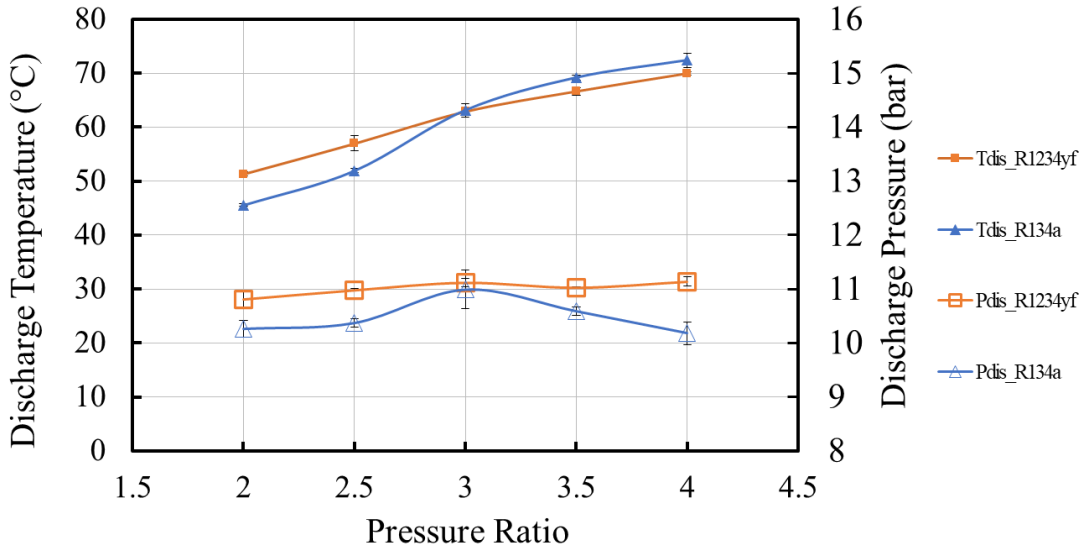

Fig. 6.2 Discharge temperature and discharge pressure against pressure ratio at a fixed condenser temperature of 40 °C and a fixed compressor stroke of 12 mm.

Fig. 6.3 shows the evaporator temperature against compressor stroke with pressure ratios from 2.0 to 4.0 at a fixed condenser temperature of 40 °C. The evaporator temperature for two refrigerants decreases with the pressure ratio at a fixed condenser temperature. The evaporator temperature ranges from -3 °C to 25 °C. For a fixed pressure ratio, the evaporator temperature hardly varies with the compressor stroke which is adjusted for cooling capacity modulation. For the same operating condition, the evaporator temperatures are very close between R134a and R1234yf. The maximum difference is only 1.5 °C which can be attributed to the thermocouple accuracy (1.5 °C). Since evaporator temperatures are similar for both refrigerants at various operating conditions, the subsequent parameters can then be compared to evaluate two refrigerants.

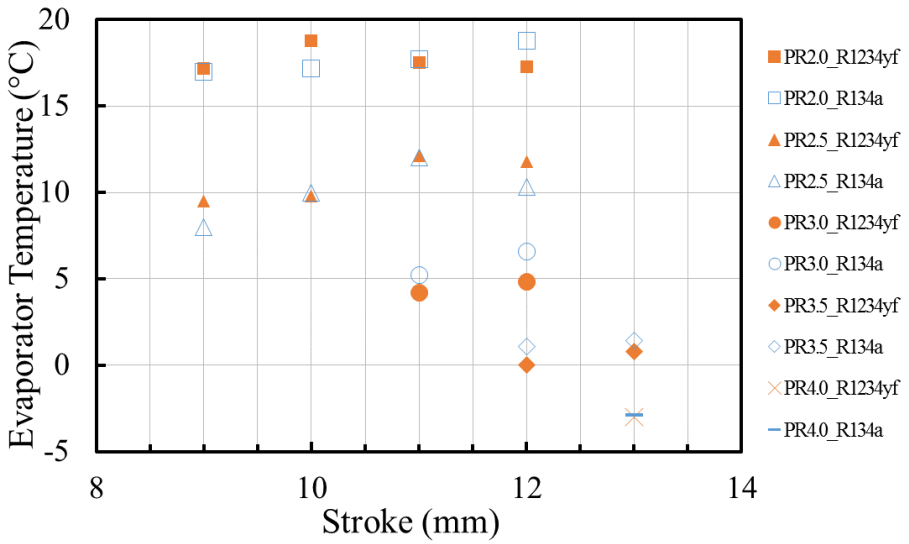

Fig. 6.3 Evaporator temperature against compressor stroke for pressure ratios of 2.0 to 4.0, at a condenser temperature of 40 °C

Fig. 6.4 (a) shows the subcooling for the ORS using R1234yf and R134a. The subcooling for both refrigerants increases with the increase of the compressor stroke due to the increase of the refrigerant vapour in the system resulting in higher discharge pressure. R1234yf shows a higher subcooling than R134a for the same condition due to lower latent heat. It is worth mentioning that R134a has only 0-2 ° C subcooling among the test conditions which indicated that the ORS is undercharged for R134a. Fig. 6.4 (b) shows the superheat for R1234yf and R134a with pressure ratios of 2.0, 2.5, and 3.5 at a condenser temperature of 40 ° C. The superheat for both refrigerants decreases with the increase of the evaporator temperature. R1234yf has higher superheat than R134a. For a condenser temperature of 50 °C, the average difference of the superheat between the two refrigerants is about 6 °C. For a lower condenser temperature, the difference increases with the evaporator temperature. A higher superheat of R1234yf has a negative influence on mass flow rate due to the reduction of the refrigerant vapour density. Higher superheat results in higher in-cylinder temperature thus higher heat transfer loss via cylinder wall and thus lower CoP.

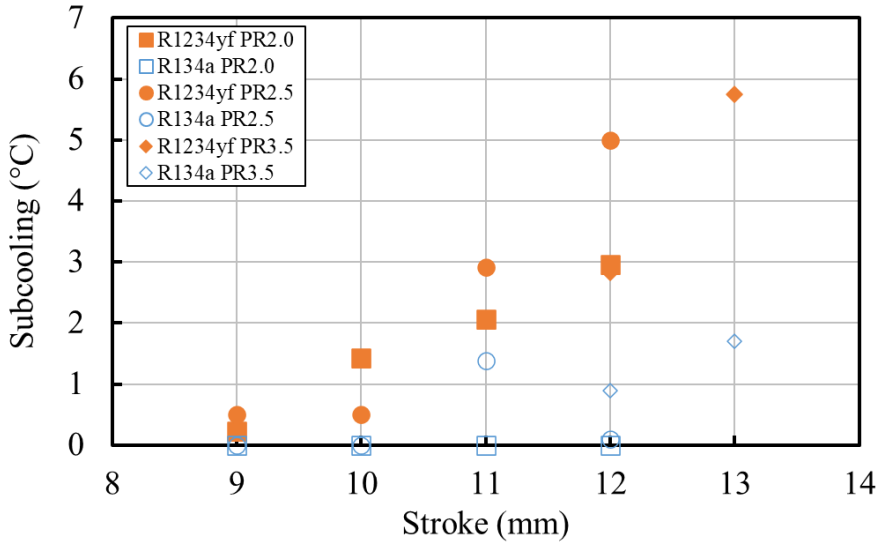

(a) Subcooling of the ORS using R1234yf and R134a

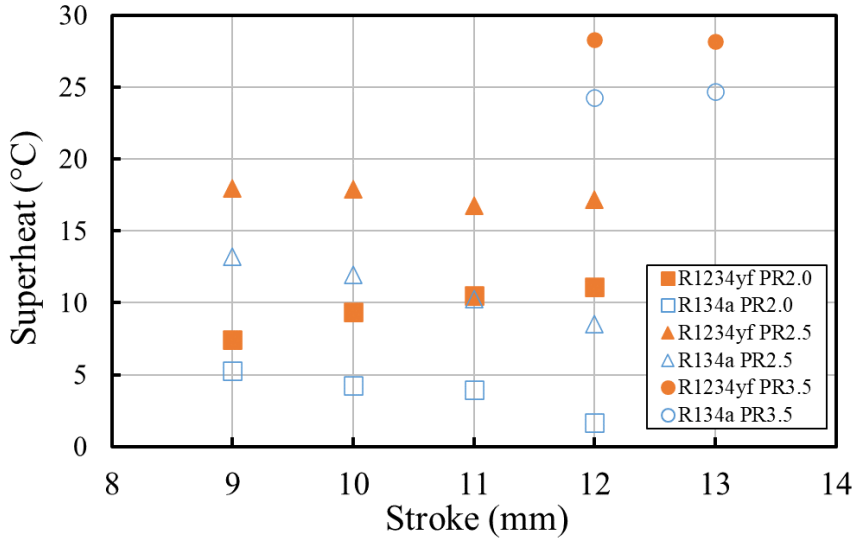

(b) Superheat of the ORS using R1234yf and R134a.

Fig. 6.4 Subcooling and superheat against evaporator temperature for R1234yf and R134a at condenser temperatures of 40 °C and 50 °C.

Fig. 6.5 shows the discharge pressure, evaporator temperature, and subcooling of the ORS using R1234yf, R134a, and R152a. The discharge pressure for R152a increases with pressure ratio while the discharge pressure for R1234yf and R134a remains relatively the same. The evaporator temperature does not change obviously with pressure ratio due to increasing discharge pressure. At a pressure ratio of 4.0, the subcooling for R152a can as high as 20 °C. The increasing discharge temperature and extremely high subcooling for

R152a, indicate that the ORS was overcharged using R152a with a charge of 250 g. The overcharged refrigerant floods in the condenser resulting in an increase of discharge pressure, extremely high subcooling, and high evaporator temperature. The low optimal refrigerant charge of R152a can due to its low liquid density and saturation pressure than that of R134a and R1234yf. As the overcharge system can significantly decrease the overall efficiency, R152a is not included in the comparison of the system performance of the ORS.

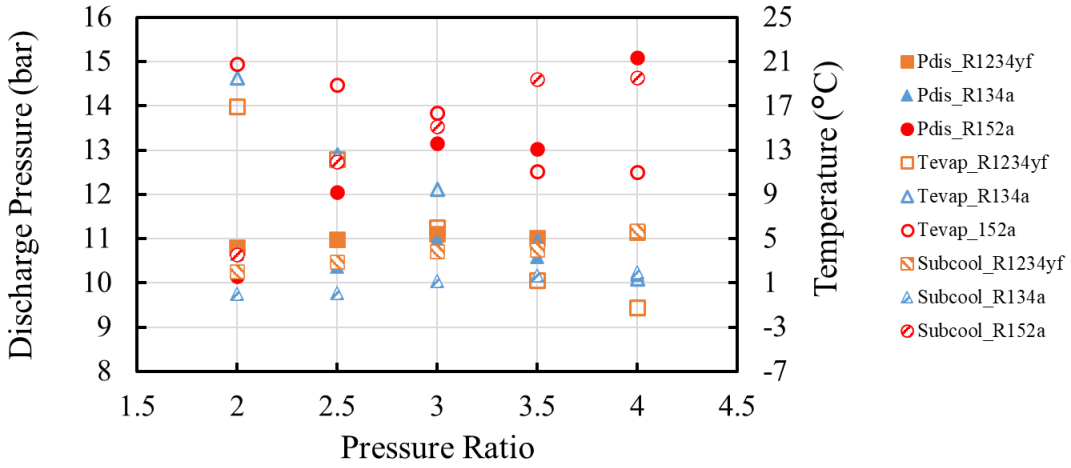

Fig. 6.5 Discharge pressure, evaporator temperature, and subcooling of the ORS using R1234yf, R134a, and R152a.

Fig. 6.6 shows that the evaporator pressure drop as a function of the mass flow rate for R1234yf and R134a at condenser temperatures of 40 °C, 45 °C, and 50 °C. It can be seen that the evaporator pressure drop for R1234yf is higher than R134a for the same mass flow rate. This may due to higher friction loss and vapour density of R1234yf. For a mass flow rate of 2.3 g/s at a fixed condenser temperature of 45 °C, the pressure drop across the evaporator for R1234yf is 0.016 bar higher than R134a. Higher pressure ratio leads to higher pressure drop. Higher mass flow rate will also cause much higher pressure drop. This is due to larger friction of R1234yf than R134a.

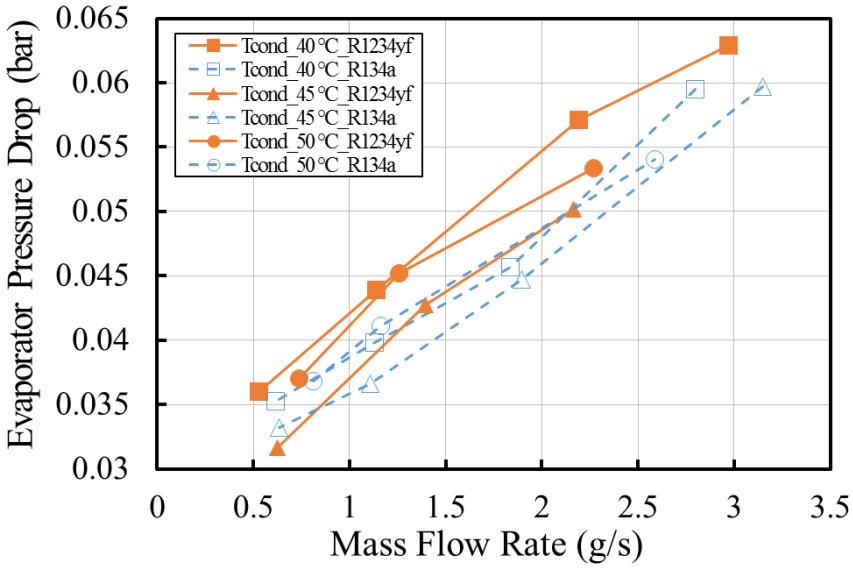

Fig. 6.6 Power input against mass flow rate for R1234yf and R134a for pressure ratios of 2.5 to 3.5 at a fixed condenser temperature of 40 °C.

6.4 Compressor Performance

Fig. 6.7 shows the resonant frequency of the ORS using R1234yf and R134a with pressure ratios from 2.0 to 3.0 at a fixed condenser temperature of 40 °C. For both refrigerants, higher pressure ratio leads to higher resonant frequency due to higher induced gas spring stiffness. For a fixed pressure ratio, higher compressor stroke causes lower gas spring thus lower resonant frequency. Generally, R1234yf has higher resonant frequency than R134a. This is because the discharge pressure is higher for R1234yf owing to its low latent heat and high vapour density.

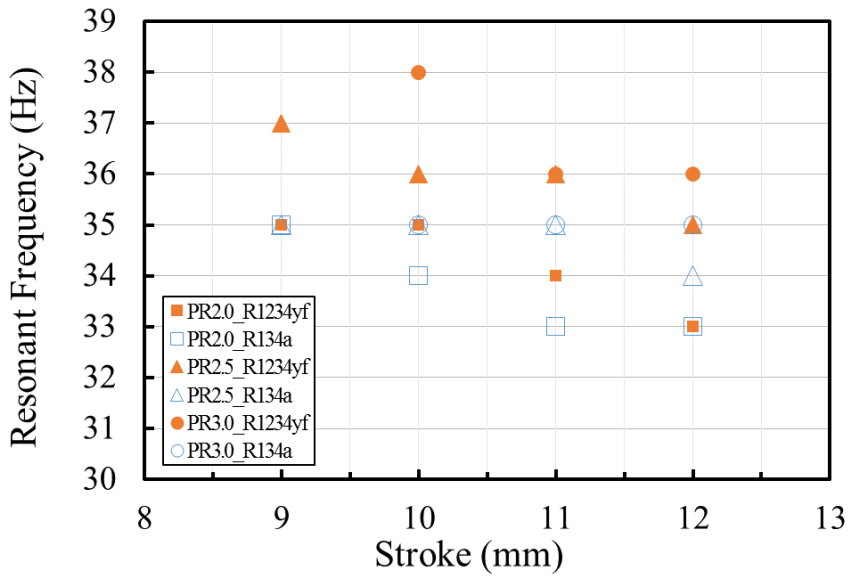

Fig. 6.7 Resonant frequency against compressor stroke of the ORS using R1234yf and R134a with various pressure ratios at a condenser temperature of 40 °C.

Fig. 6.8 shows the mass flow rate of R1234yf and R134a varying with the compressor stroke for pressure ratios of 2.0 to 3.5 at a fixed condenser temperature of 40 °C. Overall, R1234yf provides an average 5% higher mass flow rate than R134a due to high vapour density and resonant frequency. The vapour density of R1234yf is 14% higher than R134a as mentioned in Chapter 2. High seal leakage loss due to high in-cylinder pressure deteriorates the mass flow rate of R1234yf. At a pressure ratio of 2.5 and a compressor stroke of 12 mm, the mass flow rate of R1234yf is 0.36 g/s (16%) higher than R134a.

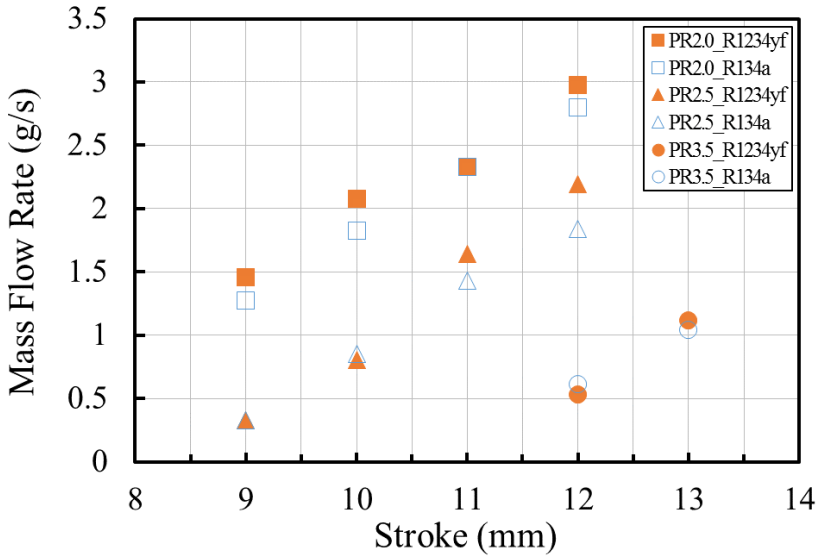

Fig. 6.8 Mass flow rate against compressor stroke using R1234yf and R134a for pressure ratios of 2.5 to 3.5 at a fixed condenser temperature of 40 °C.

Fig. 6.9 shows the power input varying with the mass flow rate for R1234yf and R134a for pressure ratios from 2.0 to 3.5 at a fixed condenser temperature of 40 °C. It can be seen that the power input increases very linearly with the mass flow rate due to increasing compressor stroke at a fixed pressure ratio. Overall, due to higher vapour density, R1234yf requires 6-15% lower power input to achieve the same mass flow rate for R134a. The lower power input for R1234yf results in lower copper loss because of lower input current. It is interesting to see that the rate of increasing is nearly the same for both refrigerants with various pressure ratios. At a fixed pressure ratio of 2.0 and a mass flow rate of 2 g/s, the power input for R1234yf is 16% lower than R134a with an average difference of 7 W. However, at a fixed pressure ratio of 3.5, the different of power input is negligible.

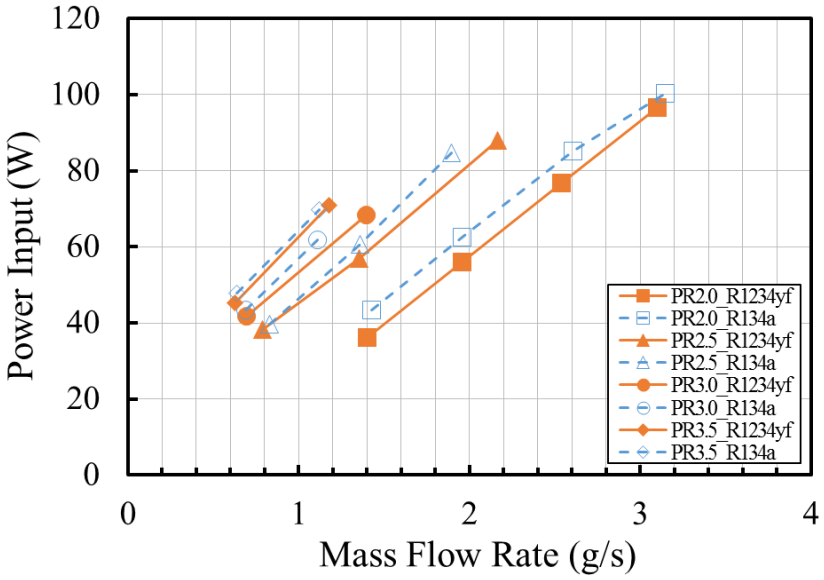

Fig. 6.9 Power input against mass flow rate for R1234yf and R134a with pressure ratios of 2.5 to 3.5 at a fixed condenser temperature of 40 °C.

Fig. 6.10 illustrates the specific mass flow rate against condenser temperature using R1234yf and R134a for pressure ratios of 2.5 and 3.5. It can be seen that for a fixed condenser temperature, specific mass flow rate decreases as the pressure ratio increases due to the decrease of volumetric efficiency. For a fixed pressure ratio, the specific mass flow rate for two refrigerants decreases as the discharge pressure increases thus electrical power input. The decrease of the mass flow rate has degraded specific mass flow rate.

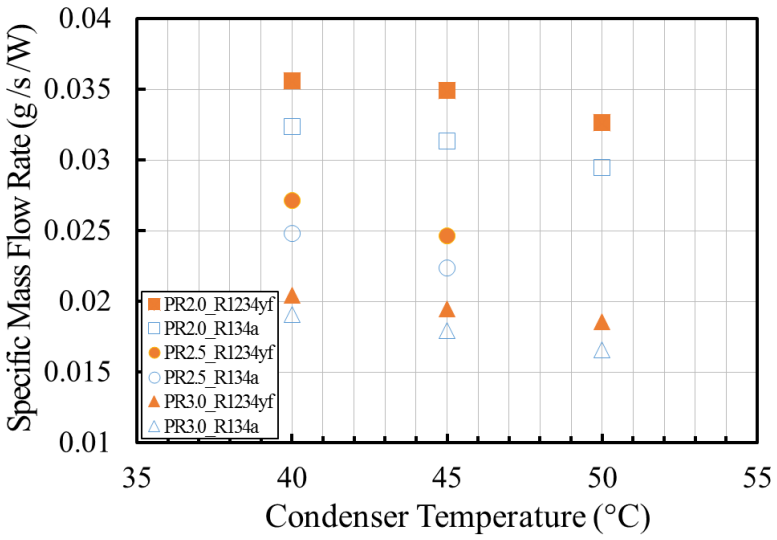

Fig. 6.10 Specific mass flow rate against condenser temperature using R1234yf and R134a for pressure ratios of 2.5 and 3.5.

Fig. 6.11 shows the volumetric efficiency against the evaporator temperature for R1234yf and R134a at condenser temperatures of 40 °C, 45 °C, and 50 °C. It can be seen that the volumetric efficiency for both refrigerants increases linearly with the evaporator temperature due to decreasing pressure ratio. Higher condenser temperature causes lower mass flow rate and thus lower volumetric efficiency for both refrigerants. At a fixed condenser temperature of 40 °C, the volumetric efficiency of R1234yf is 1-4% lower than R134a due to the higher suction pressure and resonant frequency of R1234yf though the mass flow rate of R1234yf is slightly higher than R134a.

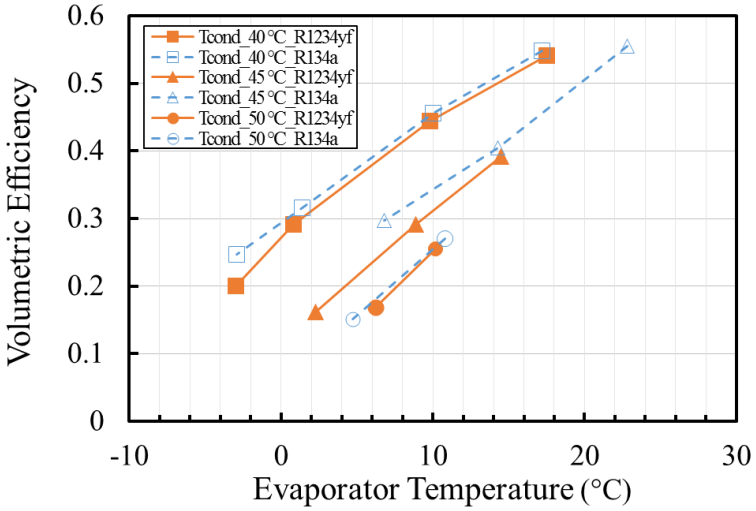

Fig. 6.11 Volumetric efficiency against evaporator temperature for R1234yf and R134a at condenser temperatures of 40 °C, 45 °C, and 50 °C.

6.5 Cooling Capacity and CoP

Fig. 6.12 shows the cooling capacity against the evaporator temperature for R1234yf and R134a at condenser temperatures of 40 °C, 45 °C, and 50 °C. The cooling capacity for both refrigerants increases with the evaporator temperature. A higher condenser temperature tends to have a lower cooling capacity for both refrigerants due to lower mass flow rate. The cooling capacity for R1234yf is 5-20% lower than R134a. This is due to the lower latent heat of R1234yf in comparison with R134a. The difference of cooling capacity between the two refrigerants doesn't change much with the increase of condenser temperature. At an evaporator temperature of -3 °C and a condenser temperature of 40 °C, the cooling capacities for R1234yf and R134a are 93 W and 118 W, respectively. To produce the same amount of cooling capacity for a fixed evaporator and condenser temperature, the compressor using R1234yf needs to operate at higher compressor stroke or displacement (for conventional compressors). This could be a major modification if R1234yf replaces R134a in a refrigeration system.

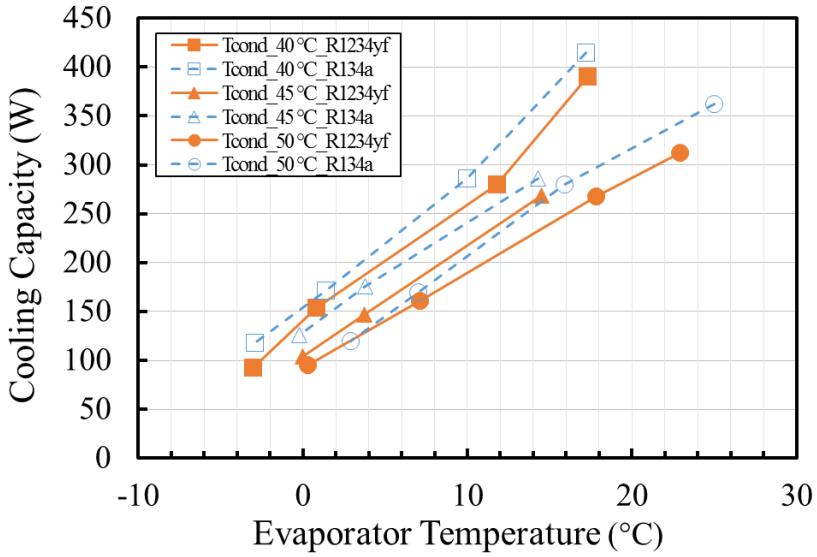

Fig. 6.12 Cooling capacity against evaporator temperature for R1234yf and R134a at condenser temperatures of 40 °C, 45 °C, and 50 °C.

Fig. 6.13 shows the CoP against evaporator temperature for R1234yf and R134a at condenser temperatures of 40 °C, 45 °C, and 50 °C. For both refrigerants, the CoP increases with evaporator temperature. R1234yf has lower CoP than R134a due to its low cooling capacity and volumetric efficiency. The CoPs at an evaporator temperature of -3 °C and a condenser temperature of 40 °C for R1234yf and R134a are 1.8 and 2.3, respectively. The CoPs at an evaporator temperature of 17 °C and a condenser temperature of 40 °C for R1234yf and R134a are 4.4 and 4.8, respectively. At a condenser temperature of 40 °C, the CoP of R1234yf is 5-20% lower than R134a. At a fixed condenser temperature of 50°C, the CoPs of R1234yf are almost the same as R134a.

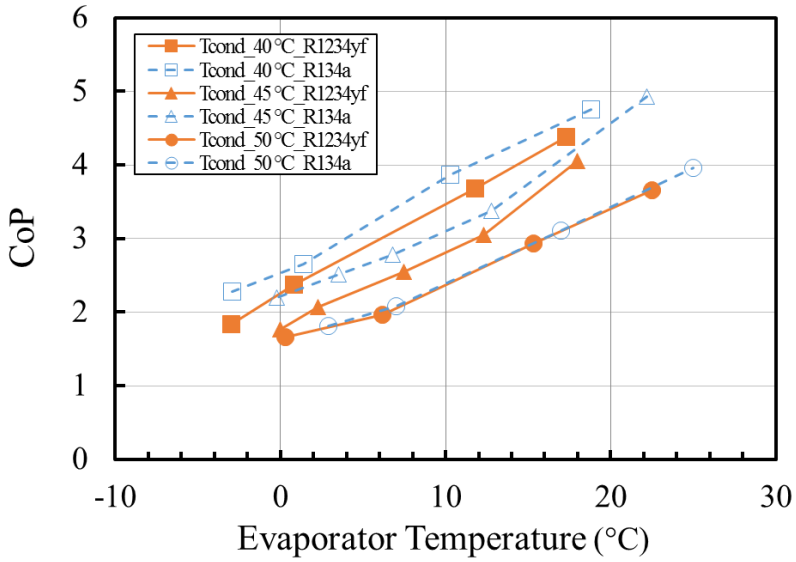

Fig. 6.13 CoP against evaporator temperature for R1234yf and R134a at condenser temperatures of 40 °C, 45 °C, and 50 °C.

Fig. 6.14 shows the cooling capacity and CoP against condenser temperature for R1234yf and R134a with an evaporator temperature of 5 °C. The cooling capacities for two refrigerants remain relatively the same with the increase of condenser temperature due to the fixed compressor stroke resulting in rarely the same mass flow rate. The CoP decreases linearly with increasing condenser temperature due to the reduction of the enthalpy between evaporator inlet and outlet for R1234yf and R134a. Moreover, an increase of electrical power input degrades the CoP. The CoP of R1234yf is 10-25% lower than R134a, while the cooling capacity of R1234yf is 10-30% lower than R134a. It is worth mentioning that with increasing condenser temperature, the difference of CoP between R1234yf and R134a decreases as R1234yf is less sensitive to condenser temperature.

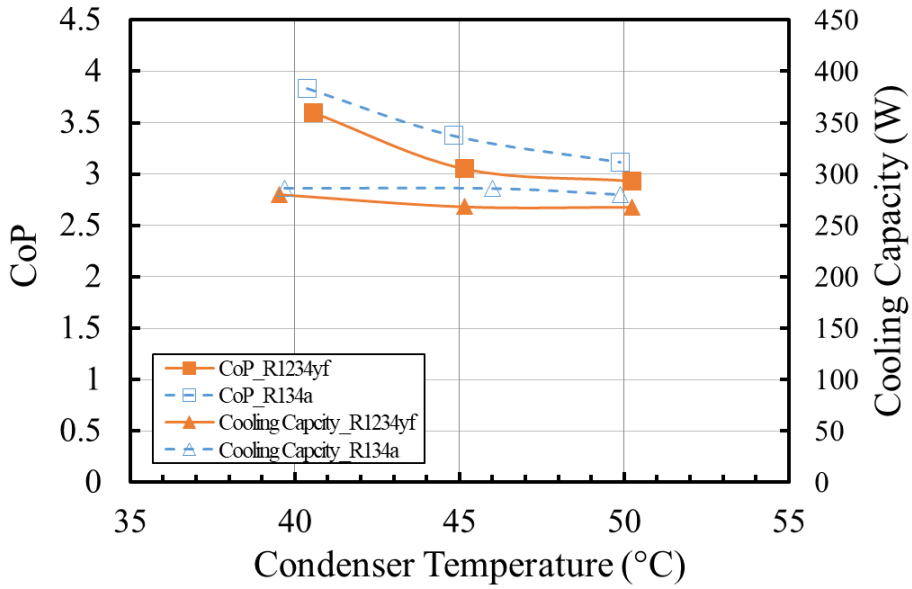

Fig. 6.14 Cooling capacity and CoP against condenser temperature for R1234yf and R134a with an evaporator inlet temperature of 5 °C.

6.6 Summary

In this chapter, the system performance of the low GWP refrigerant R1234yf as a drop-in replacement for R134a in the ORS is presented for wide range of operating conditions. Generally, R1234yf deteriorates the performance if it replaces R134a. Further modification of refrigeration system is needed for the use of R1234yf including higher compressor stroke or displacement. Tests of the ORS using R152a were also conducted. However, due to the low liquid density and saturation pressure, the system was overcharged and the system performance was not discussed in details. Key findings from the experiments are listed as below:

(1) For given pressure ratio and compressor stroke, the resonant frequency of R1234yf is higher than R134a due to higher superheat.

(2) At a fixed pressure ratio, the mass flow rate of R1234yf is 5% higher than R134a. The power input for R1234yf is 6-15% lower than R134a for a given mass flow rate.

(3) The evaporator pressure drop for R1234yf is higher than R134a for a given mass flow rate due to higher friction.

(4) With the increase of the evaporator temperature, the volumetric efficiency for both refrigerants increases and higher condenser temperature tends to have lower volumetric efficiency.

(5) The optimal charge of R134a can higher than that of R1234yf due to its low vapour density and similar saturation pressure.

(6) At a condenser temperature of 40 °C, the CoP of R1234yf is 5-20% lower than R134a depending on the evaporator temperature and compressor stroke. The CoP increases linearly with decreasing condenser temperature. However, the CoP of R1234yf is less sensitive to condenser temperature.

(7) Though pressure drop in the evaporator and cooling performance of two refrigerants were measured, the heat transfer coefficient and pressure drop need to be further investigated to enable a better understand of two refrigerants. Correlations of pressure drop and heat transfer coefficient are also needed to predict the system performance and assist system optimization.

Chapter 7 Evaporation Heat Transfer and Pressure Drop of Low GWP Refrigerants in a Horizontal Annular Evaporator

7.1 Introduction

Pressure drop and heat transfer in evaporators have significant influence on the efficiency and capacity of any VCR system. Wongwises and Polsongkram **[171]** investigated the two-phase heat transfer coefficient and pressure drop of R134a during evaporation inside a smooth helically coiled. The correlations for evaporation pressure drop and heat transfer were developed utilizing the Martinelli parameter, Dean number and boiling number. Li and Hibiki **[172]** developed a correlation to predict the two-phase frictional pressure drop for R134a using two-phase Reynolds number, two-phase viscosity number and gas quality. The mean absolute percentage error for the correlation is 17.4%. Dione et al. **[173]** developed correlations of local heat transfer and pressure drop. The newly developed correlations are able to predict the evaporation heat transfer in geothermal operating conditions. Laohalertdecha et al. **[174]** proposed correlations for evaporation heat transfer coefficient and two-phase friction factor of R134a flowing through horizontal corrugate tubes. Smooth tube and corrugated tubes with inner diameters of 8.7 mm and lengths of 2000 mm were used as the inner tube. The correlations are based on Reynolds number, Prandtl number, corrugation pitch, depth and inside diameter. Several studies have been carried out to investigate the condensation pressure drop and boiling heat transfer performance of R1234yf and R152a. Zhang et al. **[175]** proposed correlations to predict the boiling heat transfer and pressure drop of R134a, R1234yf, and R1234ze. Based on proposed heat transfer and pressure drop correlations, agreements within ±25% were obtained for experimental data in similar experiments with high saturation temperature. Liu et al. **[176]** presents an experimental work for heat transfer and pressure drop during condensation of R152a in circular and square microchannel with hydraulic diameters of

1.152 mm and 0.952 mm, respectively. Hirose et al. **[177]** proposed new general correlations for heat transfer and frictional pressure drop during condensation process. The proposed general correlations agree well with measured data of R32, R410a and R152a, within ±30%.

Despite a number of works have been carried out on evaporation heat transfer and pressure drop, studies mentioned above all involved oil lubricants which inevitably reduces the performance of the heat exchanger. Also, the correlations mentioned above mainly are valid for specific geometry and the correlations for low GWP refrigerants are rarely reported. In this chapter, improved correlations of Nusselt number and frictional pressure drop based on Foust and Christian correlation **[178]** and Lockhart and Martinelli correlation **[179]** for two-phase flow of the ORS using three refrigerants (R152a, R1234yf and R134a) are presented. The improved correlation can be used in the numerical model to assist the design of ORS. The numerical model is presented in Chapter 9.

Measurements were carried out based on the test rig for the ORS as mentioned in Chapter 3. Fig. 7.1 shows the simplified schematic diagram of the refrigerant circuit. Six thermocouples and three pressure transducers were used to measure the temperatures (discharge, condenser outlet, evaporator inlet, evaporator wall, evaporator outlet and suction) and pressures (discharge, evaporator inlet and evaporator outlet). The pressure drop within the evaporator is the pressure difference between the evaporator inlet pressure and the evaporator outlet pressure. Also, as can be seen from Fig. 7.1, a U-type heat exchanger was used as evaporator. The pressure drop at corner of the bend is neglected. R1234yf, R134a, R152a were used as working fluid for the experiments. One hundred and twenty-five steady-state tests were conducted to investigate the heat transfer coefficient and pressure drop of three refrigerants in the horizontal tube evaporator. The evaporator inlet pressure ranges from 2.7 bar to 6.6 bar. The mass flux and the evaporator inlet temperature were controlled from 6 kg/m^2/s to 65 kg/m^2/s and -1 °C to 22 °C,

respectively, by changing the compressor stroke and expansion valve. The condenser temperature was kept at 40 °C.

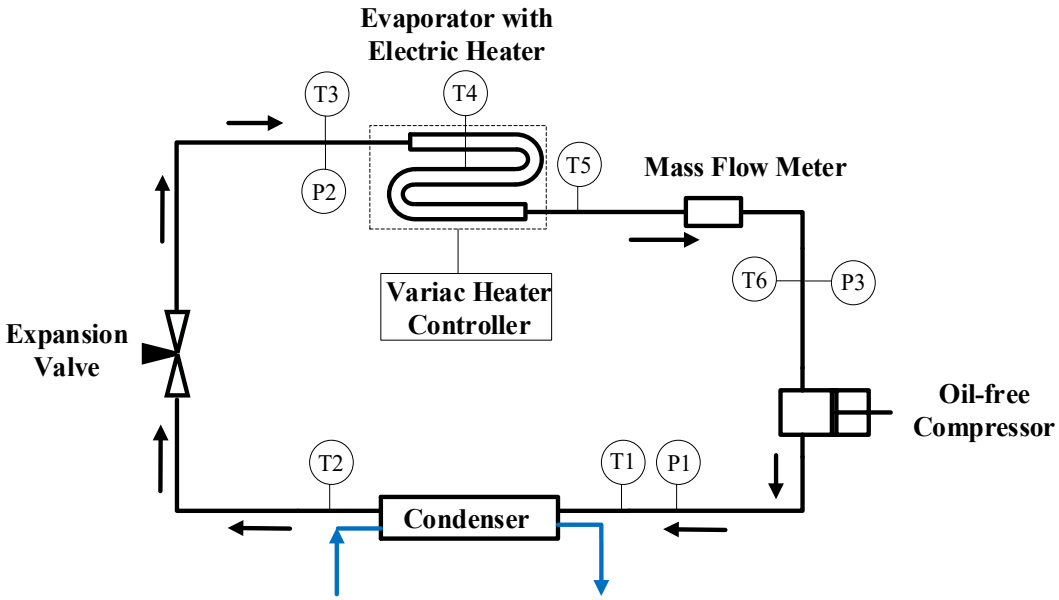

Fig. 7.1 Simplified schematic diagram of the refrigerant circuit

7.2 Existing Correlation for Heat Transfer and Pressure Drop

7.2.1 Vapour Quality and Void Fraction

The heat transfer in the evaporator is convection evaporation. Unlike the flow regime for boiling heat transfer, a simplified physical description of the flow is assumed to describe the evaporation in the annular evaporator. The heat flux in the evaporator is considered as constant. Thus, the vapour quality changes linearly in the evaporator. The vapour quality at the evaporator inlet can be expressed as

$$x_{\mathrm{in}} = \frac{h_{\mathrm{in}} - h_{\mathrm{l}}}{h_{\mathrm{g}} - h_{\mathrm{l}}} \tag{7.1}$$

where h_{in} is the enthalpy at the evaporator inlet, h_{g} is the enthalpy of the saturated vapour and h_{l} is the enthalpy of the saturated liquid.

The two-phase length in the evaporator can be calculated as

$$L_{\mathrm{tp}} = L_{\mathrm{total}} \frac{h_{\mathrm{g}} - h_{\mathrm{in}}}{h_{\mathrm{out}} - h_{\mathrm{in}}} \tag{7.2}$$

where L_{total} is the total length of evaporator (1280 mm), h_{out} is the enthalpy at evaporator outlet.

Void fraction is the fraction of the channel volume that is occupied by the gas phase. The selection of the void fraction model can affect heat transfer coefficient and pressure drop. According to Hughmark Model **[180]**, the void fraction α can be expressed as

$$\alpha = \left(-\frac{0.8454}{Z} + 0.7266 + 0.06011 Z^{\frac{1}{3}} - 0.0003482 Z\right) a_0 \tag{7.3}$$

in which

$$a_0 = \frac{1}{1 + \left(\frac{1}{x} - 1\right)\frac{\rho_{\mathrm{g}}}{\rho_{\mathrm{l}}}} \tag{7.4}$$

$$Z = \frac{Re_{\mathrm{tp}}^{\frac{1}{6}} Fr^{\frac{1}{8}}}{(1 - a_0)^{\frac{1}{4}}} \tag{7.5}$$

where ρ_{g} is the vapour density of refrigerant and ρ_{l} is the liquid density of refrigerant.

The two-phase Reynolds number Re_{tp} can be expressed as

$$Re_{\mathrm{tp}} = \frac{\mathrm{D_h} G}{\mu_{\mathrm{l}} + \alpha(\mu_{\mathrm{g}} - \mu_{\mathrm{l}})} \tag{7.6}$$

where $\mathrm{D_h}$ is the hydraulic diameter, μ_{l} is the liquid viscosity and μ_g is the vapour viscosity.

G is the mass flux which can be calculated as

$$G = \frac{\dot{m}}{\mathrm{A}} \tag{7.7}$$

where A is the cross section area of the evaporator and $\dot{m}$ is the mass flow rate.

Fr is the Froude number which can be expressed as

$$Fr = \frac{1}{\mathrm{g}\mathrm{D}_\mathrm{h}}\left(\frac{xG}{\alpha\rho_\mathrm{g}}\right)^2 \tag{7.8}$$

where g is the gravitational acceleration.

7.2.2 Nusselt Number and Heat Transfer Coefficient for Two-phase Flow

Most of correlations for Nusselt number are proposed as a function of annular diameter ratio, Reynolds number and Prandtl number **[181]**. Foust and Christian correlation **[178]**, Dirker and Meyer correlation **[181]**, and Davis correlation **[182]** are used to be compared with experimental Nusselt number. Foust and Christian **[178]** correlation for calculating Nusselt number can be expressed as

$$Nu = 0.04\frac{\mathrm{c}}{(\mathrm{c}+1)^{0.2}}Re_{\mathrm{tp}}{}^{0.8}Pr_\mathrm{l}{}^{0.4} \tag{7.9}$$

where c is the annular diameter ratio and Pr_l is the liquid Prandtl number.

Davis correlation **[182]** can be expressed as

$$Nu = 0.038\mathrm{c}^{0.15}(\mathrm{c}-1)^{0.2}Re^{0.8}Pr_\mathrm{l}^{\frac{1}{3}}\left(\frac{\mu}{\mu_\mathrm{w}}\right)^{0.14} \tag{7.10}$$

where μ is the viscosity of the refrigerant, μ_w is the viscosity of the refrigerant along the wall.

Dirker and Meyer correlation **[181]** can be expressed as

$$P = 1.013e^{-0.067\mathrm{c}} \tag{7.11}$$

$$C_\mathrm{o} = \frac{0.003\mathrm{c}^{1.86}}{0.063\mathrm{c}^3-0.674\mathrm{c}^2+2.225\mathrm{c}-1.157} \tag{7.12}$$

$$Nu = C_\mathrm{o}Re^{P}Prl_\mathrm{l}^{\frac{1}{3}}\left(\frac{\mu}{\mu_\mathrm{w}}\right)^{0.14} \tag{7.13}$$

According to the method mentioned by Yan and Lin **[183]**, the heat transfer coefficient *h* and experimental Nusselt number can be expressed as

$$h = \frac{\dot{W}}{\mathrm{A}_\mathrm{e}(T_\mathrm{w}-T_\mathrm{r})} \tag{7.14}$$

$$Nu = \frac{h\mathrm{D}_\mathrm{h}}{k_\mathrm{l}} \tag{7.15}$$

where A_e is the total heat transfer area of the evaporator, T_w is the average pipe wall temperature, T_r is the mean refrigerant temperature, and k_l is the conductivity of the refrigerant. $\dot{W}$ is the cooling capacity which can be calculated as

$$\dot{W} = \dot{m}(h_{out} - h_{in}) \tag{7.16}$$

The definition of Mean Absolute Percentage Error (MAPE) is

$$MAPE = \frac{100\%}{n}\sum_{t=1}^{n}\left|\frac{A_t - F_t}{A_t}\right| \tag{7.17}$$

where A_t is the experimental value, F_t is the predicted value and n is the number of sample.

Fig. 7.2 shows the predicted Nusselt number for three refrigerants using three existing correlations **[178, 181, 182]** against experimental Nusselt number. The predicted Nusselt number using Foust and Christian correlation **[178]** for R1234yf, R152a, and R134a have MAPE of 81%, 84%, and 74%, respectively. Dirker and Meyer correlation **[181]** predicts the Nusselt number with MAPEs of 91%, 94%, and 94% for R1234yf, R152a and R134a, respectively. Davis correlation **[182]** predicts the Nusselt number with MAPEs of 88%, 89%, and 83%. The high MAPEs for the three literature correlations may be due to the difference in mass flux, working fluid and diameter ratio.

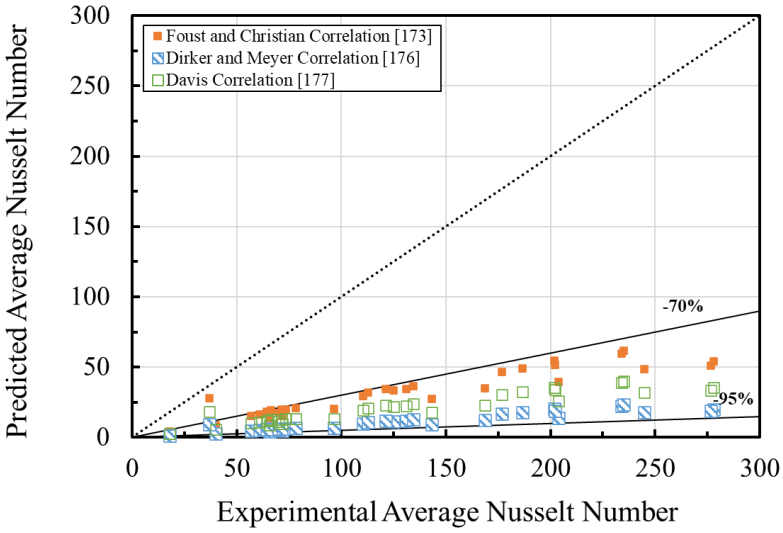

(a)

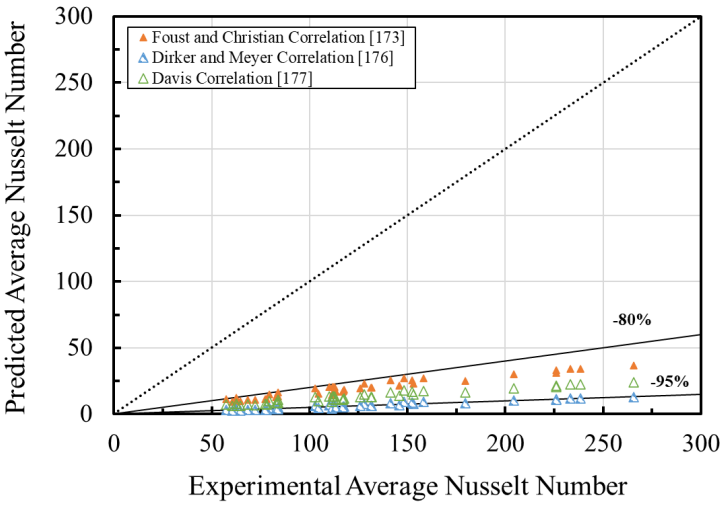

(b)

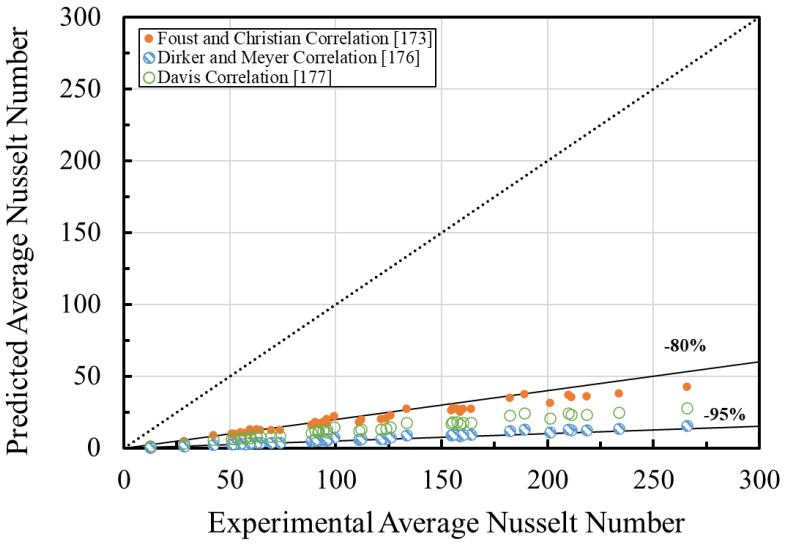

(c)

Fig. 7.2 Predicted Nusselt number against experimental Nusselt number for horizontal evaporator using Foust and Christian correlation **[178]**, Dirker and Meyer correlation **[181]**, and Davis correlation **[182]**: (a) R1234yf; (b) R152a; (c) R134a.

7.2.3 Pressure Drop

The experimental pressure drop is calculated as

$$\Delta P_{\mathrm{d}} = P_{\mathrm{in}} - P_{\mathrm{out}} \tag{7.18}$$

where P_{in} is the pressure at the evaporator inlet and P_{out} is the pressure at the evaporator outlet.

The total pressure drop in the evaporator can be expressed as

$$\Delta P = \int ((\frac{dp}{dz})_{\mathrm{l}} + (\frac{dp}{dz})_{\mathrm{g}} + (\frac{dp}{dz})_{\mathrm{tp}} + (\frac{dp}{dz})_{a})dz \tag{7.19}$$

where $(\frac{dp}{dz})_{\mathrm{l}}$ is the liquid-phase frictional pressure drop, $(\frac{dp}{dz})_{\mathrm{g}}$ is the vapour-phase frictional pressure drop, $(\frac{dp}{dz})_{\mathrm{tp}}$ is the two-phase frictional pressure drop and $(\frac{dp}{dz})_{a}$ is the acceleration pressure drop.

The acceleration pressure drop can be expressed as

$$(\frac{dp}{dz})_{a} = G^2(\frac{(1-x_{\mathrm{out}})^2}{\rho_{\mathrm{l}}(1-\alpha_{\mathrm{in}})} + \frac{{x_{\mathrm{out}}}^2}{\rho_g \alpha_{\mathrm{out}}} - \frac{(1-x_{\mathrm{in}})^2}{\rho_{\mathrm{l}}(1-\alpha_{\mathrm{in}})} - \frac{{x_{\mathrm{in}}}^2}{\rho_g \alpha_{\mathrm{in}}}) \tag{7.20}$$

where x_{out} is the gas fraction at the evaporator outlet, x_{in} is the gas fraction at the evaporator inlet, α_{in} is the void fraction at the evaporator inlet and α_{out} is the void fraction at the evaporator.

The liquid-phase and vapour-phase frictional pressure drop can be expressed as

$$\Delta P_{\mathrm{l}} = 4f_{\mathrm{l}}(\frac{\mathrm{L}}{\mathrm{D_h}})(G(1-x))^2(\frac{1}{\rho_{\mathrm{l}}}) \tag{7.21}$$

$$\Delta P_{\mathrm{g}} = 4f_{\mathrm{g}}(\frac{\mathrm{L}}{\mathrm{D_h}})(Gx)^2(\frac{1}{\rho_{\mathrm{g}}}) \tag{7.22}$$

where f_{l} and f_{g} is liquid frictional factor and vapour frictional factor which can be calculated as

$$f_{\mathrm{l}} = \frac{0.079}{Re_{\mathrm{l}}^{0.25}} \tag{7.23}$$

$$f_{\mathrm{g}} = \frac{0.079}{Re_{\mathrm{g}}^{0.25}} \tag{7.24}$$

where Re_{l} is the Reynold number for refrigerant liquid and Re_{l} is the Reynold number for refrigerant vapour.

Lockhart and Martinelli **[179]** proposed a correlation to predict the two-phase frictional pressure drop base on a two-phase multiplier as

$$\Delta P_{\mathrm{f}} = \Phi_{\mathrm{l}}^2 \Delta P_{\mathrm{l}} \tag{7.25}$$

$$\Phi_{\mathrm{l}}^2 = 1 + \frac{\mathrm{C}}{X} + \frac{1}{X^2} \tag{7.26}$$

where C is a constant value depending on the regimes of the fluid and X is the Martinelli parameter which can be expressed as

$$X = (\frac{1-x}{x})^{0.9}(\frac{\rho_g}{\rho_l})^{0.5}(\frac{\mu_l}{\mu_g})^{0.1} \tag{7.27}$$

Moreno and Thome **[184]** developed a correlation to predict the two-phase frictional pressure drop for annular flow structure. The correlation can be expressed as

$$\Delta P_{annular} = 2(f_i)_{annular}\frac{L_{tp}\rho_g u_g^2}{D_o} \tag{7.28}$$

where D_o is the tube outer diameter, u_g is the true average velocity of vapour which can be calculated as

$$u_g = \frac{G}{\rho_g \alpha}x \tag{7.29}$$

The interfacial film friction factor for annular flow can be calculated as

$$(f_i)_{annular} = 0.67\left(\frac{\delta}{D_o}\right)^{1.2}\left(\frac{(\rho_l-\rho_g)g\delta^2}{\sigma}\right)^{-0.4}(\frac{\mu_g}{\mu_l})^{0.08}We^{-0.034} \tag{7.30}$$

where σ is the surface tension and the δ is the liquid film thickness which can be calculated as

$$\delta = \frac{D_o(1-\alpha)}{4} \tag{7.31}$$

In this method, the liquid Weber number is calculated as

$$We = \frac{\rho_l u_l^2 D_o}{\sigma} \tag{7.32}$$

where u_l is the true average velocity of liquid which can be calculated as

$$u_l = \frac{G}{\rho_l(1-\alpha)}(1-x) \tag{7.33}$$

Fig. 7.3 shows the predicted pressure drop for three refrigerants using the Lockhart and Martinelli correlation **[179]** and Moreno and Thome correlation **[184]** against experimental pressure drop. The predicted pressure drops using Lockhart correlation **[179]** for R1234yf, R152a and R134a have MAPE of 62%, 82% and 73%, respectively. Moreno

and Thome correlation **[184]** predicts the pressure drop with MAPEs of 87%, 72% and 41%.

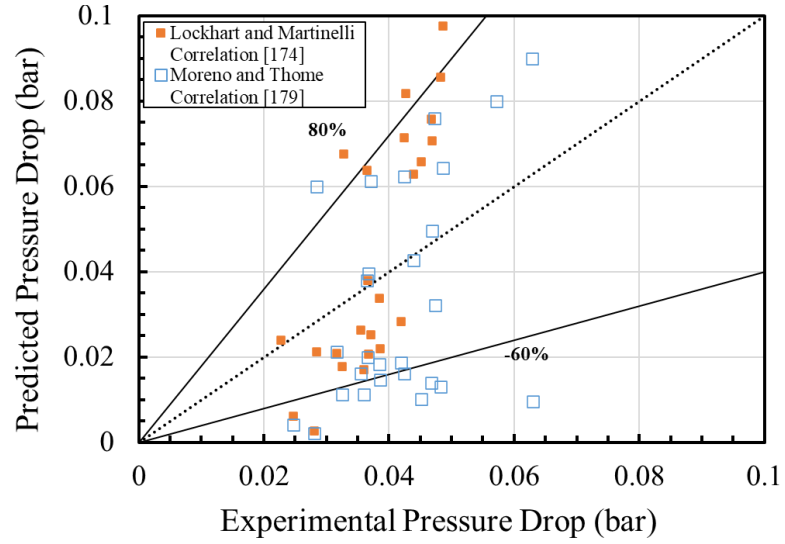

(a)

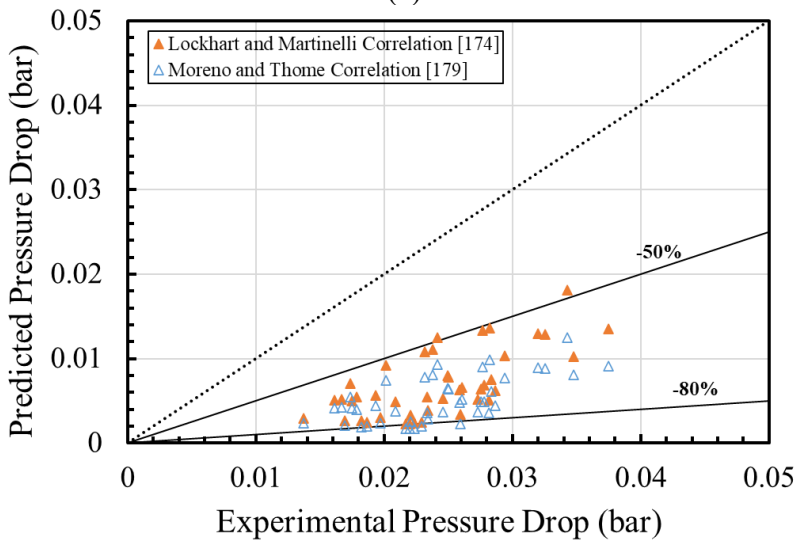

(b)

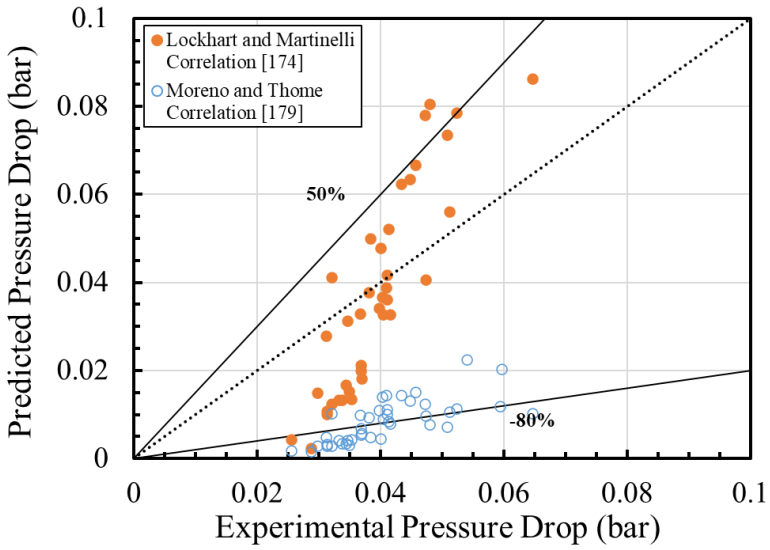

(c)

Fig. 7.3 Predicted pressure drop against experimental pressure drop for horizontal evaporator using Lockhart and Martinelli correlation **[179]** and Moreno and Thome correlation **[184]**: (a) R1234yf; (b) R152a; (c) R134a.

7.2.4 New Correlations

In this work, a newly improved correlation Nusselt number for two-phase flow is developed based on the Foust and Christian **[178]** correlation as a function of annular diameter ratio c, Reynolds number, and Prandtl number. The newly developed correlation can be expressed as

$$Nu = 0.1522 \frac{c}{(c+1)^{0.0027}} Re_{tp}^{0.8} (Pr_l)^{\frac{1}{3}} \tag{7.34}$$

As for the improved pressure drop correlation, Lockhart and Martinelli **[179]** and Pamitran et al. **[185]** correlations are adapted to obtain close agreement between prediction and measurements. The two-phase pressure drop is expressed as

$$\left(\frac{dp}{dz}\right)_{tp} = \Phi_l^2 \left(\frac{dp}{dz}\right)_l \tag{7.35}$$

where $\left(\frac{dp}{dz}\right)_l$ is the frictional pressure drop per unit length of liquid-phase flow. The two-phase multiplier is calculated as

$$\Phi_l^2 = 1 + \frac{C}{X} + \frac{1}{X^2} \tag{7.36}$$

The Martinelli parameter *X* and Chisholm parameter *C* are calculated as

$$X = \frac{(\frac{dp}{dz})_{\mathrm{l}}}{(\frac{dp}{dz})_{\mathrm{g}}} \tag{7.37}$$

where $(\frac{dp}{dz})_{\mathrm{g}}$ is the frictional pressure drop per unit length of vapour-phase flow

$$C = a_1 We_{\mathrm{tp}}^{a_2} Re_{\mathrm{tp}}^{a_3} \tag{7.38}$$

where a_1, a_2, a_3 are the correlation coefficients as shown in Table 7.1. The difference of correlation coefficients for three refrigerants is due to the difference of viscosity and density.

Table 7.1 Correlation coefficients for frictional pressure drop

Refrigerant	a_1	a_2	a_3
R1234yf	0.26419	-0.96554	1.3
R152a	0.0046	-0.86633	1.13
R134a	0.23	-0.86	1.23

7.3 Results and Discussions

Fig. 7.4 shows the experimental overall heat transfer coefficient against mass flux for R1234yf, R152a, and R134a. It can be seen that the overall heat transfer coefficient increases with the increase of the mass flux for three refrigerants. For a fixed mass flux, R152a has the highest overall heat transfer coefficient while the overall heat transfer coefficients for R1234yf and R134a are relatively the same. This is mainly due to the higher latent heat and thermal conductivity of R152a.

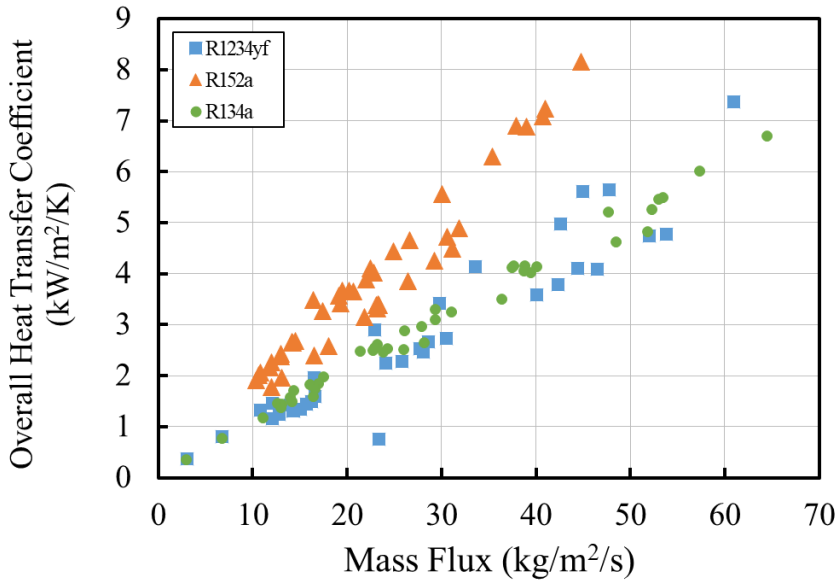

Fig. 7.4 Experimental overall heat transfer coefficient against mass flux for R1234yf, R152a and R134a

Fig. 7.5 shows the comparison of the predicted average Nusselt number using the improved correlation for the horizontal evaporator with experimental average Nusselt number. The results show that the MAPEs of the predicted average Nusselt number for R1234yf, R152a, and R134a are 14%, 10%, and 12%, respectively. Thus, the improved correlation can be considered as a general formula to calculate the Nusselt number of refrigerants in horizontal annular evaporator.

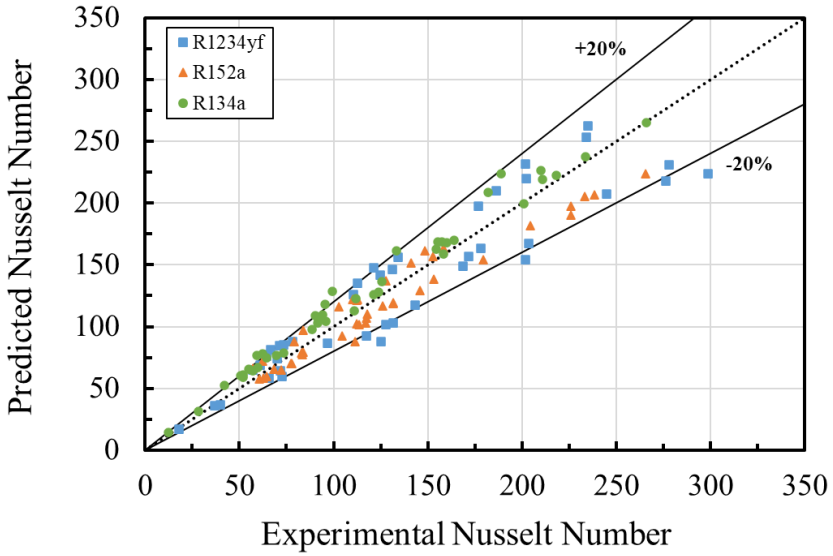

Fig. 7.5 Predicted average Nusselt number using improved correlation against experimental average Nusselt number for R1234yf, R152a and R134a

Fig. 7.6 shows the predicted local Nusselt number against Reynolds number for R1234yf, R152a, and R134a. The predicted local Nusselt numbers for three refrigerants increase with the Reynolds number. A similar trend also can be found in Dirker and Meyer **[181]**. At a Reynolds number of 1750, the predicted local Nusselt numbers of R1234yf, R152a, and R134a are 128, 124, and 131, respectively. The predicted local Nusselt numbers for three refrigerants are similar. Thus, the difference of thermal conductivity for refrigerants could be the main reason for the difference of overall heat transfer coefficient.

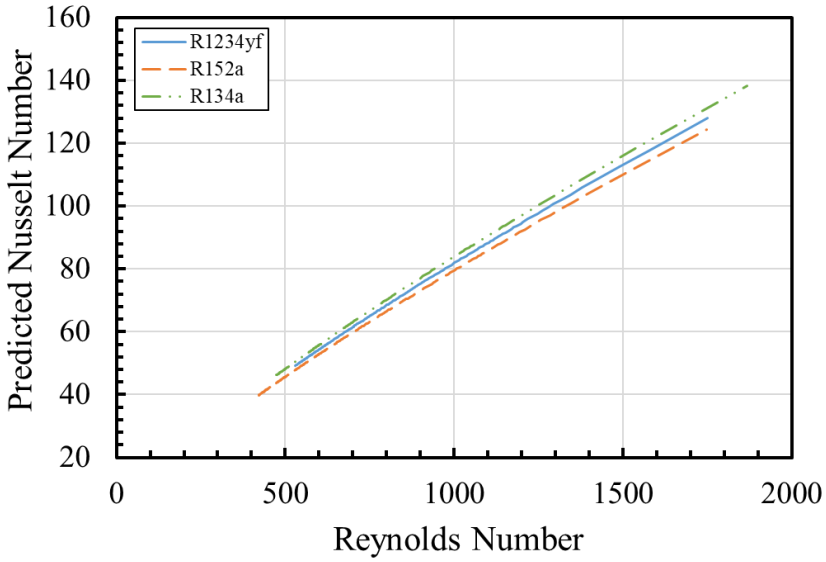

Fig. 7.6 Predicted local Nusselt number against Reynolds number for R1234yf, R152a, and R134a

Fig. 7.7 shows the evaporator pressure drop as a function of the mass flux for R1234yf, R152a, and R134a. Overall, the evaporator pressure drop increases with mass flux for three refrigerants. R1234yf and R134a have similar evaporator pressure drop due to similar liquid density while the evaporator pressure drop of R152a is significantly lower than the other two. At a mass flux of 30 kg/m^2/s the evaporator pressure drop of R152a is 47% and 53% lower than that of R134a and R1234yf, respectively. This is mainly due to the low density of R152a resulting in a low superficial velocity of the two-phase mixture thus low evaporator pressure drop **[186]**. A higher pressure drop of R1234yf and R134a can lead to lower efficiency and higher power input than these of R152a.

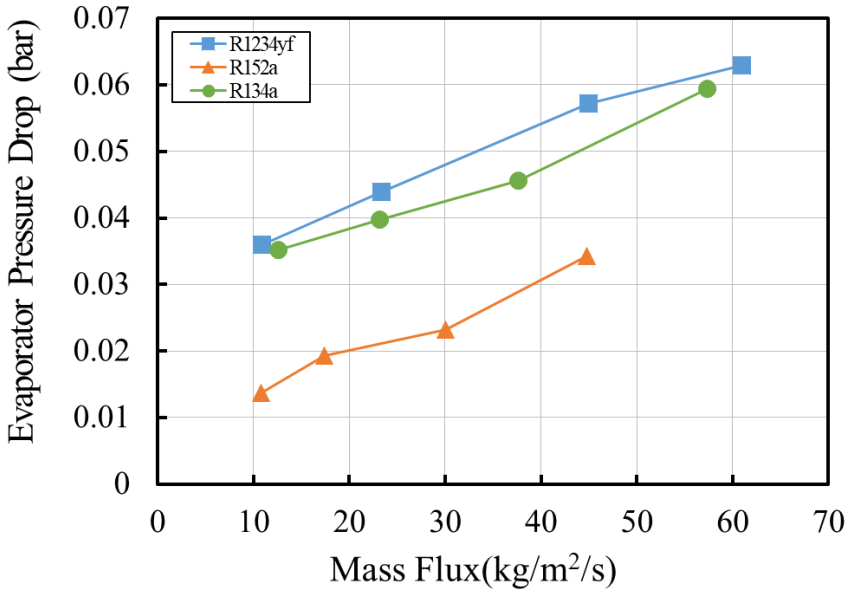

Fig. 7.7 Evaporator pressure drop against mass flux for R1234yf, R152a, and R134a

Fig. 7.8 shows the predicted pressure drop against experimental pressure drop for the horizontal evaporator using R1234yf, R152a, and R134a. The MAPEs of the predicted pressure drop in the evaporator for R1234yf, R152a, and R134a are 9.2%, 16% and 9.1%, respectively. The comparison of the prediction accuracy between literature correlations and the improved correlation demonstrates that the present correlation is capable of higher accuracy. Thus, the improved two-phase frictional pressure drop correlation can be adopted in refrigeration system model to optimize the design of evaporators.

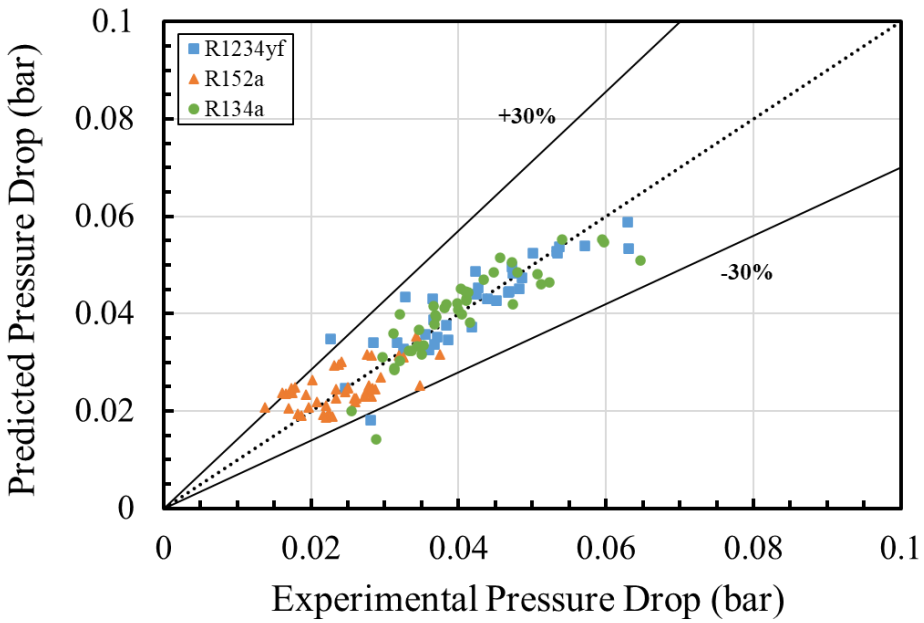

Fig. 7.8 Predicted pressure drop against experimental pressure drop for the horizontal evaporator for R1234yf, R152a, and R134a

Fig. 7.9 shows the predicted two-phase multiplier against Reynolds number for R1234yf, R152a, and R134a. The predicted two-phase multipliers for three refrigerants increase with Reynolds number. The overall trend is similar to the results reported in **[186]**. For a fixed Reynolds number, R134a and R1234yf have similar two-phase multiplier due to similar thermal properties while R152a has the lowest predicted two-phase multiplier. The difference of the two-phase multiplier for three refrigerants contributes to the difference of pressure drop as shown in Fig. 7.8. It is worth mentioning that the evaporator pressure drop of R1234yf is slightly higher than R134a in Fig. 7.8 while the two-phase multiplier of R1234yf is slightly lower than R134a. This may due to the greater liquid-phase of R1234yf than that of R134a resulted by higher liquid density.

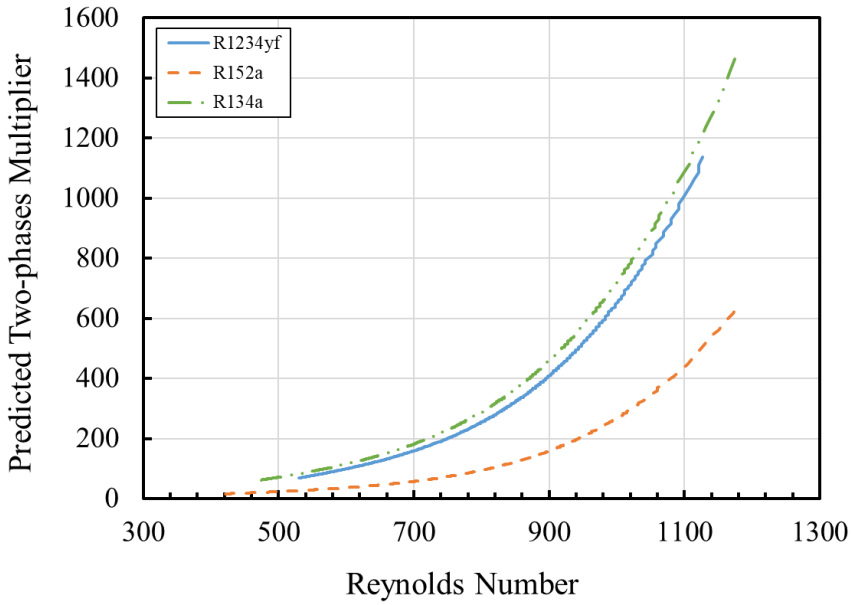

Fig. 7.9 Predicted two-phase multiplier against Reynolds number for R1234yf, R152a, and R134a

7.4 Summary

One hundred and twenty-five steady-state tests have been conducted to study the evaporation heat transfer and pressure drop of low GWP refrigerants in a horizontal annular evaporator. The improved correlations for the Nusselt number and two-phase pressure drop for three refrigerants (R152a, R1234yf and R134a) are presented in this study. The MAPEs for both Nusselt number and two-phase frictional pressure drop correlations are lower than 16%. The key findings are listed below:

(1) For a fixed mass flux, R152a has the highest overall heat transfer coefficient while the overall heat transfer coefficients for R1234yf and R134a are similar to each other.

(2) For a fixed max flux, R152a has the lowest evaporator pressure drop while R1234yf and R134a have similar evaporator pressure drop. This is due to the low liquid density of R152a.

(3) The improved Nusselt number correlation for R1234yf, R152a and R134a has MAPEs of 14%, 10% and 12%, respectively.

(4) The improved two-phase frictional pressure drops for R1234yf, R152a and R134a have MAPEs of 9.2%, 16% and 9.1%, respectively. The present correlations can be adopted in refrigeration system model with high confidence to optimize the design of components and predict the system performance.

Chapter 8 Refrigerant Distribution and Charge Optimization in the ORS

8.1 Introduction

One significant issue caused by wide use of refrigeration systems is refrigerant leakage which leads to an increasing contribution to the greenhouse effect. Reduction of the refrigerant charge can effectively slash the refrigerant cost and refrigerant leakage. However, excessive contraction of refrigerant charge can lead to an undercharged system resulting in loss of cooling capacity, thus performance deterioration. Numerous studies have been reported in literature to evaluate the impact of refrigerant charge. Lee and Yoo **[187]** developed a computer program for performance analysis of condensing capacity with different refrigerant charges and condenser sizes. Deymi-Dashtebayz et al. **[188]** carried out experiments to evaluate the performance of an air conditioning system with different refrigerant charges and ambient air temperatures. Vjacheslav et al. **[189]** developed a model to predict the optimal refrigerant charge of a traditional VCR system. Pisano et al. **[106]** studied the combined effects of capillary tube diameter and refrigerant charge on the system performance for a light freezer. The results show that once the optimal design has been selected, if the ambient temperature changes, the optimal refrigerant charge also changes.

Analyzing the refrigerant distribution can acquire a deeper knowledge of refrigerant flow pattern and refrigerant charge optimization. Several researches have been carried out to investigate the impacts of the refrigerant charge by evaluating the refrigerant distribution. Palm **[32]** and Ghoubail et al. **[97]** pointed out that for an undercharged VCR system, the quality of the refrigerant increases with the increase of the total refrigerant charge. For an overcharged system, over 50% refrigerant is contained in the condenser and the quality of the refrigerant in other components remaining nearly the same. Rossi et al. **[28]** and

Macchi et al. **[190]** mentioned that over 30% of refrigerant is contained in the liquid pipe. Poggi et al. **[191]** reviewed the refrigerant charge in refrigeration systems and the strategies for charge reduction, and concluded that an overcharge involves condenser flooding resulting in a rise of the condenser pressure thus lower volumetric efficiency and CoP. Though numerous works have been done on refrigerant charge impacts, experimental works mentioned above all involve oil lubricants for compressor. Youbi-Idrissi et al. **[192]** pointed out that over 20% refrigerant can be dissolved in oil lubricant at a low superheat condition. The oil lubricant not only inevitably affects the heat transfer in heat exchangers, but also increases the refrigerant consumption of refrigeration system. Most studies mentioned above mainly evaluated the effect of refrigerant charge on cooling capacity and energy efficiency. Moreover, due to the limitations of the experimental setup, the pressure ratio and condenser temperature were not controlled.

In this Chapter, the effect of refrigerant charge and system efficiency of the ORS are experimentally evaluated using R134a. The refrigerant distribution is also calculated according to Eq. 7.1-Eq. 7.8 to help analyze the system performance. The elimination of oil lubricant enables comparable test conditions for better evaluating the impact of refrigerant charge.

8.2 Experimental Method

Fig. 8.1 shows the simplified schematic of the ORS. Different section of the system are represented by different colors. Discharge line, liquid refrigerant line, two-phase line, suction refrigerant line, and bleed flow line are shown as red, dark blue, blue, orange, and black in the figure, respectively. The refrigerant distribution is calculated according to the refrigerant state in different sections and dimensions as listed in Table 3.2. The ORS was evacuated by a vacuum pump before each charge. Two hundred and five steady-state measurements were conducted for the system using R134a with various refrigerant charges. Table 8.1 shows the test conditions of the ORS for refrigerant charge

optimization using R134a. As the refrigerant charge can vary with compressor stroke when using the linear compressor, the system was also tested under different compressor strokes. The resistances were powered to heat the compressor to ensure fully vacuumed. Two one-meter charging tubes were used to connect the refrigerant cylinder, four-valve manifold, and refrigerant system. The charging line between refrigerant cylinder and four-valve manifold was fully filled by refrigerant liquid before charging. During the charging process, an extra 15 g refrigerant was charged to the system to offset the refrigerant containing in the tube and leakage when cutting off the connection between refrigerant system and charging tube.

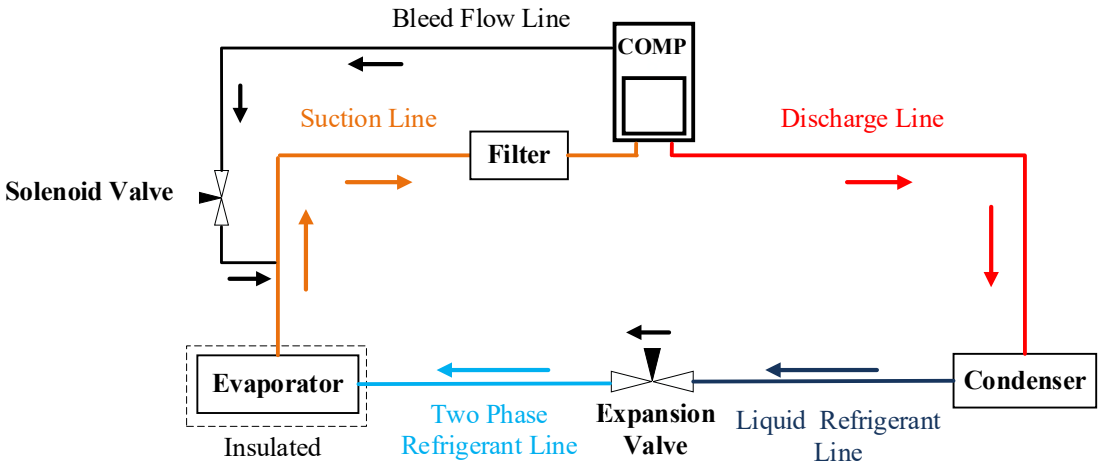

Fig. 8.1 Simplified schematic of the ORS

Table 8.1 Test conditions of the ORS refrigerant charge optimization using R134a

Charge (g)	220, 250, 280, 300, 330
Pressure ratio	2.0, 2.5, 3.0, 3.5, 4.0
Compressor stroke (mm)	9, 10, 11, 12, 13
Condenser temperature (°C)	40, 45, 50
Operating frequency (Hz)	32-38
Suction temperature (°C)	20-30
Compressor body temperature (°C)	>35
Ambient temperature (°C)	22

8.3 Refrigerant Distribution

8.3.1 Evaporator

The two-phase length in the evaporator is given in Chapter 7 as

$$L_{\mathrm{tp}} = L_{\mathrm{total}} \frac{h_{\mathrm{g}} - h_{\mathrm{in}}}{h_{\mathrm{out}} - h_{\mathrm{in}}} \tag{8.1}$$

Thus, the gas phase length in the evaporator can be calculated as

$$L_{\mathrm{g}} = L_{\mathrm{total}} - L_{\mathrm{tp}} \tag{8.2}$$

Based on Eq. 7.1-Eq. 7.8, the void fraction α in the evaporator and condenser can be calculated. Thus, the refrigerant mass as two-phase and gas phase in the evaporator can be calculated as

$$M_{\mathrm{tp}} = \mathrm{A}_{\mathrm{evap}} \int_0^{L_{\mathrm{tp}}} \left(\alpha \rho_{\mathrm{g}} + (1-\alpha)\rho_{\mathrm{l}}\right) dl \tag{8.3}$$

where $\mathrm{A}_{\mathrm{evap}}$ is the cross section area of the evaporator.

$$M_{\mathrm{g}} = \mathrm{A}_{\mathrm{evap}} \int_0^{\mathrm{L_g}} \rho_{\mathrm{g}} dl \tag{8.4}$$

The total refrigerant mass accumulates in the evaporator can be expressed as

$$M_{\mathrm{evap}} = M_{\mathrm{g}} + M_{\mathrm{tp}} \tag{8.5}$$

8.3.2 Condenser

The refrigerant enters the condenser as superheated vapour and flows out as subcooled refrigerant liquid. Thus, gas phase, two-phase, and liquid-phase refrigerant all involve in the condenser. The length for each state of refrigerant can be expressed as

$$L'_{\mathrm{tp}} = L'_{\mathrm{total}} \frac{h'_{\mathrm{g}} - h'_{\mathrm{l}}}{h'_{\mathrm{in}} - h'_{\mathrm{out}}} \tag{8.6}$$

where L'_{total} is the total length of condenser (2325 mm), h'_{g} is the saturated vapour enthalpy in the condenser, h'_{l} is the saturated liquid enthalpy in the condenser, h'_{out} is the refrigerant enthalpy at the condenser outlet, and h'_{in} is the refrigerant enthalpy at the condenser inlet.

$$L'_{\mathrm{g}} = L'_{\mathrm{total}} \frac{h'_{\mathrm{in}} - h'_{\mathrm{g}}}{h'_{\mathrm{in}} - h'_{\mathrm{out}}} \tag{8.7}$$

$$L'_{\mathrm{l}} = L'_{\mathrm{total}} - L'_{\mathrm{tp}} - L'_{\mathrm{g}} \tag{8.8}$$

The void fraction within the condenser can also be driven by Eq. 7.1-Eq. 7.8. Thus, the total refrigerant mass in the condenser can be expressed as

$$M_{\mathrm{cond}} = \mathrm{A}_{\mathrm{cond}} \int_0^{L'_{\mathrm{g}}} \rho_{\mathrm{g}} dl + \mathrm{A}_{\mathrm{cond}} \int_0^{L'_{\mathrm{l}}} \rho_{\mathrm{l}} dl + \mathrm{A}'_{\mathrm{tp}} \int_0^{L'_{tp}} (\alpha \rho_g + (1-\alpha)\rho_{\mathrm{l}}) dl \tag{8.9}$$

8.3.3 Refrigerant Line and Filter

The heat transfer in the two-phase refrigerant line, liquid refrigerant line, bleed flow line, discharge line, suction line, and filter are neglected. Thus, the state of refrigerant in these sections remains constant. The refrigerant in the filter, liquid refrigerant line, bleed flow line, discharge line, and suction line belongs to single-phase refrigerant and the mass in these sections can be calculated as

$$M_{\mathrm{sp}} = \mathrm{A}_{\mathrm{sp}} \int_0^{L_{\mathrm{sp}}} \rho_{\mathrm{g}} dl \tag{8.10}$$

where A_{sp} is the cross section area of the single-phase section and L_{sp} is the length of single-phase section.

For the refrigerant in the two-phase refrigerant line, the mass M''_{tp} can be expressed as

$$M'_{\mathrm{tp}} = \mathrm{A}''_{\mathrm{tp}} \int_0^{L''_{\mathrm{tp}}} \rho_{\mathrm{tp}} dl \tag{8.11}$$

where A''_{tp} is the cross section area of the two-phase section and L''_{tp} is the length of two-phase section.

8.3.4 Results and Discussions

Fig. 8.2 compares the difference between the calculated refrigerant charge and experimental refrigerant charge. The experimental refrigerant charge is 280 g in the figure. Overall, the deviation between the experimental results and calculated results is within ±10%. The largest deviation is -17%. It is worth mentioning that the most calculated results are lower than 280 g. This is due to the refrigerant leakage of the ORS over time resulting in lower system pressures thus lower predictive results. The calculated total refrigerant charge has a MAPE of 6.7% indicating that the method can be considered as a reliable method to predict refrigerant distribution.

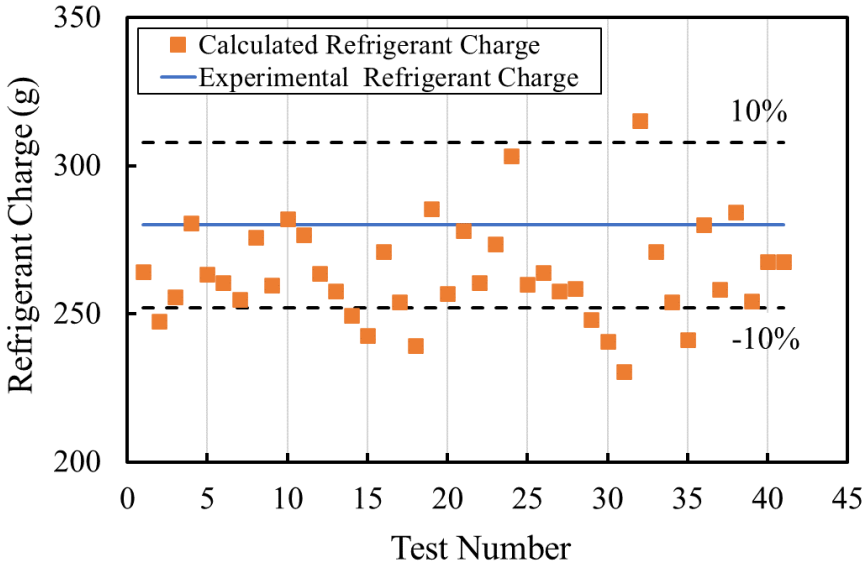

Fig. 8.2 Calculated refrigerant charge comparing with experimental results

Fig. 8.3 shows the calculated two-phase length in the heat exchangers. For a fixed compressor stroke, the length of the two-phase region decreases with the increase of the pressure ratio in the heat exchangers due to the decrease of the mass flow rate. For a fixed pressure ratio, the two-phase length in the condenser decreases with the compressor stroke while a reverse trend is found in the evaporator. This is because higher compressor stroke

for the ORS tends to have greater refrigerant circulating in the system resulting in lower refrigerant mass in the condenser and higher mass flow rate.

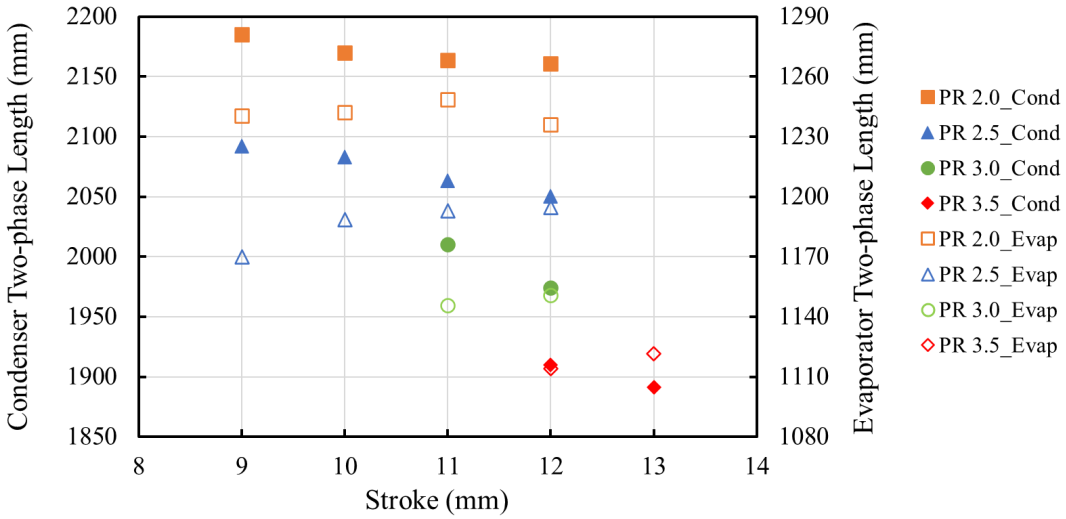

Fig. 8.3 Length of two-phase region in the heat exchangers

Fig. 8.4 shows the refrigerant distribution in the ORS with various compressor strokes at a pressure ratio of 2.5 and a total refrigerant charge of 280 g. Overall, over 70% of refrigerant is accumulated in the condenser while the evaporator and liquid lines contain approximately 10% of the total refrigerant charge, respectively. Gas lines and filter contain the minimal refrigerant due to the low density of the refrigerant vapour. A slight increase can be found in gas lines, liquid lines, and filter due to the increase of system pressures leading to an increase of refrigerant density. The refrigerant mass fraction of the condenser decreases with the increase of the compressor stroke due to the increase of refrigerant mass circulating in the system. It is worth mentioning that the refrigerant mass fraction for the evaporator almost remains the same even though the length of the two-phase region increased as mentioned in Fig. 8.3. Based on Eq. 7.1-Eq. 7.8, the void fraction increases from 0.5 to 0.7 with the increase of the compressor stroke and mass flow rate. The increasing void fraction together with the increasing two-phase length result in approximately the same amount of refrigerant accumulated in the evaporator.

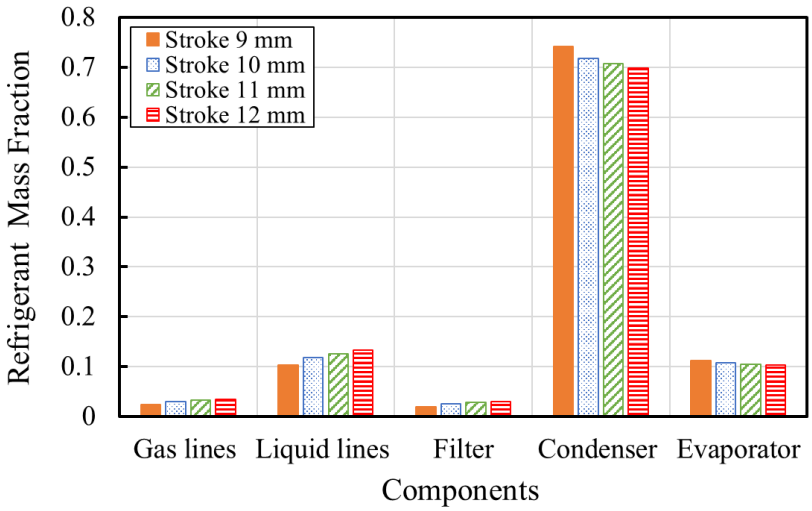

Fig. 8.4 Calculated refrigerant distribution in the ORS with various compressor strokes at a pressure ratio of 2.5 and a refrigerant charge of 280 g.

Fig. 8.5 illustrates the refrigerant mass fraction in the ORS with various pressure ratios. The refrigerant mass fraction of the condenser increases with the pressure ratio while the refrigerant mass fraction decreases in the gas lines, filter, and evaporator due to the decrease of vapour density and amount of circulating refrigerant. At a pressure ratio of 3.5, 75% of the refrigerant is accumulated in the condenser.

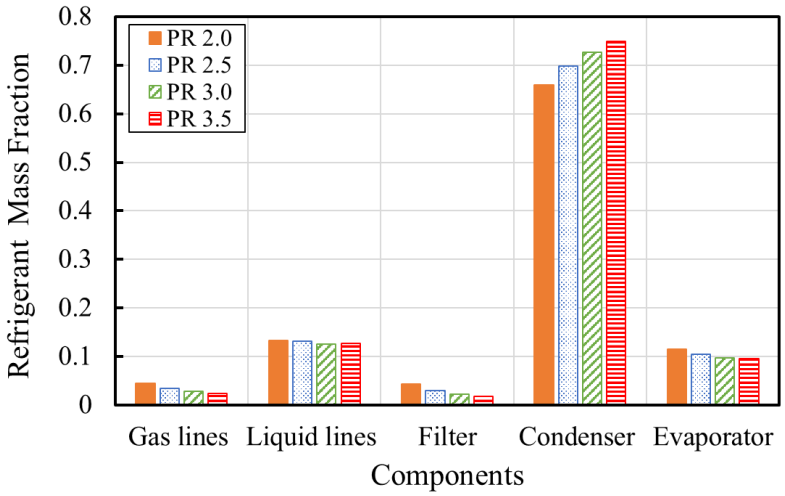

Fig. 8.5 Calculated refrigerant distribution in the ORS with various pressure ratios at a refrigerant charge of 280 g.

Fig. 8.6 shows the calculated refrigerant mass fraction for the components in the ORS with various refrigerant charges. The refrigerant mass fraction of the condenser increases with the refrigerant charge which means the additional refrigerant is mainly stored in the condenser. The refrigerant mass fraction is increased by 6.8% with the refrigerant charge

increasing from 220 g to 330 g. At a refrigerant charge of 330 g, 201 g refrigerant is accumulated in the condenser which accounts for 72.1% of the overall refrigerant charge. Excessive refrigerant stores in the condenser leading to flooding thus a deterioration of the system performance and an overcharged refrigeration unit. The refrigerant mass ratio hardly varies in the other components with the change of the total refrigerant charge.

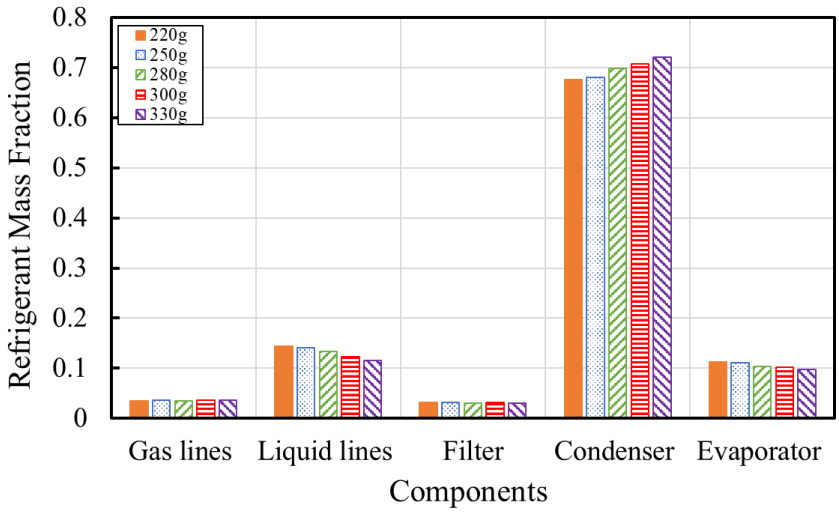

Fig. 8.6 Refrigerant mass fraction for the components in the ORS with various refrigerant charges.

8.4 Refrigerant Charge Optimization

Fig. 8.7 shows the *p-h* diagram of the ORS with various refrigerant charges for a pressure ratio of 3.5, a compressor stroke of 13 mm, a condenser temperature of 40 °C, and an evaporator inlet temperature of 5 °C. The enthalpy difference between the evaporator inlet and outlet increases slightly with the increase of the refrigerant charge due to the increase of the discharge and suction pressures. The enthalpy difference with a refrigerant charge of 330 g is 4% higher than a refrigerant charge of 220 g. This will lead to a high cooling capacity if the mass flow rate is the same. However, the highest cooling capacity of the ORS for given conditions is achieved with a refrigerant charge of 280 g. This is mainly due to the variation of the mass flow rate with the refrigerant charge.

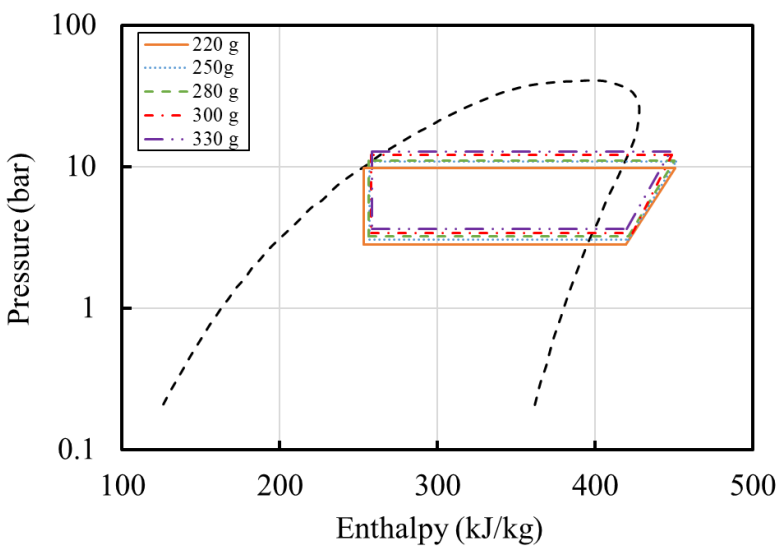

Fig. 8.7 *p-h* diagram of the oil-free VCR system with various refrigerant charges for a pressure ratio of 3.5, a compressor stroke of 13 mm and a condenser temperature of 40 °C.

Fig. 8.8 shows the discharge and suction pressures against the refrigerant charge with different condenser temperatures. For a fixed condenser temperature, both discharge and suction pressures increase with the refrigerant charge. For a fixed refrigerant charge, the discharge pressure and suction pressure increase with the condenser temperature. Higher suction and discharge pressures lead to higher in-cylinder pressure resulting in higher shaft force thus higher power input and copper loss. For a condenser temperature of 40 °C, the discharge pressure and suction pressure are 9.8 bar and 2.8 bar at a refrigerant charge of 220 g which is 23% lower than that of 330 g (12.7 bar and 3.6 bar). For a refrigerant charge of 220 g, both discharge pressure and suction pressure at a condenser temperature of 40 °C are 25% lower than 50 °C.

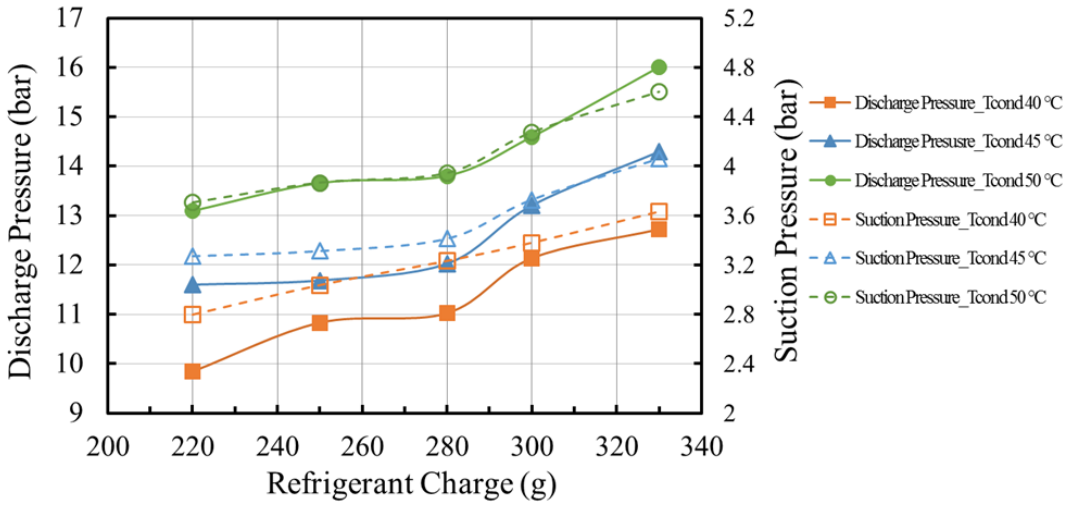

Fig. 8.8 Discharge pressure and suction pressure against refrigerant charge with various condenser temperatures at a pressure ratio of 3.5 and a compressor stroke of 13 mm.

Fig. 8.9 shows the condenser inlet and evaporator inlet temperatures against the refrigerant charge with various condenser temperatures at a pressure ratio of 3.5 and a compressor stroke of 13 mm. Both condenser temperature and evaporator inlet temperature increase with refrigerant charge. This is because higher refrigerant charge leads to higher system pressure resulting in higher discharge temperature and evaporator inlet pressure thus higher condenser temperature and evaporator inlet temperature. With a refrigerant charge of 220 g, the ORS can achieve an evaporator inlet temperature of 3.7 °C. With the increase of the condenser temperature, both condenser temperature and evaporator inlet temperature present a growing tendency. It is worth mentioning that the increasing rate of evaporator inlet temperature with the increase of refrigerant charge is higher at low condenser temperature. This is due to the small increment of the saturation pressure at low temperature.

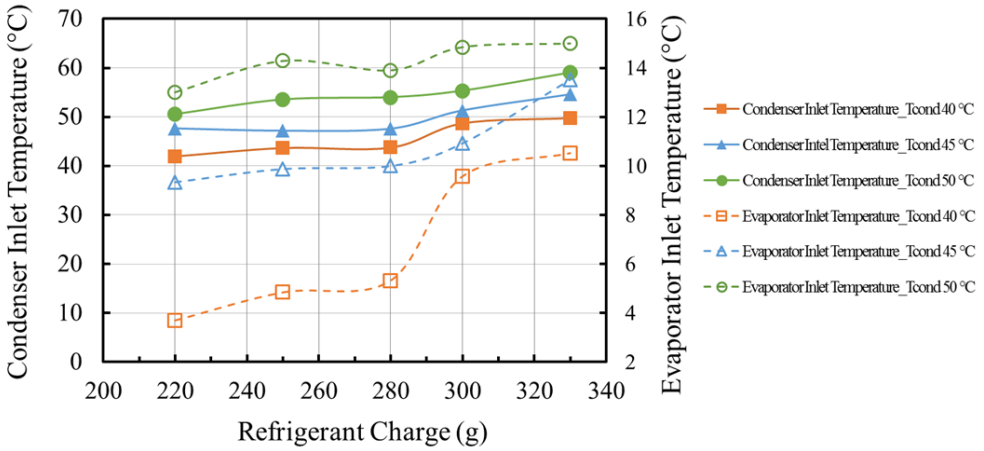

Fig. 8.9 Condenser inlet and evaporator inlet temperatures against refrigerant charge with various condenser temperatures at a pressure ratio of 3.5 and a compressor stroke of 13 mm.

Fig. 8.10 shows the superheat and subcooling varying with refrigerant charge at a pressure ratio of 3.5, a compressor stroke of 13 mm and condenser temperature of 40 °C, 45 °C, and 50 °C. For a fixed condenser temperature, superheat decreases with the increase of refrigerant charge as the increase of suction pressure results in a rise in the suction saturation temperature. For a fixed refrigerant charge, higher condenser temperature tends to have lower superheat due to the increase of discharge and suction pressures. Subcooling shows a reverse trend compared with superheat. The maximum superheat and subcooling are 26.5 K (at the refrigerant charge of 220 g) and 8.5 K (at the refrigerant charge of 330 g), respectively. Several researchers **[188, 193, 194]** pointed out that the subcooling of a system is an indicator of the quality of the refrigerant in the condenser. Higher subcooling represents greater length of subcooled region thus higher quality of refrigerant in the condenser.

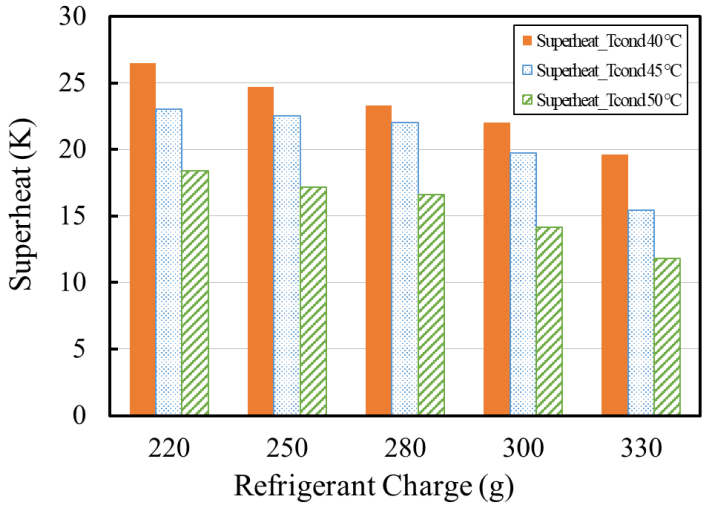

(a)

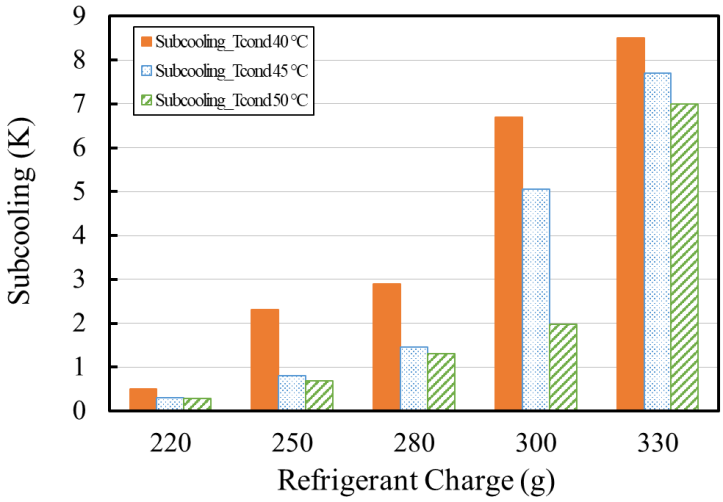

(b)

Fig. 8.10 Superheat (a) and subcooling (b) against refrigerant charge at a pressure ratio of 3.5, a compressor stroke of 13 mm and condenser temperatures of 40 °C, 45 °C, and 50 °C

The variation of power input with refrigerant charge at a pressure ratio of 3.5, a compressor stroke of 13 mm and condenser temperatures of 40 °C, 45 °C, and 50 °C is shown in Fig. 8.11. At a fixed condenser temperature, the power input increases with the refrigerant charge due to the requirement of higher shaft force caused by the increasing in-cylinder pressure. The highest power input of the ORS occurs at a refrigerant charge of 330 g and a condenser temperature of 50 °C. High refrigerant charge could lead to

higher gas spring stiffness thus higher resonant frequency as well. Higher power input also causes higher copper loss and relatively lower motor efficiency.

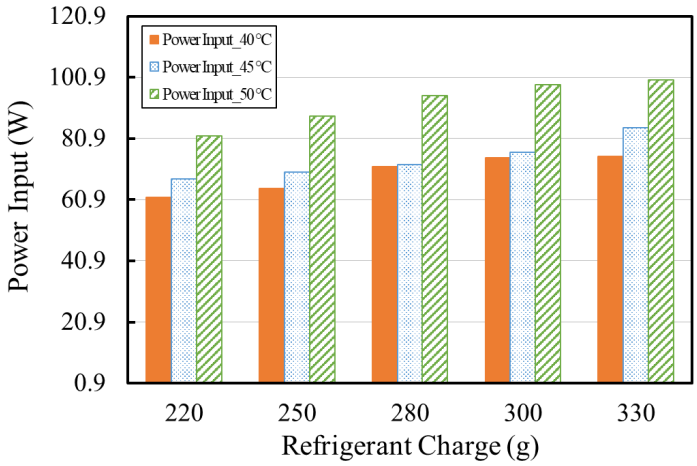

Fig. 8.11 Variation of power input with refrigerant charge at a pressure ratio of 3.5, a compressor stroke of 13 mm and condenser temperatures of 40 °C, 45 °C, and 50 °C.

Fig. 8.12 shows the mass flow rate against refrigerant charge with various condenser temperatures at a compressor stroke of 13 mm and a pressure ratio of 3.5. For a fixed refrigerant charge, the mass flow rate decreases as the condenser temperature increases. This is because the high condenser temperature causes more refrigerant vapour to circulate in the ORS rather than condensing in the condenser. For an undercharged system, the mass flow rate increases with the refrigerant charge until reaching the optimal refrigerant charge. With the increase of the refrigerant charge, the increasing subcooling region occupies a larger portion of the condenser resulting in a reduction of the area for condensation. The reduction of the heat transfer efficiency decreases the quality of refrigerant circulating in the system. For condenser temperatures of 40 °C and 45 °C, the highest mass flow rate is achieved at the refrigerant charge of 280 g. For a condenser temperature of 50 °C, the highest mass flow rate is achieved at the refrigerant charge of 300 g. High operating frequency due to high suction and discharge pressures could also contribute to the increase of mass flow rate at the high condenser temperature. The highest mass flow rate is 1.51 g/s at a condenser temperature of 50 °C with a refrigerant charge

of 300 g while the lowest is 0.93 g/s at a condenser temperature of 40 °C with a refrigerant charge of 220 g.

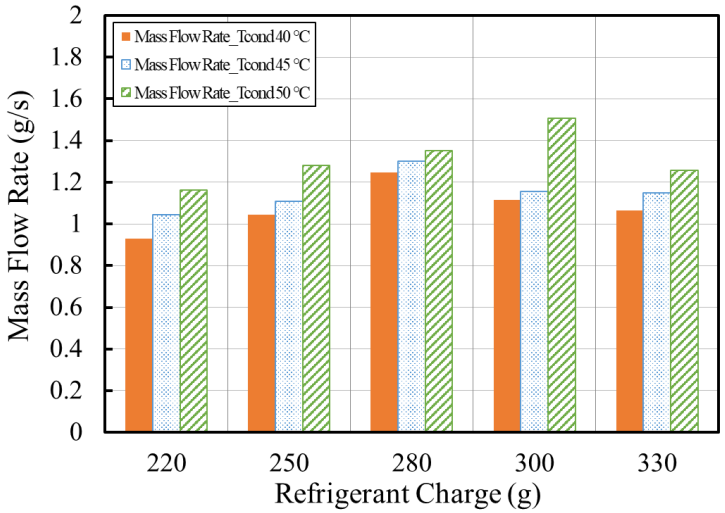

Fig. 8.12 Variation of mass flow rate with refrigerant charge at a pressure ratio of 3.5, a compressor stroke of 13 mm and condenser temperatures of 40 °C, 45 °C, and 50 °C.

Fig. 8.13 shows the variation of volumetric efficiency with refrigerant charge at a pressure ratio of 3.5, a compressor stroke of 13 mm and condenser temperatures of 40 °C, 45 °C, and 50 °C. For a fixed condenser temperature, the variation of the volumetric efficiency has a similar trend to the mass flow rate as shown in Fig. 8.12. The ORS can achieve a volumetric efficiency of 35.5% at a condenser temperature of 40 °C. For a fixed refrigerant charge, higher mass flow rate does not lead to higher volumetric efficiency. Mass flow rate is increased by 16% with the increase of the condenser temperature from 40 ° to 50 ° while the suction pressure is increased by 22%. The low increment of the mass flow rate compared with the suction pressure leads to a decrease of the volumetric efficiency with the increase of the condenser temperature.

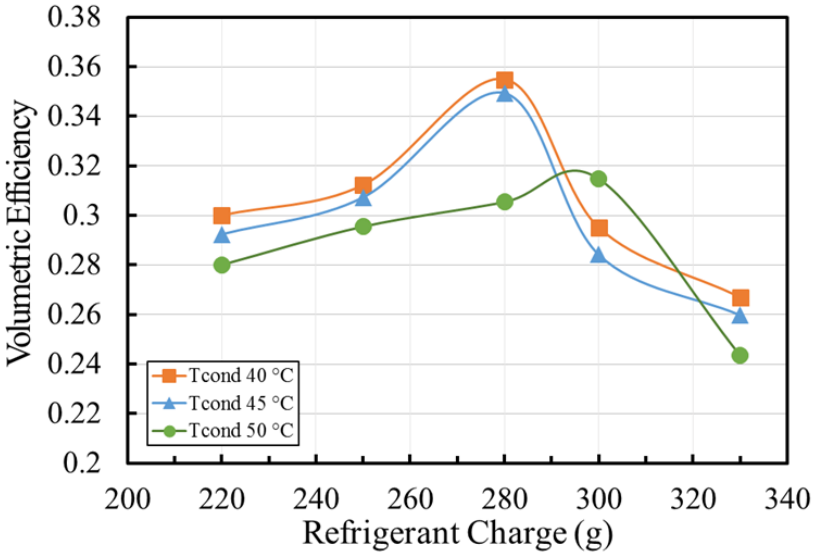

Fig. 8.13 Volumetric efficiency against refrigerant charge for the ORS at a pressure ratio of 3.5, a compressor stroke of 13 mm and condenser temperatures of 40 °C, 45 °C, and 50 °C

Fig. 8.14 shows the variation of cooling capacity with refrigerant charge at a pressure ratio of 3.5, a compressor stroke of 13 mm and condenser temperatures of 40 °C, 45 °C, and 50 °C. The cooling capacity shows a similar trend with mass flow rate shown in Fig. 8.12. Both enthalpy difference and mass flow rate affect the cooling capacity. For the measurements shown in Fig. 8.7, the enthalpy difference only decreases by about 3% with the increase of the refrigerant charge from 220 g to 280 g while the mass flow rate is increased by 25%. The cooling capacity reaches the maximum value while the system provides the highest mass flow rate. For undercharged conditions, the insufficient refrigerant in the system resulting in a small mass flow rate is the main reason for the low cooling capacity. For the overcharged system, the excessive liquid refrigerant contained in the condenser which reduces the heat transfer area of the two-phase refrigerant is the main reason for the cooling capacity deterioration. The highest cooling capacity of the ORS is 218.5 W at a condenser temperature 50 °C, a compressor stroke of 13 mm, a pressure ratio of 3.5, and a refrigerant charge of 300 g.

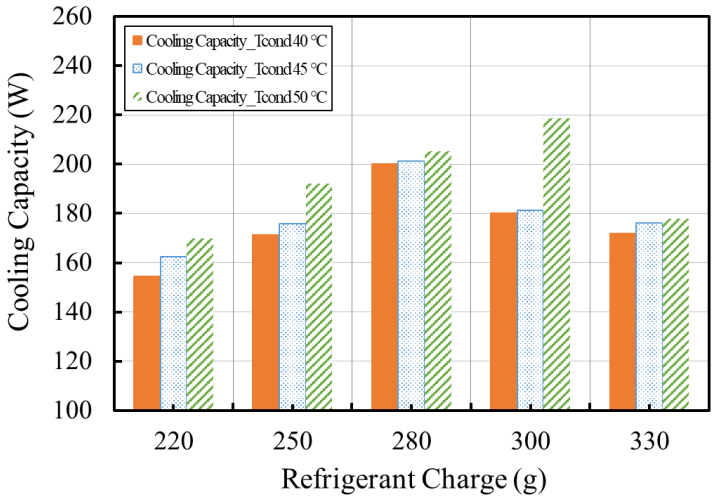

Fig. 8.14 Variation of cooling capacity with refrigerant charge at a pressure ratio of 3.5, a compressor stroke of 13 mm and condenser temperatures of 40 °C, 45 °C, and 50 °C.

Fig. 8.15 shows the variation of the CoP with the refrigerant charge at a pressure ratio of 3.5, a compressor stroke of 13 mm, and condenser temperatures of 40 °C, 45 °C, and 50 °C. For a condenser temperature of 40 °C, the CoP increases with refrigerant charge before reaching the optimal charge (280 g). With further increased refrigerant charge, the condenser flooding and high in-cylinder pressure result in a decrease of mass flow rate and high power input thus a decrease of CoP. For a fixed refrigerant charge, the CoP decrease with the increase of the condenser temperature. Though a higher condenser temperature tends to have higher cooling capacity, the excessive power input results in a decrease of CoP. The maximum CoP is 2.9 with a refrigerant charge of 280 g and a condenser temperature of 40 °C. By reducing 11.3% of refrigerant charge, the CoP of the system is reduced by 7.5%. Thus, to operate the system under a slightly undercharged condition may be considered to reduce the refrigerant charge thus leakage.

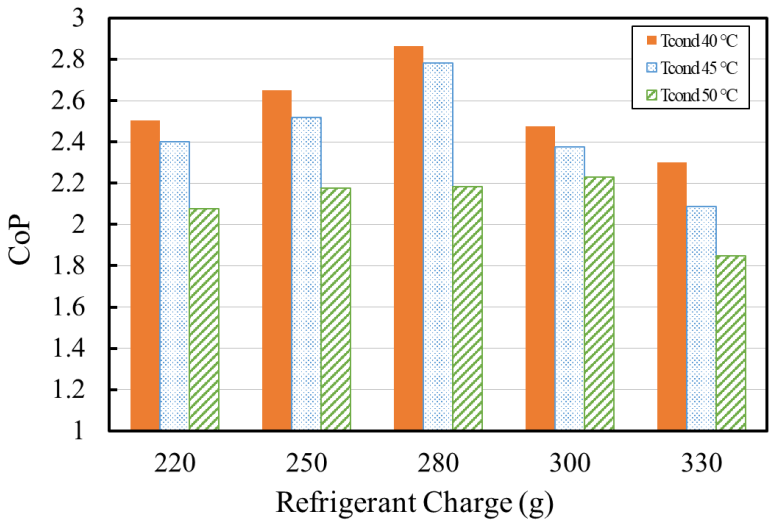

Fig. 8.15 CoP against refrigerant charge for the ORS at a pressure ratio of 3.5, a compressor stroke of 13 mm, and condenser temperatures of 40 °C, 45 °C, and 50 °C.

Fig. 8.16 shows the CoP against refrigerant charge for the ORS with various compressor strokes at a pressure ratio of 2.5 and condenser temperatures of 40 °C, 45 °C, and 50 °C. For a fixed refrigerant charge, the CoP increases with the compressor stroke due to the improvement of the volumetric efficiency. For a fixed compressor stroke, the CoP increases first with the refrigerant charge until reaching the optimal charge. With an increase of the compressor stroke, the optimal charge of the ORS increases.

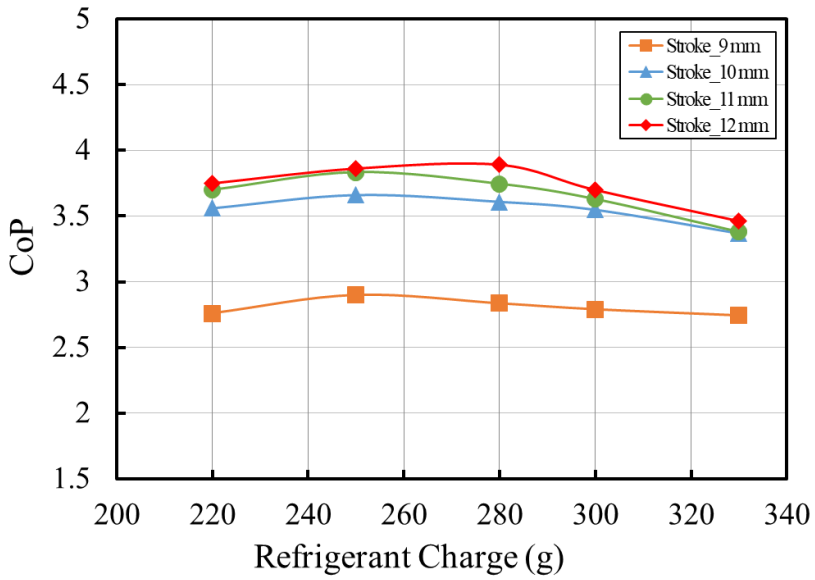

Fig. 8.16 CoP against refrigerant charge for the ORS with various compressor strokes at a pressure ratio of 2.5, and condenser temperatures of 40 °C, 45 °C, and 50 °C.

Fig. 8.17 shows the optimal charge of the ORS for various operating conditions at a condenser temperature of 40 °C. For a fixed compressor stroke, the optimal charge decreases with the pressure ratio. For a fixed pressure ratio, the optimal charge increases with the compressor stroke. This is because higher compressor stroke and lower pressure ratio tend to have higher volumetric efficiency resulting in an increase of mass flow rate. The ORS can be charged at the optimal charge for the most frequently used part-load conditions to reduce refrigerant charge and energy consumption. This feature can have significant advantage for the air conditioning due to the smaller range of the operating conditions. Table 8.2 lists the optimal charge of the ORS for various compressor strokes and condenser temperatures at a pressure ratio of 2.5. At a condenser temperature of 40 °C, by increasing compressor stroke by 25%, the optimal refrigerant charge is increased by 11%. The same amount of the increment of optimal refrigerant charge can be achieved by increasing 20% (40 °C to 50 °C) of the condenser temperature. The optimal refrigerant charge is more sensitive to the condenser temperature than the compressor stroke. A higher condenser capacity tends to have a higher optimal refrigerant charge. Ghoubali et al. **[97]** reported that using a microchannel heat exchanger as condenser can reduce 13%

of the total refrigerant charge concentrating in the condenser. Moreover, more than 18% of refrigerant can be contained in liquid line **[28]**. To minimise the diameter of the liquid line also can be a potential choice for the refrigerant charge reduction.

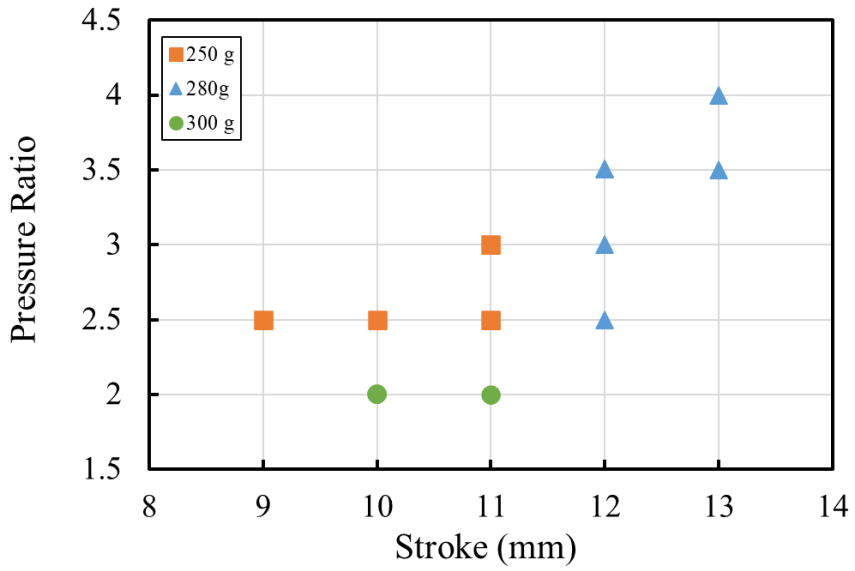

Fig. 8.17 Variation of the optimal refrigerant charge for the ORS with various pressure ratios and compressor strokes at a fixed condenser temperature of 40 °C.

Table 8.2 The optimal charge of the ORS for various compressor strokes and condenser temperatures at a pressure ratio of 2.5

Stroke (mm) / Tcond (°C)	9	10	11	12	13
40	250	250	250	280	None
45	None	280	280	280	None
50	None	None	280	280	300

8.5 Summary

Operating a refrigeration system with an optimal refrigerant charge can reduce the refrigerant leakage without losing capacity and energy efficiency. In this chapter, the refrigerant distribution, optimal refrigerant charge, and energy efficiency of the ORS using R134a are investigated for a wide range of operating conditions. The key findings are shown below:

(1) The calculated total refrigerant charge has a MAPE of 6.7% indicating reasonable

accuracy for investigating the refrigerant distribution in the system components.

(2) Condenser is the most sensitive component to the change of system operating conditions and total refrigerant charges.

(3) Overall, over 70% of refrigerant is accumulated in the condenser while evaporator and liquid lines contain approximately 10% of the total refrigerant charge, respectively.

(4) For given pressure ratio and stroke, and compressor stroke, the discharge pressure and suction pressures increase with the increase of the refrigerant charge. This leads to increasing power input and copper loss.

(5) At a fixed condenser temperature, compressor stroke, and pressure ratio, the superheat increases with the refrigerant charge while the subcooling shows a reverse trend due to the increase of the suction and discharge pressures.

(6) At a fixed condenser temperature, the mass flow rate increases first with the refrigerant charge, then decreases due to the flooding in the condenser and the increase of the in-cylinder pressure.

(7) For a fixed compressor stroke and a fixed pressure ratio, both cooling capacity and CoP reach the maximum value at the optimal refrigerant charge. The cooling capacity decreases with the condenser temperature while the CoP increases with the condenser temperature.

(8) The optimal charge varies with operating conditions. A higher compressor stroke and a lower pressure ratio tend to have a higher optimal refrigerant charge.

(9) The knowledge of refrigerant distribution and charge optimization form basis of the numerical model presented in next chapter.

Chapter 9 Numerical Model of the ORS

With measurements and modelling works presented in previous chapters, a comprehensive numerical model for the complete ORS is presented in this chapter. The numerical ORS model mainly consists of a linear compressor model, a heat exchanger model, and a refrigerant distribution model. The model was developed by using MATLAB and Simulink. REFPROP **[195]** is called in the model to calculate the thermodynamic properties according to the model inputs. MATLAB is a user friendly computer program that can be used to process varies type of calculations. The language for MATLAB is easier than the other programming language such as C++. Also, MATLAB can call any other programming language ensuring a highly flexible programming strategy. The equations for the ORS model are automatically solved in the Simulink. The model can predict mass flow rate, power input, pressure drop and heat transfer in heat exchangers, and CoP of the ORS by inputting discharge pressure, suction pressure, body pressure, shaft force, and operating frequency. The ORS model can be used to help design and optimize the ORS in the future for the purpose of low charge, high efficiency and compactness.

9.1 Flowchart and Assumptions of the ORS Model

Fig. 9.1 shows the flowchart of the ORS model. At the beginning, step length and stop time are required to be input to determine the step size and running time. Then, discharge pressure P_d, suction pressure P_s, body pressure P_b, maximum shaft force F_{max}, and operating frequency f are required to be input as model inputs to determine the operating conditions. Based on the input parameters, estimated value of the condensation temperature T_{cond} and evaporator temperature T_{evap} can be determined as initial values for the system. The thermal properties of refrigerants can then be determined according to the input parameters using REFPROP **[195]** and sent to the linear compressor model to calculate the mass flow rate $\dot{m}$, discharge temperature T_d, and shaft power $\dot{W}$. According

to the heat transfer and pressure drop correlations for the heat exchangers, the predicted condenser temperature T_{cond}, suction temperature T_s and cooling capacity $\dot{Q}$ can be determined. The predicted condenser and suction temperatures feed back to the compressor model to start a new cycle until the difference between initial discharge temperature and updated predicted temperature is smaller than 0.5 °C.

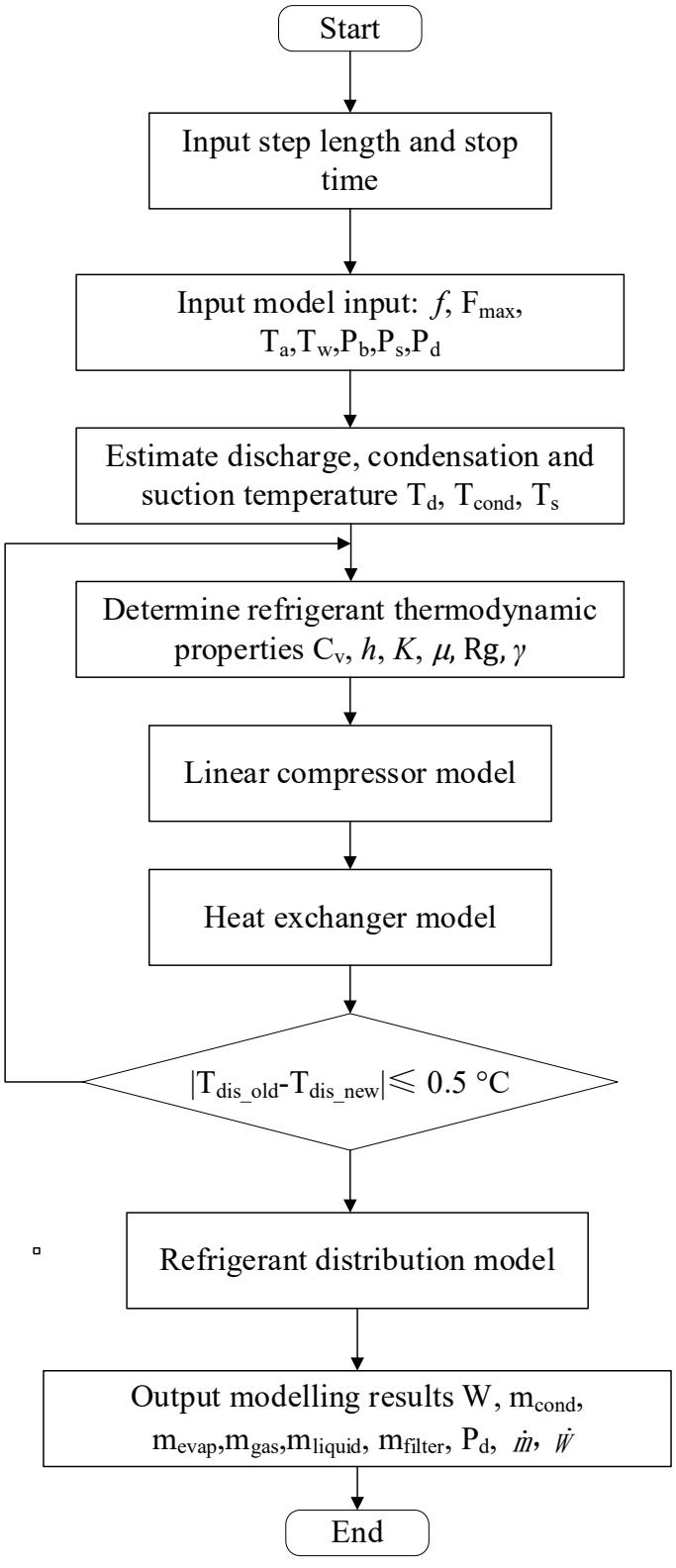

Fig. 9.1 Flowchart of the ORS model

The modelling process and vapour compression cycle are represented as a *p*-*h* diagram in Fig. 9.2. The compression process is simulated using the compressor model. Operating

frequency *f*, maximum shaft force F_{max}, and pressures are used to determine the piston dynamics. The pressures and temperature are used to calculate thermodynamic properties and solve internal balance equations. The outcomes of the compressor model (mass flow rate $\dot{m}$ and discharge temperature T_d) are send to the condenser model to calculate condenser outlet temperature T_{cond} and enthalpy h_{cond}. During the evaporation process, the cooling capacity $\dot{Q}$, evaporator pressure drop *dp*, and suction temperature T_s can be predicted using the evaporator model. Once the difference of the initial discharge temperature and updated discharge temperature is lower than 0.5 °C, the modelling results are stable. Thus, the refrigerant distribution and CoP can be determined.

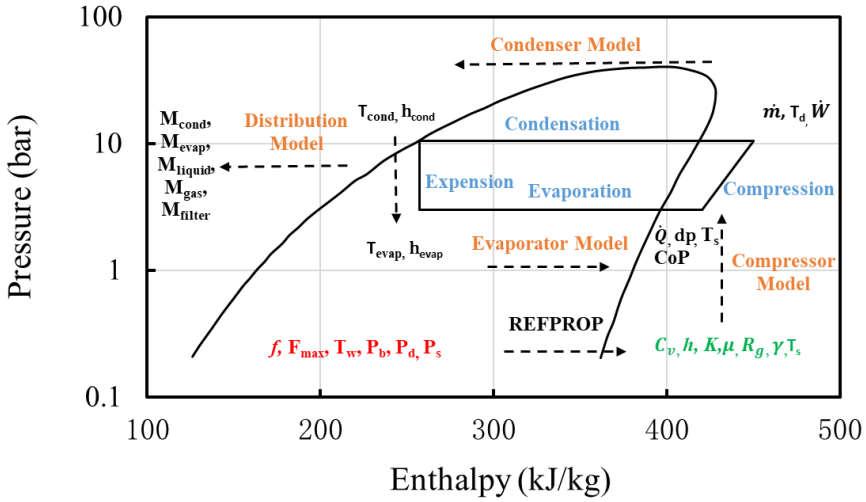

Fig. 9.2 *p-h* diagram for vapour compression cycle (red: model inputs, green: calculated properties using REFPROP, black: model outputs, blue: process, and orange: sub-model)

Seven assumptions are made for the numerical ORS model as follows:

- Decrease of mass flow rate through the expansion valve is assumed to be negligible. Enthalpy doesn't change across the expansion valve.
- Compressor wall temperature is the same as ambient temperature (20 °C).
- Heat transfers of vapour, liquid and two-phase flow are same per unit length.
- Pressure drop in the condenser is negligible.

- Compressor body pressure doesn't change.
- Reed valves are rigid bodies.
- The refrigerant at the end of the heat exchangers is fully condensed or evaporated.

9.2 Linear Compressor Sub-model

Fig. 9.3 shows the flowchart of the linear compressor sub-model. After acquiring the input parameters and the initial estimated values of the condenser and evaporator outlet temperature, refrigerant mass in the cylinder, piston acceleration, cylinder temperature, and cylinder pressure can be determined by using energy balance equations and piston dynamics equations. Thus, the movement of the reed valve for the next time step can be calculated. According to the valve movement, piston movement, and cylinder pressure, the mass flow rate and shaft work can be calculated and passed to the next calculation.

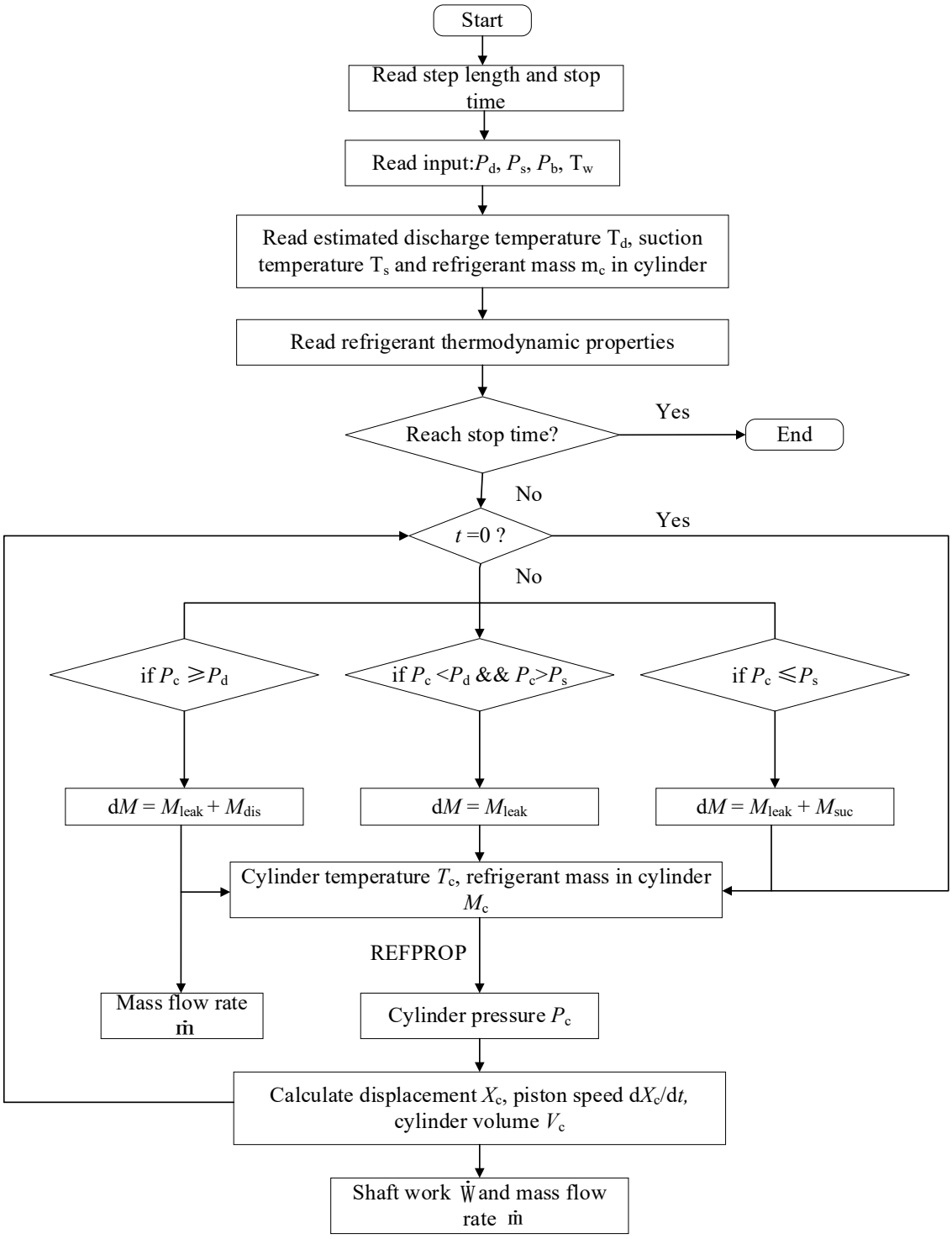

Fig. 9.3. Flowchart of the linear compressor sub-model

9.2.1 Overall Energy Balance

According to the energy conservation equations, the internal energy change can be expressed as

$$\frac{dU}{\mathrm{dt}} = \dot{Q} + \dot{W} + \sum_{\mathrm{in}} \dot{m}_{\mathrm{in}} h_{\mathrm{in}} - \sum_{\mathrm{out}} \dot{m}_{\mathrm{out}} h_{\mathrm{out}} \tag{9.1}$$

$$\frac{dU}{\mathrm{dt}} = \frac{d(u_{\mathrm{c}} m_{\mathrm{c}})}{dt} = m_{\mathrm{c}} \frac{du_c}{dt} + u_{\mathrm{c}} \frac{dm_c}{dt} \tag{9.2}$$

where $\dot{Q}$ is the heat transfer per time step, $\dot{W}$ is the shaft work per time step, h is the enthalpy of the refrigerant, $\dot{m}_{\mathrm{in}}$ is the total inlet mass flow rate, $\dot{m}_{\mathrm{out}}$ is the total outlet mass flow rate, u_{c} is the internal energy, and m_{c} is the refrigerant mass in the compressor cylinder.

The compressor total inlet mass flow rate $\dot{m}_{\mathrm{in}}$ and the total outlet mass flow rate are introduced in Section 9.2.3. The heat transfer $\dot{Q}$ in the compressor is introduced in Section 9.2.5.

The internal energy change due to the temperature and volume can be expressed as

$$du = c_{\mathrm{v}} dT + [T \left(\frac{\partial P}{\partial T}\right)_v - P] dv \tag{9.3}$$

$$u = h - Pv \tag{9.4}$$

where c_{v} is the specific heat capacity at constant volume, *T* is the temperature, *P* is the pressure, *v* is the volume, and *h* is the enthalpy.

The shaft power per time step can be calculated as

$$\dot{W} = -P \frac{dV}{dt} \tag{9.5}$$

The cylinder pressure can also be expressed as

$$P = T(\frac{\partial P}{\partial T})_v \tag{9.6}$$

By using the Eq. 9.2 to Eq. 9.6, Eq. 9.1 can be re-arranged as

$$m_{\mathrm{c}} C_{\mathrm{v}} \frac{dT_{\mathrm{c}}}{dt} + T_{\mathrm{c}} \left(\frac{\partial P}{\partial T}\right)_v (\frac{dV_{\mathrm{c}}}{dt} - \frac{1}{\rho} \frac{dm_{\mathrm{c}}}{dt}) + h_{\mathrm{c}} \frac{dm_{\mathrm{c}}}{dt} = \dot{Q} + \sum_{\mathrm{in}} \dot{m}_{\mathrm{in}} h_{\mathrm{in}} - \sum_{\mathrm{out}} \dot{m}_{\mathrm{out}} h_{\mathrm{out}} \tag{9.7}$$

Thus, the cylinder temperature change can be written as

$$\frac{dT_c}{dt} = \frac{1}{m_c C_v}[\dot{Q} + \sum_{in} \dot{m}_{in} h_{in} - \sum_{out} \dot{m}_{out} h_{out} - h_c \frac{dm_c}{dt} - T_c \left(\frac{\partial P}{\partial T}\right)_v \left(\frac{dV_c}{dt} - \frac{1}{\rho}\frac{dm_c}{dt}\right)] \quad (9.8)$$

The refrigerant mass change in the compressor cylinder can be expressed as

$$\dot{m}_{in} = dm_{suc} + dm_{leak} \quad (9.9)$$

$$\dot{m}_{out} = dm_{dis} + dm_{leak} \quad (9.10)$$

$$\frac{dm_c}{dt} = \frac{dm_{in}}{dt} - \frac{dm_{out}}{dt} \quad (9.11)$$

The mass flow rate of the system and discharge pressure temperature of the compressor can be calculated by integrating the outlet mass flow rate and averaging the discharge temperature over one cycle.

9.2.2 Piston Dynamics

As only axial motion occurs in the compressor chamber, the compressor piston is driven by the resultant force of the mechanical spring force F_{spring}, damping force due to the friction between cylinder wall and piston $F_{damping}$, motor force F_{motor}, cylinder force caused by cylinder pressure F_c, and body gas pressure force F_b. The overall balance equation for the forces acting on the compressor piston can be expressed as

$$F_{piston} = F_{spring} - F_{damping} + F_{motor} + (F_c - F_b) \quad (9.12)$$

Thus, the F_{piston} can be expressed and expanded as

$$F_{piston} = M_p \ddot{X}_p \quad (9.13)$$

$$M_p \ddot{X}_p = F_{max} \cos(2\pi f t) + k_s X_p - \beta \dot{X}_p + A_p (P_c - P_b) \quad (9.14)$$

where $\mathrm{M_p}$ is the moving mass, $F_{\max}$ is the maximum motor force, f is the operating frequency, t is the simulation time, $\mathrm{k_s}$ is the mechanical stiffness, β is damping coefficient, $\mathrm{A_p}$ is the piston area, X_p is the piston displacement (initial value is set as zero), $\dot{X}_\mathrm{p}$ is the piston velocity (the initial value is set as zero), and $\ddot{X}_\mathrm{p}$ is the piston acceleration (the initial value is set as zero).

Thus, the piston velocity and displacement for next time step can then be calculated as

$$\dot{X}_\mathrm{p}^{\mathrm{n+1}} = \dot{X}_\mathrm{p}^{\mathrm{n}} + \ddot{X}_\mathrm{p}^{\mathrm{n}}\mathrm{dt} \tag{9.15}$$

$$X_\mathrm{p}^{\mathrm{n+1}} = X_\mathrm{p}^{\mathrm{n}} + \dot{X}_\mathrm{p}^{\mathrm{n}}\mathrm{dt} + \frac{1}{2}\ddot{X}_\mathrm{p}^{\mathrm{n}}\mathrm{dt}^2 \tag{9.16}$$

The new cylinder volume can be expressed as

$$V_\mathrm{c}^{\mathrm{n+1}} = V_\mathrm{c}^{\mathrm{n}} + (\dot{X}_\mathrm{p}^{\mathrm{n}}\mathrm{dt} + \frac{1}{2}\ddot{X}_\mathrm{p}^{\mathrm{n}}\mathrm{dt}^2)\mathrm{A_p} \tag{9.17}$$

9.2.3 Compressor Valves

As compressor valves are assumed to be a rigid body, no deformation occurs during the valve opening and closing. The valve movement for the suction valve and discharge valve can be expressed as follow.

For suction valve:

$$\mathrm{m_{sv}}\ddot{x}_\mathrm{sv} + \mathrm{c_{sv}}\dot{x}_\mathrm{sv} + \mathrm{k_{sv}}x_\mathrm{sv} = \beta(P_\mathrm{s} - P_\mathrm{c})\mathrm{A_{sv}} \tag{9.18}$$

where $\mathrm{m_{sv}}$ is the equivalent mass, $\mathrm{c_{sv}}$ is the equivalent damping coefficient, $\mathrm{k_{sv}}$ is the equivalent spring coefficient, $\ddot{x}_\mathrm{sv}$ is the suction valve acceleration, $\dot{x}_\mathrm{sv}$ is the suction valve velocity, x_sv is the valve displacement, $\mathrm{A_{sv}}$ is the cross area of the suction valve, P_s is the suction pressure, P_c is the cylinder pressure, and β is the thrust coefficient which is assumed to be 0.85.

The equivalent mass m_{sv}, equivalent damping coefficient c_{sv} and cross area A_{sv} of the suction valve can be calculated by following equations

$$m_{sv} = \frac{k_{sv}}{(2\pi f_{resonant})^2} \tag{9.19}$$

$$c_{sv} = 2\zeta\sqrt{m_{sv}k_{sv}} \tag{9.20}$$

$$A_{sv} = \frac{1}{4}\pi D_{sv}^2 \tag{9.21}$$

where $f_{resonant}$ is the resonant frequency of the suction valve, ζ is the damping ratio, which is assumed to be 0.1 **[196]**, and D_{sv} is the diameter of the valve port.

The acceleration of the suction valve can be re-written as

$$\ddot{x}_{sv}^{n+1} = \frac{\beta(P_s - P_c)A_{sv} - c_{sv}\dot{x}_{sv}^{n} - k_{sv}\dot{x}_{sv}^{n}dt - k_{sv}x_{sv}^{n}}{m_{sv} + c_{sv}dt + 0.5k_{sv}dt^2} \tag{9.22}$$

The initial velocity and displacement for discharge and suction valve are set to be zero. Thus, the suction valve velocity $\dot{x}_{sv}$ and suction valve displacement x_{sv} (valve lift) can be extended as

$$\dot{x}_{sv}^{n+1} = \dot{x}_{sv}^{n} + \ddot{x}_{sv}^{n+1}dt \tag{9.23}$$

$$x_{sv}^{n+1} = x_{sv}^{n} + \dot{x}_{sv}^{n}dt + \frac{1}{2}\ddot{x}_{sv}^{n}dt^2 \tag{9.24}$$

For discharge valve:

$$m_{dv}\ddot{x}_{dv} + c_{dv}\dot{x}_{dv} + k_{dv}x_{dv} = \beta(P_c - P_d)A_{dv} \tag{9.25}$$

where P_d is the discharge pressure.

By using Eq. 9.22, Eq. 9.24, and Eq. 9.25, according to the parameters of the discharge valve, the acceleration of the discharge valve $\ddot{x}_{dv}$ can be expressed as

$$\ddot{x}_{\mathrm{dv}}^{\mathrm{n+1}} = \frac{\beta(P_{\mathrm{c}}-P_{\mathrm{d}})\mathrm{A}_{\mathrm{dv}}-\mathrm{c}_{\mathrm{dv}}\dot{x}_{\mathrm{dv}}^{\mathrm{n}}-\mathrm{k}_{\mathrm{dv}}\dot{x}_{\mathrm{dv}}^{\mathrm{n}}\mathrm{dt}-\mathrm{k}_{\mathrm{dv}}x_{\mathrm{dv}}^{\mathrm{n}}}{\mathrm{m}_{\mathrm{dv}}+\mathrm{c}_{\mathrm{dv}}\mathrm{dt}+0.5\mathrm{k}_{\mathrm{dv}}\mathrm{dt}^2} \tag{9.26}$$

Thus, the discharge valve velocity $\dot{x}_{\mathrm{dv}}$ and discharge valve displacement x_{dv} (valve left) can be extended as

$$\dot{x}_{\mathrm{dv}}^{\mathrm{n+1}} = \dot{x}_{\mathrm{dv}}^{\mathrm{n}} + \ddot{x}_{\mathrm{dv}}^{\mathrm{n+1}}\mathrm{dt} \tag{9.27}$$

$$x_{\mathrm{dv}}^{\mathrm{n+1}} = x_{\mathrm{dv}}^{\mathrm{n}} + \dot{x}_{\mathrm{dv}}^{\mathrm{n}}\mathrm{dt} + \frac{1}{2}\ddot{x}_{\mathrm{dv}}^{\mathrm{n+1}}\mathrm{dt}^2 \tag{9.28}$$

After acquiring the valve lift, the mass flow rate through the suction valve and discharge valve can then be calculated as

$$\frac{dm_{\mathrm{suc}}}{dt} = A_{\mathrm{ee\_sv}}P_{\mathrm{s}}\sqrt{\frac{2\gamma}{(\gamma-1)R_{\mathrm{g}}T_{\mathrm{s}}}}\sqrt{\left(\frac{P_{\mathrm{c}}}{P_{\mathrm{s}}}\right)^{\frac{2}{\gamma}}-\left(\frac{P_{\mathrm{c}}}{P_{\mathrm{s}}}\right)^{\frac{\gamma+1}{\gamma}}} \tag{9.29}$$

$$\frac{dm_{\mathrm{dis}}}{dt} = A_{\mathrm{ee\_dv}}P_{\mathrm{c}}\sqrt{\frac{2\gamma}{(\gamma-1)R_{\mathrm{g}}T_{\mathrm{c}}}}\sqrt{\left(\frac{P_{\mathrm{d}}}{P_{\mathrm{c}}}\right)^{\frac{2}{\gamma}}-\left(\frac{P_{\mathrm{d}}}{P_{\mathrm{c}}}\right)^{\frac{\gamma+1}{\gamma}}} \tag{9.30}$$

where A_{ee} is the effective cross area, R_{g} is the gas constant, γ is the isentropic index, and T_{c} is the cylinder temperature.

The effective cross area for suction and discharge valves can be calculated as

$$A_{\mathrm{ee\_sv}} = \alpha_{\mathrm{f}}\pi\mathrm{D}_{\mathrm{sv}}x_{\mathrm{sv}} \tag{9.31}$$

$$A_{\mathrm{ee\_dv}} = \alpha_{\mathrm{f}}\pi\mathrm{D}_{\mathrm{dv}}x_{\mathrm{dv}} \tag{9.32}$$

where α_{f} is the flow coefficient which is set as 0.6.

9.2.4 Compressor Leakage

Unlike conventional reciprocating compressors, oil-free linear compressors have a radial gap of 10-20 μm, which leads to a significantly higher clearance seal leakage. Kim and Groll **[197]** mentioned that the clearance seal leakage is the main leakage for linear

compressors, and the leakage caused by the reed valves can be ignored. To calculate the leakage flow rate across the clearance, Liang et al. **[198]** proposed the following equation

$$\dot{m}_{\mathrm{leak}} = \frac{\pi \mathrm{D_p} \mathrm{C_{Clr}^3} (P_c^2 - P_b^2)}{24 \mu \mathrm{L_p} \mathrm{R_g} T_c} \tag{9.33}$$

where $\mathrm{C_{clr}}$ is the clearance between piston and cylinder wall and $\mathrm{L_p}$ is the length of clearance.

9.2.5 Heat Transfer in Cylinder

The instantaneous heat transfer coefficient between the gaseous refrigerant and cylinder is calculated by using the correlation proposed by Fagotti and Prata **[199]**.

$$h_c = (0.28 Re^{0.65} + 0.25 L \frac{T_w}{T_c - T_W}) \frac{k}{D_p} \tag{9.34}$$

where *Re* is the Reynold number, T_w is the cylinder wall temperature, k is the thermal conductivity, and *L* is the compressibility factor.

The *Re* number and *L* can be expressed as

$$Re = \frac{\rho |\dot{X}_p| D_p}{\mu} \tag{9.35}$$

$$L = \frac{\gamma - 1}{V_c} \frac{dV_c}{dt} \sqrt{\frac{D_p^3}{\alpha |\dot{X}_p|}} \tag{9.36}$$

where μ is the viscosity and α is the gas diffusivity.

The heat transfer through the compressor wall can then be written as

$$\dot{Q} = \frac{1}{dt} h_c A_c (T_c - T_W) \tag{9.37}$$

where

$$A_c = \pi D_p^2 (X_p + 0.00757) \tag{9.38}$$

By combining the Eq. 9.34 – 9.38, the temperature and refrigerant density in the compressor cylinder can be solved.

9.3 Heat Exchanger Sub-model

Fig. 9.4 shows the flowchart of the heat exchangers sub-model. After acquiring discharge pressure, suction pressure, discharge temperature, and mass flow rate from the compressor sub-model, the refrigerant thermodynamic properties are calculated using REFPROP **[195]**. According to the calculated thermodynamic properties and the correlations for the heat transfer and pressure drop in heat exchangers, the condenser outlet temperature, evaporator outlet temperature, and pressure can then be determined. The predicted evaporator pressure drop, evaporator temperature, and discharge temperature will be feedbacked to the compressor model to increase the accuracy of the modelling results.

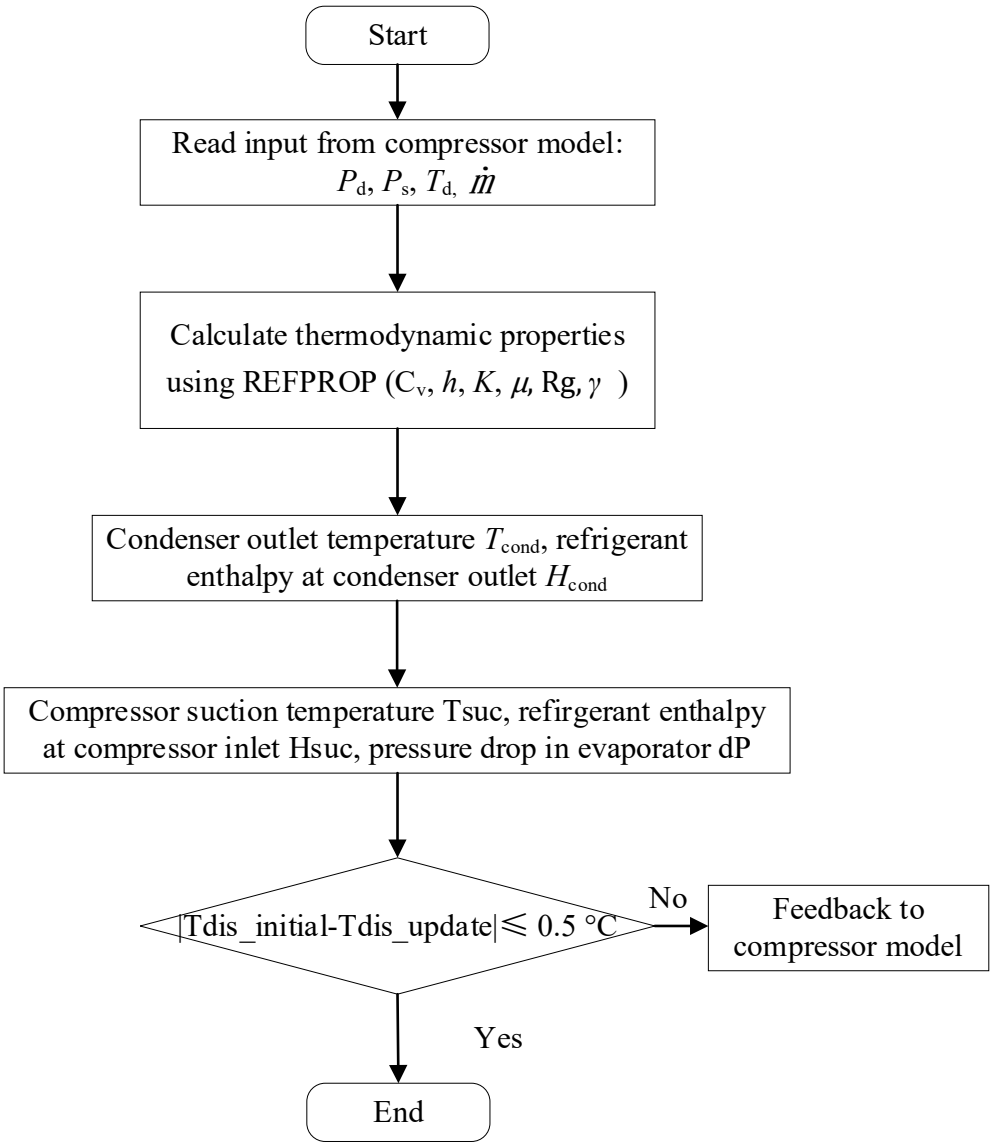

Fig. 9.4 Heat exchanger modelling flowchart

9.3.1 Evaporator

The enthalpy at the evaporator inlet is the same as the enthalpy at the condenser outlet. Thus, the evaporator inlet vapour quality can be calculated as

$$x_{\text{evap\_in}} = \frac{h_{\text{evap\_in}} - h_l}{h_g - h_l} \tag{9.39}$$

where $h_{\text{evap\_in}}$ is the enthalpy at the evaporator inlet, h_g is the enthalpy of the saturated vapour and h_l is the enthalpy of the saturated liquid.

As mentioned in Chapter 7, the vapour quality changes linearly in the heat exchangers. The vapour quality changing from x_{in} to 1.0 can be divided into 1000 step lengths. Thus, the local Nu number and the local heat transfer coefficient can be calculated as

$$Nu = 0.1522 \frac{\mathrm{c}}{(\mathrm{c}+1)^{0.0027}} Re_{\mathrm{tp}}{}^{0.8} (Pr_{\mathrm{l}})^{\frac{1}{3}} \tag{9.40}$$

$$\mathrm{h} = \frac{Nuk_{\mathrm{l}}}{\mathrm{D_h}} \tag{9.41}$$

Combining with the mass flow rate and suction pressure, the heat absorbed for the two-phase regime can be calculated as

$$\dot{W}_{\mathrm{evap\_tp}} = \dot{m}(h_{\mathrm{g}} - h_{\mathrm{evap\_in}}) \tag{9.42}$$

The cooling capacity for each step length can then be calculated as

$$\dot{W}_{\mathrm{evap\_step}} = \dot{W}_{\mathrm{evap\_tp}} \frac{h_{\mathrm{evap\_local}}}{\sum h_{\mathrm{evap\_local}}} \tag{9.43}$$

The physical length per step length for two-phase flow in the evaporator can be calculated as

$$A_{\mathrm{e\_step}} = \frac{\dot{W}_{\mathrm{evap\_step}}}{h_{\mathrm{evap\_local}}(T_{\mathrm{w}} - T_r)} \tag{9.44}$$

$$L_{\mathrm{evap\_step}} = \frac{A_{\mathrm{e\_step}}}{\pi \mathrm{D_{in}}} \tag{8.45}$$

Thus, the length of gas phase in the evaporator can be calculated as

$$L_{\mathrm{evap\_gas}} = L_{\mathrm{evap\_total}} - \sum L_{\mathrm{evap\_step}} \tag{9.46}$$

The pressure drop can then be calculated according to the correlation and predicted phase length.

The heat absorbed by the gas phase and suction temperature can then be calculated as

$$\dot{W}_{\mathrm{evap\_gas}} = \dot{W}_{\mathrm{evap\_tp}} \frac{L_{\mathrm{evap\_gas}}}{\sum L_{\mathrm{evap\_step}}} \tag{9.47}$$

$$T_{\mathrm{s}} = T_{\mathrm{suc\_sat}} - \frac{\dot{W}_{\mathrm{evap\_gas}}}{\dot{m}\mathrm{c_p}} \tag{9.48}$$

where $\mathrm{c_p}$ is the specific heat capacity.

The cooling capacity and CoP of the ORS can be expressed as

$$\dot{Q}_{\mathrm{c}} = \dot{m}(h_{\mathrm{suc}} - h_{\mathrm{evap\_in}}) \tag{9.49}$$

$$CoP = \frac{0.9\dot{Q}_{\mathrm{c}}}{\dot{W}} \tag{9.50}$$

where h_{suc} is the enthalpy at the compressor suction, $h_{\mathrm{evap\_in}}$ is the enthalpy at the evaporator inlet which is the same as condenser outlet enthalpy, the motor efficiency was set as 90%.

9.3.2 Condenser

The heat rejection for gas phase and two-phase refrigerant in the condenser can be calculated as

$$\dot{W}_{\mathrm{cond\_gas}} = \dot{m}\left(h_{\mathrm{cond\_in}} - h_{\mathrm{g}}\right) \tag{9.51}$$

$$\dot{W}_{\mathrm{cond\_tp}} = \dot{m}\left(h_{\mathrm{g}} - h_{\mathrm{l}}\right) \tag{9.52}$$

Similar to the void fraction calculation in Section 9.3.1, the local Nu number and the local heat transfer coefficient for two-phase flow can then be calculated as

$$Nu_{\mathrm{cond\_local}} = 1.3346\frac{\mathrm{c}}{(\mathrm{c}+1)^{0.0158}}Re_{\mathrm{tp}}{}^{0.8}(Pr_{\mathrm{l}})^{\frac{1}{3}} \tag{9.53}$$

$$h_{\mathrm{cond\_local}} = \frac{Nu_{\mathrm{cond\_local}}k_{\mathrm{l}}}{\mathrm{D_h}} \tag{9.54}$$

Thus, the physical length per step length for two-phase flow in the condenser can be calculated as

$$A_{\text{cond\_step}} = \frac{\dot{W}_{\text{cond\_step}}}{h_{\text{cond\_local}}(T_{\text{w}} - T_r)} \tag{9.55}$$

$$L_{\text{cond\_step}} = \frac{A_{\text{cond\_step}}}{\pi \text{D}_{\text{in}}} \tag{9.56}$$

The Nu number and heat transfer coefficient for gas phase in the condenser can be expressed as

$$Nu_{\text{cond\_gas}} = (9.137 \times 10^{-5}) \frac{\text{c}}{(\text{c}+1)^{-8.88\times10^{-10}}} Re_{\text{tp}}{}^{0.8} (Pr_{\text{l}})^{\frac{1}{3}} \tag{9.57}$$

$$h_{\text{cond\_gas}} = \frac{Nu_{\text{cond\_gasl}} k_{\text{g}}}{\text{D}_{\text{h}}} \tag{9.58}$$

where k_{g} is the gas thermal conductivity.

The length of the gas phase in the condenser can be expressed as

$$L_{\text{cond\_gas}} = \frac{\dot{W}_{\text{cond\_gas}}}{\pi \text{D}_{\text{in}} h_{\text{cond\_gas}} (T_{\text{w}} - T_r)} \tag{9.59}$$

The length of liquid-phase of the refrigerant in the condenser can be calculated as

$$L_{\text{cond\_liquid}} = L_{\text{cond\_total}} - L_{\text{cond}_{\text{gas}}} - \sum L_{\text{cond\_step}} \tag{9.60}$$

Thus, the heat rejected by liquid-phase and condenser outlet temperature can be calculated as

$$\dot{W}_{\text{cond\_liquid}} = \dot{W}_{\text{cond\_tp}} \frac{L_{\text{cond\_liquid}}}{\sum L_{\text{cond\_step}}} \tag{9.61}$$

$$T_{\text{cond}} = T_{\text{cond\_sat}} - \frac{\dot{W}_{\text{cond\_liquid}}}{\dot{m} \text{c}_{\text{p}}} \tag{9.62}$$

9.4 Refrigerant Distribution Sub-model

The flowchart of the refrigerant distribution calculation is shown in Fig. 9.5. Once the difference between the initial compressor discharge temperature and updated compressor discharge temperature becomes lower than 0.5 °C, the mass flow rate, suction temperature,

discharge temperature, and condenser outlet temperature are passed to the refrigerant distribution sub-model. The local void fraction and phase length can be determined according to the Eq. 7.1 - Eq. 7.8 in Chapter 7. Combined with the predicted heat exchanger inlet and outlet temperature and pressure, the density of each section in the ORS can be calculated using REFPROP **[195]**, thus the refrigerant distribution. The predicted refrigerant distribution can be used to assist the design of the system components. With different body pressure, the shaft force will be changed resulting in different shaft power and mass flow rate thus different refrigerant total charge.

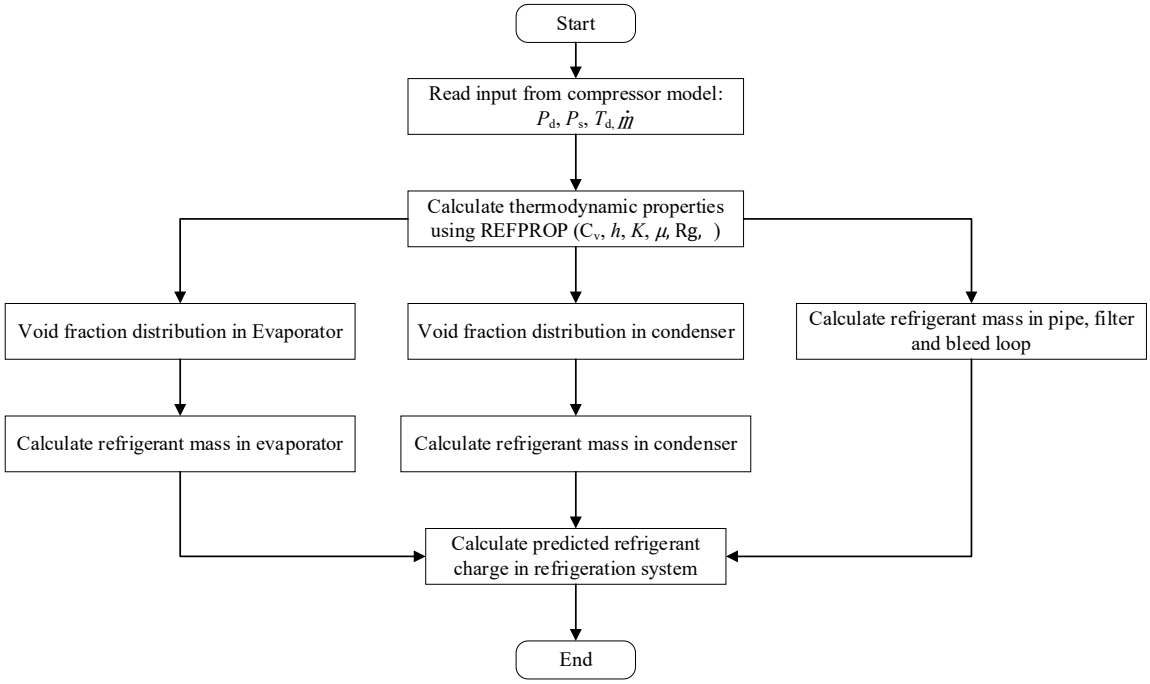

Fig. 9.5 Flowchart of the refrigerant distribution sub-model

9.5 Model Setup

The simulation object is the ORS using a novel linear compressor. This system was introduced previously in Chapter 3. The detailed parameters for the system and linear compressor can be found in Table 3.1-3.3. The experiments of the ORS were carried out under a large range of conditions. Table 9.1 shows the test conditions for the ORS model.

Table 9.1 Test conditions for the ORS model

Working fluid	R134a
Compressor stroke (mm)	9 -13
Operating frequency (Hz)	30-40
Refrigerant charge (g)	250
Pressure ratio	2.0-4.0
Condenser temperature (°C)	40, 45, 50

Fig. 9.6 shows the ORS model structure in Simulink. The required model inputs are placed in an Excel spreadsheet titled 'LDAQ Selected'. These model inputs are passed to the main model to generate initial estimated values. The estimated values together with the model inputs are then be sent to sub-model in Simulink to predict system performance. The main model is called as 'Refrigeration_System'. The modelling results are sent back to the main model and saved in an Excel spreadsheet titled 'Refrigeration Modelling Results'. The details of main model and sub-model code are presented in Appendix D-F.

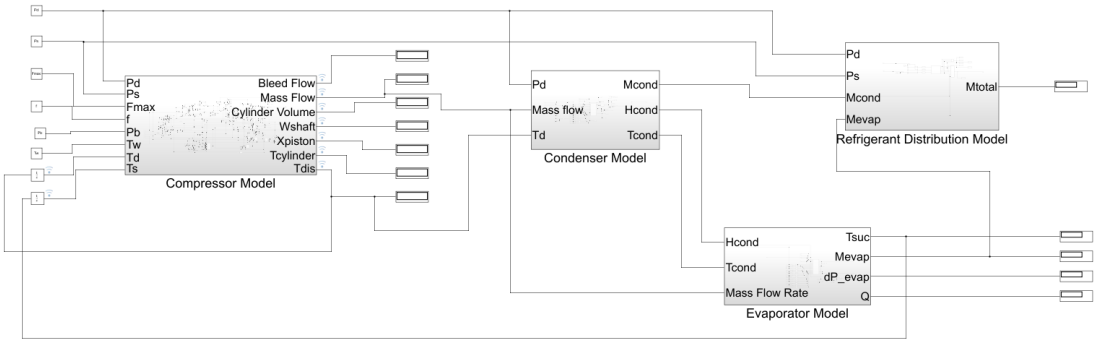

Fig. 9.6 ORS model structure in Simulink

9.6 Results and ORS Model Validation

9.6.1 Compressor Performance

Fig. 9.7 compares the *P-V* loop from the compressor model and measurement at a compressor stroke of 12 mm, a pressure ratio of 3.0, and a condenser temperature of 40 °C. Overall, the *P-V* loop from the ORS model is fairly close to the measurement particularly for the compression and expansion processes.

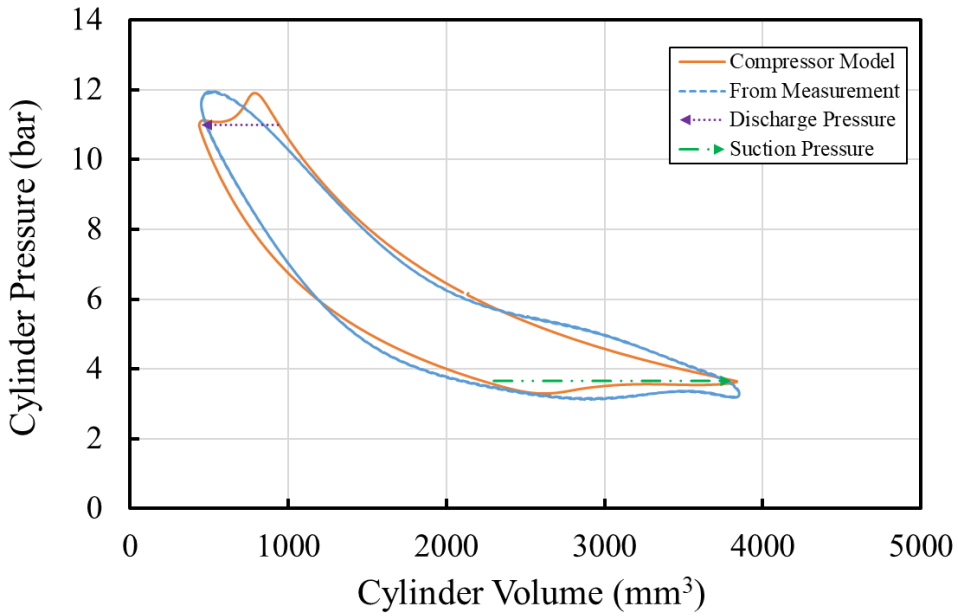

Fig. 9.7 *P-V* loop comparison between model and measurement using R134a for a compressor stroke of 12 mm, a pressure ratio of 3.0, and a fixed condenser temperature of 40 °C.

Fig. 9.8 shows the piston displacement against time for a pressure ratio of 3.0, a compressor stroke of 12 mm, and a condenser temperature of 40°C at 36 Hz. The piston displacement is close to a sinusoidal motion.

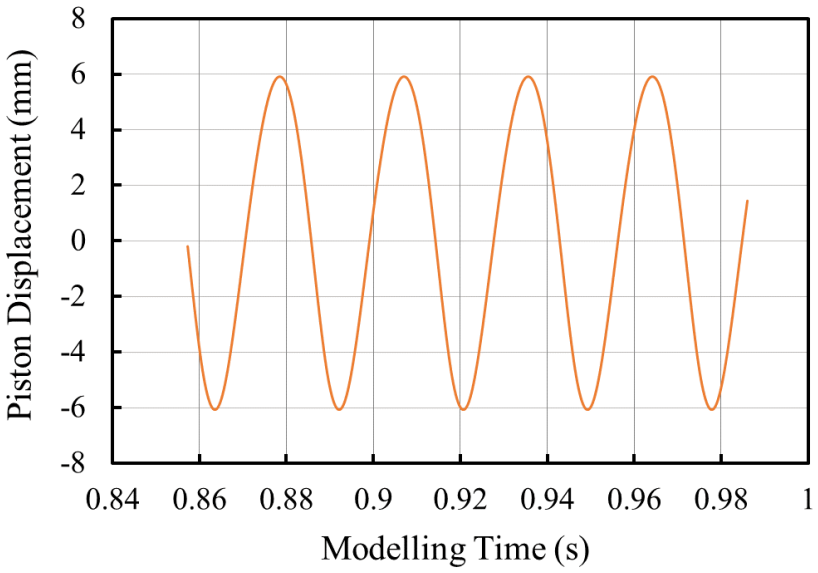

Fig. 9.8 Piston displacement against modelling time for a pressure ratio of 3.0, a compressor stroke of 12 mm, and a condenser temperature of 40 °C.

Fig. 9.9 shows the predicted compressor stroke against experimental compressor stroke for the linear compressor using R134a. Overall, the predicted compressor strokes agree

well with the measurements. The MAPE is 4.8% with all points falling within ±10% of the experimental data.

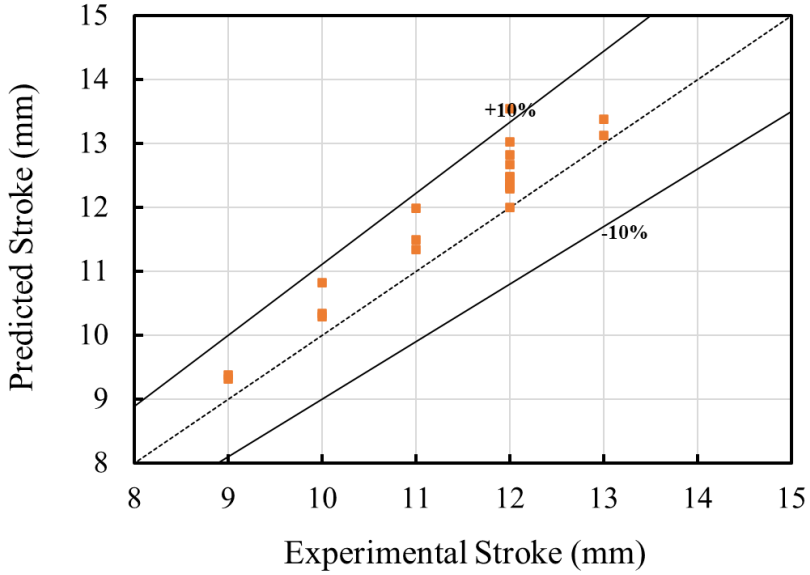

Fig. 9.9 Predicted compressor stroke against experimental compressor stroke for the linear compressor using R134a.

Fig. 9.10 shows the reed valve motion for a pressure ratio of 3.0, a compressor stroke of 12 mm, and a compressor frequency of 36 Hz. Once there is a pressure difference, the suction valve will start to open towards the maximum valve lift of 1 mm and then rebound to the balance position. The reed valves can rise and rebound several times within one process due to the in-cylinder pressure change resulting by the piston motion. The suction process accounts for 11% of one cycle while discharge process occupies 28% of one cycle. This is due to higher stiffness of the discharge valve.

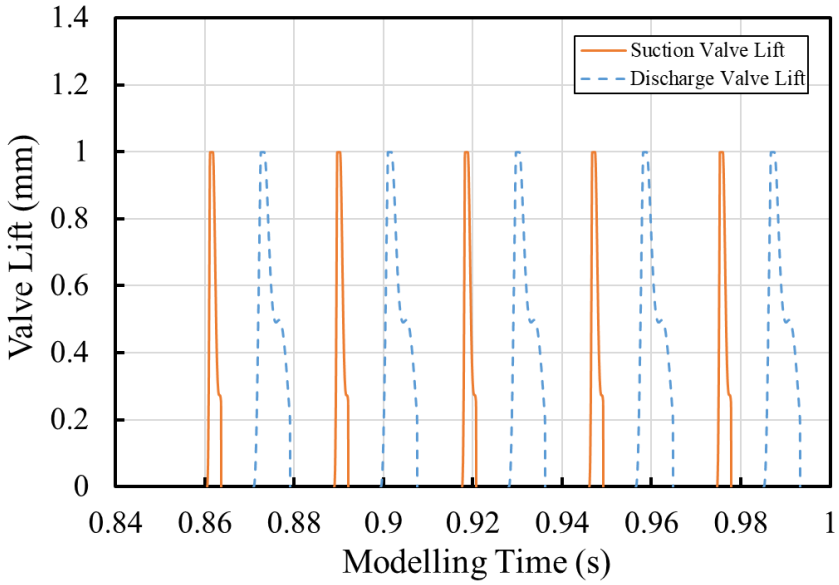

Fig. 9.10 Reed valve motion for a pressure ratio of 3.0, a compressor stroke of 12 mm, a condenser temperature of 40 °C, and an operating frequency of 36 Hz.

Fig. 9.11 shows the cylinder temperature variation for a pressure ratio of 3.0, a compressor stroke of 12 mm, and a condenser temperature of 40 °C. The maximum cylinder temperature is 68.5 °C while the minimum is 23 °C. A noticeable cylinder temperature change can be found at the beginning of the discharge and suction processes due to the mass and heat exchange when reed valves open.

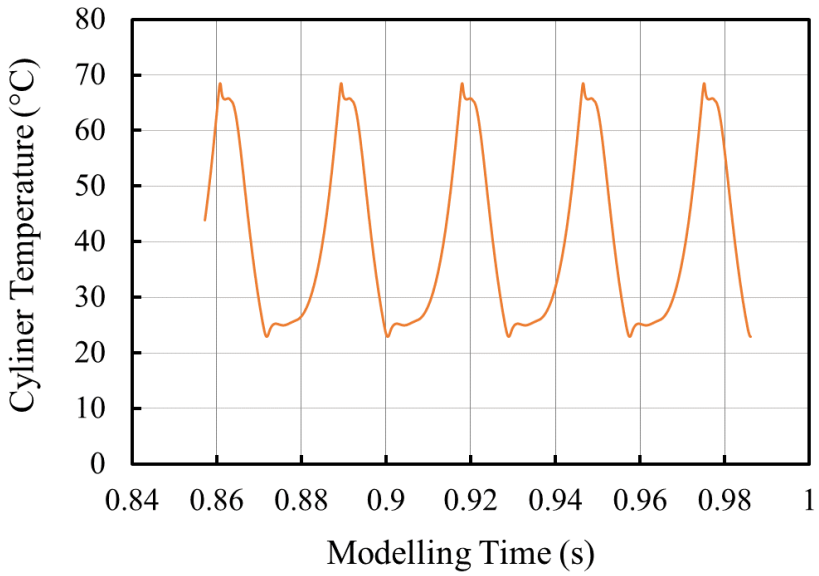

Fig. 9.11 Cylinder temperature variation for a pressure ratio of 3.0, a compressor stroke of 12 mm, a condenser temperature of 40 °C and an operating frequency of 36 Hz.

Fig. 9.12 shows the discharge temperature against the pressure ratio with various condenser temperatures at a compressor stroke of 12 mm. For all condenser temperatures, the discharge temperature increases with the pressure ratio. For a fixed pressure ratio, a higher condenser temperature leads to a slightly higher discharge temperature due to higher discharge pressure. At a condenser temperature of 50 °C and a pressure ratio of 4.0, the linear compressor can reach a discharge temperature of 78.7 °C.

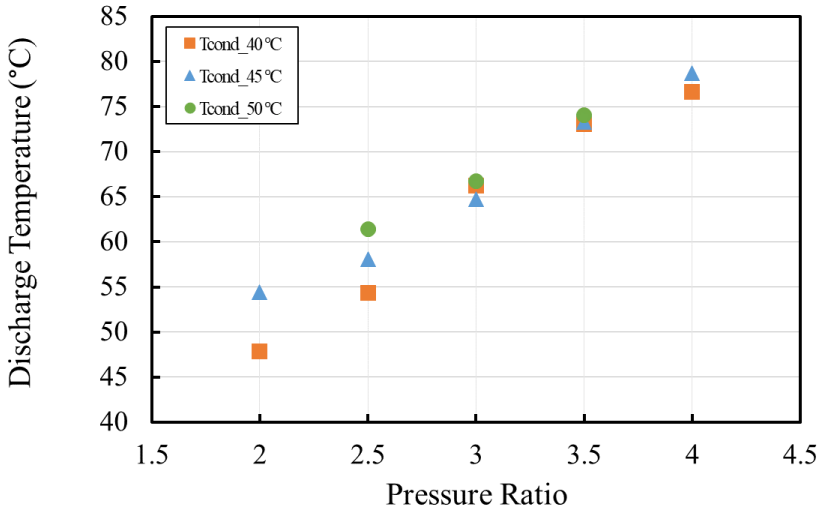

Fig. 9.12 Discharge temperature against pressure ratio for a compressor stroke of 12 mm with various condenser temperatures.

Fig. 9.13 shows the predicted mass flow rate against the experimental mass flow rate of the ORS using R134a. The MAPE for the modelling results is 5.8% while all modelling points fall within ±15% of the experimental mass flow rates.

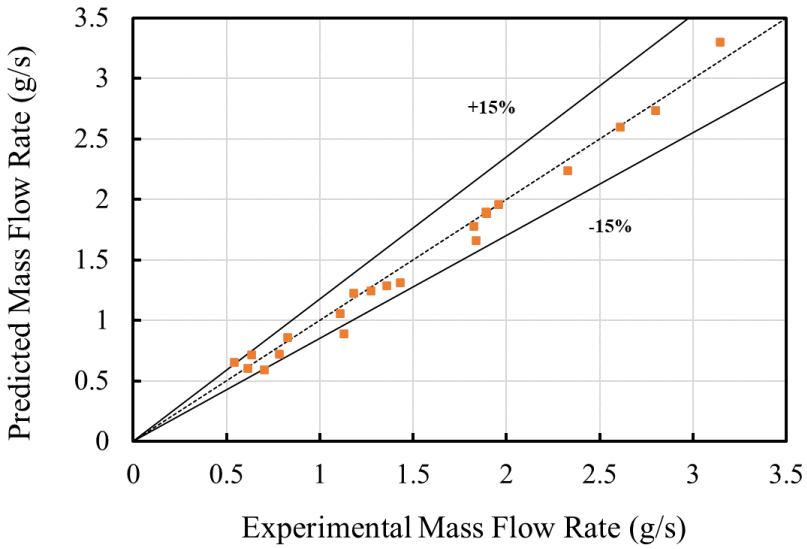

Fig. 9.13 Predicted mass flow rate against experiments using R134a.

Fig. 9.14 shows the predicted power input against experiments using R134a. Overall, the MAPE for the modelling results is 4.3% while all modelling points fall within ±10% of the experimental values. The motor efficiency is assumed to be 90% in this model. An electric motor model can further improve the accuracy, which is in the scope of future work.

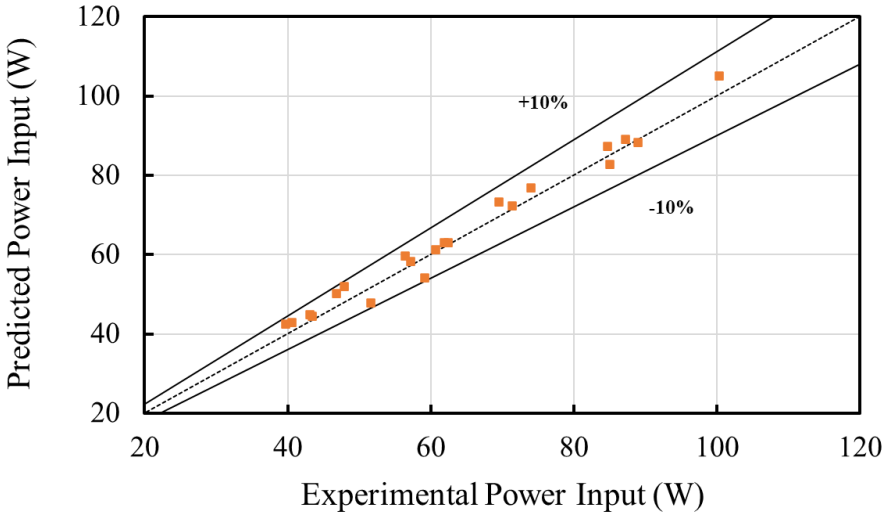

Fig. 9.14 Predicted power input against experiments using R134a.

9.6.2 System Performance

As can be seen in Fig. 9.15, the predicted suction temperatures are compared with the experimental results. The predicted suction temperatures have a MAPE of 13%. Note that the temperature for the thermodynamic property calculations in the ORS modelling uses Kelvin as the unit.

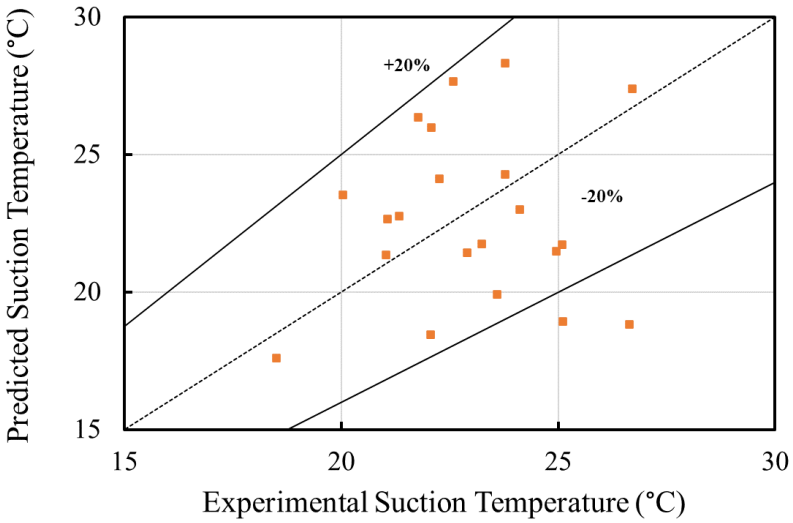

Fig. 9.15 Predicted suction temperature against measurements using R134a.

The comparison of the predicted cooling capacities and the measurements are shown in Fig. 9.16. The predicted cooling capacity can be calculated using Eq. 9.49. The predicted

cooling capacities match the experiments within 7.6% while all modelling data fall between -20% and 10% of the experimental data.

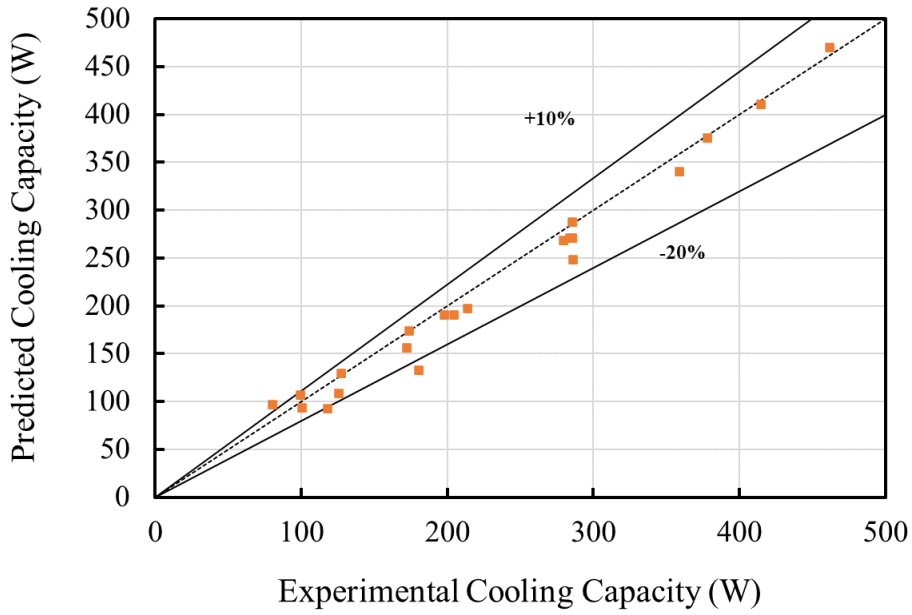

Fig. 9.16 Predicted cooling capacity against experimental cooling capacity using R134a.

Fig. 9.17 shows the predicted bleed flow rate against the measurements. The MAPE of the predicted bleed flow rate is 14.3% with all modelling data falling within -30% to 10% of the experimental data.

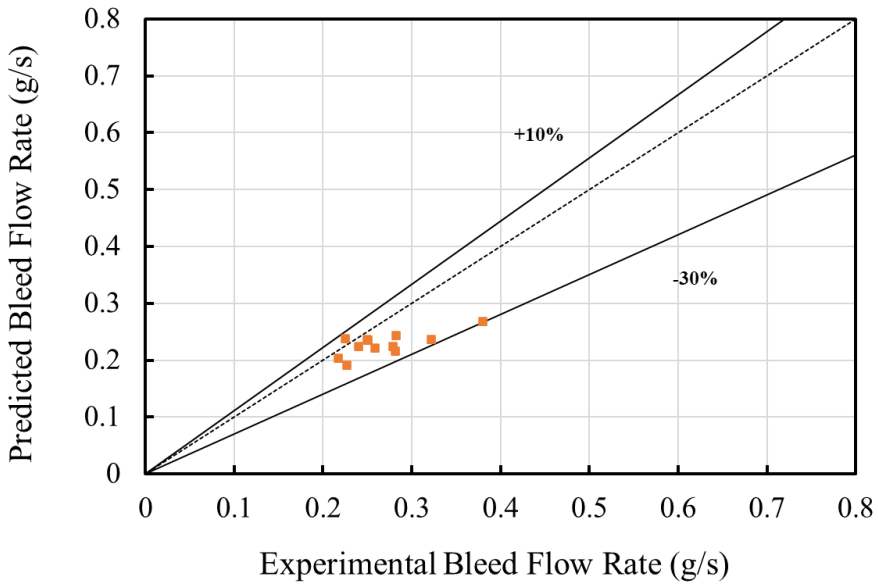

Fig. 9.17 Predicted bleed flow rate against measurements using R134a.

Fig. 9.18 shows the predicted main flow rate and bleed flow rate for a fixed compressor stroke of 13 mm. The main flow rate increases with the increase of the evaporator temperature due to the increase of the compressor volumetric efficiency while a reverse trend can be found in bleed flow rate due to small difference between cylinder pressure and body pressure. With the decrease of the evaporator temperature, the bleed flow fraction is increased from 3% to 11%. Higher bleed flow rate leads to higher efficiency loss in the system.

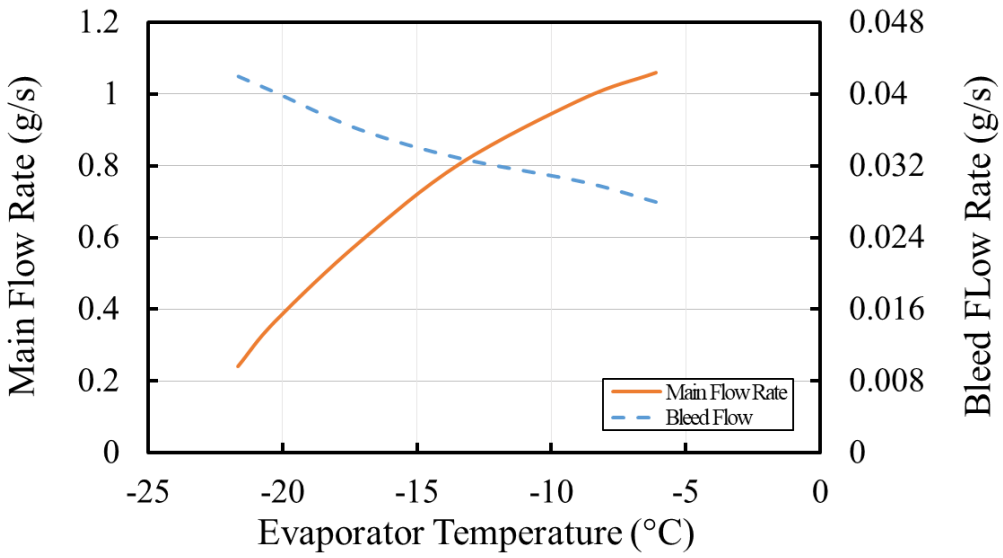

Fig. 9.18 Predicted main flow rate and bleed flow rate with various evaporator temperatures for a fixed compressor stroke of 13 mm and a condenser temperature of 40 °C.

Fig. 9.19 shows the predicted cooling capacity and CoP with various evaporator temperatures at a condenser temperature of 40 °C and a compressor stroke of 13 mm. Both the cooling capacity and CoP increase with the increase of the evaporator temperature due to the increase of the mass flow rate and volumetric efficiency. A cooling capacity of 45 W and a CoP of 1.7 are achieved at an evaporator temperature of -21 °C while a cooling capacity of 160 W and a CoP of 2.1 are achieved at an evaporator temperature of -5 °C. The oil-free linear compressor used in the model is not designed for higher pressure ratios (low evaporator temperature). Further modification and design work need to be carried out to allow linear compressor to work at higher pressure ratios.

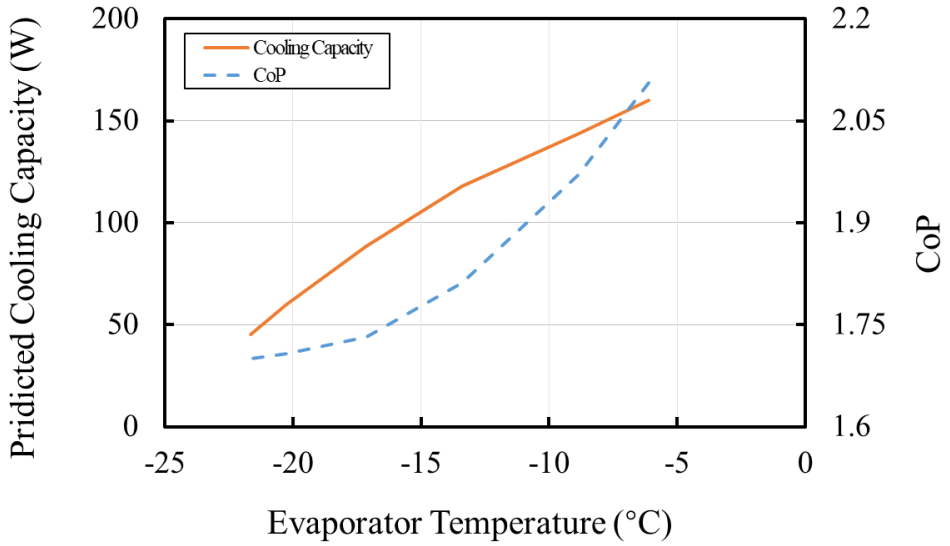

Fig. 9.19 Predicted cooling capacity and CoP against evaporator temperature at condenser temperature of 40 °C, compressor stroke of 13 mm and an operating frequency of 36 Hz.

9.6.3 Refrigerant Distribution

Fig. 9.20 shows the predicted refrigerant charge for the ORS using R134a. 250 g is used as the reference refrigerant charge. The MAPE of the predicted refrigerant charge is 19.6%. The average predicted refrigerant charge is 201.2 g, which is about 50 g lower than the reference refrigerant charge.

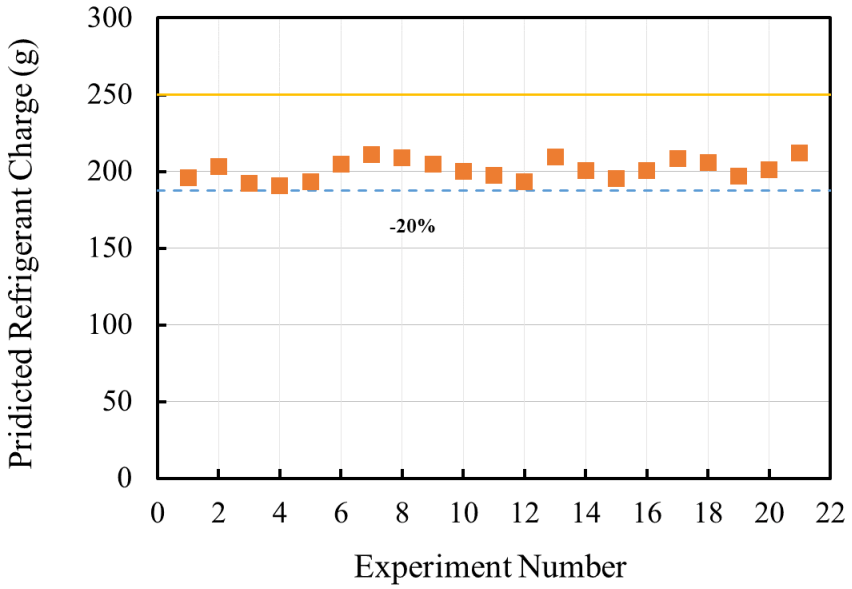

Fig. 9.20 Predicted refrigerant charge for the ORS using R134a

Fig. 9.21 shows the predicted refrigerant distribution with different evaporator temperature at a compressor stroke of 13 mm, a condenser temperature of 40 °C and an operating frequency of 36 Hz. Overall, the condenser contains the most refrigerant in the system which is about 70% of the total refrigerant mass while gas line and filter contain about 2% of the total refrigerant. Evaporator and liquid line contain about 10% and 15% refrigerant, respectively. The majority of the refrigerant is contained in the condenser instead of circulating in the system due to the low effective compressor stroke leading to the low cooling capacity and CoP as shown in Fig. 9.19. With the decrease of the evaporator temperature, more refrigerant accumulates in the condenser leading to even lower CoP. The refrigerant in the gas line and filter increase with the evaporator temperature due to the increase of the evaporator pressure leading to higher refrigerant density.

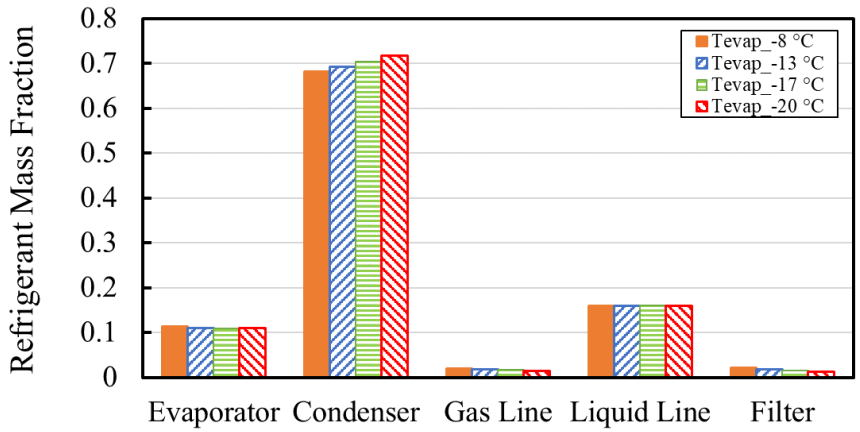

Fig. 9.21 Predicted refrigerant distribution in the refrigeration system with different evaporator temperature

9.7 Summary

A comprehensive numerical model of the ORS is presented in this chapter based on the measurements and modelling in the previous chapters. The ORS model is validated with the experimental results of the ORS using R134a. A good agreement is found between modelling and measurements. This model can assist the optimization of the ORS and design of the system with microchannel heat exchangers. Key findings are listed below:

(1) The discharge process takes longer time than the suction process due to higher stiffness of the discharge valve. Overshoots of the in-cylinder pressure are found during the discharge process and suction process. Further works need to be done on reed valve movement to improve the accuracy of the ORS model.

(2) Higher pressure ratio tends to have higher discharge temperature. At a condenser temperature of 50 °C and a pressure ratio of 4.0, the linear compressor can reach a discharge temperature of 78.7 °C. The discharge temperatures for the low GWP refrigerants with flammability at high pressure ratios need to be investigated.

(3) Higher evaporator temperature presents higher mass flow rate and lower bleed flow rate. Higher bleed flow rate leads to higher efficiency loss in the system.

(4) A cooling capacity of 45 W and a CoP of 1.7 are achieved at an evaporator temperature of -21 °C while a cooling capacity of 160 W and a CoP of 2.1 are achieved at an evaporator temperature of -5 °C.

(5) At a compressor stroke of 13 mm, a condenser temperature of 40 °C and an operating frequency of 36 Hz, over 70% of the refrigerant can be accumulated in the condenser at high pressure ratios. Microchannel heat exchangers can significantly improve the utilization of refrigerant and reduce refrigerant charge.

Chapter 10 Conclusions and Future Work

10.1 Conclusions

An ORS mainly consists of an oil-free linear compressor, a condenser, an evaporator, and a bleed flow loop. Benefited from the absence of oil lubricants and use of linear compressor, the ORS offers several advantages over conventional refrigeration systems, such as avoiding on-off compressor operation, eliminating heat transfer reduction due to oil lubricants, reducing refrigerant charge, and providing potential for the use of microchannel heat exchangers. Moreover, to diminish the impact on the environment, high GWP refrigerants are required to be phased out by environment-friendly refrigerants for refrigeration units, such as R1234yf, R717, and R152a. Though numerous works have been done to investigate the performance of linear compressor itself and system performance using low GWP refrigerants, studies are hardly found in literature to evaluate the characteristics and performance of ORS using low GWP refrigerants. This work introduced and evaluated an ORS using low GWP refrigerants based on experiments and numerical models. The measurements and modelling for the oil-free linear compressor were reported in Chapter 4 and Chapter 5. The evaluation of the characteristics of the ORS was reported in Chapter 6-8. A comprehensive numerical model for the ORS was presented in Chapter 9. The main findings are listed below:

- The performance of the novel oil-free linear compressor was tested over a wild range of conditions. The experimental results reveal that operating the linear compressor at its resonant frequency can reach the highest motor efficiency for given conditions. The linear compressor is able to achieve capacity modulation with high motor efficiency and can achieve even higher efficiency at part-load conditions due to lower power input. A motor efficiency of 86%-92% is achieved over the experimental conditions.

- An analytical model was developed to investigate the performance of the oil-free linear compressor using low GWP refrigerants. The modelling results show that R717 provides the highest cooling capacity and the second highest CoP among R717, R1234yf, R152a, R600a, and R134a. R717 has potential to be used for domestic refrigeration.

- Experiments have been conducted based on the ORS using R1234yf and R134a. The experimental results show that R1234yf can be used as a drop-in replacement for the refrigerant unit using R134a with an acceptable deterioration of the performance. The CoP of R1234yf is 10-25% lower than R134a, while the cooling capacity of R1234yf is 10-30% lower than R134a. Experiments also have been carried out using R152a. However, due to the low liquid density and saturation pressure, the system was overcharged. The component structure needs to be modified when using R152a as a replacement to R134a.

- Correlations of pressure drop and heat transfer in heat exchangers have been developed for R1234yf, R152a, and R134a. The predicted pressure drop and Nusselt number agree well with measurements. Theses correlations can be used to develop heat exchanger model and help to calculate refrigerant distribution.

- The refrigerant distribution was calculated. The results show that over 70% of refrigerant is accumulated in the condenser while the evaporator and liquid lines keep approximately 10% of the total refrigerant charge, respectively.

- Experiments have been carried out to investigate the impact of refrigerant charge. The optimal refrigerant charge varies with operating conditions. Higher compressor stroke and lower pressure ratio tend to have higher optimal refrigerant charge. For a fixed compressor stroke and a fixed pressure ratio, both cooling capacity and CoP reach the maximum value at the optimal refrigerant charge. The

cooling capacity decreases with the condenser temperature while the CoP increases with the condenser temperature.

- A comprehensive model of the ORS including a linear compressor model, a heat exchanger model, and a refrigerant distribution model has been developed. The modelling results show a good agreement with measurements. The modelling results show that the ORS can achieve a cooling capacity of 45 W and a CoP of 1.7 at an evaporator temperature of -21 °C and a cooling capacity of 160 W and a CoP of 2.1 at an evaporator temperature of -5 °C.

10.2 Future Work

10.2.1 Lubricant Impact on System Performance

As pointed by Youbi-Idrissi et al. **[192]**, over 20% of refrigerant can be dissolved in oil lubricant resulting in increasing costs and greenhouse gas emissions. Also, the oil film formed at the evaporator internal surface can reduce the heat transfer coefficient, and this issue can even worse when using microchannel heat exchanger. The blockage caused by oil lubricants when using microchannel can be another problem. In this study, the performance of the ORS using several refrigerants was studied. An experimental and numerical comparative study between the ORS and oil lubricated VCR systems is needed to have a deeper evaluation of the superiority of the ORS.

10.2.2 Design of Ultra-low Charge and High-Pressure Ratio Refrigeration System

Reducing the refrigerant charge and providing compact refrigeration units for domestic, mobile, and electrical cooling are two requirements for the future refrigeration systems. Microchannel as a high efficiency and compact heat transfer element has been studied in some pioneering works **[37-42]**. Due to the compactness of the microchannel heat exchangers, the refrigerant charge can be dramatically reduced. In addition, as pointed by

Liang **[116]**, linear compressor can be further minimised by increasing operating frequency and reducing compressor stroke.

The test rig introduced in current study can achieve a pressure ratio of 2.0-4.0 which only cover a part of the working conditions for domestic refrigeration. The next stage of the work will be to use compact heat exchanger and minimise the scale of linear compressors for VCR systems running at higher pressure ratios.

10.2.3 Refrigeration System using Natural Refrigerants

As mentioned in Chapter 2, R717 has superior thermodynamic properties over R600a, R1234yf, R152a. Liang **[137]** pointed out that placing the windings outside the pressure containment provides possibility to design a linear compressor with no copper or copper alloys in contact with working fluids which shows the compatibility of linear compressors with R717. To develop a linear compressor which can work with R717 can be one of the future works.

10.2.4 Improvement of the ORS Model

A comprehensive ORS model was developed in this study and the predicted values show good agreements with the measurements. However, there still have several parts can be improved. The motor efficiency is assumed to be 90% in the model. An electrical system model including shaft power, power input, and motor losses can be added to the ORS model. Fuzzy technique, finite volume method, and moving boundary method can be used to develop a general heat exchanger model allowing a wider applicability and higher accuracy **[200, 201]**. The leakage loss crossing the compressor reed valves can also be added to improve the accuracy. In addition, a control strategy can be proposed for the ORS based on the model to achieve capacity modulation automatically.

References

[1] H. C. Kim, G. A. Keoleian, and Y. A. Horie, "Optimal household refrigerator replacement policy for life cycle energy, greenhouse gas emissions, and cost," *Energy Policy,* vol. 34, no. 15, pp. 2310-2323, 2006.

[2] S. Buffa, M. Cozzini, M. D'Antoni, M. Baratieri, and R. Fedrizzi, "5th generation district heating and cooling systems: A review of existing cases in Europe," *Renewable and Sustainable Energy Reviews,* vol. 104, pp. 504-522, 2019.

[3] (2020, 15th May). *How much electricity is used for cooling in the United States?,* . Available: https://www.eia.gov/tools/faqs/faq.php?id=1174&t=1#:~:text=In%20the%20Annual%20Energy%20Outlook,about%2010%25%20of%20total%20U.S

[4] W. Azmi, M. Sharif, T. Yusof, R. Mamat, and A. Redhwan, "Potential of nanorefrigerant and nanolubricant on energy saving in refrigeration system–A review," *Renewable and Sustainable Energy Reviews,* vol. 69, pp. 415-428, 2017.

[5] Z. Tong, Y. Chen, A. Malkawi, Z. Liu, and R. B. Freeman, "Energy saving potential of natural ventilation in China: The impact of ambient air pollution," *Applied energy,* vol. 179, pp. 660-668, 2016.

[6] Z. Ma, J. Song, and J. Zhang, "Energy consumption prediction of air-conditioning systems in buildings by selecting similar days based on combined weights," *Energy and Buildings,* vol. 151, pp. 157-166, 2017.

[7] C. Francis, G. Maidment, and G. Davies, "An investigation of refrigerant leakage in commercial refrigeration," *International Journal of Refrigeration,* vol. 74, pp. 12-21, 2017.

[8] W. B. Gosney, "Principles of refrigeration," 1982.

[9] P. Bansal and A. Martin, "Comparative study of vapour compression, thermoelectric and absorption refrigerators," *International Journal of Energy Research,* vol. 24, no. 2, pp. 93-107, 2000.

[10] K. Liang, Z. Li, M. Chen, and H. J. A. T. E. Jiang, "Comparisons between heat pipe, thermoelectric system, and vapour compression refrigeration system for electronics cooling," *Applied Thermal Engineering,* vol. 146, pp. 260-267, 2019.

[11] J. S. Brown and P. A. Domanski, "Review of alternative cooling technologies," *Applied Thermal Engineering,* vol. 64, no. 1-2, pp. 252-262, 2014.

[12] O. Ekren, "Refrigeration System: Capacity Modulation Methods," *We Are IntechOpen, the World's Leading Publisher of Open Access Books Built by Scientists, for Scientists, IntechOpen, London, UK,* pp. 119-143, 2017.

[13] B. Li and A. G. Alleyne, "Optimal on-off control of an air conditioning and refrigeration system," in *Proceedings of the 2010 American Control Conference*, 2010, pp. 5892-5897: IEEE.

[14] G. Yan, Y. Liu, S. Qian, and J. Yu, "Theoretical study on a vapor compression refrigeration system with cold storage for freezer applications," *Applied Thermal Engineering,* vol. 160, p. 114091, 2019.

[15] H. Cho, Y. Kim, and I. Jang, "Performance of a showcase refrigeration system with multi-evaporator during on–off cycling and hot-gas bypass defrost," *Energy,* vol. 30, no. 10, pp. 1915-1930, 2005.

[16] M. Janssen, J. De Wit, and L. Kuijpers, "Cycling losses in domestic appliances: an experimental and theoretical analysis," *International Journal of Refrigeration,* vol. 15, no. 3, pp. 152-158, 1992.

[17] A. Jakobsen, *Energy optimisation of refrigeration systems: the domestic refrigerator-a case study*. Refrigeration Laboratory, The Technical University of Denmark, 1995.

[18] W. H. Coulter and C. W. Bullard, "An experimental analysis of cycling losses in domestic refrigerator-freezers," Air Conditioning and Refrigeration Center. College of Engineering …1995.

[19] E. Björk, "Energy efficiency improvements in household refrigeration cooling systems," KTH Royal Institute of Technology, 2012.

[20] B. J. Dechesne, F. M. Tello-Oquendo, S. Gendebien, and V. Lemort, "Residential air-source heat pump with refrigerant injection and variable speed compressor: Experimental investigation and compressor modeling," *International Journal of Refrigeration* vol. 108, pp. 79-90, 2019.

[21] O. Ekren, S. Sahin, and Y. J. I. J. o. R. Isler, "Comparison of different controllers for variable speed compressor and electronic expansion valve," *International Journal of Refrigeration,* vol. 33, no. 6, pp. 1161-1168, 2010.

[22] L. Chretien, R. Becerra, N. Salts, and E. Groll, "System solution to improve energy efficiency of HVAC systems," in *10th International Conference on Compressors and their Systems*, 2017.

[23] S. Tassou, "Experimental investigation of the dynamic performance of variable-speed heat pumps," *Journal of the Institute of Energy,* vol. 64, no. 459, pp. 95-98, 1991.

[24] S. Tassou, R. Green, D. Wilson, and M. Searle, "Energy Conservation Through the Use of Capacity Control in Heat Pumps," *Journal of the Institute of Energy,* vol. 54, no. 418, pp. 30-35, 1981.

[25] S. Tassou, C. t. Marquand, and D. Wilson, "Comparison of the performance of capacity controlled and conventional on/off controlled heat pumps," *Applied energy,* vol. 14, no. 4, pp. 241-256, 1983.

[26] K. B. Heo, C. W. Lee, G. Y. Song, and W. H. Jung, "Capacity modulation of linear compressor for household refrigerator," presented at the International Compressor Engineering Conference, 2004.

[27] H.-K. Lee, G. Song, J.-S. Park, E. Hong, W. Jung, and K. Park, "Development of the linear compressor for a household refrigerator," presented at the International Compressor Engineering Conference, 2000.

[28] F. De Rossi, A. Mauro, M. Musto, and G. P. Vanoli, "Long-period food storage household vertical freezer: Refrigerant charge influence on working conditions during steady operation," *International Journal of Refrigeration* vol. 34, no. 5, pp. 1305-1314, 2011.

[29] H. C. Kim, G. A. Keoleian, and Y. A. Horie, "Optimal household refrigerator replacement policy for life cycle energy, greenhouse gas emissions, and cost," *Energy Policy* vol. 34, no. 15, pp. 2310-2323, 2006.

[30] F. Poggi, H. Macchi-Tejeda, D. Leducq, and A. Bontemps, "Refrigerant charge in refrigerating systems and strategies of charge reduction," *International Journal of Refrigeration* vol. 31, no. 3, pp. 353-370, 2008.

[31] S. K. G. Shanmugam and M. Mital, "An ultra-low ammonia charge system for industrial refrigeration," *International Journal of Refrigeration* vol. 107, pp. 344-354, 2019.

[32] B. Palm, "Refrigeration systems with minimum charge of refrigerant," *Applied Thermal Engineering,* vol. 27, no. 10, pp. 1693-1701, 2007.

[33] P. Hrnjak and A. D. Litch, "Microchannel heat exchangers for charge minimization in air-cooled ammonia condensers and chillers," *International Journal of Refrigeration* vol. 31, no. 4, pp. 658-668, 2008.

[34] V. D. Baxter and D. H. Walker, "Analysis of Advanced, Low-Charge Refrigeration Systems for Supermarkets ".

[35] P. Hrnjak and X. Tu, "Single phase pressure drop in microchannels," *International Journal of Heat Fluid Flow* vol. 28, no. 1, pp. 2-14, 2007.

[36] S. Palaskar and V. W. Khond, "Review on Performance of Different Micro-channel Condensers," *International Journal of Innovations in Engineering and Science,* vol. 2, no. 5, p. 5, 2017.

[37] E. Dollera and E. Villanueva, "A Study of the Heat Transfer Coefficient of a Mini Channel Evaporator with R-134a as Refrigerant," in *IOP Conference Series. Materials Science and Engineering (Online)*, 2015, vol. 88, no. 1.

[38] Z. Qi, J. Chen, and R. Radermacher, "Investigating performance of new mini-channel evaporators," *Applied Thermal Engineering,* vol. 29, no. 17-18, pp. 3561-3567, 2009.

[39] Y.-Y. Yan and T.-F. Lin, "Evaporation heat transfer and pressure drop of refrigerant R-134a in a small pipe," *International Journal of Heat Mass Transfer,* vol. 41, no. 24, pp. 4183-4194, 1998.

[40] B. Agostini and A. Bontemps, "Vertical flow boiling of refrigerant R134a in small channels," *International Journal of Heat Fluid Flow* vol. 26, no. 2, pp. 296-306, 2005.

[41] B. Kwon, N. I. Maniscalco, A. M. Jacobi, and W. P. King, "High power density air-cooled microchannel heat exchanger," *International Journal of Heat Mass Transfer* vol. 118, pp. 1276-1283, 2018.

[42] N. A. Qasem and S. M. Zubair, "Compact and microchannel heat exchangers: A comprehensive review of air-side friction factor and heat transfer correlations," *Energy Conversion Management,* vol. 173, pp. 555-601, 2018.

[43] Y.-G. Park and A. M. Jacobi, "Air-side heat transfer and friction correlations for flat-tube louver-fin heat exchangers," *Journal of Heat Transfer,* vol. 131, no. 2, 2009.

[44] D. Junqi, C. Jiangping, C. Zhijiu, Z. Yimin, and Z. Wenfeng, "Heat transfer and pressure drop correlations for the wavy fin and flat tube heat exchangers," *Applied Thermal Engineering,* vol. 27, no. 11-12, pp. 2066-2073, 2007.

[45] J. Deng, "Improved correlations of the thermal-hydraulic performance of large size multi-louvered fin arrays for condensers of high power electronic component cooling by numerical simulation," *Energy Conversion Management,* vol. 153, pp. 504-514, 2017.

[46] M. K. Aliabadi, F. Hormozi, and E. H. Rad, "New correlations for wavy plate-fin heat exchangers: different working fluids," *International Journal of Numerical Methods for Heat Fluid Flow,* 2014.

[47] C.-C. Wang, A. Hafner, C.-S. Kuo, and W.-D. Hsieh, "Influence of lubricant on the nucleate boiling heat transfer performance of refrigerant—a review," *Heat Transfer Engineering,* vol. 35, no. 6-8, pp. 651-663, 2014.

[48] L. Cremaschi, L. Molinaroli, and C. Andres, "Experimental analysis and modeling of lubricant effects in microchannel evaporators working with low global warming potential refrigerants," *Science Technology for the Built Environment,* vol. 22, no. 8, pp. 1104-1117, 2016.

[49] O. Lottin, P. Guillemet, and J.-M. Lebreton, "Effects of synthetic oil in a compression refrigeration system using R410A. Part I: modelling of the whole system and analysis of its response to an increase in the amount of circulating oil," *International Journal of Refrigeration,* vol. 26, no. 7, pp. 772-782, 2003.

[50] M. Youbi-Idrissi and J. Bonjour, "The effect of oil in refrigeration: Current research issues and critical review of thermodynamic aspects," *International Journal of Refrigeration,* vol. 31, no. 2, pp. 165-179, 2008.

[51] P. Popovic, "Investigation and analysis of lubricant effects on the performance of an HFC-134a refrigeration system," Iowa State University, 1999.

[52] V. Geller and N. Lapardin, "Solubility and miscibility of refrigerants R407C and R410A with synthetic compressor oils," *Refrigeration Engineering Technology,* vol. 52, no. 3, 2016.

[53] R. Tuomas, "Properties of oil and refrigerant mixtures: lubrication of ball bearings in refrigeration compressors," Luleå tekniska universitet, 2006.

[54] Y. Zou, H. Li, and P. Hrnjak, "Lubricant impact on R134a distribution and microchannel heat exchanger performance," SAE Technical Paper0148-7191, 2014.

[55] L. Cremaschi, A. S. Yatim, and S. K. Mulugurthi, "Experimental study of oil retention in microchannel type evaporators of air-source heat pump systems," *International Journal of Refrigeration,* vol. 91, pp. 158-166, 2018.

[56] G. Kuang, M. Ohadi, and Y. Zhao, "Experimental study of miscible and immiscible oil effects on heat transfer coefficients and pressure drop in microchannel gas cooling of supercritical CO2," in *Heat Transfer Summer Conference*, 2003, vol. 36940, pp. 671-675.

[57] M. Lissandrin, M. Rampazzo, L. Cecchinato, and A. Beghi, "Optimal operational efficiency of chillers using oil-free centrifugal compressors," *International Journal of Refrigeration,* vol. 82, pp. 83-96, 2017.

[58] A. Pearson, "R-1234ze for variable speed centrifugal chillers," *Proc. Institute of Refrigeration, session,* vol. 13, p. 2013, 2012.

[59] F. W. Yu, K. T. Chan, and R. K. Y. Sit, "Analysis of centrifugal chillers with oil-free magnetic bearings for enhancing building energy performance," *Science Technology for the Built Environment,* vol. 23, no. 2, pp. 334-344, 2017.

[60] J. Deng, Q. Wei, Y. Qian, and H. Zhang, "Does magnetic bearing variable-speed centrifugal chiller perform truly energy efficient in buildings: Field-test and simulation results," *Applied Energy,* vol. 229, pp. 998-1009, 2018.

[61] T. Yanagisawa, M. Fukuta, Y. Ogi, and T. Hikichi, "Performance of an oil-free scroll-type air expander," in *Proc. of the ImechE Conf. Trans. on compressors and their systems*, 2001, no. C591/027, pp. 167-174.

[62] L. Wang, Y. Zhao, L. Li, G. Bu, and P. Shu, "Research on oil-free hermetic refrigeration scroll compressor," *Proceedings of the Institution of Mechanical Engineers, Part A: Journal of Power Energy,* vol. 221, no. 7, pp. 1049-1056, 2007.

[63] B. Peng, S. Zhao, and Y. Li, "Thermodynamic Model and Experimental Study of Oil-free Scroll Compressor," in *J. Phys. Conf. Ser*, 2017, vol. 916, p. 012048.

[64] P. Bin, A. Legros, V. Lemort, X. Xiaozheng, and G. Haifeng, "Recent Advances on the oil-free Scroll Compressor," *Recent Patents on Mechanical Engineering,* vol. 9, no. 1, pp. 37-47, 2016.

[65] Y. Tian, H. Yuan, C. Wang, H. Wu, and Z. Xing, "Numerical investigation on mass and heat transfer in an ammonia oil-free twin-screw compressor with liquid injection," *International Journal of Thermal Sciences,* vol. 120, pp. 175-184, 2017.

[66] O. Dmitriev and I. M. Arbon, "Comparison of energy-efficiency and size of portable oil-free screw and scroll compressors," in *IOP Conference Series: Materials Science and Engineering*, 2017, vol. 232, no. 1, p. 012057: IOP Publishing.

[67] Z. Tang, T. Wang, B. Zhao, M. Wang, and X. Peng, "Modelling the Cylinder Cooling in an Oil-free Reciprocating Air Compressor," in *IOP Conference Series: Materials Science and Engineering*, 2019, vol. 604, no. 1, p. 012024: IOP Publishing.

[68] P. Bansal, E. Vineyard, and O. Abdelaziz, "Advances in household appliances-A review," *Applied Thermal Engineering,* vol. 31, no. 17-18, pp. 3748-3760, 2011.

[69] (2015, 7th September). *EU legislation to control F-gases*. Available: https://ec.europa.eu/clima/policies/f-gas/legislation_en

[70] E. W. Lemmon, M. L. Huber, and M. O. McLinden, "NIST reference fluid thermodynamic and transport properties–REFPROP," ed: Version, 2002.

[71] C. Kondou, F. Mishima, J. Liu, and S. Koyama, "Condensation and evaporation of R134a, R1234ze (E) and R1234ze (Z) flow in horizontal microfin tubes at higher temperature," presented at the International Refrigeration and Air Conditioning Conference, 2014.

[72] J. K. Vaghela, "Comparative evaluation of an automobile air-conditioning system using R134a and its alternative refrigerants," *Energy Procedia,* vol. 109, pp. 153-160, 2017.

[73] Ashrae., *2005 ASHRAE Handbook: Fundamentals*. ASHRAE, 2005.

[74] M. M. Joybari, M. S. Hatamipour, A. Rahimi, and F. G. Modarres, "Exergy analysis and optimization of R600a as a replacement of R134a in a domestic refrigerator system," *International Journal of Refrigeration,* vol. 36, no. 4, pp. 1233-1242, 2013.

[75] Y. Lee and C. Su, "Experimental studies of isobutane (R600a) as the refrigerant in domestic refrigeration system," *Applied Thermal Engineering,* vol. 22, no. 5, pp. 507-519, 2002.

[76] E. Hihara, "Risk assessment of mildly flammable refrigerants," *Graduate School of Frontier Sciences, The University of Tokyo,* pp. 1-8, 2012.

[77] J. M. Calm, "The next generation of refrigerants–Historical review, considerations, and outlook," *International Journal of Refrigeration,* vol. 31, no. 7, pp. 1123-1133, 2008.

[78] M. Feidt, A. Kheiri, and S. Pelloux-Prayer, "Performance optimization of low-temperature power generation by supercritical ORCs (organic Rankine cycles) using low GWP (global warming potential) working fluids," *Energy,* vol. 67, pp. 513-526, 2014.

[79] B. Palm, "Hydrocarbons as refrigerants in small heat pump and refrigeration systems–a review," *International Journal of Refrigeration,* vol. 31, no. 4, pp. 552-563, 2008.

[80] R. K. Gond, R. P. Chaudhary, M. A. Khan, and G. Jain, "Performance and exergy analysis of vapour compression refrigeration system using various alternative of R134a," *International Research Journal of Engineering Technology,* vol. 3, no. 5, pp. 187-193, 2016.

[81] S. Gupta, N. K. Karanam, R. Konijeti, and A. Dasore, "Thermodynamic analysis and effects of replacing HFC by fourth-generation refrigerants in VCR systems," *International Journal of Air-Conditioning Refrigeration,* vol. 26, no. 02, p. 1850013, 2018.

[82] M.-H. Yang and R.-H. Yeh, "Thermo-economic optimization of an organic Rankine cycle system for large marine diesel engine waste heat recovery," *Energy,* vol. 82, pp. 256-268, 2015.

[83] B. O. Bolaji, Z. Huan, and F. O. Borokinni, "Energy Performance of Eco-friendly R152a and R600a Refrigerants as Alternative to R134a in Vapour Compression Refrigeration System," *Mechanical Journal Publications,* vol. 3, pp. 354-367, 2014.

[84] C. H. de Paula, W. M. Duarte, T. T. M. Rocha, R. N. de Oliveira, R. de Paoli Mendes, and A. A. T. Maia, "Thermo-economic and environmental analysis of a small capacity vapor compression refrigeration system using R290, R1234yf, and R600a," *International Journal of Refrigeration,* vol. 118, pp. 250-260, 2020.

[85] A. Hamza and T. A. Khan, "Comparative Performance of Low-GWP Refrigerants as Substitutes for R134a in a Vapor Compression Refrigeration System," *Arabian Journal for Science Engineering,* pp. 1-16, 2020.

[86] D. Sánchez, R. Cabello, R. Llopis, I. Arauzo, J. Catalán-Gil, and E. Torrella, "Energy performance evaluation of R1234yf, R1234ze (E), R600a, R290 and R152a as low-GWP R134a alternatives," *International Journal of Refrigeration,* vol. 74, pp. 269-282, 2017.

[87] J. Navarro-Esbrí, J. M. Mendoza-Miranda, A. Mota-Babiloni, A. Barragán-Cervera, and J. M. Belman-Flores, "Experimental analysis of R1234yf as a drop-in replacement for R134a in a vapor compression system," *International Journal of Refrigeration,* vol. 36, no. 3, pp. 870-880, 2013.

[88] Y. Lee and D. Jung, "A brief performance comparison of R1234yf and R134a in a bench tester for automobile applications," *Applied Thermal Engineering,* vol. 35, pp. 240-242, 2012.

[89] R. Cabello, D. Sánchez, R. Llopis, I. Arauzo, and E. Torrella, "Experimental comparison between R152a and R134a working in a refrigeration facility equipped with a hermetic compressor," *International Journal of Refrigeration,* vol. 60, pp. 92-105, 2015.

[90] A. Jakobsen, B. D. Rasmussen, and S. E. J. S. R. Andersen, "CoolPack–Simulation tools for refrigeration systems," vol. 28, no. 4, pp. 7-10, 1999.

[91] Y. Kwak, S. Hwang, and J. H. Jeong, "Effect of part load operating conditions of an air conditioner on the number of refrigerant paths and heat transfer performance of a condenser," *Energy Conversion Management,* vol. 203, p. 112257, 2020.

[92] Z. Lei and Zaheeruddin, "Dynamic simulation and analysis of a water chiller refrigeration system," *Applied Thermal Engineering,* vol. 25, no. 14-15, pp. 2258-2271, 2005.

[93] Y. Yao, W. Wang, and M. Huang, "A state-space dynamic model for vapor compression refrigeration system based on moving-boundary formulation," *International Journal of Refrigeration,* vol. 60, pp. 174-189, 2015.

[94] A. Polzot, P. D'Agaro, P. Gullo, and G. J. I. J. o. R. Cortella, "Modelling commercial refrigeration systems coupled with water storage to improve energy efficiency and perform heat recovery," *International Journal of Refrigeration,* vol. 69, pp. 313-323, 2016.

[95] N. Vjacheslav, A. Rozhentsev, and C.-C. Wang, "Rationally based model for evaluating the optimal refrigerant mass charge in refrigerating machines," *Energy Conversion Management,* vol. 42, no. 18, pp. 2083-2095, 2001.

[96] N. Liu, X.-L. Lai, K. Yan, and H. Zhang, "Investigation of flow and heat transfer characteristics on different heat exchangers of air conditioner," *Applied Thermal Engineering,* vol. 103, pp. 428-433, 2016.

[97] R. Ghoubali, P. Byrne, and F. Bazantay, "Refrigerant charge optimisation for propane heat pump water heaters," *International Journal of Refrigeration,* vol. 76, pp. 230-244, 2017.

[98] G. D. E. E. R. V. L. A. M. S. J. H. P. Vázquez, "TransientAnalysis of a Single-stage Vapor CompressionRefrigeration SystemUsing Lumped Parameter Approaches," *International Journalon Advances in Systems and Measurements,* vol. 11, no. 4, p. 11, 2018.

[99] R. Roy, M. S. Emani, and B. K. Mandal, "Numerical Simulation of Vapour Compression Refrigeration System Using Refrigerant R152a R404A and R600a," *Indian J. Sci. Res,* vol. 15, no. 2, pp. 62-67, 2017.

[100] R. Siddharth, K. Jagannath, P. K. Giridhar, and K. K. Vishnumurthy, "Design and Simulation of a Vapour Compression Refrigeration System Using Phase Change Material," in *MATEC Web of Conferences*, 2018, vol. 144, p. 04002: EDP Sciences.

[101] D. Nasution, A. Siregar, and F. Bukit, "Modelling a simple-vapour compression refrigeration cycle for Fish-Storage boxes," in *Journal of Physics: Conference Series*, 2020, vol. 1542, no. 1, p. 012066: IOP Publishing.

[102] S. D. Jackson, "Control Strategies for Multi-Evaporator Vapor Compression Cycles," 2019.

[103] L. C. Schurt, C. J. Hermes, and A. T. Neto, "A model-driven multivariable controller for vapor compression refrigeration systems," *International Journal of Refrigeration,* vol. 32, no. 7, pp. 1672-1682, 2009.

[104] S. M. Zubair, "Design and rating of an integrated mechanical-subcooling vapor-compression refrigeration system," *Energy Conversion Management,* vol. 41, no. 11, pp. 1201-1222, 2000.

[105] B. P. Rasmussen and A. G. Alleyne, "Dynamic modeling and advanced control of air conditioning and refrigeration systems," Air Conditioning and Refrigeration Center. College of Engineering …2006.

[106] A. Pisano, S. Martínez-Ballester, J. M. Corberán, and A. W. Mauro, "Optimal design of a light commercial freezer through the analysis of the combined effects of capillary tube diameter and refrigerant charge on the performance," *International Journal of Refrigeration,* vol. 52, pp. 1-10, 2015.

[107] L. A. Tagliafico, F. Scarpa, and G. Tagliafico, "A compact dynamic model for household vapor compression refrigerated systems," *Applied Thermal Engineering,* vol. 35, pp. 1-8, 2012.

[108] K. Brun and R. Kurz, *Compression Machinery for Oil and Gas*. Gulf Professional Publishing, 2018.

[109] K. Park, E. Hong, and H. Lee, "Linear motor for linear compressor," presented at the International Compressor Engineering Conference, 2002.

[110] B. Ku, J. Park, Y. Hwang, and J. Lee, "Performance evaluation of the energy efficiency of crank-driven compressor and linear compressor for a household refrigerator," presented at the International Compressor Engineering Conference, 2010.

[111] K. Liang, R. Stone, W. Hancock, M. Dadd, and P. Bailey, "Comparison between a crank-drive reciprocating compressor and a novel oil-free linear compressor," *International Journal of Refrigeration,* vol. 45, pp. 25-34, 2014.

[112] H. Lee, S. Ki, S. Jung, and W. Rhee, "The innovative green technology for refrigerators development of innovative linear compressor," presented at the nternational Compressor Engineering Conference, 2008.

[113] C. R. Bradshaw, E. A. Groll, and S. V. Garimella, "Linear compressors for electronics cooling: Energy recovery and its benefits," *International Journal of Refrigeration,* vol. 36, no. 7, pp. 2007-2013, 2013.

[114] C. R. Bradshaw, E. A. Groll, and S. V. Garimella, "A comprehensive model of a miniature-scale linear compressor for electronics cooling," *International Journal of Refrigeration,* vol. 34, no. 1, pp. 63-73, 2011.

[115] M. Lamantia, A. Contarini, and S. Giovanni, "Numerical and experimental analysis of a linear compressor," presented at the International Compressor Engineering Conference, 2002.

[116] K. Liang, "A review of linear compressors for refrigeration," *International Journal of Refrigeration,* vol. 84, pp. 253-273, 2017.

[117] X. Zhang, D. Ziviani, J. E. Braun, and E. A. Groll, "Experimental Analysis of an Oil-Free Linear Compressor for a Domestic Refrigerator," presented at the International Conference on Compressor and Refrigeration, 2019.

[118] H. Lee, S. Ki, S. Jung, and W. Rhee, "The innovative green technology for refrigerators development of innovative linear compressor," presented at the International Compressor Engineering Conference, 2008.

[119] H. Lee, S. S. Jeong, C. W. Lee, and H. K. Lee, "Linear compressor for air-conditioner," presented at the International Compressor Engineering Conference, 2004.

[120] R. Unger, "Development and testing of a linear compressor sized for the european market," in *Proceedings International Appliance Technical Conference*, 1999, pp. 74-79.

[121] M. A. Alzoubi and T. Zhang, "Characterization of energy efficient vapor compression cycle prototype with a linear compressor," *Energy Procedia,* vol. 75, pp. 3253-3258, 2015.

[122] H. Hasegawa, A. Okaichi, H. Shintaku, M. Ikoma, and F. Nishiwaki, "A study of a linear compressor with a gas spring," presented at the International Compressor Engineering Conference, 2002.

[123] H. Zou, X. Li, M. Tang, C. Tian, and X. Chen, "Performance analysis of linear compressor using R290 for commercial refrigerator," *International Journal of Refrigeration,* vol. 109, pp. 55-63, 2020.

[124] X. Zhang, D. Ziviani, J. E. Braun, and E. A. Groll, "Experimental Analysis of an Oil-Free Linear Compressor for a Domestic Refrigerator," presented at the International Compressor Engineering Conference, 2019.

[125] A. Jomde *et al.*, "Modeling and measurement of a moving coil oil-free linear compressor performance for refrigeration application using R134a," *International Journal of Refrigeration,* vol. 88, pp. 182-194, 2018.

[126] A. Bijanzad, A. Hassan, and I. Lazoglu, "Analysis of solenoid based linear compressor for household refrigerator," *International Journal of Refrigeration,* vol. 74, pp. 116-128, 2017.

[127] F. Possamai, D. E. Lilie, A. J. Zimmermann, and R. Mongia, "Miniature vapor compression system," presented at the International Compressor Engineering Conference, 2008.

[128] R. Mongia *et al.*, "Small scale refrigeration system for electronics cooling within a notebook computer," in *Thermal and Thermomechanical Proceedings 10th Intersociety Conference on Phenomena in Electronics Systems, 2006. ITHERM 2006.*, 2006, pp. 751-758: IEEE.

[129] K. Liang, R. Stone, M. Dadd, and P. Bailey, "A novel linear electromagnetic-drive oil-free refrigeration compressor using R134a," *International Journal of Refrigeration,* vol. 40, pp. 450-459, 2014.

[130] Z. Zhang, K. Cheng, and X. Xue, "Study on the performance and control of linear compressor for household refrigerators," in *2013 5th International Conference on Power Electronics Systems and Applications (PESA)*, 2013, pp. 1-4: IEEE.

[131] H. Zou, S. Shao, M. Tang, L. Zhang, and G. Peng, "Performance investigation of linear compressor with one side springs," presented at the nternational Compressor Engineering Conference, 2012.

[132] G.-s. Choe and K.-J. Kim, "Analysis of nonlinear dynamics in a linear compressor," *International Journal Series C Mechanical Systems, Machine Elements Manufacturing,* vol. 43, no. 3, pp. 545-552, 2000.

[133] K. Liang, R. Stone, M. Dadd, and P. Bailey, "The effect of clearance control on the performance of an oil-free linear refrigeration compressor and a comparison between using a bleed flow and a DC current bias," *International Journal of Refrigeration,* vol. 69, pp. 407-417, 2016.

[134] H. Jiang, Z. Li, and K. Liang, "A Novel Sensor-less Stroke Detection Technique using Low-cost Inductive Coil for Resonant Free-Piston Machines," *IEEE Transactions on Industrial Electronics,* 2020.

[135] K. Liang, R. Stone, M. Dadd, and P. Bailey, "Piston position sensing and control in a linear compressor using a search coil," *International Journal of Refrigeration,* vol. 66, pp. 32-40, 2016.

[136] K. Liang, M. Dadd, and P. Bailey, "Clearance seal compressors with linear motor drives. Part 1: Background and system analysis," *Proceedings of the Institution of Mechanical Engineers, Part A: Journal of Power Energy,* vol. 227, no. 3, pp. 242-251, 2013.

[137] K. Liang, "A novel linear electromagnetic-drive oil-free refrigeration compressor," University of Oxford, 2014.

[138] B. Huang and Y. Chen, "System dynamics and control of a linear compressor for stroke and frequency adjustment," *Journal of Dynamic Systems, Measurement, and Control,* vol. 124, no. 1, pp. 176-182, 2002.

[139] K. B. Park, E. P. Hong, K. C. Choi, and W. H. Jung, "Linear compressor without position controller," presented at the International Compressor Engineering Conference, 2004.

[140] Y.-P. Yang and B.-J. Huang, "Fuzzy control on the phase and stroke of a linear compressor of a split-Stirling cryocooler," *Cryogenics,* vol. 38, no. 2, pp. 231-238, 1998.

[141] X. You, L. Qiu, C. Duan, X. Jiang, C. Huang, and X. Zhi, "Study on the stroke amplitude of the linear compressor," *Applied Thermal Engineering,* vol. 129, pp. 1488-1495, 2018.

[142] J. K. Kim and J. H. Jeong, "Performance characteristics of a capacity-modulated linear compressor for home refrigerators," *International Journal of Refrigeration,* vol. 36, no. 3, pp. 776-785, 2013.

[143] A. Jomde, A. Anderson, V. Bhojwani, P. Shinde, S. Deshmukh, and S. Phadkule, "Resonance Analysis of Valved Linear Compressor for Refrigeration Application," *Journal of Engineering Applied Science,* vol. 11, pp. 13810-13814, 2016.

[144] H. Dang, L. Zhang, and J. Tan, "Dynamic and thermodynamic characteristics of the moving-coil linear compressor for the pulse tube cryocooler. Part A: Theoretical analyses and modeling," *International Journal of Refrigeration,* vol. 69, pp. 480-496, 2016.

[145] P. S. Dainez, J. de Oliveira, and A. Nied, "An adaptive resonant controller applied to a linear resonant compressor," *International Journal of Refrigeration,* vol. 104, pp. 521-529, 2019.

[146] M. Xia and X. Chen, "Analysis of resonant frequency of moving magnet linear compressor of stirling cryocooler," *International Journal of Refrigeration,* vol. 33, no. 4, pp. 739-744, 2010.

[147] H. Kim, C.-g. Roh, J.-k. Kim, J.-m. Shin, Y. Hwang, and J.-k. J. I. j. o. r. Lee, "An experimental and numerical study on dynamic characteristic of linear compressor in refrigeration system," *International Journal of Refrigeration,* vol. 32, no. 7, pp. 1536-1543, 2009.

[148] H. Jiang, K. Liang, and Z. Li, "Characteristics of a novel moving magnet linear motor for linear compressor," *Mechanical Systems Signal Processing,* vol. 121, pp. 828-840, 2019.

[149] G. F. Davies *et al.*, "Cooling microprocessors using vapor compression refrigeration," in *2010 12th IEEE Intersociety Conference on Thermal and Thermomechanical Phenomena in Electronic Systems*, 2010, pp. 1-8: IEEE.

[150] N. Chen, Y. Tang, Y. Wu, X. Chen, and L. Xu, "Study on static and dynamic characteristics of moving magnet linear compressors," *Cryogenics,* vol. 47, no. 9-10, pp. 457-467, 2007.

[151] M. Park, J. Lee, H. Kim, and Y. Ahn, "Experimental and numerical study of heat transfer characteristics using the heat balance in a linear compressor," *International Journal of Refrigeration,* vol. 74, pp. 550-559, 2017.

[152] M. Alzoubi, G. Li, and T. Zhang, "First-principle dynamic modeling of a linear micro-compressor," in *ASME International Mechanical Engineering Congress and Exposition*, 2013, vol. 56291, p. V06BT07A012: American Society of Mechanical Engineers.

[153] M. Oliveira, M. Diniz, and C. Deschamps, "Thermal modelling and analysis of an oil-free linear compressor," in *IOP Conference Series: Materials Science and Engineering*, 2015, vol. 90, no. 1, p. 012016: IOP Publishing.

[154] F. P. Disconzi, C. J. Deschamps, and E. L. Pereira, "Development of an in-cylinder heat transfer correlation for reciprocating compressors," presented at the International Compressor Engineering Conference, 2012.

[155] J. Tuhovcák and M. Jícha, "Heat transfer analysis in the cylinder of reciprocating compressor," presented at the International Compressor Engineering Conference, 2016.

[156] I. S. Hwang and Y. L. Lee, "CFD analysis of transient flows in a linear compressor using a 1D-CFD coupled model," *International Journal of Refrigeration,* vol. 91, pp. 20-27, 2018.

[157] (2020, 8th December). *Thermocouple Selection Guide*. Available: https://docs.rs-online.com/96d5/0900766b815e5302.pdf

[158] (2020, 1st August). *Gas Correction Factors for Thermal-based Mass Flow*. Available: https://www.mksinst.com/n/gas-correction-factors-for-thermal-based-mass-flow-controllers

[159] (2020, 1st August). *Flow Measurement & Control Frequently Asked Questions*. Available: https://www.mksinst.com/n/flow-measurement-control-frequently-asked-questions

[160] (2020, 1st August). *300 Gas Table*. Available: http://www.teledyne-hi.com/resourcecenter/Documents/Gas%20Conversion%20Factors%20for%20300%20Series.pdf#search=gas%20factor

[161] H. Jiang, K. Liang, and Z. Li, "Characteristics of a novel moving magnet linear motor for linear compressor," *Mechanical Systems and Signal Processing,* vol. 121, pp. 828-840, 2019.

[162] K. Liang, M. Dadd, and P. Bailey, "Clearance seal compressors with linear motor drives. Part 2: Experimental evaluation of an oil-free compressor," *Proceedings*

of the Institution of Mechanical Engineers, Part A: Journal of Power and Energy, vol. 227, no. 3, pp. 252-260, 2013.

[163] K. Manske, D. Reindl, and S. Klein, "Evaporative condenser control in industrial refrigeration systems," *International Journal of Refrigeration,* vol. 24, no. 7, pp. 676-691, 2001.

[164] (2018, 8th September). *The potential to improve the energy efficiency of refrigeration, air-conditioning and heat pumps*

[165] (8th September). *New Generation CS.3 Compact Screw Compressors: Improved energy efficiency at full and part load operation*.

[166] K. Liang, "Analysis of oil-free linear compressor operated at high pressure ratios for household refrigeration," *Energy,* vol. 151, pp. 324-331, 2018.

[167] (2017, 26th September). *Thermophysical Properties of Fluid Systems*. Available: https://webbook.nist.gov/chemistry/fluid/

[168] Z. Meng, H. Zhang, J. Qiu, and M. Lei, "Theoretical analysis of R1234ze (E), R152a, and R1234ze (E)/R152a mixtures as replacements of R134a in vapor compression system," *Advances in Mechanical Engineering,* vol. 8, no. 11, p. 1687814016676945, 2016.

[169] A. Sethi, E. V. Becerra, and S. Y. Motta, "Low GWP R134a replacements for small refrigeration (plug-in) applications," *International Journal of Refrigeration,* vol. 66, pp. 64-72, 2016.

[170] J. M. Belman-Flores, A. Rodríguez-Muñoz, C. G. Pérez-Reguera, and A. Mota-Babiloni, "Experimental study of R1234yf as a drop-in replacement for R134a in a domestic refrigerator," *International Journal of Refrigeration,* vol. 81, pp. 1-11, 2017.

[171] S. Wongwises and M. Polsongkram, "Evaporation heat transfer and pressure drop of HFC-134a in a helically coiled concentric tube-in-tube heat exchanger," *International Journal of Heat and Mass Transfer,* vol. 49, no. 3-4, pp. 658-670, 2006.

[172] X. Li and T. Hibiki, "Frictional pressure drop correlation for two-phase flows in mini and micro single-channels," *International Journal of Multiphase Flow,* vol. 90, pp. 29-45, 2017.

[173] K. R. Dione, H. Louahlia, M. Marion, and J. Berçaits, "Evaporation heat transfer and pressure drop for geothermal heat pumps working with refrigerants R134a and R407C," *International Communications in Heat and Mass Transfer,* vol. 93, pp. 1-10, 2018.

[174] S. Laohalertdecha, A. S. Dalkilic, and S. Wongwises, "Correlations for evaporation heat transfer coefficient and two-phase friction factor for R-134a flowing through horizontal corrugated tubes," *International Communications in Heat and Mass Transfer,* vol. 38, no. 10, pp. 1406-1413, 2011.

[175] J. Zhang, A. Desideri, M. R. Kærn, T. S. Ommen, J. Wronski, and F. Haglind, "Flow boiling heat transfer and pressure drop characteristics of R134a, R1234yf

and R1234ze in a plate heat exchanger for organic Rankine cycle units," *International Journal of Heat and Mass Transfer,* vol. 108, pp. 1787-1801, 2017.

[176] N. Liu, J. M. Li, J. Sun, and H. S. Wang, "Heat transfer and pressure drop during condensation of R152a in circular and square microchannels," *Experimental Thermal and Fluid Science,* vol. 47, pp. 60-67, 2013.

[177] M. Hirose, J. Ichinose, and N. Inoue, "Development of the general correlation for condensation heat transfer and pressure drop inside horizontal 4 mm small-diameter smooth and microfin tubes," *International Journal of Refrigeration,* vol. 90, pp. 238-248, 2018.

[178] A. Foust and G. Christian, "Non-boiling heat transfer coefficients in annuli," *American Institute of Chemical Engineers,* vol. 36, pp. 541-554, 1940.

[179] H. J. Lee and S. Y. Lee, "Pressure drop correlations for two-phase flow within horizontal rectangular channels with small heights," *International Journal of Multiphase Flow,* vol. 27, no. 5, pp. 783-796, 2001.

[180] C. Rice, "The effect of void fraction correlation and heat flux assumption on refrigerant charge inventory predictions," *ASHRAE transactions,* vol. 93, no. 1, pp. 341-367, 1987.

[181] J. Dirker and J. Meyer, "Convective heat transfer coefficients in concentric annuli," *Heat Transfer Engineering,* vol. 26, no. 2, pp. 38-44, 2005.

[182] E. S. Davis, "Heat transfer and pressure drop in annuli," *Trans. Asme,* vol. 65, p. 755, 1943.

[183] Y.-Y. Yan and T.-F. Lin, "Evaporation heat transfer and pressure drop of refrigerant R-134a in a small pipe," *International Journal of Heat and Mass Transfer,* vol. 41, no. 24, pp. 4183-4194, 1998.

[184] J. M. Quibén and J. R. Thome, "Flow pattern based two-phase frictional pressure drop model for horizontal tubes, Part II: New phenomenological model," *International Journal of Heat and Fluid Flow,* vol. 28, no. 5, pp. 1060-1072, 2007.

[185] A. S. Pamitran, K.-I. Choi, J.-T. Oh, and P. Hrnjak, "Characteristics of two-phase flow pattern transitions and pressure drop of five refrigerants in horizontal circular small tubes," *International Journal of Refrigeration,* vol. 33, no. 3, pp. 578-588, 2010.

[186] D. F. Sempértegui-Tapia and G. Ribatski, "Two-phase frictional pressure drop in horizontal micro-scale channels: experimental data analysis and prediction method development," *International Journal of Refrigeration,* vol. 79, pp. 143-163, 2017.

[187] G. Lee and J. Yoo, "Performance analysis and simulation of automobile air conditioning system," *International Journal of Refrigeration,* vol. 23, no. 3, pp. 243-254, 2000.

[188] M. Deymi-Dashtebayaz, M. Farahnak, M. Moraffa, A. Ghalami, and N. Mohammadi, "Experimental evaluation of refrigerant mass charge and ambient air temperature effects on performance of air-conditioning systems," *Heat and Mass Transfer,* vol. 54, no. 3, pp. 803-812, 2018.

[189] N. Vjacheslav, A. Rozhentsev, and C.-C. Wang, "Rationally based model for evaluating the optimal refrigerant mass charge in refrigerating machines," *Energy Conversion and Management,* vol. 42, no. 18, pp. 2083-2095, 2001.

[190] H. Macchi, J. Guilpart, and A. Mahungu, "Reduction de charge: comparaison entre detente directe, recirculation et réfrigération indirecte," *Journée Française du Froid–Interclima,* pp. 47-63, 1999.

[191] F. Poggi, H. Macchi-Tejeda, D. Leducq, and A. Bontemps, "Refrigerant charge in refrigerating systems and strategies of charge reduction," *International Journal of Refrigeration,* vol. 31, no. 3, pp. 353-370, 2008.

[192] M. Youbi-Idrissi, J. Bonjour, C. Marvillet, and F. Meunier, "Impact of refrigerant–oil solubility on an evaporator performances working with R-407C," *International Journal of Refrigeration,* vol. 26, no. 3, pp. 284-292, 2003.

[193] E. Björk and B. Palm, "Refrigerant mass charge distribution in a domestic refrigerator. Part II: steady state conditions," *Applied Thermal Engineering,* vol. 26, no. 8-9, pp. 866-871, 2006.

[194] G. Pottker and P. Hrnjak, "Effect of the condenser subcooling on the performance of vapor compression systems," *International Journal of Refrigeration,* vol. 50, pp. 156-164, 2015.

[195] (2013, 5th August). *Reference Fluid Thermodynamic and Transport Properties Database (REFPROP)*. Available: https://www.nist.gov/srd/refprop

[196] S. J. Park, I. S. Hwang, W. S. Oh, Y. L. J. J. o. M. S. Lee, and Technology, "A study on cycle performance variation of a linear compressor considering valve behavior," *Journal of Mechanical Science,* vol. 31, no. 9, pp. 4481-4488, 2017.

[197] J.-H. Kim and E. A. J. I. j. o. r. Groll, "Feasibility study of a bowtie compressor with novel capacity modulation," *International Journal of Refrigeration,* vol. 30, no. 8, pp. 1427-1438, 2007.

[198] K. Liang, R. Stone, G. Davies, M. Dadd, and P. Bailey, "Modelling and measurement of a moving magnet linear compressor performance," *Energy,* vol. 66, pp. 487-495, 2014.

[199] F. Fagotti and A. T. Prata, "A new correlation for instantaneous heat transfer between gas and cylinder in reciprocating compressors," presented at the International Compressor Engineering Conference, West Lafayette, 1998.

[200] J. I. Chowdhury, B. K. Nguyen, and D. Thornhill, "Modelling of evaporator in waste heat recovery system using finite volume method and fuzzy technique," *Energies,* vol. 8, no. 12, pp. 14078-14097, 2015.

[201] J. Bonilla, S. Dormido, and F. E. Cellier, "Switching moving boundary models for two-phase flow evaporators and condensers," *Communications in Nonlinear Science Numerical Simulation,* vol. 20, no. 3, pp. 743-768, 2015.

Appendix A Mass Flow Meter Calibration

Main flow rate and bleed flow rate were measured by Hastings HFM-201 and Tylan FM-360, respectively. Referring to MKS **[159]**, the gas correction factors (GCF) for R134a and R1234yf can be calculated as follow

$$\mathrm{GCF} = \frac{0.3106(\sum_{i=1}^{n} a_i S_i)}{\sum_{i=1}^{n} a_i d_i c_{\mathrm{p}i}} \tag{A.1}$$

where a is the fraction flows of gas, S is the molecular structure factor, d is the density of gas (g/l), c_p is the specific heat at constant pressure of gas (cal/g/°C), and n is the number of gases in mixture gas.

The molecular structure correction factor for monoatomic gases, diatomic gases, triatomic gases and polyatomic gases (four or more atoms) is 1.30,1.00, 0.941, and 0.88, respectively. Thus, the GCF for R134a and R1234yf is 1.098 and 1.075, respectively. HFM-201 and Tylan FM-360 shows a mass flow rate of 0.72 g/s and 0.059 g/s corresponding to 1 V voltage signal for N_2. The mass flow rate calibration factor for R134a and R1234yf.

Table A.1 Mass flow rate (g/s) corresponding to 1 V voltage

	HFM 201	Tylan 360
N_2	0.72	0.059
R134a	0.8	0.065
R1234yf	0.774	0.063

Appendix B LDAQ and HDAQ Channel Allocation

Channel Number	LDAQ	HDAQ
AI-0	Discharge pressure	Compressor 1 displacement
AI-1	Evaporator inlet pressure	Compressor 2 displacement
AI-2	Suction pressure	Compressor 1 current
AI-3	Body pressure	Compressor 2 current
AI-4	Discharge temperature	Compressor voltage
AI-5	Condenser outlet temperature	Discharge pressure
AI-6	Evaporator inlet temperature	Evaporator inlet pressure
AI-7	Suction temperature	Suction pressure
AI-8	Evaporator outlet temperature	Body pressure
AI-9	Compressor 1 current	N/A
AI-10	Body temperature	N/A
AI-11	Evaporator wall temperature	N/A
AI-12	Main flow rate	N/A
AI-13	Bleed flow rate	N/A
AI-14	Compressor 1 displacement	N/A
AI-15	Compressor voltage	N/A
AO-0	Compressor stroke control signal	N/A
AO-1	Solenoid valve control signal	N/A

Appendix C Uncertainty Analysis

In the analysis of experimental results, key parameters such as power input, cooling capacity, CoP, and volumetric efficiency are not directly measured. The combined uncertainty for multiplying measurement can be calculated according to Eq. 3.6. The experiment using R134a at a condenser temperature of 45 °C, a compressor stroke of 12 mm, and a pressure ration of 2.5 is used for the case study of uncertainty analysis. The detailed parameters for the experiments are listed in Table A.2. As the transient current and voltage are used for power input uncertainty calculation, the detailed values of current and voltage are not given in Table A.2

Table A.2 Uncertainty of sensors and detailed experimental parameters

Type of sensor	Measurement	Uncertainty
Pressure transducer	Pd (11.88 bar)	±0.15 %
Pressure transducer	Ps (4.729 bar)	±0.15 %
Mass flow meter	$\dot{m}$ (1.89 g/s)	± 1 %
K-type thermocouple	Ts (21 °C)	± 1.5 °C
K-type thermocouple	Tcond (45.6 °C)	± 1.5 °C
LVDT	S (12 mm)	± 0.025 mm
I (A)	N/A	± 0.5 %
U (V)	N/A	± 0.5 %

The uncertainty of power input, cooling capacity, CoP, and volumetric efficiency can be calculated as follow:

Power Input:

The absolute uncertainty for transient power input $\Delta\dot{W}_{\mathrm{tran}}$ can be expressed as:

$$\Delta\dot{W}_{\mathrm{tran}} = \sqrt{(\frac{\partial\dot{W}}{\partial I} I_{\mathrm{mea}} Err_{\mathrm{I}})^2 + (\frac{\partial\dot{W}}{\partial U} U_{\mathrm{mea}} Err_{\mathrm{U}})^2} \tag{A.2}$$

where I_{mea} is the measured transient current, Err_{I} is the relative uncertainty for current transducer, U_{mea} is the measured transient voltage, and Err_{U} is the voltage transducer.

Thus, the absolute uncertainty for real power $\Delta\dot{W}_{\mathrm{real}}$ can be calculated as

$$\Delta\dot{W}_{\mathrm{real}} = \frac{1}{t}\int \Delta\dot{W}_{\mathrm{tran}}\mathrm{d}t \tag{A.3}$$

The relative uncertainty for power input can be calculated as

$$\Delta\dot{W}_{\mathrm{Perc}} = \frac{\Delta\dot{W}_{\mathrm{real}}}{\dot{W}} \tag{A.4}$$

Based on Eq A.2 and Eq A.3, the power input for linear compressor at the given conditions is 84.77 W with an absolute uncertainty of ±0.79 W and a relative uncertainty of 0.93%.

Cooling Capacity:

The absolute uncertainty of cooling capacity $\Delta\dot{Q}$ for the ORS is calculated as:

$$\Delta\dot{Q} = \sqrt{(\frac{\partial\dot{Q}}{\partial\dot{m}}\dot{m}Err_{\mathrm{m}})^2 + (\frac{\partial\dot{Q}}{\partial h}\frac{\partial h}{\partial T_{\mathrm{S}}}\Delta Err_{\mathrm{T}})^2 + (\frac{\partial\dot{Q}}{\partial h}\frac{\partial h}{\partial P_{\mathrm{S}}}P_{\mathrm{S}}Err_{\mathrm{P}})^2 + (\frac{\partial\dot{Q}}{\partial h}\frac{\partial h}{\partial T_{\mathrm{d}}}\Delta Err_{\mathrm{T}})^2 + (\frac{\partial\dot{Q}}{\partial h}\frac{\partial h}{\partial P_{\mathrm{d}}}P_{\mathrm{d}}Err_{\mathrm{P}})^2} \tag{A.5}$$

where Err_{m} is the relative uncertainty of mass flow meter, ΔErr_{T} is the absolute uncertainty of K-type thermocouple, and Err_{P} is the relative uncertainty of pressure transducer.

The relative uncertainty for cooling capacity can be calculated as

$$\Delta\dot{Q}_{\mathrm{Perc}} = \frac{\Delta\dot{Q}}{\dot{Q}} \tag{A.6}$$

Thus, the cooling capacity for the ORS at the given conditions is 285.8 W with an absolute uncertainty of 5.85 W and a relative uncertainty of 2%.

CoP:

The uncertainty of CoP ΔCoP for the ORS can be calculated as:

$$\Delta CoP = \sqrt{(\frac{\partial CoP}{\partial\dot{Q}}\Delta\dot{Q})^2 + (\frac{\partial CoP}{\partial\dot{W}}\Delta\dot{W}_{\mathrm{real}})^2} \tag{A.7}$$

The relative uncertainty for CoP can be calculated as

$$\Delta CoP_{\mathrm{Perc}} = \frac{\Delta CoP}{CoP} \tag{A.8}$$

Thus, the CoP for the ORS at the given conditions is 3.4 with an absolute uncertainty of 0.076 and a relative uncertainty of 2.2%.

Volumetric efficiency:

The uncertainty of volumetric efficiency $\Delta\eta_{\mathrm{V}}$ of the oil-free linear compressor can be calculated as:

$$\Delta\eta_{\mathrm{V}} = \sqrt{(\frac{\partial\eta_{\mathrm{V}}}{\partial\dot{m}}\dot{m}Err_{\mathrm{m}})^2 + (\frac{\partial\eta_{\mathrm{V}}}{\partial T_{\mathrm{s}}}\Delta Err_{\mathrm{T}})^2 + (\frac{\partial\eta_{\mathrm{V}}}{\partial S}\Delta Err_{\mathrm{S}})^2 + (\frac{\partial\eta_{\mathrm{V}}}{\partial P_{\mathrm{s}}}P_{\mathrm{s}}Err_{\mathrm{P}})^2} \tag{A.9}$$

where ΔErr_{S} is the absolute uncertainty of the LVDT.

The relative uncertainty for volumetric efficiency can be calculated as

$$\Delta\eta_{\mathrm{V\_Perc}} = \frac{\Delta\eta_{\mathrm{V}}}{\eta_{\mathrm{V}}} \tag{A.10}$$

The volumetric efficiency for the oil-free linear compressor at the given conditions is 0.4043 with an absolute uncertainty of 0.00093 and a relative uncertainty of 0.23%

Appendix D Main Code for ORS Model

```
% Import Recorded Data
exp_name2 = strcat('LDAQ_Selected.xls');
Data= xlsread(exp_name2);
fluid='R134a';

for i = 1:4 % NO of Experiments
dt = 0.00005; % sample rate sample/s
%% Define the Input Parameters for Compressor Model with Valve

Dp = 18.99/1000; % Piston Diameter m
A = 283.2303642/1000000; % Piston Area (m^3)
Ks = 16284.85; % Mechanical Stiffness (N/m)
DpC = 0.047503588; % Damping Coefficient (N*s/m)
M = 0.66; % Moving Mass kg

S0 = Data(i,23);
S = S0/1000; % Compressor Stroke (m)

f = Data(i,21); % Operating Frequency (Hz)
Fmax = Data(i,22); % Shaft Force N

Pd0 = Data(i,2);
Pd = Pd0*10^5; % Discharge Pressure (Pa)

Pb0 = Data(i,5);
Pb = (Pb0-1)*10^5;% Body Pressure (Pa)

Ps0 = Data(i,4);
Ps = (Ps0)*10^5;    % Suction Pressure (Pa)

Ts0 = Data(i,9);
Ts = Ts0+273.15; % Suction Temperature K

Td0 = Data(i,6);
Td2 = Td0+0+273.15; % Discharge Temperature K

Tb0 = Data(i,12);
Tb = Tb0+273.15; % Body Temperature K
```

```
Tw = 20+273.15; % Compressor Wall Temperature K


C = 12*10^(-6); % m Clearance Width
Vmean = 7.57*A/1000; % Cylinder Volume at the middle position
Entropy = refpropm('S','T',Ts,'P',Ps/1000,fluid); %Entropy
Td3 = refpropm('T','P',Pd/1000,'S',Entropy,fluid); %isothermal compression Tdis
Td = Td3;
% Rg kj/kg/k or j/g/K Checked should use j/kg/k here
Vmin = (7.57/1000-S/2)*A;
L = 31/1000; % Piston Length m
Vmid = 7.57/1000*A;
Molar= refpropm('M','T',Td,'P',Pd/1000,fluid);
Rg = 8.31*1000/Molar;
n = refpropm('K','T',Tb,'P',Pb/1000,fluid); %Ratio of specific heats
K = refpropm('L','T',Ts,'P',Ps/1000,fluid); %Thermal Conductivity (W/m/k)
Thermal_Diff = refpropm('%','T',Tb,'P',Pb/1000,fluid); % Thermal diffusity cm^2/s

%% Valve parameters
Alpha = 0.6; % Flow coefficient can lower than 0.6 due to lower clearance 0.5-1 0.6
Beta =0.85; % Thrust coefficient 0.5-1 0.85
Zeta =0.1; % %0.1

%% Discharge Valve Details

dv_thickness = 0.2; %mm
Max_dv_lift = 1.0; %mm 1.05
fdv = 405; % Hz
kdv =0.561*1000; % N/m 0.561*1000 10.561 5.865
ddv = 5/1000;    % mm
Ddv = 8/1000; % m
Adv = 0.25*pi()*ddv^2;
Mdv_equal = kdv/((2*pi()*fdv)^2); % kg
Cdv = 2*6*Zeta*(Mdv_equal*kdv)^0.5; % kg/s


%% Suction Valve Details

ds_thickness = 0.3; %mm
Max_sv_lift = 1; %mm
fsv = 246; % Hz
```

```
ksv = 0.361*1000; % N/mm 0.361*1000
dsv = 5/1000 ; % m
Dsv = 8/1000; % m
Asv = 0.25*pi()*dsv^2;
Msv_equal = ksv/((2*pi()*fsv)^2); % kg
Csv = 2*8*Zeta*(Msv_equal*ksv)^0.5; % kg/s

%% Dischagre
Density_dis = refpropm('D','T',Td,'P',Pd/1000,fluid); % (kg/m^3) Discharge
Rg_dis = refpropm('K','T',Td,'P',Pd/1000,fluid);
Cp_dis = refpropm('C','T',Td,'P',Pd/1000,fluid); % (kJ/kg*K) j/kg/k
Cv_dis = refpropm('O','T',Td,'P',Pd/1000,fluid); % (kJ/kg*Deg C)j/kg/k
DyV_dis = refpropm('V','T',Td,'P',Pd/1000,fluid);% Dynamic Viscosity (Pa*s)
Hdis = refpropm('H','T',Td,'P',Pd/1000,fluid); % Enthalpy
%% Suction
Density_suc = refpropm('D','T',Ts,'P',Ps/1000,fluid); % (kg/m^3)
Rg_suc =refpropm('K','T',Ts,'P',Ps/1000,fluid); % Isentropic index
Cp_suc = refpropm('C','T',Ts,'P',Ps/1000,fluid);% (kJ/kg*K)j/kg/k
Cv_suc = refpropm('O','T',Ts,'P',Ps/1000,fluid); % (kJ/kg*Deg C)j/kg/k
DyV_suc = refpropm('V','T',Ts,'P',Ps/1000,fluid);% Dynamic Viscosity (Pa*s)
Hsuc = refpropm('H','T',Ts,'P',Ps/1000,fluid); % Enthalpy
%% Body
Density_body = refpropm('D','T',Tb,'P',Pb/1000,fluid); % (kg/m^3)
Rg_body = refpropm('K','T',Tb,'P',Pb/1000,fluid);
Cp_body = refpropm('C','T',Tb,'P',Pb/1000,fluid); % (kJ/kg*K)j/kg/k
Cv_body = refpropm('O','T',Tb,'P',Pb/1000,fluid); % (kJ/kg*Deg C)j/kg/k
DyV_body = refpropm('V','T',Tb,'P',Pb/1000,fluid);% Dynamic Viscosity (Pa*s)
Hbody = refpropm('H','T',Tb,'P',Pb/1000,fluid); % Enthalpy


 sim('Compressor_Model_with_REFPROP_R134a_4th_good');

%% Data Logging for compressor
for j = 1:20001
Sim_DV_Lift(i,j) = ans.DV_lift(j);
Sim_SV_Lift(i,j) = ans.SV_lift(j);
Sim_M_dis(i,j) = ans.M_dis(j);
Sim_Pc(i,j) = ans.P_cylinder(j);
Sim_Vc(i,j) = ans.V_cylinder(j);
Sim_W_shaft(i,j) = ans.W_shaft(j);
Sim_Tc(i,j) = ans.T_cylinder(j);
Sim_X(i,j) = ans.Displacement(j);
```

```
Sim_Leak(i,j) = ans.Leak(j);
end

%% Data Processing
Sample_Per_cycle = (20000-mod(20000,f))/f;
n = 1;
  M_dis_sum(i) = 0;
  Tc_sum(i) = 0;
  W_shaft_sum(i) = 0;
  Tdis_sum(i) = 0;
  Bleed_flow_sum(i) = 0;
  count = 0;
for j = 20001-Sample_Per_cycle:20001
        DisPlacement(i,n) = Sim_X(i,j);
        Pc_plot(n,i) =    Sim_Pc(i,j);
        Vc_plot(n,i) =    Sim_Vc(i,j);
        W_shaft_plot(i,n) =    Sim_W_shaft(i,j);
        W_shaft_sum(i) = W_shaft_sum(i)+W_shaft_plot(i,n);
        M_dis_plot(i,n) = Sim_M_dis(i,j);
        M_dis_sum(i) = M_dis_sum(i)+M_dis_plot(i,n);
        Dv_lift_plot(n,i) = Sim_DV_Lift(i,j);
        Sv_lift_plot(n,i) = Sim_SV_Lift(i,j);
        Bleed_flow_plot(n,i)    = Sim_Leak(i,j);
        Bleed_flow_sum(i) = Bleed_flow_sum(i)+ Bleed_flow_plot(n,i);
        Tc_plot(n,i) = Sim_Tc(i,j);

        Tc_sum(i) =    Tc_sum(i)+Tc_plot(n,i);
        X_plot(n,1) = Sim_X(i,j);

        n = n+1;
end

%% Displacement
Top_x(i) = max(DisPlacement(i,1:Sample_Per_cycle));
Bot_x(i) = min(DisPlacement(i,1:Sample_Per_cycle));
Piston_offset(i) = Top_x(i)+Bot_x(i);
Displacement_sim(i) = (Top_x(i)-Bot_x(i))*1000;

% plot( Vc_plot(i,1:Sample_Per_cycle),Pc_plot(i,1:Sample_Per_cycle));
  Pshaft_sim(i) = -1*W_shaft_sum(i)/Sample_Per_cycle;
  Mass_flow_sim(i) = -0.58*(M_dis_sum(i)/Sample_Per_cycle);
  Mass_flow_sim2    =Mass_flow_sim(i)*2;
```

```
 Bleed_flow_sim(i) = -0.58*Bleed_flow_sum(i)/Sample_Per_cycle;
%% Cylinder Temperature and Discharge Temperature
Tc_average(i) = Tc_sum(i)/Sample_Per_cycle-273.15;
for     n = 1:Sample_Per_cycle
            if Dv_lift_plot(n,i) > 0
            Tdis_sum(i) =    Tdis_sum(i) + Tc_plot(n,i);
            count = count+1;
            end
end
Tdis_sim(i) = Tdis_sum(i)/count-273.15;
Td_sim = Tdis_sum(i)/count;

%% Condenser Calculation
      Ltotal = 2325/1000; %mm
      Di_HP = 12.7/1000;
      Do_HP = 16/1000;
      Dh_HP = Do_HP-Di_HP;
      Areage=0.0003/2.325; %Cross Section Condenser m^2
      G_HP=Mass_flow_sim2*10^-3/Areage; % kg/m^3/s
      c_HP = 16/12.7;
%% Evaporator Calculation
      c_LP = 11.16/7.9;
      Ltotal = 1280/1000; % m
      Dh_LP = (12.7-7.9-0.77*2)/1000;
      areage=77.66e-6; %m^2%Cross Section Evaporator m^2
      G_LP=Mass_flow_sim2*10^-3/areage; % kg/m^3/s
%% Heat Exchanger Model running
sim('Heat_Exchanger_R134a_3rd',0.1);

%% Data Logging for Heat Exchanger
M_evap_sim(i) = ans.M_evap(1);
M_cond_sim(i) = ans.m_cond(1);
M_Gas_Phase_sim(i) = ans.M_Gas_Phase(1);
M_Liquid_Phase_sim(i) = ans.M_Liquid_Phase(1);
M_Filter_sim(i) = ans.M_Filter(1);
Mtotal_sim(i) = ans.Mtotal(1);
Tcond_sim(i) = ans.Tcond_out(1);
Tcond_model_sim(i) = ans.Tcond_out1(1);
Tsuc_sim(i) = ans.Tsuc_evap(1);
dP_cond_sim(i) = ans.dP_cond(1);
dP_evap_sim(i) = ans.dP_evap(1);
Q_cooling_sim(i) = ans.Cooling_Capacity_sim(1);
```

```
%% Define the Data record
Record(i,1) = i;                                    % Test No
Record(i,2) = S0;                                   % Stroke
Record(i,3) = Displacement_sim(i);                  % Stroke_sim
Record(i,4) =    Data(i,20);                        % Real_Power
Record(i,5) = Pshaft_sim(i);                        % Shaft_Power_sim
Record(i,6) = Data(i,14);                           % Mass_flow
Record(i,7) = Mass_flow_sim(i);                     % Mass_flow_sim
Record(i,8) = Bleed_flow_sim(i);                    % Bleed Flow rate_sim
Record(i,9) =    Data(i,2);                         % Pdis
Record(i,10) = Ps0;                                 % Psuc
Record(i,11) = Td-273.15;                           % Tdis_adb
Record(i,12) = Tdis_sim(i);                         % Tdis_sim
Record(i,13) =    Data(i,7);                        % Tcond out
Record(i,14) = Tcond_sim(i)-273.15;                 % Tcond_out_sim
Record(i,15) = Ts0;                                 % Tsuc
Record(i,16) = Tsuc_sim(i)-273.15;                  % Tsuc_sim
Record(i,17) = dP_cond_sim(i);                      % Condenser Pressure Drop
Record(i,18) = dP_evap_sim(i);                      % Evaporator Pressure Drop
Record(i,19) = M_evap_sim(i);                       % M_evap
Record(i,20) = M_cond_sim(i);                       % M_cond
Record(i,21) = M_Gas_Phase_sim(i);                  % M_Gas_Phase
Record(i,22) = M_Liquid_Phase_sim(i);               % M_liquid_Phase
Record(i,23) = M_Filter_sim(i);                     % M_Filter
Record(i,24) = Mtotal_sim(i);                       % M_total
Record(i,25) = Tcond_model_sim(i);                  % T_cond_model2
Record(i,26) = Q_cooling_sim(i)/1000;               % Cooling_Capacity_Sim
Record(i,27) = Piston_offset(i);                    % Piston Offset
Record2 = [0];
for n = 1:Sample_Per_cycle
Record2(n,1) = Pc_plot(n,i)*10^-5;
Record2(n,2) = Vc_plot(n,i)*10^9;
Record2(n,3) = Tc_plot(n,i)-273.15;
Record2(n,4) = Dv_lift_plot(n,i)*1000;
Record2(n,5) = Sv_lift_plot(n,i)*1000;
Record2(n,6) = Bleed_flow_plot(n,i);
end
%% Data Record
      d = {'Test
No','Stroke','Stroke_sim','Real_Power','Shaft_Power_sim','Mass_flow','Mass_flow_sim',
'Bleed_flow_sim','Pdis','Psuc','Tdis_adb','Tdis_sim',...
            'Tcond out','Tcond_out_sim','Tsuc',...
```

```
            'Tsuc_sim',
'dP_cond_sim','dP_evap_sim','M_evap_sim','M_cond_sim','M_Gas_Phase_sim','M_Liq
uid_Phase_sim','M_Filter_sim','Mtotal_sim','Tcond_model_sim',...
            'Q_cooling_sim','offset',;' ','mm','mm','W','W','g/s','g/s','g/s','bar','bar','Deg
C','Deg C','Deg C','Deg C','Deg C','Deg C','bar','bar','g',...
            'g','g','g','g','g','K','W','mm',};
      Title = 'Pc','Vc','Tc','SV_Lift','DV_Lift','Bleed_flow', ;'bar','mm^3','Deg
C','mm','mm','g/s';
            file_name = strcat('Refrigeration Modelling Results','.xls');
            xlswrite(file_name,d,'sheet1', 'A1');
            xlswrite(file_name,Record,'sheet1', 'A3');

end
```

Appendix E Condenser Model

```
function [T_cond_out,M_cond,dp_cond]= fcn(Di,Dh,G_HP,Mass_flow,
Areage,Vl_HP,Vg_HP,Dg_HP,Dl_HP,c_HP,Prl_HP,Prg_HP,kl_HP,kg_HP,T_cond_sat
,Hdis,Hg_HP,Hl_HP,Cpl_HP)
x_HP=1:1000;
VF_HP=1:1000;
Nu = 1:1000;
Re = 1:1000;
h = 1:1000;
Percent_cond = 1:1000;
q_step = 1:1000;
A_two_Predict = 1:1000;
f_liquid= 1:1000;
X = 1:1000;
Phi = 1:1000;


    %% Calculate the Basic Parameters
      U = Mass_flow*10^-3/Dl_HP/(Areage); % % superficial velocity m/s
      Rel_HP = G_HP*Dh/Areage/Vl_HP;    % Re Number for liquid refringent
      Reg_HP = G_HP*Dh/(Areage)/Vg_HP;    % Re Number for gas refringent
      Q_two =    (Hg_HP-Hl_HP)*Mass_flow*10^-3;
      Q_gas=(Hdis-Hg_HP)*Mass_flow*10^-3; % Vapour Heat transfer



      H_cond = 0;
      dPg = 0;
      dPa = 0;
for j=1:1/0.001
            % Calculate the Void Fraction and Re Number
            x_HP(j)=-(j)*0.001+1; % x mass fraction

VF_HP(j)=hughmark3(x_HP(j),Dg_HP,Dl_HP,Vg_HP,Vl_HP,Mass_flow*1e-3);
            Re(j) = G_HP*Dh/((Vl_HP+VF_HP(j)*(Vg_HP-Vl_HP)));

            % Calculate the Nusselt Number
            Nu(j) =0.377967370352302*0.5*(c_HP./((c_HP+1).^-
0.001279003824478)).*(Re(j).^0.8).*(Prl_HP)^(1/3);
```

```
            h(j) = Nu(j).*(kl_HP)./Dh;
            H_cond = h(j)+H_cond;

            % Pressure Drop In Condenser (Gravity Lose)
            dPg = dPg+(VF_HP(j)*Dg_HP+(1-
VF_HP(j))*Dl_HP)*9.81*0.1478*0.135*0.001; % The pressure loss for gravity was
assumed only for two-phase due to the large percentage of the two-phase length
sin(135/4/(135^2/16+225^2)^0.5) % 0.135 is the hight of Condenser

            % Pressure Drop In Condenser (Acceleration Loss)
            dPa = dPa+G_HP*(x_HP(j)^2/(VF_HP(j)*Dg_HP)+(1-x_HP(j)^2)^2/((1-
VF_HP(j))*Dl_HP));

end

%% Determine the Two-Phase Length
L_two_Predict_cond = 0;

 for j=1:1/0.001
       % Predict the Two-Phase Length in the Condenser
            Percent_cond(j) = h(j)/H_cond; % the percentage of the Heat transfer for
single step according to total heat transfer coefficient
            q_step(j) = Q_two*Percent_cond(j); % the Heat transfer per step
            A_two_Predict(j) = q_step(j)/h(j)/2.3; %    heat transfer area per step
            L_two_Predict_cond =
L_two_Predict_cond+A_two_Predict(j)*10^6/12.7/pi();
 end

%% Calculate the Length of Gas phase
Nu_cond_gas3
=0.000262593510471631.*0.27*(c_HP./((c_HP+1).^1.09002732179146)).*(Reg_HP.^
0.915882127512914).*(Prg_HP)^(-2.44020843488143); % Gas Nussle number
correlation
h_cond_gas3 = Nu_cond_gas3.*(kg_HP)./Dh;
A_gas_Predict3 = Q_gas/h_cond_gas3/2.3; % (12.7*pi()*L_gas(i)/10^6);
L_gas_Predict3 = A_gas_Predict3*10^6/12.7/pi();
L_Gas_Two = L_gas_Predict3+ L_two_Predict_cond;

%% Calculate the Length of Liquid phase
if L_Gas_Two >=2325
      Lcond_liquid_predic = 0;
      Tcond_out_Predic = T_cond_sat;
```

```
else
    Lcond_liquid_predic = 2325-L_Gas_Two;
    Qcond_Liquid_prdict = Lcond_liquid_predic*Q_two/ L_two_Predict_cond;
    Tcond_out_Predic = T_cond_sat-Qcond_Liquid_prdict/(Mass_flow*Cpl_HP);

end


%% Calculate the Two-Phase pressure drop and Refrigerant Mass

L_two_step = L_two_Predict_cond/10^6;
dPtp = 0;
M_tp = 0;
 for j=1:1/0.001
        % Two-Phase Frictional Loss
        f_liquid(j) = (0.00725+0.076*(Rel_HP*c_HP^(-2))^(-0.25))/(c_HP)^0.5;
        dPl = 2*f_liquid(j)*Dl_HP*U^2/Di* L_two_step;
        X(j) = ((1-
x_HP(j))/x_HP(j))^0.9*(Dg_HP/Dl_HP)^0.5*(Vl_HP/Vg_HP)^0.1;
        Phi(j) = 1+10/X(j)+1/X(j)^2;
        dPtp    = dPtp + dPl* Phi(j);
       % Refrigerant Mass as Two-phase form

        M_tp=M_tp+(VF_HP(j)*Dg_HP+(1-
VF_HP(j))*Dl_HP)*Areage*L_two_step;
 end


    fl_cond = 0.079/Rel_HP^0.25;
    fg_cond = 0.079/Reg_HP^0.25;
    dPL = 4*fl_cond*(Lcond_liquid_predic*0.001/Dh)*G_HP^2/Dl_HP;
    dPV = 4*fg_cond*(L_gas_Predict3*0.001/Dh)*G_HP^2/Dg_HP;
    dp_cond =( dPtp+dPa+ dPg+dPL+dPV)/10^5;
    M_gas = L_gas_Predict3*Areage*Dg_HP;
    M_liquid = Lcond_liquid_predic*Areage*Dl_HP;
    M_two =    M_tp*1000;
    % Refrigerant Mass in Condenser
M_cond =
M_tp*1000+L_gas_Predict3*Areage*Dg_HP/1000+Lcond_liquid_predic*Areage*Dl_
HP/1000;
```

```
T_cond_out =    Tcond_out_Predic;
```

Appendix F Evaporator Model

```
function [T_suc,M_evap,Pd_evap]=
fcn(c_LP,Dh_LP,areage,Mass_flow,G_LP,Hcond_out,Hg_LP,Hl_LP,Vl_LP,Vg_LP,Dg
_LP,Dl_LP,Prg_LP,Prl_LP,T_suc_sat,ST,Cpg_LP,kl_LP,kg_LP)

Nu_evap = 1:1000;
Re = 1:1000;
h_evap = 1:1000;
X_LP = 1:1000;
VF =1:1000;
Percent = 1:1000;
q_step_evap = 1:1000;
A_two_Predict_evap = 1:1000;
fl = 1:1000;
fg = 1:1000;
pdl = 1:1000;
pdg = 1:1000;
XX = 1:1000;
We = 1:1000;
O = 1:1000;


%% Calculate the basic parameters
      Qe_two= (Hg_LP-Hcond_out)*Mass_flow*10^-3;
      Xin = (Hg_LP-Hcond_out)/(Hg_LP-Hl_LP);
      Rel_LP = G_LP*Dh_LP/areage/Vl_LP;    % Re Number for liquid refrigents
      Reg_LP = G_LP*Dh_LP/areage/Vg_LP;    % Re Number for gas refrigents

%%    Calculate the Heat transfer Coefficienct and Void Fraction


Hevap = 0;

for j = 1:1000
   X_LP(j) =j*(1.-Xin)/1000+Xin;
   VF(j)=hughmark2(X_LP(j),Dg_LP,Dl_LP,Vl_LP,Vg_LP,Mass_flow*1e-3); %voild
Fraction
   Re(j) =    G_LP*Dh_LP/((Vl_LP+VF(j)*(Vg_LP-Vl_LP)));
```

```
    Nu_evap(j) =
(0.1871594.*(c_LP./((c_LP+1).^0.0265)).*(Re(j).^0.8).*(Prl_LP)^(1/3));
    h_evap(j) = Nu_evap(j)*(kl_LP)/Dh_LP;
    Hevap = h_evap(j)+Hevap;

    end


%% Predicted Two-Phase Length
    L_two_Predict = 0;
    QEVAP = 0;
    m_tp = 0;
  for j=1:1/0.001

            Percent(j) = h_evap(j)/Hevap;
            q_step_evap(j) = Qe_two*Percent(j);
            QEVAP = q_step_evap(j)+ QEVAP;
            A_two_Predict_evap(j) = q_step_evap(j)/h_evap(j)/2; %
(12.7*pi()*L_gas(i)/10^6);
            L_two_Predict = L_two_Predict+A_two_Predict_evap(j)*10^6/7.9/pi();
end




% para= [608.948913703319,-0.000879197419872556,0.0184892924576491,-
0.000145504641325100];
%% Gas Length
Nu = 608.948913703319.*(c_LP./((c_LP+1).^-
0.000879197419872556)).*(Reg_LP.^0.0184892924576491).*(Prg_LP)^-
0.000145504641325100; %[-1.693616695239245e-06,-0.889662502137089,-
0.172038565848078,-0.163392322990127]
h_evap_gas = Nu.*(kg_LP)./Dh_LP;
%    q =h_evap_gas.*l_gas*7.9*pi().*2*10^-6;    % [-
1.082143174860021e+02,47.974831360653276,1.216414993195849,-
78.353083496415020]

%    Predicted Tsuc
l_gas_predict = 1280-L_two_Predict;
q_superheat = h_evap_gas.*l_gas_predict*7.9*pi().*0.5*10^-6;
Tsuc_predict = q_superheat*1.2/Cpg_LP/(Mass_flow*10^-3)+T_suc_sat;
Ts_prdicC = Tsuc_predict-273.15;
```

```
%% Pressure Drop and Refrigerant Mass
  Pd_evap    = 0;
l_step = L_two_Predict/10^6;
for j=1:999
  % Accerlerating pressure drop
       c1 = ((1- X_LP(999))^2)/(Dl_LP*(1-VF(999)));
       c2 = (X_LP(999)^2)/(Dg_LP*VF(999));
       c3 = ((1-X_LP(1))^2)/(Dl_LP*(1-VF(1)));
       c4 = (X_LP(1)^2)/(Dg_LP*VF(1));
       Pda = (G_LP^2)*(c1+c2-c3-c4)/100000;

       % frictional pressure drop
     fl(j) = 64/Rel_LP;
     fg(j) = 64/Reg_LP;
     pdl(j) = fl(j)*2*(G_LP*(1-X_LP(j)))^2*l_step/(Dl_LP*Dh_LP);
     pdg(j) = fg(j)*2*(G_LP*X_LP(j))^2*l_step/(Dg_LP*Dh_LP);

     A2 = (pi()*(12.7-0.77*2)^2/4-pi()*7.9^2/4)/1000000;
     XX(j) = ((fl(j)/ fg(j))^(0.5))*((1-X_LP(j))/(X_LP(j))).*(Dg_LP/Dl_LP)^0.5;
     We(j) = (Mass_flow*0.001)^2*Dh_LP/(A2^2*(Dl_LP*(1-
VF(j))+Dg_LP*VF(j))*ST);
     O(j) = 1+(1192.59571216070*We(j).^(-
0.793104586985613).*Re(j).^(1.23))/XX(j)+1/(XX(j))^2; % [1192.59571216070,-
0.793104586985613]
     Pd_evap =    Pd_evap +O(j)*pdl(j)/10^5+Pda/999; %[0.110097832415533,-
1.16497012645422], [0.553582113960738,-1.16498308032863]
     m_tp=m_tp+(VF(j)*Dg_LP+(1-VF(j))*Dl_LP)*areage*l_step;
end
  M_test=(VF(1)*Dg_LP+(1-VF(1))*Dl_LP)*2.46E-05;
  M_evap =( m_tp+L_two_Predict*areage*Dg_LP/1000+M_test)*1000;


  T_suc =    Tsuc_predict;
```

Publications

1. **Z. Li**, K. Liang*, and H. Jiang, “Thermodynamic analysis of linear compressor using R1234yf.” *International Journal of Refrigeration*, vol. 104, pp. 530-539, 2019. (associated with Chapter 3 and 4)

2. **Z. Li**, H. Jiang, X. Chen, and K. Liang*, “Comparative study on energy efficiency of low GWP refrigerants in domestic refrigerators with capacity modulation.” *Energy and Buildings*, vol. 192, pp. 93-100, 2019. (associated with Chapter 5)

3. **Z. Li,** K. Liang*. and H. Jiang, “Experimental study of R1234yf as a drop-in replacement for R134a in an oil-free refrigeration system.” *Applied Thermal Engineering*, vol. 153, pp. 646-654, 2019. (associated with Chapter 3 and 6)

4. **Z. Li**, H. Jiang, X. Chen, and K. Liang*, “Evaporation heat transfer and pressure drop of low-GWP refrigerants in a horizontal tube.” *International Journal of Heat and Mass Transfer*, vol. 148, pp. 119-150, 2020. (associated with Chapter 3 and 7)

5. **Z. Li**, H. Jiang, X. Chen, and K. Liang*, “Optimal refrigerant charge and energy efficiency of an oil-free refrigeration system using R134a.” *Applied Thermal Engineering*, 164, p.114473, 2020. (associated with Chapter 3 and 8)

6. X. Chen, **Z. Li** *, Y. Zhao, H. Jiang, K. Liang *. and J. Chen*, “Modelling of refrigerant distribution in an oil-free refrigeration system using R134a.” *Energies*, vol. 12, no. 24, p.4792, 2019. (associated with Chapter 3 and 8)

7. **Z. Li**, and K. Liang*, and H. Jiang, "Performance of an oil-free linear compressor using R1234yf." in *Proceedings of 1st IIR International Conference on the Application of HFO Refrigerants*. Vol. 1128. International Institute of Refrigeration, 2018.

8. **Z. Li**, and K. Liang*, and H. Jiang, “Experimental study of R1234yf as a low global warming potential alternative for R134a in an oil-free vapour compression refrigeration system.” in *Proceedings of the 25th IIR International Congress of Refrigeration*: Montréal, Canada, August 24-30, 2019.

9. **Z. Li**, and K. Liang*, and H. Jiang, “Performance of an oil-free vapour compression refrigeration system using R134a.” in *Proceedings of the 25th IIR International Congress of Refrigeration*: Montréal, Canada, August 24-30, 2019.

10. K. Liang*, **Z. Li**, M. Chen, and H. J. A. T. E. Jiang, "Comparisons between heat pipe, thermoelectric system, and vapour compression refrigeration system for electronics cooling," *Applied Thermal Engineering*, vol. 146, pp. 260-267, 2019.

11. H. Jiang, K. Liang*, and **Z. Li**, "Characteristics of a novel moving magnet linear motor for linear compressor," *Mechanical Systems Signal Processing*, vol. 121, pp. 828-840, 2019.

12. H. Jiang, **Z. Li,** and K. Liang*, "Performance of a linear refrigeration compressor with small clearance volume," *International Journal of Refrigeration,* vol. 109, pp. 105-113, 2020.

13. H. Jiang, **Z. Li**, and K. Liang*, "A Novel Sensor-less Stroke Detection Technique using Low-cost Inductive Coil for Resonant Free-Piston Machines," *IEEE Transactions on Industrial Electronics*, accepted for publication, 2020.

14. H. Jiang, K. Liang*, **Z. Li**, Z. Zhu, X. Zhi, and L. Qiu, "A sensor-less stroke detection technique for linear refrigeration compressors using artificial neural network," *International Journal of Refrigeration*, vol. 114, pp. 62-70, 2020.

15. X. Chen, H. Jiang*, **Z. Li**, and K. Liang*, "Modelling and Measurement of a Moving Magnet Linear Motor for Linear Compressor," *Energies*, vol. 13, no. 15, p. 4030, 2020.